PREDICTIVE MODELING AND MULTI-OBJECTIVE OPTIMIZATION OF MACHINING-INDUCED RESIDUAL STRESSES: INVESTIGATION OF MACHINING PARAMETER EFFECTS

by

DURUL ULUTAN

A dissertation submitted to the

Graduate School–New Brunswick

Rutgers, The State University of New Jersey

In partial fulfillment of the requirements

For the degree of

Doctor of Philosophy

Graduate Program in Industrial and Systems Engineering

Written under the direction of

Assoc. Prof. Tuğrul ÖZEL

And approved by

_____

_____

_____

_____

New Brunswick, New Jersey

JANUARY 2013

ABSTRACT OF THE DISSERTATION

PREDICTIVE MODELING AND MULTI-OBJECTIVE OPTIMIZATION OF MACHINING-INDUCED RESIDUAL STRESSES: INVESTIGATION OF MACHINING PARAMETER EFFECTS

by DURUL ULUTAN

Dissertation Director:

Assoc. Prof. Tuğrul ÖZEL

In the aerospace industry, titanium and nickel-based alloys are frequently used for critical structural components, especially due to their higher strength at both low and high temperatures, and higher wear and chemical degradation resistance. However, because of their unfavorable thermal properties, deformation and friction-induced microstructural changes prevent the end products from having good surface integrity properties. In addition to surface roughness, microhardness changes, and microstructural alterations, the machining-induced residual stress profiles of titanium and nickel-based alloys contribute in the surface integrity of these products. Therefore, it is essential to create a comprehensive method that predicts the residual stress outcomes of machining processes, and understand how machining parameters (cutting speed, uncut chip thickness, depth of cut, etc.) or tool parameters (tool rake angle, cutting edge radius, tool material/coating, etc.) affect the machining-induced residual stresses. Since experiments involve a certain

amount of error in measurements, physics-based simulation experiments should also involve an uncertainty in the predicted values, and a rich set of simulation experiments are utilized to create expected value and variance for predictions.

As the first part of this research, a method to determine the friction coefficients during machining from practical experiments was introduced. Using these friction coefficients, finite element-based simulation experiments were utilized to determine flow stress characteristics of materials and then to predict the machining-induced forces and residual stresses, and the results were validated using the experimental findings. A sensitivity analysis on the numerical parameters was conducted to understand the effect of changing physical and numerical parameters, increasing the confidence on the selected parameters, and the effect of machining parameters on machining-induced forces and residual stresses was also investigated. Finally, these predictions were inputted to a multi-objective optimization methodology utilizing Particle Swarm Optimization algorithm to select the optimal machining parameters where competing or conflicting objectives constitute hurdles in the decision-making process of manufacturing plans in the industrial applications.

ACKNOWLEDGEMENTS

Throughout the few years I worked towards my PhD study, I have had my share of adventures that brought me to this day, and I would not be able to overcome various obstacles along the road without the support of several people. I would like to take this opportunity to express my appreciation and gratitude to them.

My advisor Dr. Tuğrul Özel has been a great mentor, supporting and guiding me through my studies at Rutgers University. I would like to thank him for believing in me and encouraging me in my academic efforts as well as in my personal endeavors.

I appreciate the sound advice and constructive suggestions of my committee members: Dr. Melike Baykal-Gürsoy, Dr. James T. Luxhøj, and Dr. Haim Baruh.

I cannot thank enough the administrative and technical support I received from Ms. Cindy Ielmini, Ms. Helen Pirello, and Mr. Joe Lippencott.

I would also like to thank the National Science Foundation for funding my research via graduate research assistantships and Rutgers University Industrial and Systems Engineering Department for offering teaching assistantships that improved me as a teacher.

I want to thank all my friends and family members for having faith in me and motivating me in pursuing my ambitions.

Finally, I feel indebted to my wife, Gizem Surenkok for her love, support, understanding and sacrifices through all these years and standing by my side with her never ending trust and encouragement in my passion and dream. I dedicate this to you.

TABLE OF CONTENTS

LIST OF TABLES

LIST OF ILLUSTRATIONS

LIST OF SYMBOLS

A,B,C	Original JC material model coefficients
a-$h_{1\text{-}2}$	Coefficients of the non-linear relationships
a,b,d,p,p_2,r,s	Modified JC material model coefficients
b	Depth of cut
$c_{1\text{-}2}$	Acceleration terms used in Particle Swarm Optimization
c_p	Specific heat capacity
D,D_2	Modified JC material model coefficient
E	Young's Modulus
F_c	Total cutting force
F_f	Total feed force
F_{c_0}	Cutting force for the 3rd zone – ploughing or edge components
F_{f_0}	Feed force for the 3rd zone – ploughing or edge components
$F_{i,exp}$	Experimental value of force components
$F_{i,sim}$	Simulated value of force components
$F_{n_{1-3}}$	Normal force components
$F_{n_{1-3_c}}$	Cutting force components due to normal stresses
$F_{n_{1-3_f}}$	Feed force components due to normal stresses
F_p	Total thrust force
$F_{t_{1-3}}$	Tangential force components
$F_{t_{1-3_c}}$	Cutting force components due to tangential stresses
$F_{t_{1-3_f}}$	Feed force components due to tangential stresses

$gbest$	Global best solution in Particle Swarm Optimization
h	Heat transfer coefficient
l_c	Chip-tool contact length along the tool rake face
l_p	Plastic contact length along the tool rake face
M	Number of simulations in a set of experiments
m,n	Original JC material model coefficients
m	Exponential coefficient for Region III & Friction factor
N	Number of dimensions in a set of experiments & Number of elements in a mesh
n	Exponential coefficient for Region I
PTS	Peak tensile residual stress
PCS	Peak compressive residual stress
$pbest_i$	Personal best solution of particle i in Particle Swarm Optimization
RS	Residual Stress
r_β	Cutting edge radius
T	Temperature
T_0	Ambient temperature
T_m	Melting temperature
t_u	Uncut chip thickness
VB	Tool flank wear length
V_c	Cutting speed
v_i^k	Velocity of a particle i at generation k for the Particle Swarm Optimization
$x_{1\text{-}2}$	Distance along the rake and flank faces from edge face

x_i^k	Position of a particle i at generation k for the Particle Swarm Optimization
α	Angle measured from cutting speed direction for Region II
α_0	Starting angle for Region II
α_f	Final angle for Region II
α_t	Thermal expansion constant
$\beta_{0,1,2,11,12,22}$	Coefficients of regression equations
γ_1	Rake angle
γ_2	Clearance angle
γ_s	Stagnation point angle
δ	Random number used to avoid local minima in Particle Swarm Optimization
ε	True strain
ε_{tot}	Total resultant error of a set of simulations
$\dot{\varepsilon}_0$	Reference true strain rate
$\dot{\varepsilon}$	True strain rate
θ	Tool flank wear angle & Incident beam half angle
λ	Thermal conduction coefficient & Radiation beam wavelength
μ	Mean friction coefficient
μ_{ap}	Apparent friction coefficient
μ_{sl}	Sliding friction coefficient
μ_1	Friction coefficient along the rake face
μ_2	Friction coefficient along the flank face
σ	Flow stress & Normal stress

σ_{1-3}	Normal stress at the rake, edge, and flank faces
$\sigma_{1_{max}}$	Maximum normal stress at the rake face
$\tilde{\sigma}_2$	Normal stress at the stagnation point in Region II for the worn tool
$\sigma_{3_{max}}$	Maximum normal stress at the flank face
σ_{std}	Standard deviation
τ_{1-3}	Shear stress at the rake, edge, and flank faces
$\tau_{1_{max}}$	Maximum shear stress along the tool rake face
$\tilde{\tau}_2$	Frictional shear stress at the stagnation point in Region II for the worn tool
$\tau_{3_{max}}$	Maximum shear stress along the tool flank face

CHAPTER 1

INTRODUCTION

1. Introduction

Manufacturing of titanium alloys and nickel-based super alloys that are critical structural components of the aerospace industry is an important issue, since these alloys are mostly very difficult to machine at productive regimes due to their low thermal conductivity and modulus of elasticity, and high chemical affinity with tool materials. These difficulties in machining usually result in unfavorable accuracy of the machined product dimensions, or end product quality issues such as surface integrity and lower lifetime proneness. The final manufacturing processes such as finish machining and grinding are, in general, decisive about the product surface quality, therefore finish machining processes need to be controlled and optimized in order to achieve required product quality and accuracy and prolonged service life. Surface integrity after finish machining determines the performance and quality of the end product, and it includes the mechanical properties such as residual stresses and hardness, metallurgical states of the material such as phase transformation and microstructural changes, and topological parameters such as surface roughness. When high reliability levels for the critical structural components are required, the residual stresses created by the machining processes become the most important issue in evaluating the surface integrity of the product, hence its quality and performance capabilities.

In order to adjust the mechanical, metallurgical, and topological properties of the end product as required, input parameters for the machining process such as cutting

speed, feed rate, depth of cut, cutting tool geometry and material, or tool coating are changed. However, experimentation for every possible combination of these parameters (as well as many others) would be highly impractical if not impossible. Hence, selected representative combinations of these parameters would be experimentally evaluated to determine the possible outputs for those inputs. From those experimental results, process simulations are designed to represent the experiments in the computational domain, and after validation, these simulations are utilized to predict the effects of each input parameter on each output parameter. It is essential that these process simulations are physics-based, as the physics of the problem is very complicated to be solved analytically and should be well understood and incorporated into the simulations for accuracy in predicting.

There are many different methods to simulate the physics of machining processes, but Finite Element Analysis (FE or FEA) has been found through time to simulate the mechanics with more accuracy and ease. In FEA, the machining tool and the machined workpiece are both divided into smaller elements and the interactions of these elements between and within each other are investigated separately but simultaneously. In order to simulate a machining process that takes time in the order of few seconds, the simulation only moves in the order of microseconds at each step, and after every step, the interactions between every element are investigated and updated. When enough number of steps is achieved to simulate the machining process, the output parameters can be extracted and validated with the experiments.

The easiest way, both experimentally and in terms of simulations, to understand the physics of machining is to design and conduct two-dimensional experiments, where

the effects of the third dimension would be zeroed in theory, and minimized in practice. Then, these two-dimensional findings are converted into three dimensional mechanics and dynamics using the angles of three dimensional machining processes. However, it is both not possible to convert two-dimensional experiments/simulations to some of three-dimensional counterparts, and not representative enough. Hence, after two-dimensional practices, three-dimensional experimentations and validations also follow most of the time for more accurate information about the processes. The main disadvantage of the three-dimensional (3D) process simulations is that their run-time is considerably more than two-dimensional (2D) process simulations. In addition, with the current level of technology in FEA software, it is not optimal to run three-dimensional (3D) process simulations with elastic-viscoplastic workpiece assumption for titanium alloys such as Ti-6Al-4V and nickel-based superalloys such as IN-100 and IN-718, but it is possible and more practical to run these process simulations in two-dimensional solution space under plain strain assumption. Therefore, best approximation to this technological constraint is to run two-dimensional process simulations with elastic-viscoplastic workpiece, and use their results of predicted forces, stress, strain and temperature fields to validate and calibrate three-dimensional process simulations with plastic workpiece assumptions. Then, it is possible to safely use plastic workpiece assumption in three-dimensional FE-based process simulations.

The main parameter that cannot be directly measured during machining, but is very important in determining the outputs of the process, is the friction coefficient between the cutting tool and the machined workpiece. This coefficient affects the stress distributions and frictional forces, which cause additional temperature rise during

machining. Together, cutting forces and temperatures create mechanical and thermal loads on machined workpiece, which increase stress and strain, eventually changing residual stresses and thickness of the affected surface layers during machining. In the end, these stresses and mechanical/metallurgical/topological changes in the surface layer affects product reliability. Thus, it is essential to study and optimize the friction coefficients during machining to get desired results, and validate these coefficients by process simulations, which is possible by validating the cutting forces, temperatures, and stresses.

After the process simulation results are validated with experimentations, using them to predict further machining conditions becomes possible. However, these process simulations can only predict the experimental findings with some certainty, giving a mean and a standard deviation of the output parameters. As much as it is essential to correctly predict the experimental results with the mean of simulation findings, it is also important to reduce the standard deviation of the predictions obtained through simulations so that they can be valuably utilized in the industry for process design and planning. Hence, an optimization procedure including both reducing the error between the experimental results and simulation results, as well as the standard deviation of the predictions, is necessary.

In summary, it is essential to study the machining processes of titanium and nickel-based alloy parts used in the aerospace industry, in order to optimize their end product quality and performances, and using experimental results to validate the results of FEA-based simulations, it is possible to simulate the effects of input parameters of the machining processes and select the optimal machining and tool parameters (tool material,

coating, tool angles, edge micro-geometry, etc.). Determining the coefficients of friction between the cutting tool and the machined workpiece is the first step to start the validation, and after the coefficients are validated, it is possible to utilize them in conducting simulations to achieve a mean and standard deviation of output parameters to be optimized. Optimized output parameters can then be used in industrial applications. These methods to achieve the aforementioned goals are described in summary below, and the details can be found through this dissertation.

1.1 Aerospace Alloy Manufacturing

Mission-critical parts in the aerospace industry are considered to be hard-to-machine, due to their mechanical properties. Therefore, optimizing their machining has been a point of emphasis. Titanium alloys (e.g. Ti-5Al-2.55n (alpha), Ti-13V-11Cr-3AL (beta) or Ti-6Al-4V (alpha-beta)) offer high strength-to-weight ratio, toughness, corrosion and creep resistance, and bio-compatibility, and are used mainly in aerospace (e.g. jet engine sections in Figure 1.1), gas turbine, rocket, nuclear, chemical vessels and increasingly in biomedical applications (M'Saoubi et al. 2008, Guo et al. 2009, Wu 2007). Recent developments in technology have made it possible for titanium and its alloys to be used more frequently in the industry, mainly because of increased machinability of these alloys. The major challenge against machining titanium alloys besides low machinability and tool wear has been determined as machined surface quality, but compared to many nickel-based alloys used in the aerospace industry such as IN-718 and IN-100, they still offer higher machinability and lower machining temperatures (Kitagawa et al. 1997, Mantle & Aspinwall 1997, Zoya & Krishnamurthy 2000, Che-Haron 2001, Mantle & Aspinwall 2001, Rahman et al. 2003, Che-Haron &

Jawaid 2005, Wang et al. 2005). Most widely-studied titanium alloy has been Ti-6Al-4V, or shortly Ti-64, due to its heavy utilization in the aerospace industry (Chen et al. 2004, Che-Haron & Jawaid 2005, Wang et al. 2005, Nurul-Amin et al. 2007, Sun et al. 2009, Sun & Guo 2009, Thomas et al. 2010). Aircraft of near future are expected to use excessive amounts of carbon fiber compounds that utilize titanium and its alloys, especially if the machinability and productivity of these alloys can be increased via studies on their properties and interactions between those and tool materials.

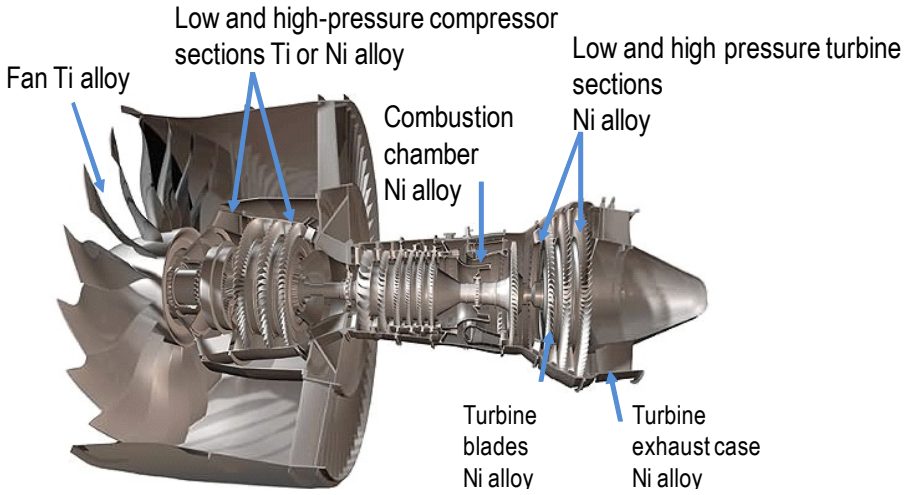

Figure 1.1: Cross section of a jet engine (courtesy of Pratt & Whitney)

On the other hand, nickel-based alloys such as Ni-Co-Cr, Ni-Fe-Cr or Ni-Co-Fe have the ability to retain most of their strength even after long exposures to extremely high temperatures and are the only materials of choice for turbine sections of jet engines (Wu 2007, M'Saoubi et al. 2008, Guo et al. 2009). Nickel-based alloys are typically available in wrought, forged, cast and sintered (powder metallurgy) forms and are often used in the hot sections of mission-critical components in jet engines or gas turbine engines. For example, 50% of the weight of a jet engine is Inconel 718 (IN-718), a Ni-Fe-Cr alloy. This alloy exhibits very high strength and temperature resistance, but it is

difficult to machine this alloy due to these properties, causing low tool life for the tools to machine it (Sharman et al. 2004). Because of these reasons, this alloy has been studied extensively in the literature (Sadat 1987, Sadat et al. 1991, Ezugwu & Tang 1995, Liao & Shiue 1996, Derrien & Vigneau 1997, Kitagawa et al. 1997, Rahman et al. 1997, Ezugwu et al. 1999, Darwish 2000, Li et al. 2002, Schlauer et al. 2002, Arunachalam et al. 2004a&b, Coelho et al. 2004, Guerville & Vigneau 2002, Dudzinski et al. 2004, Mitrofanov et al. 2004, Sharman et al. 2004&2006&2008, Zhang et al. 2004, Axinte et al. 2006, Aspinwall et al. 2007, Pawade et al. 2007, Uhlmann et al. 2007, Outeiro et al. 2008, Pawade et al. 2008, Courbon et al. 2009, Jemielniak 2009, Lorentzon et al. 2009, Lu & Guo 2009, Pawade et al. 2009, Ranganath et al. 2009b). Another mission-critical nickel-based alloy is Inconel 100 (IN-100), which was not as widely investigated (Ranganath & Guo 2009a) because of its more recent discovery.

Due to high toughness and work hardening behavior of these alloys, machining is generally extremely difficult. Several research studies have been reported in the literature addressing issues related to machining of titanium and nickel-based alloys such as rapid tool wear and undesirable alteration of machined surfaces as workpiece easily forms a work hardened layer in response to the machining-induced strain loading on the subsurface. Low thermal conductivity of such alloys often leads to increased temperatures at the tool cutting edge and results in adhesion of workpiece material to the cutting edge and presence of hard abrasive particles in alloys structure creating accelerated tool wear. High localized heat, increased temperatures, temperature gradients and high pressure induced stresses also cause microstructural changes creating surface

integrity problems within the material in-depth direction and may cause detrimental effects on the performance of the machined part (Ulutan & Özel, 2011).

1.2 Surface Integrity

Surface integrity of machined products includes many different properties that contribute to the reliability of the part in use. Together, they directly influence part processing through a) frictional and wear behavior at the interfaces of bodies in contact, b) effectiveness and control of lubrication during processing (forging, stamping, rolling) and in end use (bearing, shafts, all rotating and moving elements), c) appearance and role of surface in subsequent surface finishing operations (cleaning, coating, or surface treating), d) initiation of surface cracks and residual stresses that influence fatigue life and corrosion properties, and e) heat transfer and electrical conductivity between two bodies contacting each other (Ghanem et al. 2002).

A typical surface of metals includes a contaminated thin layer (1-10 nm), an oxidation layer (10-100 nm) followed by a work hardened layer whose thickness depends on material processing conditions and the environment. Unless the metal is processed and kept in an inert (oxygen free) environment, or it is a noble metal, an oxide layer usually develops on top of the work-hardened or amorphous layer (Kalpakjian & Schmid 2007). At microscale, surface layer of a manufactured part is not smooth and may show various different features: microcracks, craters, folds, laps, seams, inclusions, plastic deformations, residual stresses, oxide layers, and metallurgical transformations (heat affected zone, decarburization, recast layer, phase transformation, alloy depletion). The surface layer characteristics that can change through processing include plastic deformation, residual stresses, cracks, hardness, overaging, phase changes,

recrystallization, intergranular attack, and hydrogen embrittlement. When a machining process is applied, the surface layer sustains local plastic deformation. Surface integrity of the final part is crucial in machining processes. In most applications, having the smoothest possible surface is desired, especially when the fatigue life of a machined part is important (Novovic et al. 2004). However, in some cases, having a rougher surface can be preferred. These cases generally occur in the biomedical field (Chrzanowski et al. 2008). A classification of the surface integrity features is presented below.

1.2.1 Surface Defects

During machining, there are many reasons for the machined surface to start creating some surface defects. These defects usually stay on the surface and create reliability issues for the end product, so they should be removed when necessary by post-processing. Most of these defects cannot be quantified, and preventing them from happening is not easy either. Main forms of surface defects are surface drag, material pull-out/cracking, feed marks, adhered material particles, tearing surface, chip layer formation, debris of microchips, surface plucking, deformed grains, surface cavities, slip zones, laps (material folded onto the surface), and lay patterns (Field et al. 1974, Mantle & Aspinwall 1997, Dudzinski et al. 2004, Sharman et al. 2004, Axinte et al. 2006, Pawade et al. 2007, Pawade et al. 2008, Ginting & Nouari 2009, Ranganath et al. 2009b, Zou et al. 2009). Some of these defects are shown in Figure 1.2. One way to minimize such defects is adjusting the temperature of the process so that thermal softening of the material is increased, which helps compressive stresses to be increased and such surface flaws to clear out of the machined surface (Pawade et al. 2007). This was also shown to

help to enable the workpiece to reconstruct its surface layer easily, also helping decreasing the number and effect of these defects.

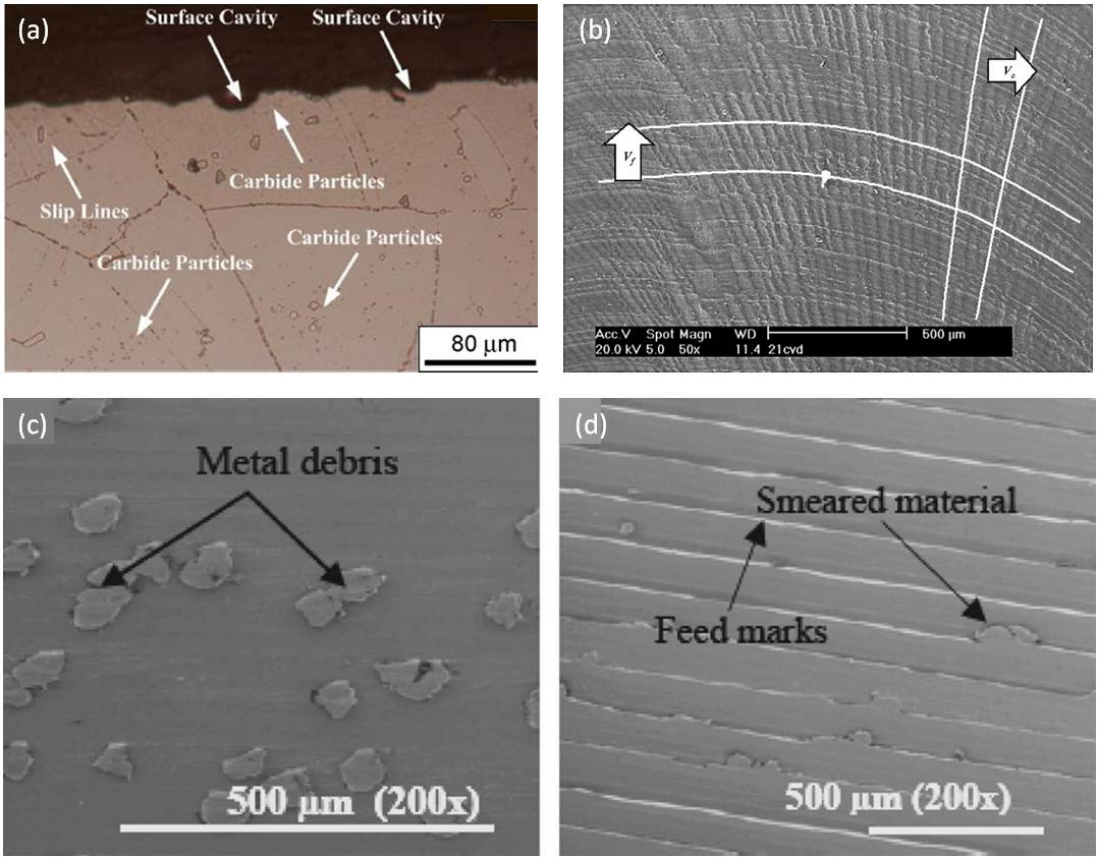

Figure 1.2: Surface damages in machining of nickel-based and titanium-based alloys: (a) Metallographical microstructure (Zou et al. 2009), (b) lay pattern (Ginting & Nouari 2009), (c) metal debris (Pawade et al. 2007), and (d) smeared material and feed marks (Pawade et al. 2007)

1.2.2 Microstructural Alterations

During machining operations, workpiece material is exposed to thermal, mechanical, and chemical energy that can lead to strain aging and recrystallization of the material. Due to the strain aging process, the material may become harder but less ductile, and recrystallization may cause the material to become softer but more ductile.

These thermal (high temperature and rapid quenching) and mechanical (high stress and strain) effects are the main reasons for the microstructural alterations in the material, as well as phase transformations and plastic deformations (Yang & Liu 1999). Studies showed that a very thin layer of plastic deformation was formed in the immediate subsurface of the workpiece, and as the tool wears out, plastic deformation and subsequently the thickness of the deformed layer was increased, due to microstructural alterations (Che-Haron 2001, Sharman et al. 2004, Che-Haron & Jawaid 2005). The immediate subsurface of the workpiece affected by machining was observed to exhibit different behavior than the interior (bulk) of the material. The most important different behavior of this layer was that this layer was harder than the bulk of the workpiece material. This layer was observed to be white under optical microscope; hence it is called the 'white layer' (Figure 1.3). It is often accompanied by a 'dark layer', which exhibits material properties that are in between the white layer and bulk workpiece material, and these layers are highly unpredictable. White layer generally possesses fine grains, in some cases a nanocrystalline structure. It is harder than the bulk material but more brittle, which eases crack development and propagation in the material (Zhang et al. 1997).

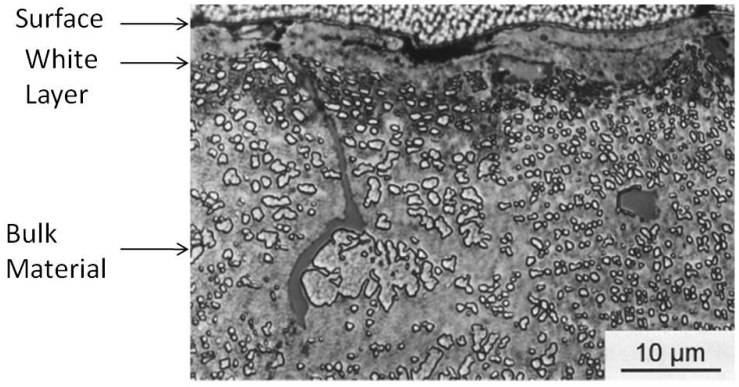

Figure 1.3: Layers created after grinding a nickel-based alloy (Österle & Li 1997)

1.2.3 Work Hardening Layer and Microhardness

Workpiece surfaces are usually created by successive machining passes such as roughing, semi-finishing, and finishing. Characteristics of machined surface layer created by sequent machining passes may have significant influence on the machining performance. This influence becomes more important for materials that exhibit high work-hardening behavior such as nickel-based alloys (Lu & Guo 2009). Workpiece easily forms a work hardened layer in response to machining-induced deformations on the subsurface. This is mainly due to work hardening tendency of nickel-based alloys under excessive strain loading, creating a highly hardened surface layer and making it extremely difficult for sequential cuts. Depth of cut in sequential cuts should be kept greater than work-hardened layer thickness, which presents a difficult problem for industrial applications (Lu & Guo 2009, Özel 2009). Hardness of material after being machined has been found to be greater on the surface of the material than through the depth of the material, where heat and strain effects are neutralized, due to this work-hardening behavior (Coelho et al. 2004). A sample microhardness graph for machined Ti-64 can be found in Figure 1.4.

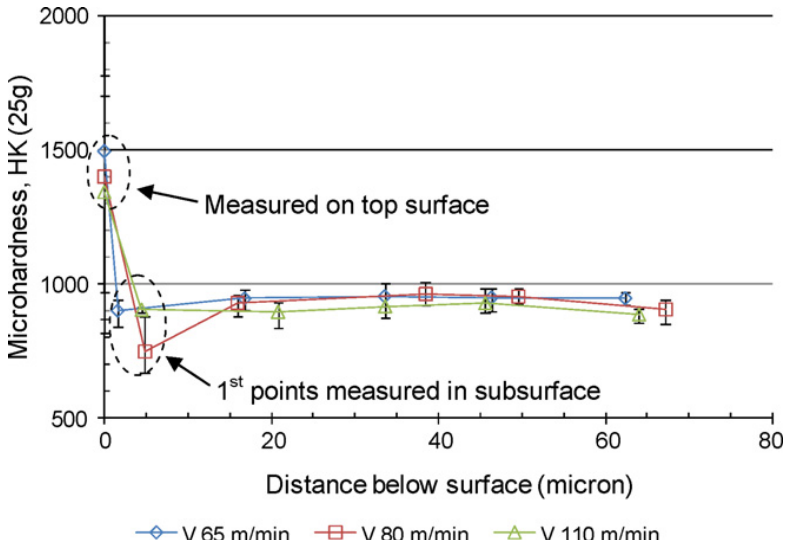

Figure 1.4: Microhardness profile of Ti-64 (Sun & Guo 2009)

1.2.4 Surface Roughness

One of the most commonly used methods to quantify surface integrity of a machined product is surface roughness. In titanium and nickel-based alloys, traditional machining processes fail to generate smooth enough surfaces to suffice for the end product, which leads to a need for post-processing techniques to decrease the surface roughness to acceptable values. Almost all cutting and tool geometry parameters have been found to be effective on surface roughness, and increasing material removal rate by increasing cutting speed or feed rate have been found deteriorating to the smoothness of the part surface. Hence, researchers have intensively studied the solution to the optimization problem between surface roughness and material removal rate.

1.2.5 Residual Stress

During machining, in addition to the mechanical loads acting on the workpiece due to the dynamics of the process, there is a significant temperature rise due to friction and shearing mechanisms. This temperature rise causes thermal loading on the workpiece. Localized temperature rise increases the magnitude of thermal strains and

promotes tensile residual stresses. Superposition of both types of loads creates plastic loading that cannot be fully recovered after the machining process is finished. This lack of full recovery causes residual stresses to remain on the workpiece (Jacobus et al. 2000, Dudzinski et al. 2004, Guo et al. 2009). These residual stresses present potential risk in terms of crack initiation and propagation, and fatigue failure of end products. It is necessary to remove tensile surface residual stresses or prevent them from occurring during machining.

As a sample residual stress graph (Figure 1.5) shows, machining processes usually induce tensile residual stresses at the surface, while ~50 μm below surface, these stresses become compressive. After ~200-300 μm into material, residual stresses are observed to diminish. The tensile layer at the first ~50 μm of material can be related to work hardened layer formation and white layers, but further research is needed to explore this possibility. It is known that for most materials, machining parameters, tool geometry, and tool wear, as well as existence, type, and thickness of tool coating material affect the direction (tensile or compressive) and magnitude of residual stresses. It is essential to understand which parameters affect residual stresses the most, especially at the surface of machined workpiece material, and adjust those parameters such that acceptable values (compressive) of residual stresses are achieved.

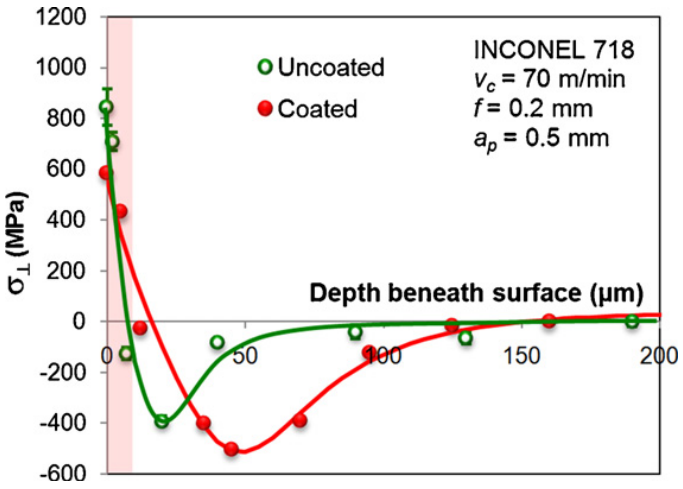

Figure 1.5: Residual stress profile of IN-718 (Outeiro et al. 2008)

Measuring residual stress is also very difficult. Although many techniques have been developed such as Eddy Current technique, Barkhausen Noise Analysis (BNA), Sectioning, Hole Drilling, Neutron Diffraction, and X-ray Diffraction (XRD), most of these techniques are either destructive, or not very reliable (Belassel et al. 2011). The ones that are not destructive and are relatively more reliable are very expensive and not very portable. Among these techniques, XRD stands out as the most reliable, non-destructive, and easily accessible technique, while it is not as expensive as some other techniques. Hence, for this study, XRD was selected as the measurement technique for residual stress experiments to validate the results of the simulations.

1.3 Physics-Based Simulation Modeling

Although experimental findings are the most reliable results that can be achieved, it is generally very hard, if not impossible, to gather enough measurement data to reach conclusions about sensitivity of output parameters to changes in inputs. Hence, it is crucial to develop and use process simulation models that illustrate the experiments. It is essential that these models are physics-based, so that there will not be too much compromise from mechanics of the process. It is also important that these process models

are verified through experimentation first, and then utilized to make predictions within limits of the experimentally validated machining conditions.

FE-based models are appropriate for such objectives. Mechanics of machining processes can be represented with tool and workpiece positioned against each other as shown in Figure 1.6 for both 2D and 3D, and moving the workpiece slowly towards the tool illustrates the cutting motion, whereas the vertical location of tool illustrates feed rate in two-dimensional simulations with plane strain assumption. While machining is simulated, each element within the workpiece has different but dependent behavior, and computation of their collaborative motion reveals the forces, temperatures, stresses, and strains, to name a few parameters that are calculated within the software. When it is concluded that the tool has progressed a satisfactory amount on the workpiece, results are extracted from the software to be compared to experimental findings.

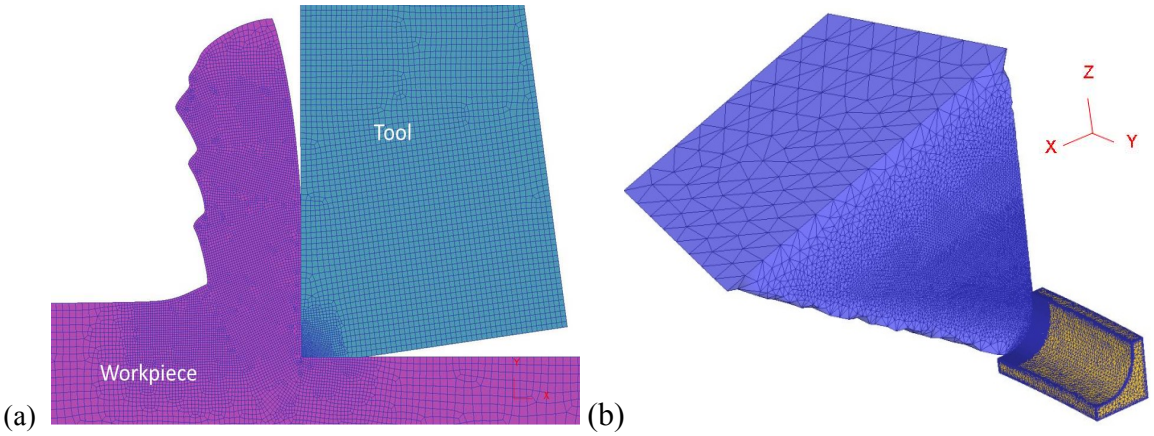

(a) (b)

Figure 1.6: Illustration of simulation models for a) 2D and b) 3D machining processes.

Once the initial simulation is designed in 2D orthogonal cutting configuration, it is very easy to change any input parameter to create a new simulation. This is one of the reasons that 2D orthogonal machining process simulations are easy to run, i.e., these simulation models take much less computational time and create less convergence issues

when compared to 3D simulations. However, this assumes a symmetric mechanical setup and plane strain assumption in deformations, where there is no significance of the third dimension. This is rarely the case during machining, but it can be used to point research in the correct direction. Once a good confidence in two-dimensional process simulations is achieved, it is possible to move the simulations to the third dimension, where all three dimensions have significant effects without symmetry. By doing this, one will be able to simulate more than experiments can conclude due to financial and temporal constraints. Any set of experimentation takes a significantly more time than designing and running the same simulation, due to set-up times and learning curve of the experimenter. Also, cost of running simulations is only the cost of the simulation software, while for experiments, raw material and experimentation costs, as well as cutting tool and measurement costs result to significantly higher costs compared to running simulations.

For this study, both 2D and 3D FE-based simulation modeling techniques were used, and the updated Lagrangian software DEFORM (2D & 3D) was utilized for all simulations (Figure 1.7). Hybrid friction models based on the results of the friction determination method described were used, and temperature-dependent flow softening models were used to better represent the results of experiments. Once simulation models are validated through experimental results, they were used to predict results of machining processes, and finally utilized to optimize machining parameters for the best possible outcomes of these processes in terms of surface integrity.

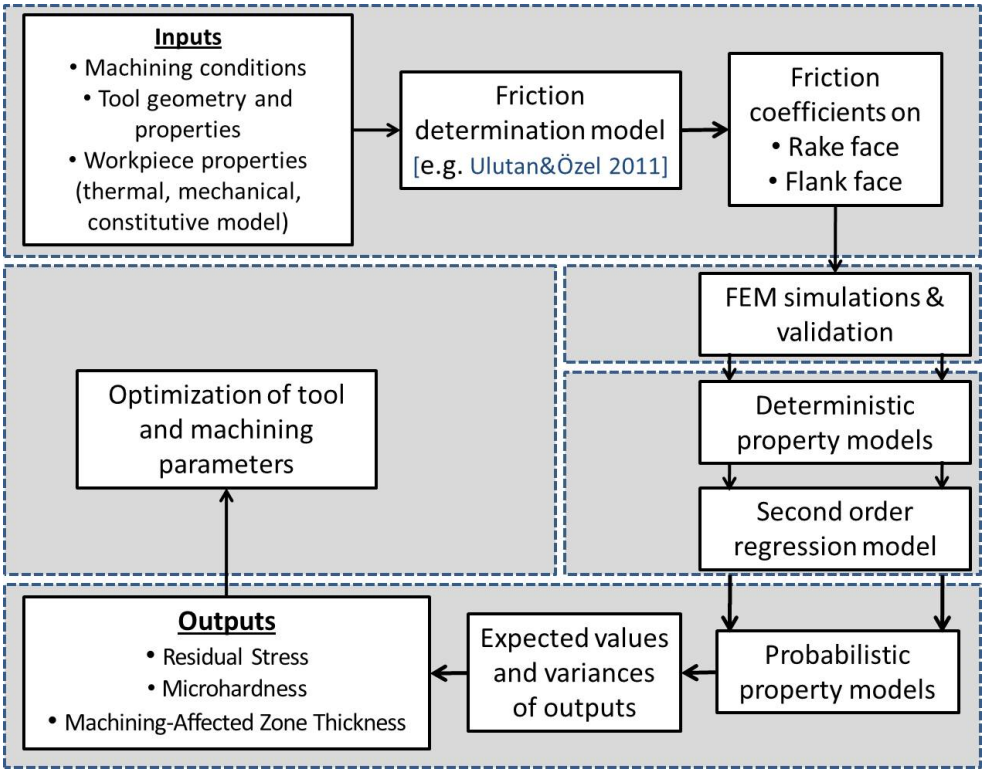

Figure 1.7: An overview of the proposed research

2. Motivation

As summarized, this research is concentrated on modeling of machining processes and developing physics-based process simulation tools that will eliminate the necessity of excessive experimental trials. Machining experiments were used to validate simulation models developed, and then these models were utilized to propose elimination of redundant experimental needs. As shown as an overview in Figure 1.7, this research work started with initial inputs as machining conditions, tool geometry and properties, and workpiece properties. Then, the proposed friction determination method was applied to obtain the friction coefficients on the rake and flank face of a given cutting tool. Then, FE-based 3D simulations were utilized to predict machining forces, temperatures, and stresses. Once these are predicted, they were validated with experimental findings, and property models were achieved, reaching expected values and standard deviations of

output parameters. The output parameters were machining forces and residual stresses, but the study can be extended to include microhardness and machining-affected zone thickness. Input parameters were optimized based on these findings. Major methods that were used to establish these relationships are described below.

1. Experimental Modeling: Relationships between inputs and outputs can be obtained by experimentation. Although reliability of results is the highest with this method, the number of results that can be gathered in unit time is too low for these results to achieve a satisfactory significance. Designing and conducting two-dimensional (orthogonal) and three-dimensional cutting tests and measuring forces and residual stresses is possible. This has been partly done for the purposes of this study, but the experiments were rather utilized to validate the simulations. 2D simulations were used to validate the friction determination method results, and 3D simulations were used to validate the force and residual stress predictions.
2. Analytical Modeling: The input-output relationships can also be gathered by purely analytical models that are based solely on the theoretical physics of the process. Usually, such models can only predict an average value for forces, stresses and temperatures. While these predictions are useful to find out about main trends in process and product relations, much detailed information can be obtained through physics-based process simulations. However, due to (1) many unexpected and unaccounted events occurring during the process, and (2) the amount of assumptions a researcher needs to make so that the problem is solvable, results of analytical models are not reliable enough to make them worthy. Also, their complex structure necessitates several assumptions, which restrains the number of simulated conditions.

Analytical models to solve stress distributions along the tool faces (rake and flank) were utilized in determining friction coefficients from measured forces and they were validated with FE-based models, but analytical models were not utilized otherwise.

3. Finite Element Modeling: FE-based techniques use continuity principles on small elements that constitute the big picture: tool and the workpiece. If inputs and sub-routines and sub-models of the FE-based model are well-defined, these techniques offer optimal results based on reliability, quickness, and cost-effectiveness, with the advantage of not involving too many assumptions. In addition, FE-based techniques provide a rich set of process outputs such as forces in time, strain, stress and temperature fields (i.e. distributions) in tool and workpiece geometry. The main problems with these models are concerned with meshing of the workpiece and the elastic-viscoplastic deformation assumption that needs to be done with 3D simulations.
4. Multi-objective Optimization Method: Experimentally measured and FE-based simulation predicted residual stresses have been utilized in constructing regression models that represent relations between machining parameters and measured or predicted residual stress of interest for optimization studies for various objectives simultaneously using Particle Swarm Optimization method. Optimum solutions have been given in decision variable and objective function spaces.

In this study, a combination of experimental and FE-based modeling was used, while also some regression models were utilized within the implementation of the friction determination method and constructing models for optimization purposes. In the end, all results for force and residual stresses were verified for some limits of input parameters,

and an optimization routine within those limits was implemented to suggest best operating conditions applicable in the industry.

3. Objectives

The overall research objective of this study is to utilize the synergies between deterministic and probabilistic modeling approaches in predicting the main surface integrity measure, residual stress, after finish machining processes in order to aid in optimization of machining parameters and tool selection (material and geometry) in the industry for sustainable manufacturing of titanium and nickel-based alloy end products. Following specific objectives of the study address the overarching research achievements:

Objective 1: Physical phenomena behind machining processes were thoroughly understood, including temperature-dependent flow softening, dynamic recrystallization, and adiabatic shearing. Reflecting this information upon formulation of physics-based models, accurate and reliable process outputs such as force, temperatures, and stresses were computed.

Objective 2: Surface integrity in machining processes was investigated and surface integrity models were generated using the developed friction determination model, and FE-based thermal and stress analysis. A systematic modeling framework was established and validated with experiments. The developed friction determination model was utilized for titanium alloy Ti-64, and nickel-based alloy IN-100 that are frequently used in the aerospace industry, and results were confirmed with experimental findings in terms of force and residual stresses.

Objective 3: Direct process models link inputs such as machining parameters (cutting speed, feed, depth of cut), tool parameters (material, coating material, coating thickness, rake angle), and workpiece parameters (material) to outputs (force, temperature, residual stresses). These models were extended to establish a probabilistic predictive modeling system that can be better utilized in the industry.

Objective 4: Main parameters within the input set such as cutting speed, feed rate, depth of cut, tool cutting edge radius, rake angle, tool material and coating, and workpiece material all have different influences on force, temperature, and residual stress outputs. In the end, these result in different surface integrity conclusions, and these different conclusions were investigated using the predictive modeling system proposed and computer simulations.

Objective 5: After investigating the influences of different parameters, the input parameter set selection was optimized. In this optimization process, multi-criteria objectives must be achieved and satisfied to the best capability. These objectives include but may be extended from minimizing tensile residual stresses and tool wear (minimizing forces), while maximizing compressive residual stresses. Other objectives can be added in consultation with industry.

4. Organization of The Dissertation

This dissertation is organized as follows:

In Chapter 2, experimental procedures and findings are reported for orthogonal (two-dimensional) cutting tests, face turning (three-dimensional) experiments, and residual stress measurements. Experimental conditions for orthogonal cutting tests and face turning tests, how and why these conditions were selected, what were measured and

how these results can be interpreted are included in this chapter. Also, details of the residual stress measurements undertaken, and their results are presented and discussed.

In Chapter 3, the friction determination method is described in detail, and the findings of the method are presented. The need to determine friction coefficients from experimentally measured cutting forces is explained in detail. Two different versions of the model are presented, i.e., for the case of fresh (unworn) cutting tools where tool retains edge micro-geometry and for the case of worn cutting tools where tool loses its cutting edge micro-geometry. Reasons for the need of both versions are described. Results of the friction determination method are presented and discussed. In addition, working mechanism of the iterative method including the modeling effort is described. Results obtained from friction determination method are validated using FE-based simulations. Comparison of these results is given in the next chapter.

In Chapter 4, physics-based simulation modeling method for orthogonal machining is presented. The need for 2D FE-based simulations is discussed, and parameters selected for running these simulations are presented, including the flow softening-based work material flow stress model parameters. Hybrid friction model (combination of shear and Coulomb friction) utilized in the simulations is explained. Results of the friction determination methodology are presented, and how these results are incorporated into the iterative method is discussed. Stress fields (distributions) on the workpiece and tool are presented, and change of stress profiles with changing input parameters is discussed. Also, effect of machining parameters on the location of stagnation point is presented.

In Chapter 5, physics-based simulation modeling method for face turning is presented. The need for 3D FE-based simulations as well as their difference from and superiority over 2D simulations are discussed, with the disadvantages also presented. Flow stress parameter determination methodology is explained in detail, and the results for this method regarding temperature-dependent flow softening-based material model are presented. Predictions obtained from 3D simulations are compared and validated using forces measured from face turning experiments and residual stresses profiles measured using XRD technique. Mean and variations of the measured stress profiles and predicted stress profiles are presented and uncertainty associated with physics-based process simulation models is identified. Error associated with predictions is also reported and discussed.

In Chapter 6, sensitivity analysis that reveals the sensitivity of the predictions to physical and numerical parameters is discussed. Importance of each parameter (such as the friction model parameters, flow stress parameters, heat transfer coefficient, and number of elements in the mesh) is explained, and how they affect the force and residual stress predictions (in terms of associated errors) is given. Also, some of the parameters affect the run-time of the simulations, so this effect of those input parameters is also discussed. In the end, selection criteria for the final parameters used in the 3D simulations is explained and justified.

In Chapter 7, multi-objective optimization is explained and discussed. Development of predictive models for the relationships between input and output parameters is presented. Possible objective functions appropriate for industrial applications are discussed, and the multiple objectives selected for this study are justified.

These objectives are minimizing the tensile peak residual stress at the surface and cutting forces, while maximizing the compressive peak residual stresses. In addition, the uncertainty associated with the residual stress predictions is added as another objective, and minimized. Particle Swarm Optimization (PSO) algorithm used to conduct the multi-objective optimization scheme was detailed, and the results for this scheme were presented.

In Chapter 8, contributions and future research directions are discussed.

CHAPTER 2

EXPERIMENTAL ANALYSIS

1. Introduction

In any study related to manufacturing processes, experimental results are of great value. The main reason for this is that it is very hard and time-consuming to set-up and conduct experiments. In addition, the cost of experiments can rapidly exceed the budgets of most projects, industrial or academic. For these reasons, it is extremely important to utilize some experimental results already gathered by other researchers in modeling studies rather than designing and conducting all the experiments within the same study. In this study, experimental results from qualified researchers were utilized in addition to the experiments conducted within the scope of this project. These experiments can be separated into three parts:

The first part of the experimental work is the orthogonal machining tests, where the tool-workpiece interaction is in symmetry in one of the Cartesian coordinates, which is the reason that it is called two-dimensional machining (Figure 2.1). Chip formation process is achieved in two-dimensional plane and measured forces in the third dimension are often negligible in this type of machining, such that they are usually not even reported. This type of machining is not conventionally utilized frequently in industry, but force and temperature measurements gathered from these experiments can be utilized in developing models, estimating three-dimensional machining results, or analytically determining the effects of machining parameters.

The second part of the experimental work is conventional machining (face turning) tests, where there is no necessary symmetry on any of the dimensions but machining process is highly similar to industrial practices. Although leading to more useful results, analyzing in three dimensions is harder due to the mechanics of the process and increased complexity of the problem, and the simulations get more complex and take more time in this type of experimentation. The third part of experimental work is concerned with the measurement of residual stresses from the machined surfaces obtained through face turning tests.

There have been a substantial number of researchers who studied the mechanics of machining processes in the last few decades. They were mostly concerned with cutting forces, temperature rise during machining, and tool wear. However, due to this significant interest, these areas have been investigated thoroughly, decreasing the need for machining tests to a minimum. Furthermore, now that researchers know how cutting forces, temperatures and tool wear react to changes in parameters for most materials, which means the machinability of the materials has been understood, interest in these areas has shifted to more modern research areas, such as accuracy and integrity of the machined product and its associated reliability. The main characteristics of accuracy and reliability reveal with the surface integrity of the final product. Surface integrity can be composed of many attributes that mainly include but are not limited to residual stresses, microhardness, surface roughness, microstructural alterations, and surface defects. Among these properties, geometrical accuracy and surface roughness was the first topic that most researchers investigated due to its ease and rapidness of measurement, and it has been thoroughly investigated

in various machining processes. However, surface roughness only measures the geometrical surface integrity at the very surface of the material, and is not related to near-surface (sub-surface) integrity. To understand this phenomenon of near-surface integrity effects on the quality (dimensional accuracy and reliability) of final product, as well as surface integrity effects, residual stresses induced during machining should be studied and understood. As a result, the third part of the experimental analysis of this study is the residual stress measurement of machined workpiece materials.

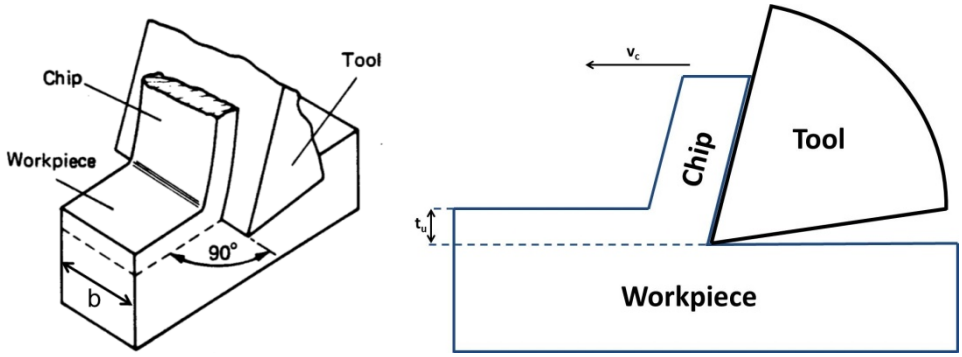

Figure 2.1: Illustration of orthogonal machining

The scope of this work includes machining induced surface integrity in titanium and nickel-based alloys. Before describing details of experimental procedures and results, chemical composition of metal alloys have been studied, and these compositions for nickel-based alloy IN-100 and the titanium alloy Ti-6Al-4V are given in Tables 2.1 and 2.2. In addition, mechanical and thermal properties of these alloys are given in Table 2.3.

Table 2.1: Chemical composition of the nickel-based alloy IN-100

Element	Ni	Co	Cr	Al	Ti	Mo	V	Fe	C	B	Zr
%	Balance	18.3	12.3	4.9	4.3	3.3	0.7	0.1	0.06	0.02	0.02

Table 2.2: Chemical composition of the titanium alloy Ti-6Al-4V

Element	Ti	Al	V	Fe	O	C	N	H	Others
%	Balance	6	4	0.25	0.13	0.08	0.03	0.01	0.4

Table 2.3: Mechanical and thermal properties of IN-100 and Ti-64

Property	Unit	Ti-64	IN-100
Ultimate Strength	MPa	896	1018
Yield Strength (0.2%)	MPa	827	850
Hardness	HRC	36	40
Thermal Expansion	K^{-1}	$9*10^{-6}$	$1.1*10^{-5}$
Density	$kg*m^{-3}$	4430	7910
Melting Point	K	1604	1490
Elastic Modulus	GPa	42	156
Thermal Conductivity	$W*m^{-1}*K^{-1}$	6.6	9.1
Specific Heat Capacity	$J*kg^{-1}*K^{-1}$	565	440

2. Experimental Analysis

2.1 Orthogonal (Two-dimensional) Machining Experiments

Orthogonal cutting experiments are very straightforward in most cases, where machining occurs by removal of material due to the coupled motion of the tool and workpiece in orthogonal directions (Figure 2.1). The third dimension does not significantly affect the process, because force results of experiments are divided by the width of cut (b) in these experiments, which is the thickness of machined workpiece in third dimension. A three dimensional illustration of the process is not necessary, since the process is symmetric in the third dimension. Uncut chip thickness (t_u) is equivalent to feed rate, and tool motion is in that direction. Cutting speed (V_c) is a result of workpiece rotation, but since this is a relative motion, one can also consider the workpiece as constant and the tool moving towards the workpiece with cutting speed. The force component in this direction is called the cutting force (F_c), while the force component in feed direction is called feed force. The force component in the direction of width of cut is called thrust force, but it is insignificant in orthogonal machining.

Orthogonal machining experiments for the nickel-based alloy IN-100 were conducted in the facilities of Rutgers University Industrial and Systems Engineering Department, and the width of cut varied between 2.45 mm and 3.52 mm. Since the forces are normalized by dividing by the width of cut, and the change in stresses does not depend on the width of cut, this does not possess any problems. The experimental results for orthogonal machining of titanium alloy Ti-6Al-4V were taken from two different sets of experimentation. For higher cutting speed (V_c=120 m/min), the experimental results were received from the orthogonal cutting tests conducted at TechSolve Inc., and the width of cut was b=5 mm. The experimental results for lower cutting speed (V_c=70 m/min) were extracted from the orthogonal cutting test results of Wyen & Wegener (2010), where the width of cut was b=2 mm. As a result, only the experimental set-up for the orthogonal machining of IN-100 will be explained, however, due to the straightforwardness of the process, it can be safely assumed that the machining process for the other two sets of experimentation were very similar. Although there were more experiments than the results are presented for, these selected conditions were both more industrially applicable and also comparison enabling.

In orthogonal machining, a cylindrical disk workpiece is rotated connected to a chuck in a turning lathe. The workpiece needs to be at least at a length to first cover the depth of the chuck, and then leave a necessary distance to make sure that machining process is long enough for reaching steady-state machining conditions (cutting forces and temperatures). When the disk is too long or when more disk stability is required, a tailstock that is located within the machine is used to hold and stabilize the workpiece from machined end, without interrupting the machining process or measurements. This

mechanism only disables the usage of workpiece after its diameter is reduced to very low values. However, at these small diameter values, effect of higher spindle speeds take place and measurement uncertainties increase, so the workpiece is already not utilized after its diameter has been decreased too much. Hence, the negative effect of tailstock is not applicable to these experiments.

After fixing the workpiece on the chuck, selected tools must be paired with corresponding toolholders that are capable of holding the tools without slipping, and supplying the required angles for the process. Selected toolholder (with the tool) is secured on the dynamometer that measures forces and outputs to the computer. The dynamometer is then placed on the turret disk of the machine. When the correct tool number on the turret disk is called within the machining program, that tool is selected and machining process is started when the program signals for feed motion of the tool. When the tool touches the workpiece, force measurements start from 0 and rapidly reach a steady state. When the pre-coded program signals the end of machining, the tool is disengaged from the workpiece. In the meantime, the operator needs to signal the data acquisition system software installed on the computer to start taking measurements before the engagement of the tool and the workpiece, also determining the duration of the measurement. The computer software is capable of eliminating the noise in the captured data, enabling to achieve the average as well as maximum and minimum values for the cutting and feed forces. Hence, the force measurements cannot be judged as equivalent to one value, but they are steady-state within an interval of minimum and maximum. Although some minor details about the machining program or the computer software might be different, the process is similar for any orthogonal machining experiment. In

addition, most of the time, no repetitions for any set of experiments are used, since the cost of workpiece material and tool tips is a major factor, and the steady state force values are accepted without the need for repetitions.

Orthogonal turning of IN-100 disks (3 mm thick) have been performed using uncoated tungsten carbide (WC) cutting tools in a rigid CNC turning center at the Manufacturing Automation Laboratory of Rutgers University. IN-100 nickel-based alloy cylindrical specimen was obtained through powder processing method different than a typical casting processing based method. This processing condition creates high strength at elevated temperature conditions. On IN-100 disks, grooves (19 mm deep and 3 mm wide) are machined at a cutting speed (V_c) of 18 m/min and a feed (h) of 0.06 mm/rev to create the test workpiece with multiple webs. Test workpieces are machined with plunge turning. This experimental set-up has resulted in the orthogonal cutting condition illustrated in Figure 2.2. Cutting and thrust forces were measured with a Kistler turret-type force dynamometer and high-speed data acquisition devices (Özel, 2009).

For the experiments of IN-100, selected conditions are given in Table 2.4. Effect of each parameter was sought for, so a lower value and a higher value for each parameter were selected. These selected conditions are all used in the industry. Rake angles for the tool were γ_1=0 and 3 degrees, and two different tools with different edge radii were used (r_β=10 and 25 μm). Among the machining parameters, the most affecting were cutting speed and uncut chip thickness (feed), so two different cutting speeds (V_c=12 and 24 m/min), and two different uncut chip thicknesses (t_u=0.05 and 0.1 mm) were used. Using a higher and a lower value for 4 parameters, a total of 16 experiments were conducted.

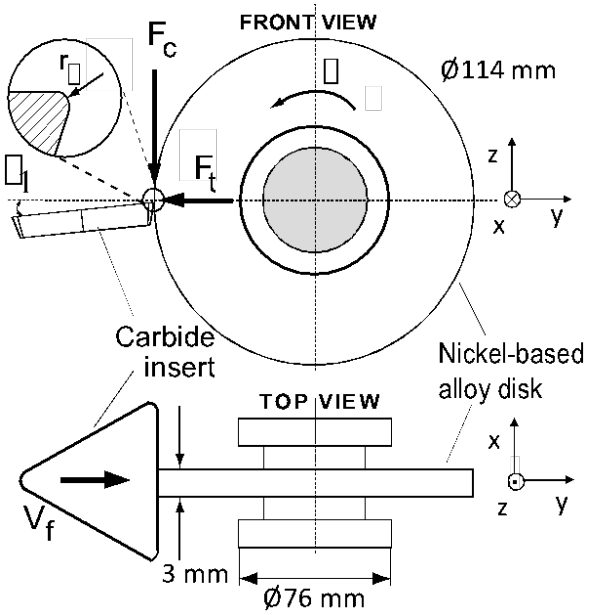

Figure 2.2: Orthogonal cutting of IN-100 nickel-based super alloy disk (Özel, 2009)

Table 2.4: Orthogonal machining conditions for the nickel-based alloy IN-100

	r_β [μm]	V_c [m/min]	t_u [mm]	b [mm]
γ_1=0°	10	12	0.05	3.52
	10	12	0.1	3.52
	10	24	0.05	2.99
	10	24	0.1	2.99
	25	12	0.05	3.09
	25	12	0.1	3.09
	25	24	0.05	2.45
	25	24	0.1	2.45
γ_1=3°	10	12	0.05	2.45
	10	12	0.1	2.45
	10	24	0.05	2.45
	10	24	0.1	2.45
	25	12	0.05	3.02
	25	12	0.1	3.02
	25	24	0.05	2.96
	25	24	0.1	2.96

For the titanium alloy Ti-6Al-4V, experimental results were obtained from two different sources, and they are given in Table 2.5. For higher cutting speed (V_c=120 m/min), the experimental results were received from TechSolve Inc., where uncut chip thicknesses were t_u=0.05 and 0.1 mm, rake angles used were γ_1=0 and 5 degrees, and the constant cutting edge radius for the tool being used was r_β=10μm. Orthogonal turning of Ti-6Al-4V tubes (50.8 mm diameter and 3.175 mm thick) have been performed using uncoated tungsten carbide (WC) cutting tools in a rigid CNC turning center. This experimental set-up creates the orthogonal cutting condition illustrated in Figure 2.3. Cutting forces were measured with a force dynamometer and high-speed data acquisition devices (Özel et al. 2009).

Table 2.5: Orthogonal machining conditions for the titanium alloy Ti-6Al-4V

	r_β [μm]	V_c [m/min]	t_u [mm]	b [mm]
γ_1=0°	10	120	0.05	5
	10	120	0.1	5
γ_1=5°	10	120	0.05	5
	10	120	0.1	5
γ_1=10°	20	70	0.06	2
	20	70	0.1	2
	30	70	0.06	2
	30	70	0.1	2

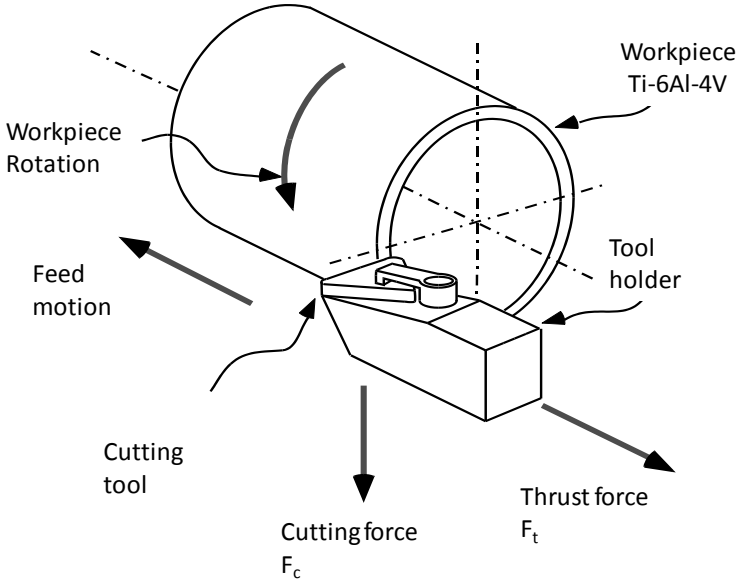

Figure 2.3: Orthogonal cutting of Ti-6Al-4V workpiece specimens (Özel et al. 2009).

For the lower cutting speed (V_c=70 m/min), orthogonal cutting test results were extracted from Wyen & Wegener's study (2010), where they used two cutting tools with different cutting edge radii of r_β=20 and 30 μm, two uncut chip thicknesses of t_u=0.06 and 0.1 mm, and a constant rake angle of γ_1=10°. Although two lower uncut chip thickness values from two different sources are different (t_u=0.05 and 0.06 mm), at these values, it is known that this difference does not have a significant effect on results. If uncut chip thickness is too low, i.e., as low as cutting edge radius (r_β=30μm=0.03mm at the maximum), then the effect of a slight change in uncut chip thickness becomes significant, due to changing geometrical concerns at those values. However, when uncut chip thickness is about twice the value of cutting edge radius, as it is the case in these experiments, the effect can be assumed to be negligible. With this assumption in mind, two different uncut chip thickness values, two different cutting speed values, three different rake angles, and three different cutting edge radii were used for a total of 8 experiments. All experiments were designed in such fashion that effects of each

parameter could be observed. For all sets of experiment, to avoid the effects of tool wear, fresh (unworn) tools were used for each experiment.

2.2 Face Turning (Three-dimensional) Experiments

In three-dimensional face turning experiments, different than orthogonal machining tests, the cutting edge is not orthogonal to the cutting velocity, so the forces in the third direction (thrust forces) are also more significant compared to orthogonal machining. To illustrate this, face turning experiments were conducted in the facilities of Rutgers University Industrial and Systems Engineering Department with IN-100 and Ti-6Al-4V (Ti-64) disks (for configuration of the experiment, see Figure 2.4). In the figure, width of cut is symbolized with a_p, which is also commonly symbolized with b. F_c, F_f, and F_p are cutting, feed, and thrust forces, whereas r_ε is the nose radius and r_β is the cutting edge radius of the tool. All cutting tools were Tungsten-Carbide/Cobalt (WC/Co) material. However, to investigate the effects of tool geometry and coating on forces and residual stresses (Özel et al. 2010, Sima et al. 2011), four different tool edge preparation/coating types were used. First tool type was the sharp edge tool without any coating. However, even the sharpest tools have some edge roundness on them, so it was assumed that the cutting edge radius was ~5 μm. There was another type where a TiAlN coating was applied on the sharp tool, and thickness of coating was assumed to be ~5 μm, which means that total edge radius for this tool was ~10 μm. There were also two more tools with variable edge preparation. This means that from the trailing edge to the leading (cutting) edge of the tool, edge radius was varied. In the trailing edge, cutting edge radius was measured to be ~40 and 25 μm for the tools. From the trailing edge towards the leading edge, these radii decreased to ~10 and 5 μm, so on average, these

tools were assumed to have 25 and 10 μm cutting edge radii. In summary, there were four different tool edges prepared: sharp (r_β=5μm), TiAlN coated (r_β=10μm), mildly variable edge (r_β=10μm), heavily variable edge (r_β=25μm).

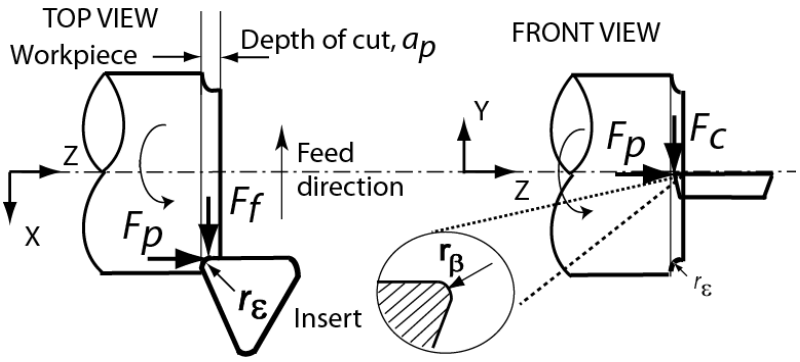

Figure 2.4: Configuration of face turning experiments (Özel & Ulutan, 2012).

For machining Ti-64, a cylindrical workpiece that was 165 mm long and 100 mm in diameter was utilized. The target was to have machining tests on the face side of these disks, and slice them for residual stress measurements. It was observed that in order to reach steady-state force values, not more than 20 seconds of machining was needed. Also, as mentioned before, it was observed that machining in the first 50 mm of the face (from the central axis) created unstable machining conditions that could impair the results, so only the last 50 mm (closest to the edge of the material) were utilized for machining. Considering that machining 25 mm of the surface took approximately 30-40 seconds (depending on feed and cutting speed), it was decided that 2 sets of experiments be conducted at every surface for Ti-64 to create tracks.

After machining two sets of experiments, the disks had to be sliced from the complete cylinder so that new experiments could be conducted. In order to enable this, cut-off tools were utilized on a manual lathe and disks were obtained in approximately 2-3 mm thickness. The actual value of the disk thickness was not significant, but it was

important that at least 2 mm thickness be used so that the effect of the cut-off tool would be limited to the last millimeter of the disk, hence not affecting at least the first millimeter depth for planned residual stress measurements. Since there was a limited number of cutting tools, only two different tools were selected for machining Ti-64 disks (TiAlN coated and 25µm variable edge). Two cutting speed values were selected (V_c=55 and 90 m/min), as well as two feed values (t_u=0.05 and 0.1 mm). For these combinations of the three variables, 8 sets of experiments (4 disks) were conducted at b=2mm width of cut. To investigate the effect of width of cut, another disk was utilized with two more experiments at the higher feed value (t_u=0.1mm) and variable edge tool (r_β=25µm), at a lower width of cut of b=1mm. These conditions were selected, because with decreasing width of cut, the forces would be less than the forces for the higher width of cut. So in order to make sure that these experiments would result in forces considerably higher than regular noise, the machining conditions with higher forces were selected. Since the effect of cutting speed might change with width of cut, both cutting speed values were utilized at these experiments, resulting in a total of 10 experiments (Table 2.6). It should be noted that in all of these experiments no cutting fluid or coolant was applied and they were run in dry cutting conditions in order to create suitable modeling conditions for experimental validation.

Table 2.6: Face turning conditions for the titanium alloy Ti-64

t_u [mm]	Tool	r_β [μm]	b [mm]	V_c [m/min]
0.05	TiAlN Coated	10	2	90
				55
	Variable edge	25		90
				55
0.1	TiAlN Coated	10		90
				55
	Variable edge	25		90
				55
			1	90
				55

For the IN-100 experiments, the effect of cutting tool was expected to be higher than that of Ti-64, so all four cutting tools were utilized in the face turning tests. Since this material exhibits different machining characteristics such as rapid work hardening at increased chip loads, considerably lower cutting speed values were needed for machining IN-100 (Özel, 2009). Hence, two cutting speeds (V_c=12 and 24m/min) were used in the experiments. Also, since the cutting speed was lower, despite the fact that reaching steady-state forces and temperatures took approximately the same amount of time, the cutting length was reduced by half. Hence, using the same amount of surface at the face of the disk, four rather than two tracks were machined. This was critical, as the IN-100 material is very expensive and only a limited amount of material was available. Hence, for the first two disks, four different tool preparations were used at lower (V_c=12m/min), and higher (V_c=24m/min) cutting speeds, respectively, at a constant feed value of t_u=0.05mm. For the third and fourth disks, total diameter that could be used was less, so three tracks were machined with the 25 μm variable edge and TiAlN coated cutting tools respectively. These disks were machined at lower cutting speed (V_c=12m/min), since

forces were required to be as low as possible. For the three tracks, feed values were changed and t_u=0.1, 0.075, and 0.025 mm were used to observe the effect of feed on results. Unfortunately, material was limited and it did not allow for a change in width of cut, so a width of cut value of b=1 mm was used for all experiments using IN-100. Therefore, a total of 14 experiments (4 disks) were conducted with IN-100, which was the amount available due to aforementioned constraints (Table 2.7). After the experiments were finished, disks were sliced to be separated from each other using wire electrical discharge machining (EDM), which does not affect residual stress values significantly.

Table 2.7: Face turning conditions for the nickel-based alloy IN-100

V_c [m/min]	t_u [mm]	b [mm]	Tool	r_β [µm]
24	0.05	1	Sharp	5
			Variable Edge	10
			Variable Edge	25
			TiAlN Coated	10
12			Sharp	5
			Variable Edge	10
			Variable Edge	25
			TiAlN Coated	10
	0.1		Variable Edge	25
	0.075		Variable Edge	25
	0.025		Variable Edge	25
	0.1		TiAlN Coated	10
	0.075		TiAlN Coated	10
	0.025		TiAlN Coated	10

2.3 Residual Stress Measurements

There are various methods that machining-induced residual stresses can be measured with. All of these measurement techniques have their advantages as well as disadvantages. Some methods are destructive, which means that during measurement,

workpiece material is physically damaged. Most of the times, workpiece material is not available for further usage or testing with these methods due to their destructiveness. Hence, these methods should be used when repetition of the measurement in the same specimen is not required, and the product will not be used after measurement. Most commonly used destructive methods are sectioning and hole drilling (also known as blind hole drilling) (Walker 2001). In sectioning method, after each measurement, a layer of material is removed by a predefined removal process, and then next measurement can be taken. Usually, the distance between measurements is in the order of 1 mm or 100 μm. In the hole drilling method, a hole (conventionally about 2 mm in diameter) is drilled into the workpiece before taking any measurements. Along that hole, measurements are taken, again with 100 μm to 1 mm distances from one another, with the help of a strain gauge rosette glued to the hole at the surface of the material (Walker 2001). Accuracy of distances between measurements is more than tens of micrometers in these destructive methods, and it is not possible to get readings from the first 100 μm, where the residual stress profile is observed for machined titanium and nickel-based alloys. Hence, they are not useful for this study. Since the stressed material is removed by drilling a hole or slicing a layer, strains (and consequently stresses) are relaxed within the material, and due to this behavior, these methods are also called Stress Relief Techniques (SRT). These methods are less costly compared to most non-destructive methods and have been utilized for many decades where accuracy and near-surface measurements are not required, but it must also be noted that the destruction characteristic of these methods are also considered to alter the stress measurement results (Belassel et al. 2011).

On the other hand, there are also many methods that are non-destructive, which means that the workpiece material can be utilized for repetition of tests or other usage. Most of these methods are qualitative rather than quantitative, which means that their results would only be informative about the whereabouts of the actual residual stress value, rather than giving specific value results (Belassel et al. 2011). In ultrasonic methods, a sound wave is sent to the machined workpiece which is stressed, and the value of the residual stress is found comparing the results of the non-stressed material. However, the coefficients of the calculation for this method need calibration using another proven method first, which makes this method ineffective by itself (Belassel et al. 2011). In the Eddy current method, a sensor coil is utilized to detect the stress changes in a material through the changes in impedance (Belassel et al. 2011). This method is very sensitive to material properties and the process properties, which makes it an unreliable source of information quantitatively. However, it can still be employed to determine whether the residual stresses are tensile or compressive (Belassel et al. 2011). In Barkhausen Noise Analysis (BNA) method, magnetic domains within the ferromagnetic materials are magnetized which creates electromagnetic noise (Ruud et al. 1985, Belassel et al. 2011). However, this method cannot be applied to non-ferromagnetic materials.

Diffraction methods (neutron and X-ray diffraction) are found to be optimal for residual stress measurements in terms of accuracy, cost, speed, repeatability, and compatibility (Belassel et al. 2011). Since these diffraction methods use the crystalline property of the materials to diffract a beam, they are only applicable to crystalline, polycrystalline, and semi-crystalline materials (Belassel et al. 2011). The penetration of the beam within the material and their diffracted angles give the quantitative information

about the strain within the material, making the inter-atomic spacing in the material act like a strain gauge. In neutron diffraction, neutrons are used to diffract and detect, but this also limits the method to proximity of a nuclear reactor for the production of neutrons. On the other hand, in X-ray diffraction (XRD), an X-ray beam is used to diffract and detect, which is comparably easier to produce. Despite this method's relatively higher cost compared to some other techniques, it is widely favored over hole drilling method due to its non-destructive nature and capability of measuring significantly closer to the surface (Walker 2001, Lord et al. 2002, Belassel et al. 2011, Kortabarria et al. 2011).

In summary, because of its advantages over the other methods, and accessibility for the researchers, XRD was selected for measuring residual stresses in this study. Residual stress measurements for the titanium alloy Ti-6Al-4V were conducted by the author in the X-ray diffraction facilities of Rutgers University Chemistry Department, and the measurements for the nickel-based alloy IN-100 were conducted by Proto Manufacturing Inc. The main reason for outsourcing one of the sets of measurements was that with the titanium alloy, university facilities were more confident in accuracy of results, whereas with the nickel-based alloy, better accuracy was foreseen when they were outsourced to a professional company. In addition, because of the learning curve, Ti-6Al-4V measurements were conducted in a few months, whereas IN-100 measurements were finished within the timeframe of a week, which shows that conducting the measurements in own facilities may not be optimal. Furthermore, sub-surface measurements required an etchant to be used, and an easily accessible titanium etchant was available, whereas the nickel-based alloy required a different process

(electro-polishing) for near-surface residual stress measurements, which was not easily available. As a result, the experimental set-up for Ti-6Al-4V residual stress measurements which are explained below are also applicable to measurements for IN-100, except for minor details that are noted.

For the residual stress measurement of the titanium alloy Ti-6Al-4V, the X-ray diffraction facility of Rutgers University Chemistry Department was utilized. In this facility, a Bruker HiStar unit using Cu-K_α radiation (λ=1.54 A°) at 40 kV, 50 mA was utilized to detect diffracted peaks originated from a 2 mm beam that was collimated at 1 mm. Basic configuration of the X-ray diffraction (XRD) based measurement system is given in Figure 2.5. In XRD measurements, an approach that has been developed to evaluate stress from 2D diffraction data was utilized. Principle of this method is to use all data points on diffraction rings to calculate stresses so as to get better measurement result with less data collection time as shown in Figure 2.6. General Area Detector Diffraction System (GADDS) software from Bruker AXS, Inc has been utilized in processing measured data to obtain stress readings.

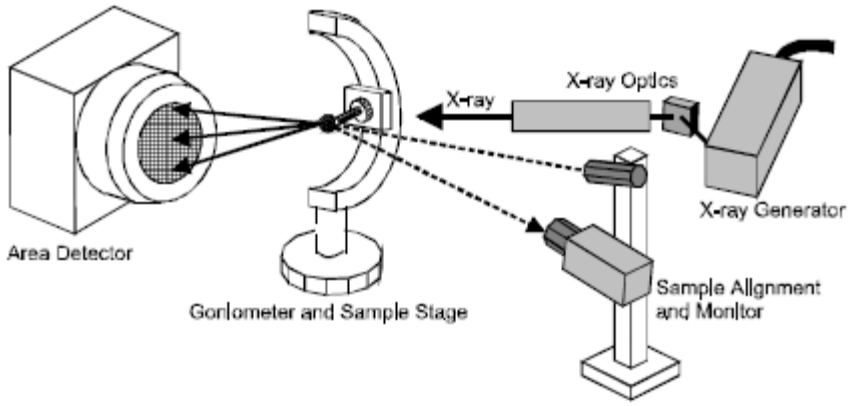

Figure 2.5: Configuration of X-ray diffraction measurement system including X-ray generator (sealed tube); X-ray optics (monochromator and collimator); goniometer and sample stage; sample alignment and monitor (laser-video); and area detector (GADDS user manual, 1999).

The diffracted peaks on diffraction rings had various crystal alignment modes, but there were a few considerations in choosing the correct one (Figure 2.7). First of all, the selected diffraction peak was required to have good peak intensity, which was at least 2-3 % of the originated beam intensity. Also, it was important to select a diffraction peak that corresponded to a crystal alignment mode having a non-zero element in all three coordinates. Also, if the peaks were too close to each other (e.g. only 1 degree apart), there was a possibility of overlap, which would cause calculation errors to become even greater. Hence, it was essential to select a distinct peak. Last, due to design constraints of the machine that was used, the peak had to be at the greatest angle possible. For all of these reasons, the 2θ=142° peak that reflected the {213} Miller indices in crystal alignment of the α-Ti (Ti-6Al-4V) alloy used was selected that exerted 4.2% of the originated beam intensity.

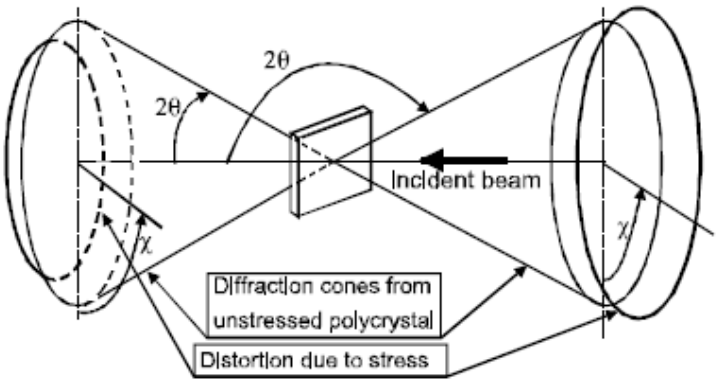

(a) (b)

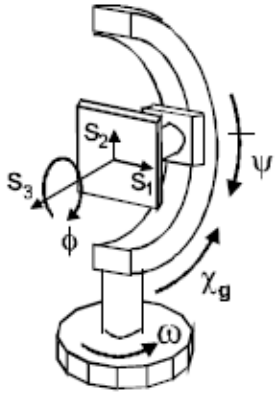

Figure 2.6: The diffraction cones from an unstressed polycrystalline sample and the diffraction cone distortion due to stresses (a). Sample orientation in terms of ω, ψ and φ angles (b) (GADDS user manual, 1999).

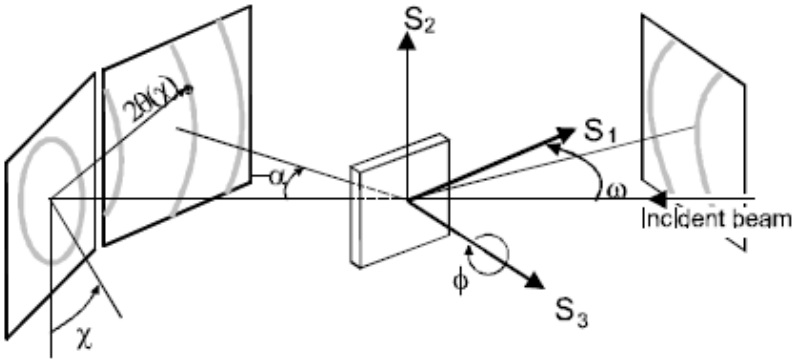

Figure 2.7: The diffraction rings collected on area detectors at on-axis or off-axis positions (GADDS user manual, 1999).

For the nickel-based alloy IN-100, it was reported by Proto Manufacturing that an X-ray diffraction measurement unit using Mn-Cu-K_α radiation (λ=2.1 A°) at 17 kV, 4 mA was utilized to detect diffracted peaks originated from a similar 2 mm beam that was collimated at 1 mm. Differences in the wavelength, voltage, and amperage are only because different crystalline behaviors of two materials require different power intensity inputs for similar outputs. The peak was selected at 2θ=155.2° that reflected the {311} Miller indices in crystal alignment of the alloy (IN-100), but the intensity percentage of the peak was not reported, since the material is not very well known.

During residual stress measurements of Ti-64, a minor hurdle that does not apply to nickel-based alloy disks was observed and was overcome. The problem was that existence of even low concentration copper (Cu) within the alloy caused formation of reflected beam “banding” on diffraction rings, which altered the results greatly, also increasing standard errors to about 100% of mean values. However, this problem was solved by the technician helping with the measurements. The technician stated that it was necessary to filter the effects of this reflection, and it was going to be possible with a nickel (Ni) or cobalt (Co) foil that is not too thick to filter the whole reflection, but thick enough to filter excess reflection that was negatively affecting the results. The choice of nickel or cobalt foil was due to their location on the periodic table. Since they were the closest elements that came right before copper on the periodic table, they were considered to filter the effects of copper best. Therefore, a nickel foil was purchased and taped in front of the detector to filter negative effects. However, since there was a filtering effect, even at greater powers than usual, the detected beam was not powerful enough at short

amounts of time. Hence, each measurement was taken in the order of minutes, compared to measurements in the order of seconds reported for IN-100.

Once the banding problem was solved by filtering the deflected beam, measurements were taken for each disk at 5 degree angle steps at 14 steps for a total of 70 degrees of different deflection angle around peak angle of 142 degrees. This was done because when there are slight imperfections with measurements at any step, the software compensated afterwards during integration using the results from other steps. Fewer number of steps would have meant higher errors for measurements and consequently higher uncertainty. Every step of 5 degrees took 2 minutes (compared to 2 seconds for IN-100 measurements), so a total of one measurement would take 28 minutes except for the set-up time. Before each set of measurement, it was necessary to place the workpiece disk into the machine, observe the focal point of a microscope falling on the correct location on the disk and with good focus, and mark the location so that measurements at the later stages would be at the same location with the least possible variation. After each set of measurement, the software printed pictures of the reflected beam, and it was necessary to integrate the correct peak selected (142 degrees for Ti-64) with reasonable values of step size and number of regions to integrate from. For different values of step size and number of regions, gathered residual stress values did not change too much for this study (less than 10%), but that is because those values were selected carefully. If less step size or number of regions were selected, results would have included a significant amount of additional uncertainty, and if more step size or number of regions were selected, results would have the same amount of uncertainty with exponentially increasing integration time for the software.

When the GADDS software finished integration of measurements from the selected peak with selected parameters, it gave results in two directions, vertical and horizontal. However, due to the placing mechanism of the disk on the machine, these directions were about 10° tilted compared to radial and tangential directions. Hence, results gathered from the software had to be converted to these directions using sine and cosine of the 10° angle.

After every measurement was finished on a disk, it was necessary to etch the disk so that another measurement within the material deeper than the previous measurement could be gathered. For this purpose, a commercially available titanium etchant solution (hydrofluoric acid) was utilized for Ti-64 disks, and it was reported that electro-polishing was utilized for IN-100 disks. Both etching methods are reported and utilized by many researchers, and no significant difference has been found between results of two methods. In addition, both methods are considered to not affect stress and strain states of materials. By taking measurements at different depths into the material within the first 100 μm below surface, residual stress profiles were obtained. However, due to geometrical reasons and calibration requirement of machines, it was necessary to obtain a measurement from bulk of the material and subtract the geometric and calibration effects from results using this measurement. For this, disks were etched more than a millimeter after all measurements were taken, and bulk material measurements were taken. Then, this value was subtracted from all results to get corrected residual stress measurements.

Since there were two tracks on each Ti-64 disk as described before, measurements from both tracks were gathered separately. Similarly, four tracks on each IN-100 disk needed to be measured separately, which was reported to be the case. In the beginning for

the Ti-64 disks, three different locations on each track were utilized so that measurement uncertainties could be minimized. However, it was observed that results did not differ from each other significantly (less than 1%), so repetitions of measurements were concluded as unnecessary due to time and budget constraints. Hence, only one measurement from each track was taken after becoming confident on results. To check this assumption, random repetitions were utilized (a total of five times), and results were still within 1% insignificant difference from each other.

3. Results and Discussions

Major measurements of two-dimensional (orthogonal machining) and three-dimensional (face turning) machining are forces and temperatures. However, since this study was not particularly targeting temperatures, and the experimental set-up for temperature measurement is different than force measurement, relevant results presented here are forces. For orthogonal machining of IN-100, machined chip thickness (t_c) is also reported, since the ratio of this value over uncut chip thickness indicates important findings for other researchers. However, for the purposes of this study, this value is only an observation. For the orthogonal machining results, normalized force values are also presented in Tables 2.8 and 2.9 for IN-100 and Ti-64 respectively, as the effect of width of cut (b) should be eliminated from results before elaborating on them. Results for face turning experiments are presented in Tables 2.10 and 2.11 for IN-100 and Ti-64, respectively.

For the nickel-based alloy IN-100, the most revealing result is that with increasing feed (uncut chip thickness, t_u), both cutting and feed forces increase significantly. It can be observed from Table 2.8 and Figure 2.8 that with increasing cutting speed, both force

components exhibit slight decrease. These results are in agreement with common knowledge about mechanics of orthogonal machining. It can also be deduced from Figure 2.8 that with increasing rake angle from γ_1=0 to 3 degrees, the cutting forces tend to increase in most cases, while no significant change can be observed for the feed forces. It can also be observed that with increasing cutting edge radius of the tool from r_β=10 to 25μm, the cutting forces tend to increase while no significant change in feed forces can be singled out. These results indicate that the major factor influencing forces in orthogonal machining of IN-100 is the feed (uncut chip thickness), and cutting forces are more affected by changes in the parameters compared to feed forces, especially with changes in rake angle and cutting edge radius.

Table 2.8: Orthogonal machining results for the nickel-based alloy IN-100

	r_β [µm]	V_c [m/min]	t_u [mm]	b [mm]	t_c [mm]	F_f [N]	F_c [N]	F_f/b [N/mm]	F_c/b [N/mm]
γ_1=0°	10	12	0.05	3.52	0.17	1185	1470	337	418
			0.1	3.52	0.32	1949	2166	554	615
		24	0.05	2.99	0.16	1090	1013	365	339
			0.1	2.99	0.27	1692	1602	566	536
	25	12	0.05	3.09	0.16	1074	967	348	313
			0.1	3.09	0.28	1756	1854	568	600
		24	0.05	2.45	0.16	882	707	360	289
			0.1	2.45	0.27	1415	1513	578	617
γ_1=3°	10	12	0.05	2.45	0.13	768	885	313	361
			0.1	2.45	0.25	1292	1645	527	671
		24	0.05	2.45	0.18	810	932	331	380
			0.1	2.45	0.37	1298	1631	530	666
	25	12	0.05	3.02	0.16	941	1138	312	377
			0.1	3.02	0.23	1710	2217	566	734
		24	0.05	2.96	0.15	1094	1233	370	417
			0.1	2.96	0.23	1506	2255	509	762

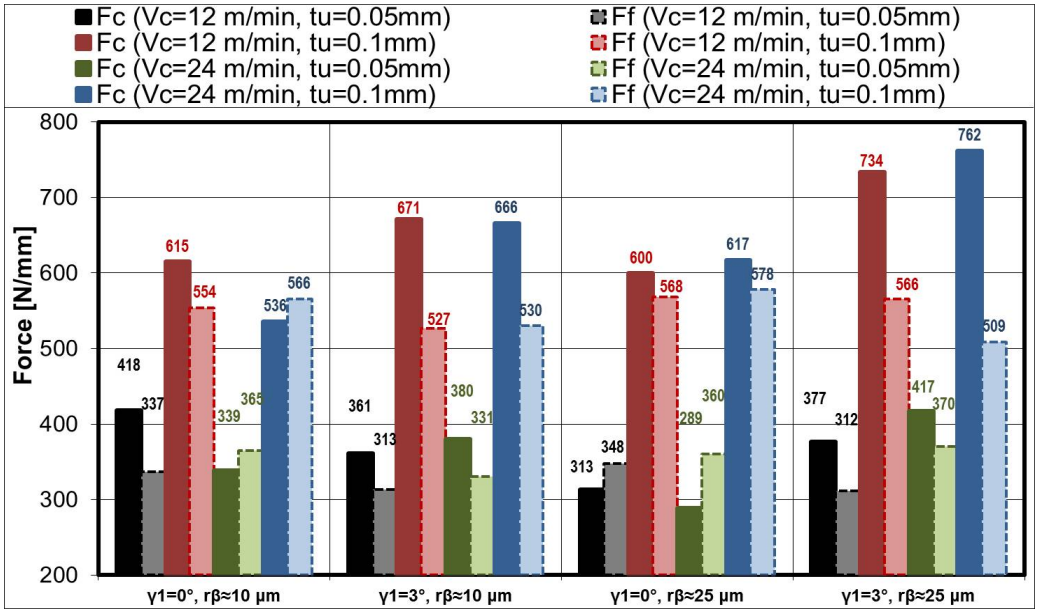

Figure 2.8: Comparison of the forces in orthogonal machining of IN-100

For the titanium alloy Ti-64, it is observed from Table 2.9 and Figure 2.9 that with increasing cutting speed from V_c=70 to 120 m/min, or with increasing feed rate from

t_u=0.05-0.06 to 0.1 mm, there is a significant increase in both force components during orthogonal machining. It is also observed from Figure 2.10 that with increasing rake angle, there are slight decreases in both force components. Cutting edge radius, interestingly, does not seem to affect cutting forces significantly, however, a non-negligible increase in feed forces seem to occur with increasing cutting edge radius.

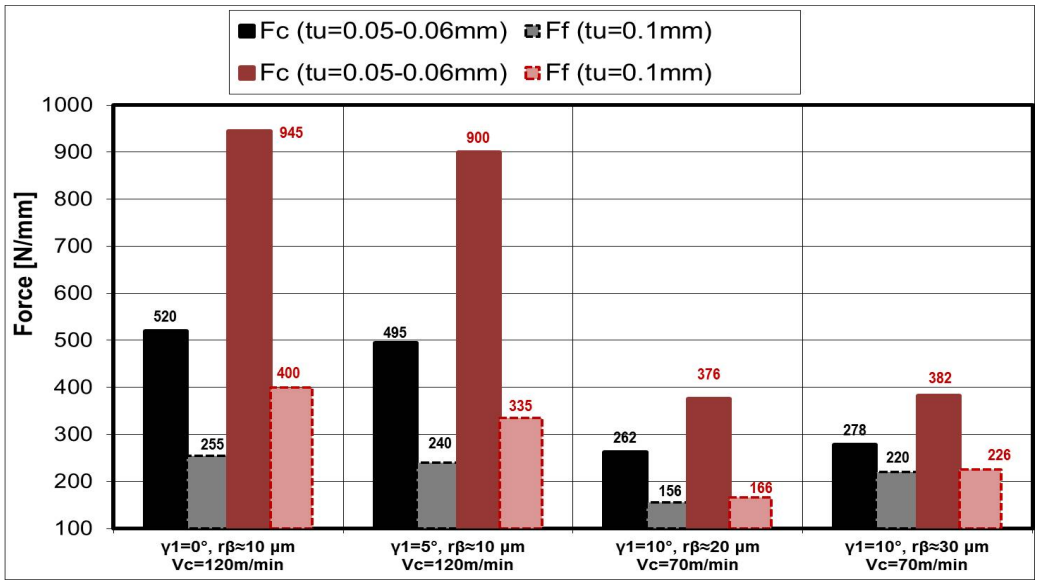

Figure 2.9: Comparison of the forces in orthogonal machining of Ti-64

Table 2.9: Orthogonal machining results for the titanium alloy Ti-6Al-4V

	r_β [µm]	V_c [m/min]	t_u [mm]	b [mm]	F_f [N]	F_c [N]	F_f/b [N/mm]	F_c/b [N/mm]
γ_1=0°	10	120	0.05	5	255	520	51	104
			0.1		400	945	80	189
γ_1=5°			0.05		240	495	48	99
			0.1		335	900	67	180
γ_1=10°	20	70	0.06	2	156	262	78	131
			0.1		166	376	83	188
	30		0.06		220	278	110	139
			0.1		226	382	113	191

Face turning experiments also resulted in noteworthy conclusions, and the observance of non-zero thrust force shows the importance of three-dimensional force measurements over orthogonal experiments. Table 2.10 presents the results of the face turning experiments for the titanium alloy Ti-64, and Figure 2.10 depicts 8 of the 10 sets of experiments for graphical aid. The first result that strikes the eye in this figure is that with increasing feed (uncut chip thickness), all the forces increase significantly. Increasing cutting speed does not seem to affect the cutting and thrust forces significantly, however, a significant decrease in feed forces occur with an increase in the cutting speed. Furthermore, using TiAlN coated tools rather than uncoated WC/Co tools with r_β=25μm cutting edge radius seems to increase all of the forces slightly. Also, decreasing the width of cut by half showed a decrease in forces by half, which is consistent with orthogonal machining results, except for the thrust force, which is the most affected force component from the changes in width of cut in face turning.

Table 2.10: Face turning results for the titanium alloy Ti-64

t_u [mm]	Tool	r_β [μm]	b [mm]	V_c [m/min]	F_c [N]	F_f [N]	F_p [N]
0.05	TiAlN Coated	10	2	90	470	330	117
				55	526	495	128
	Variable edge	25		90	443	288	114
				55	439	324	117
0.1	TiAlN Coated	10		90	850	488	179
				55	845	571	187
	Variable edge	25		90	780	356	167
				55	777	456	161
			1	90	408	200	171
				55	390	221	133

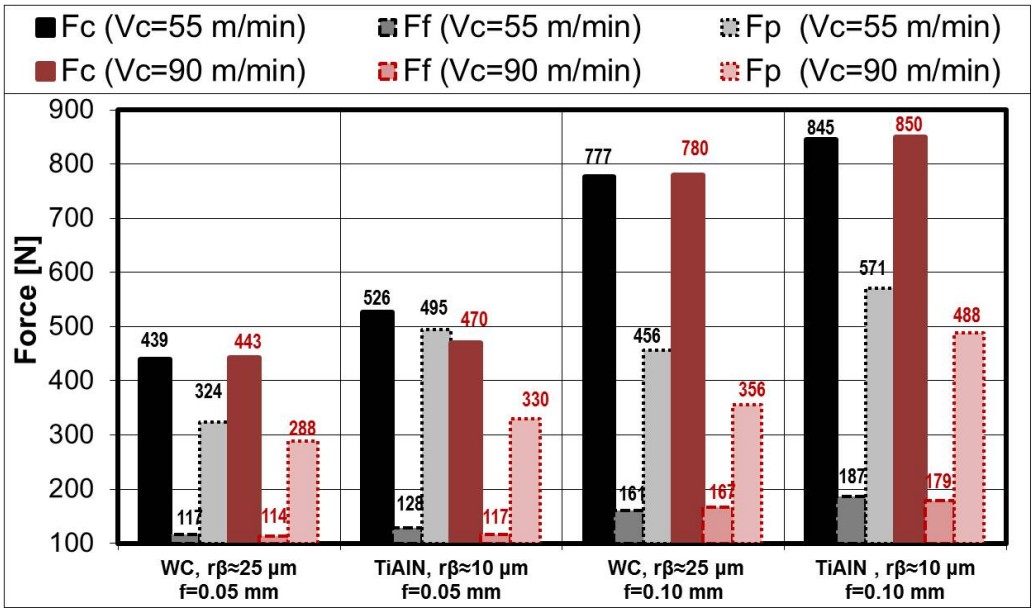

Figure 2.10: Comparison of the forces in face turning of Ti-64 (b=2mm) (Özel & Ulutan, 2012)

Table 2.11: Face turning results for the nickel-based alloy IN-100

V_c [m/min]	t_u [mm]	b [mm]	Tool	r_β [µm]	F_c [N]	F_f [N]	F_p [N]
24	0.05	1	Sharp	5	562	321	181
			Variable Edge	10	530	237	200
			Variable Edge	25	481	176	216
			TiAlN Coated	10	511	187	229
12			Sharp	5	511	279	271
			Variable Edge	10	491	286	207
			Variable Edge	25	512	313	211
			TiAlN Coated	10	488	314	183
	0.1		Variable Edge	25	887	445	356
	0.075		Variable Edge	25	627	330	248
	0.025		Variable Edge	25	520	430	125
	0.1		TiAlN Coated	10	923	555	328
	0.075		TiAlN Coated	10	565	317	267
	0.025		TiAlN Coated	10	229	247	100

Face turning experiments for the nickel-based alloy IN-100 were slightly different in design, so it was necessary to plot two different graphs to show the effects of different

variables. Figure 2.11 shows the effect of tool parameters (coating and cutting edge radius), while Figure 2.12 shows the effect of feed (uncut chip thickness) on the forces. It can be observed from Table 2.11 and Figure 2.11 that all components of forces are in a decreasing trend with increasing cutting edge radius, especially for the higher cutting speed value (V_c=24 m/min), while the addition of coating seems to decrease the forces slightly as well (consider TiAlN coated tool as the same as r_β=10μm variable edge tool, only the last layer is a coating). It can also be deduced that for most of the cases, increasing cutting speed from V_c=12 to 24 m/min increased all force components. Moreover, Figure 2.12 shows that with increasing feed (uncut chip thickness) from t_u=0.025 to 0.1mm, all force components seem to increase notably. Minor exceptions to these generalizations can be unimportant since the general picture makes sense in terms of mechanics of the process and what researchers have discovered in previous studies.

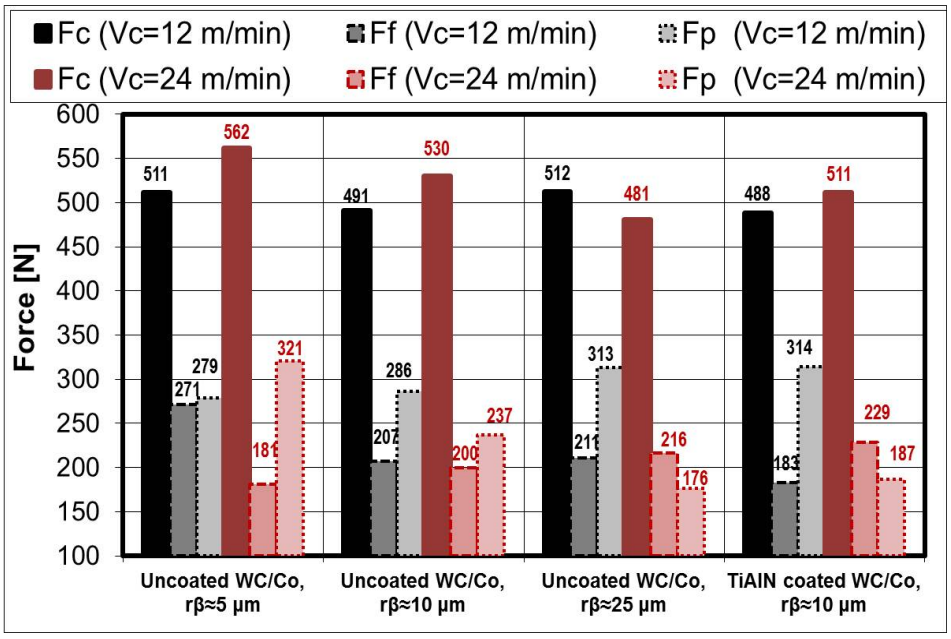

Figure 2.11: Comparison of the forces in face turning of IN-100 (effect of tool parameters)

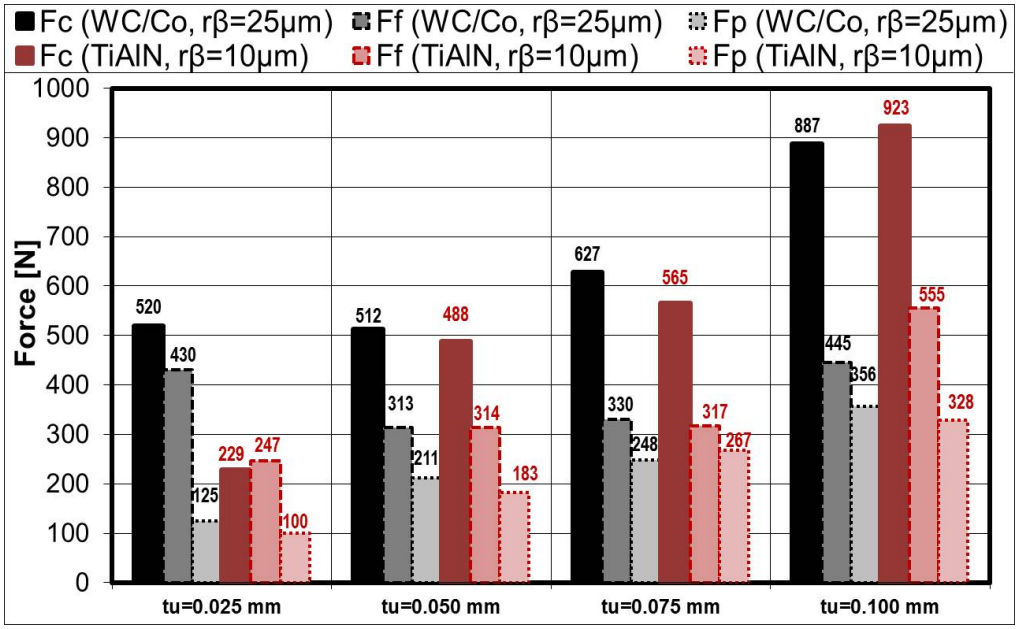

Figure 2.12: Comparison of the forces in face turning of IN-100 (effect of feedrate)

Once the machining experiments are finished, and the results are gathered and analyzed, it is essential to also measure and gather the results for residual stresses, as well as analyzing those results. Many researchers have utilized X-ray diffraction (XRD) technique for the measurement of residual stresses induced by machining, and especially for titanium and nickel-based alloys, this method is the most commonly used one. Although on a different but similar material (another nickel-based alloy, IN-718), there have been two relatively recent studies that explicitly presented the residual stress findings with similar machining parameters, and these results are noteworthy.

In a study on the effects of tool coating on machining-induced residual stresses on both hoop (cutting speed direction) and radial (feed direction) residual stresses (Outeiro et al. 2008), it was found that addition of coating material increases the depth of tensile residual stresses on the surface, but pushes the compressive residual stress peak value to deeper into the material (Figure 2.13). In another study (Ratchev et al. 2011), where also Finite Element Modeling results were discussed, the effect of width of cut (*b*) was

investigated, and they found that increasing the width of cut from *b*=0.1mm to 0.5mm made the surface residual stresses more compressive, as well as enabling the residual stress profile reach near-zero state much earlier in depth (Figure 2.14).

In yet another study (Kortabarria et al. 2011), researchers tried to compare two of the most common techniques in residual stress measurements, hole drilling and X-ray diffraction, and compare their FEM-based simulation findings with both measurements (Figure 2.15). Their results show that X-ray diffraction has the capability to gather measurements at the surface of the material, whereas hole drilling method lacks this capability. The accuracy of the two methods is debatable, and since there is no completely proven and robust method of measuring residual stress at near-surface at the moment, the results from both methods seem to be consistent with expectations. Although there are many other studies regarding residual stress measurements, too few of them are related to the titanium and nickel-based alloys, so research on parameter effects in machining these alloys for residual stresses is needed.

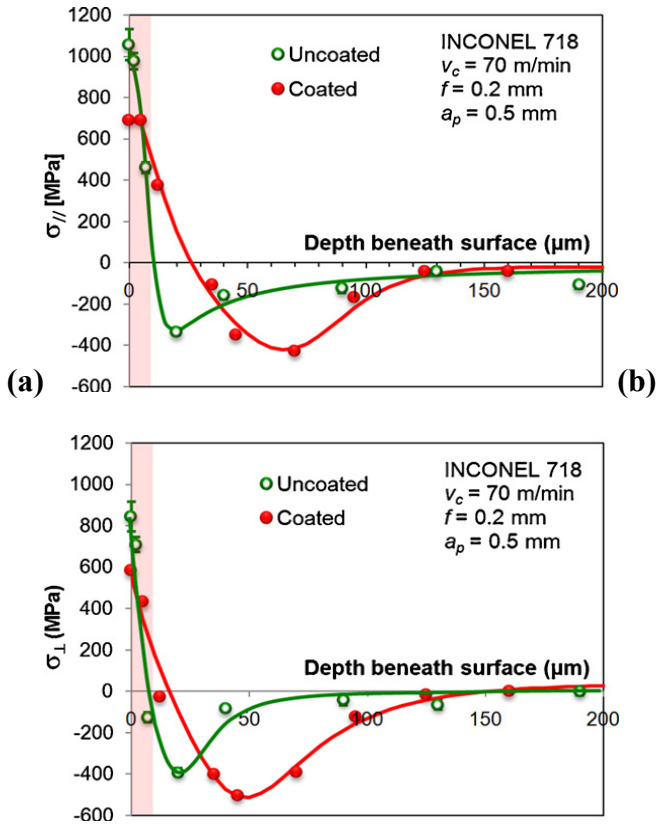

Figure 2.13: Residual stress profile of IN-718 in (a) cutting direction and (b) in feed direction after turning at V_c=70 m/min, t_u=0.2 mm, and b=0.5mm (Outeiro et al. 2008)

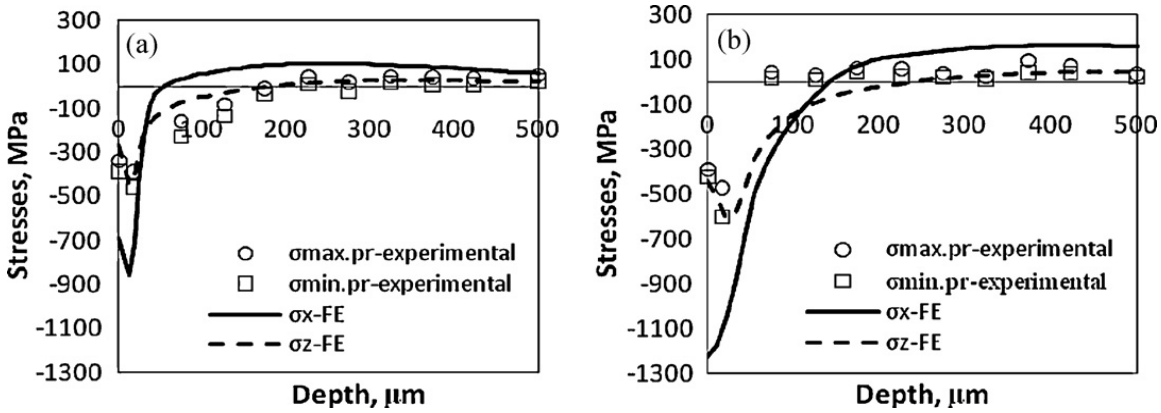

Figure 2.14: Comparison of residual stress findings for nickel-based alloy IN-718 at t_u=0.1 mm, V_c=26.4 m/min, and a) b=0.1 mm, b) b=0.5 mm (Ratchev et al. 2011).

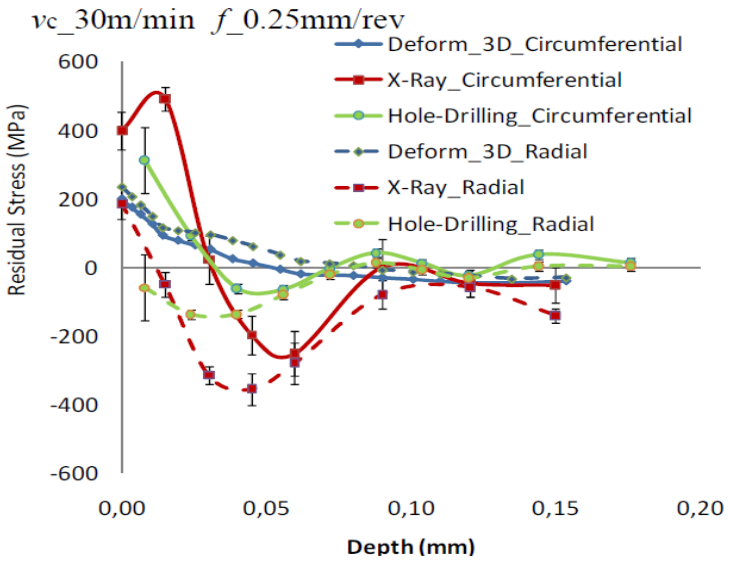

Figure 2.15: Comparison of residual stress measurements with X-ray diffraction and hole drilling, and numerical findings from FE-based model in circumferential and radial directions after face turning IN-718 (Kortabarria et al. 2011)

Residual stress measurements gathered in this study are in both radial (feed) direction, and in circumferential (cutting speed) direction of face turning configuration. Experimental results for measured residual stress profiles in machining of titanium alloy Ti-64 can be found in Figure 2.16, and the experimental results for the nickel-based alloy IN-100 can be found in Figure 2.17. For Ti-64, it was observed that the circumferential residual stresses were tensile (positive) at the surface, changing to compressive at ~30-50 µm, and making a compressive peak at ~75 µm depth, and finally settling at a near-zero state at ~100 µm depth. Increasing the cutting speed did not seem to affect circumferential residual stresses, but with addition of coating to the tool, surface residual stresses in this direction were observed to become more tensile. On the other hand, radial (feed) residual stresses were shown to be the most compressive at the surface, settling to a near-zero steady-state around 30-75 µm in depth. With increasing cutting speed, no

significant change was observed. However, with the addition of tool coating, the peak compressive residual stresses at the surface were observed to become more compressive, while the steady-state settling was observed to happen at more depth.

For IN-100, similar trends of radial and circumferential residual stresses were observed, with a tensile peak at the surface, a compressive peak at ~50 μm, and settling at or after ~125 μm (Figure 2.17). It is obvious that with increasing cutting edge radius, both residual stress components became more tensile at the surface, as well as more compressive at the compressive peak, and the location of the compressive peak becoming deeper. The addition of tool coating (with comparison to uncoated variable edge preparation at r_β=1 μm) did not seem to alter the surface residual stresses, while significantly decreasing the peak compressive residual stresses from approximately -520 MPa to -60 MPa for circumferential, and -500 MPa to -120 MPa for radial residual stresses. It was also observed that without the coating, the residual stresses did not seem to reach a bulk level at 125μm, while with the addition of coating, this settling at a bulk level occurred much earlier (~75 μm).

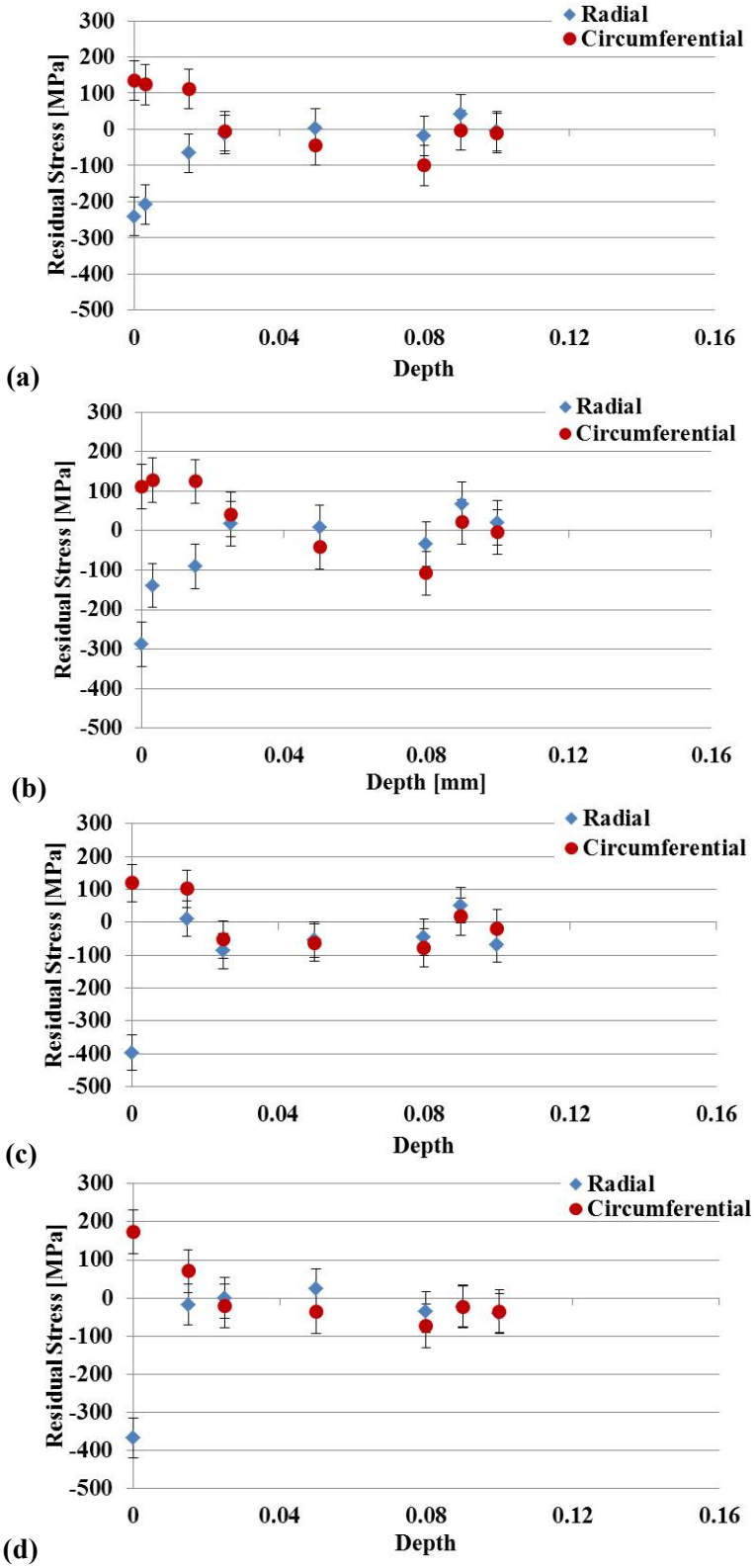

Figure 2.16: Comparison of residual stress measurements in face turning of Ti-6Al-4V with TiAlN coated WC/Co tool (r_β≈10μm) at (a) V_c=55m/min and (b) V_c=90m/min, and with uncoated variable edge WC/Co tool (r_β≈25μm) at (c) V_c=55m/min and (d) V_c=90m/min

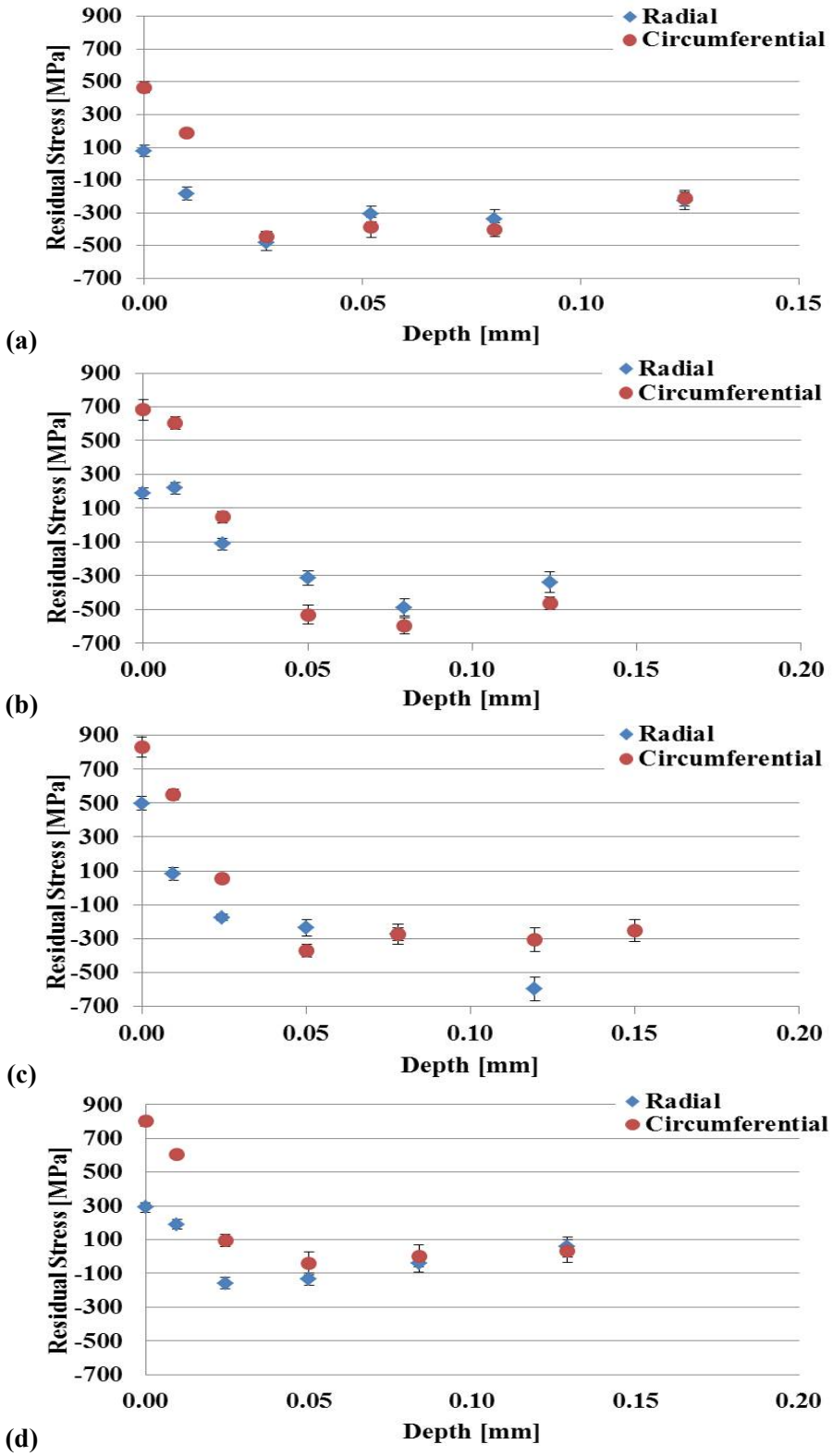

Figure 2.17: Comparison of residual stress measurements in face turning of IN-100 with WC/Co tool (a) sharp (r_β≈5µm), (b) with mild variable edge preparation (r_β≈10µm), (c) with heavy variable edge preparation (r_β≈25µm), and (d) sharp with TiAlN coating (r_β≈10µm)

4. Conclusions

In conclusion, experimental analysis for this study comprised of three major parts: Orthogonal machining tests, face turning tests, and residual stress measurements. Orthogonal machining tests showed that increases in feed caused significant increases in both cutting and feed forces, while cutting forces also seemed to be affected by rake angle, cutting edge radius, and cutting speed slightly. While with IN-100, an increase in cutting speed decreased forces, the opposite trend was observed with Ti-64.

Face turning tests agreed that increasing feed increased all components of forces, while increasing cutting speed only seemed to decrease feed forces in face turning of Ti-64, being increasing all components of forces in face turning of IN-100. For Ti-64, using a tool with TiAlN coating was observed to increase force components, while the opposite was observed for the case of IN-100.

The main conclusion of residual stress measurements was that circumferential residual stress profile for both materials, as well as radial residual stress profile for IN-100 exhibited the same behavior where surface residual stresses were tensile (positive), changing to compressive (negative) at ~30-50 μm depth, reaching a compressive peak at ~50-80μm, and settling after a short distance of ~100-200 μm. This is the prevailing observation of most researchers, which is in agreement with the findings presented here. However, for Ti-64 in radial direction, residual stresses were found to be compressive on the surface at a peak value, settling to a near-zero state around ~100-200μm. Addition of tool coating seemed to increase the compressive peak residual stresses in Ti-64, while decreasing in IN-100.

Although experimental studies are essential to understand the physical nature and mechanics of machining process, they constitute merely guidance for analytical and simulation studies. Hence, the aim of this work will be to use these results in frictional analysis and FE-based simulations to model the changes in residual stresses. Once modeled, it is valuable to predict forces and residual stresses during machining to estimate final surface integrity of the machined part, and therefore dimensional and material accuracy and reliability of the final product. The work to simulate and model residual stresses occurring during machining is described in the following chapters.

CHAPTER 3

FRICTION DETERMINATION METHOD

1. Introduction

Machining difficult-to-process materials such as titanium and nickel-based alloys has been a major hurdle for manufacturing industry in terms of productivity for a significant amount of time, and there are a number of issues that are yet to be understood. The effect of friction is an important issue and as it is the case with many other materials, there is a lack of complete understanding in how friction plays role in machining titanium and nickel-based alloys. Let alone 3D machining processes, the work on friction in 2D orthogonal machining processes still lacks entirety. It is known that with increasing friction, heat build-up and tool wear increases especially in the case of titanium and nickel-based alloys due to their low thermal conductivity and chemical affinity with tool materials at elevated temperatures. Consequently, there are surface integrity problems at the end product that will reduce product effectiveness, quality and reliability.

While it is important to understand the role of friction, attempts at measuring in-situ detailed frictional properties during machining have been a far cry from success. Attempting to get the optimum approximation in calculations to manufacturing processes by modeling friction still remains a tangible approach to this problem. As Childs (2006a) has reviewed in general for metal cutting, there has been an exhaustive amount of research on modeling friction, with all of them having their share of failure and success, as well as advantages and disadvantages. Finite Element-based models have comprised the most important part of the modeling work, and it is known that FE-based models are

used to find optimal cutting parameters and tool geometries (Arrazola et al. 2008, Arrazola & Özel 2010, Childs 2006b), as well as analytical and experimental investigations concerning friction coefficients (Özlü et al. 2009).

The scope of this study is to determine the friction coefficients between the cutting tool and the chip/workpiece during machining in order to improve the accuracy of FE-based simulations. Hence, the iterative approach presented here is utilized as a combination of the friction determination method coined in this chapter, and the FE-based simulations presented in the next chapter. Furthermore, importance of stagnation point during machining to the friction model will be presented, followed by friction models with and without tool wear. These friction models will be validated with force measurements, and FE-based model to validate the stresses.

2. Review of Friction Determination Methods in Machining

There have been many attempts to determine the friction coefficient during machining. The strengths and weaknesses of these methods should be understood to propose a new method. Despite being similar to each other in many ways, there are nuances that separate these methods, and it is important to understand these differences.

2.1 Pin-on-the-Disc Method

In this method, a tribometer with a pin is contacted with the disc. The disc is rotating, while the pin is constant, and the forces are measured by the tribometer. The ratio of the forces gives the coefficient of friction, and the method is known to provide useful information in many cases. However, the machining temperature and pressure cannot be maintained for the measurement, which leads to inaccurate measurements,

since the coefficient of friction is considered to be dependent on these factors (Bonnet et al. 2008).

In order to be able to achieve machining temperature, researchers proposed different methods where the pin follows the cutting tool, so that the workpiece is not relieved of the cutting temperature (Olsson et al. 1989, Hedenqvist & Olsson 1991). However, since this method could not imitate the cutting pressure, researchers went on to propose methods where the pin is coated by the imitated coating, and it rubs the surface of the disc with a feed provided, where a cutting tool refreshes the surface at each feed step (Bonnet et al. 2008). Using this method, researchers were able to measure the normal and tangential forces very close to the machining conditions and find the apparent friction coefficient.

2.2 Gradient Friction Coefficient Method

It has also been claimed that rather than changing with the proportion of feed forces vs. cutting forces, friction angle can be considered to change with the proportion of the derivative of feed forces with respect to cutting forces (Eq. 3.1). Starting with Albrecht's (1960) analysis, researchers proposed that graph of feed force versus cutting force with increasing feed values would create a non-linear region at low feed rates, and have a smaller slope with a linear trend when feed rates become higher (Arrazola & Meslin 2002, Arrazola et al. 2008). This suggestion needs extensive work to be developed, but it is a promising way to approach the problem.

$$\mu = tg\left(tg^{-1}\left(\frac{dF_f}{dF_c}\right) + \gamma_1\right) \qquad \text{Eq. (3.1)}$$

2.3 Mean Friction Coefficient Method

Many researchers have considered the coefficient of friction during machining processes to be quasi-steadily distributed along the friction distance. Hence, they deduced that defining a mean friction coefficient (obtained from measured cutting and thrust forces) along the friction face is enough to simulate the cutting conditions. Zorev (1963) was among these researchers to state that the ratio of frictional force to the cutting force measured by the dynamometer during machining tests would give the coefficient of friction at the friction surface (Eq. 3.2). He also stated that this coefficient changes mostly with the normal force, because the frictional force was usually constant. This model assumes that rake angle, the angle of inclination, and uncut chip thickness are the parameters affecting the results, and two zones of chip flow could be defined using this coefficient. These two zones were elastic and plastic contact zones where the ratio between the shear stress and the normal stress along the rake face during the elastic contact would be equal to the mean friction coefficient. In the following years, researchers used this idea to develop numerical models and analytical deductions, improving some aspect of the method by, for example, considering the mean friction coefficient to be dependent on mean temperature (Moufki et al. 1998).

$$\mu = \frac{F_t}{F_c} \qquad \text{Eq. (3.2)}$$

There are other studies starting from the same point, but expanding to different approaches. More than half a century ago, Albrecht (1960) believed that ploughing plays a significant yet falsely neglected role during machining, and accounting for this effect is necessary to model these processes (Eq. 3.3). He believed that calculating a mean friction coefficient, and then deducting the effect of ploughing force could be a good way

to approximate the solution. Decades later, other researchers continued to use this approach and called this the real friction coefficient, with edge forces deducted from the measured forces in tangential and normal force components, and then taking the ratio between these results (Sutter & Molinari 2005).

$$\mu = \frac{F_t - F_{t_0}}{F_c - F_{c_0}} \quad \text{Eq. (3.3)}$$

Another approach to the friction considerations was to divide the friction coefficient into two components, as apparent and sliding friction coefficients (Özlü et al. 2009, Molinari et al. 2011). The apparent friction coefficient (μ_{ap}) would be the ratio of the integration of the areas under the shear and normal stress curves along the entire friction face (Eq. 3.4); in other words it is the ratio of total friction and normal forces on the entire rake face. The sliding friction coefficient (μ_{sl}) would be the ratio of the integration of areas under the shear and normal stress curves along the sliding region at the friction face only (Eq. 3.5); namely the ratio of the friction and normal forces acting on the sliding region along the rake face. They believed that the ratio of measured friction and normal forces would be equal to the sliding friction coefficient (μ_{sl}), where the apparent friction coefficient (μ_{ap}) would be dependent on the tool-chip contact length, the plastic contact length, and the normal stress on the rake face at the tool tip. When there is no sticking in the friction zone, the sliding, apparent and mean friction coefficients would be equivalent to each other.

$$\mu_{ap} = \frac{F_c tg(\gamma_1) + F_t}{F_c - F_t tg(\gamma_1)} \quad \text{Eq. (3.4)}$$

$$\tau = \mu_{sl}\sigma \quad \text{Eq. (3.5)}$$

While this friction definition reveals more detailed friction than using a mean friction coefficient, determination of the friction coefficients by utilizing experimental

observations to identify plastic and elastic contact regions over the rake face is time consuming and laborious, and it could be not fully applicable to titanium and nickel-based alloys where these regions are only stable during the early stages of the machining process. In addition, this approach also requires these regions to be defined in Finite Element simulation models creating additional input parameters to the simulation system to be concerned about.

3. Review of Stagnation Point

Another important issue in difficult-to-process materials is the effect of tool edge radius on the chip formation process and its influence on wear development. When the workpiece is machined, it is separated to two pieces by the tool; the chip and the machined workpiece. The separated material flows in the two direction along the tool round edge, which means that the material flow velocity is zero at one point on the tool edge. This point is conventionally called the stagnation point. The location of the stagnation point has been investigated by many scholars, as it is considered to be important in determining the rate of tool wear, and eventually, the machined surface quality. Fang's (2003) study was mainly about the effects of size variables (cutting edge radius, uncut chip thickness, stagnation point) on forces, tool-chip contact length, shear strain and shear strain rate during machining using slip-line analysis. Results of that study showed that with decreasing uncut chip thickness to cutting edge radius ratio, the tool-chip contact length decreased from almost twice the uncut chip thickness to around the same value as the uncut chip thickness (Figure 3.1). They also showed that with increasing stagnation angle, the effect of ploughing force decreased (Figure 3.2), as well

as the average shear strain (Figure 3.3), whereas the average shear strain rate first decreased then increased (Figure 3.4).

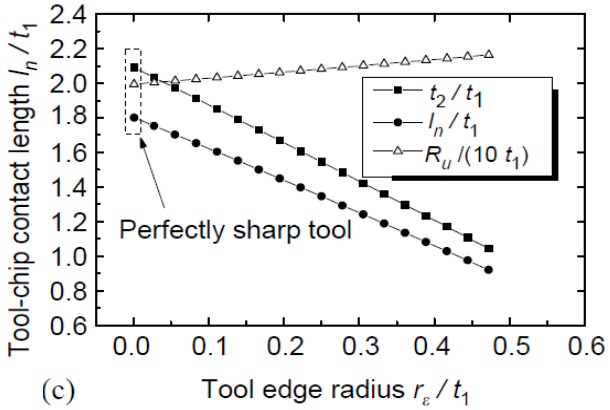

Figure 3.1: Change of tool-chip contact length with 1/Ratio (Fang 2003)

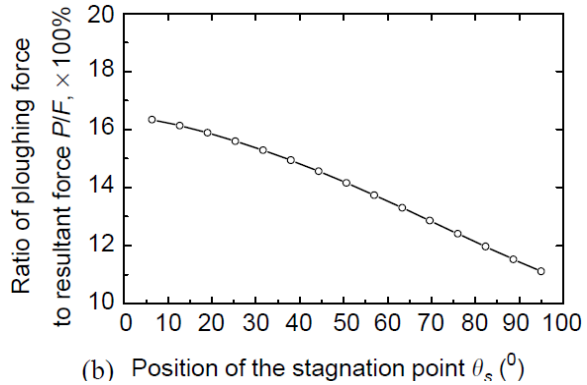

Figure 3.2: Effect of stagnation angle on ploughing force (Fang 2003)

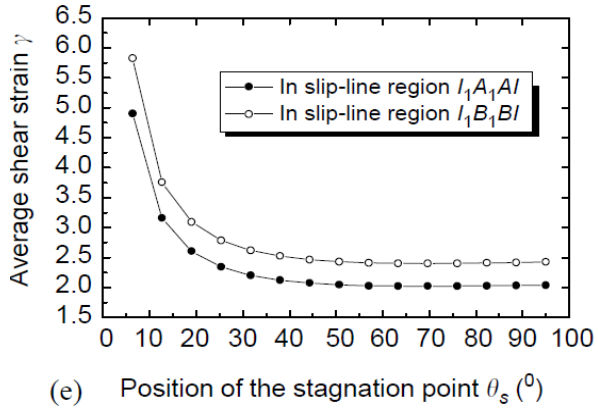

Figure 3.3: Effect of stagnation angle on shear strain (Fang 2003)

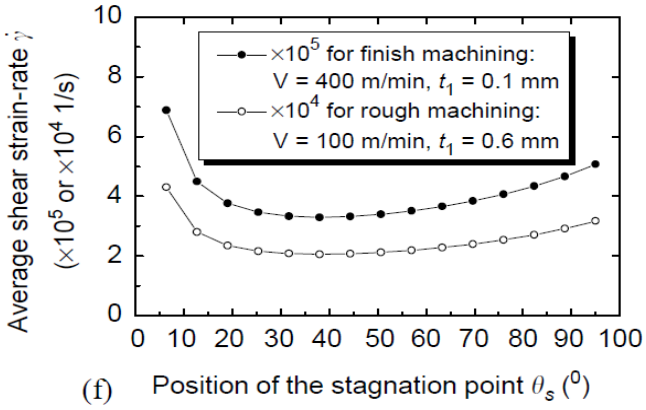

Figure 3.4: Effect of stagnation angle on shear strain rate (Fang 2003)

Yen et al. (2004) did a FE-analysis of orthogonal machining using a 0.2% plain carbon steel (AISI 1020) as the workpiece material and uncoated cemented carbide as tool material to investigate effects of different tool edge geometries. Their results showed that for round edge tools, stagnation angle is ~57-65° for 50 and 100 μm edge radius tools. Kishawy et al. (2006) also investigated effect of edge radius during orthogonal machining using a FE-based method, starting from a pre-defined chip formation. They showed that at the stagnation point, shear stress changes its sign and normal stress is close to its peak value (Figure 3.5). They also showed that stagnation angle is ~60-75° for machining of hardened AISI 4140 steel, and it decreases with increasing edge radius from 15 to 90 μm (Figure 3.6). Woon et al. (2008) studied the effects of cutting edge radius on contact variables in micromachining using a FE-based model. They divided the contact between the tool and the workpiece to three regions, and separated these regions with different types of friction (Figure 3.7). They defined these regions as a sliding region on the rake face and another sliding region on the clearance face, as well as a sticking region at the edge radius face. After their analyses, they found out that stagnation angle was ~58-59° for 2-20 μm uncut chip thickness and 100 m/min cutting speed.

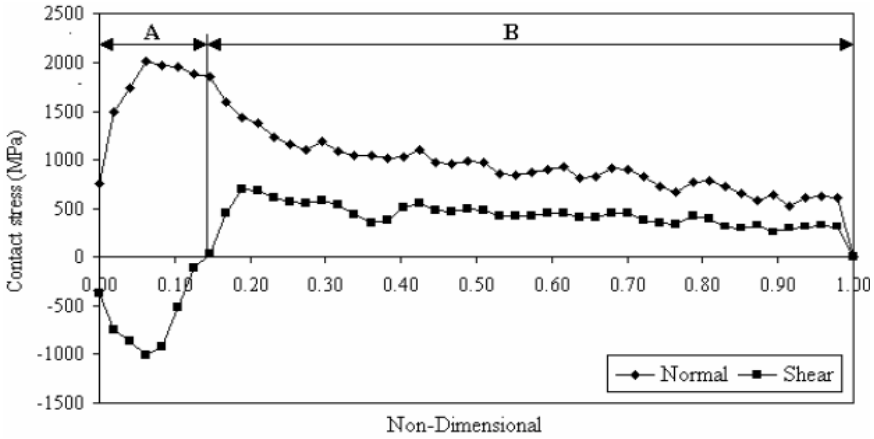

Figure 3.5: Change of normal and shear stresses with distance along chip-tool contact (Kishawy et al. 2006)

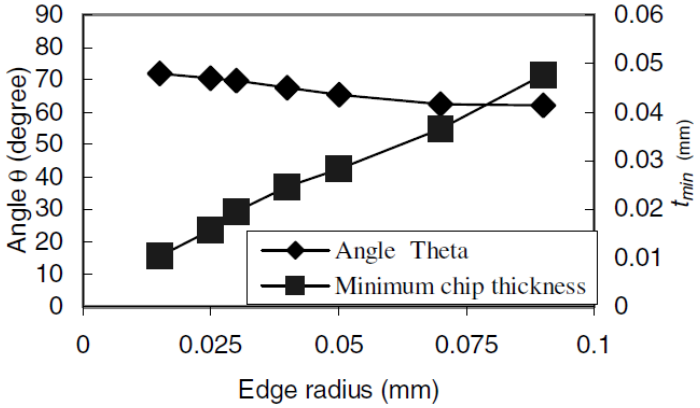

Figure 3.6: Change of the stagnation angle with cutting edge radius (Kishawy et al. 2006)

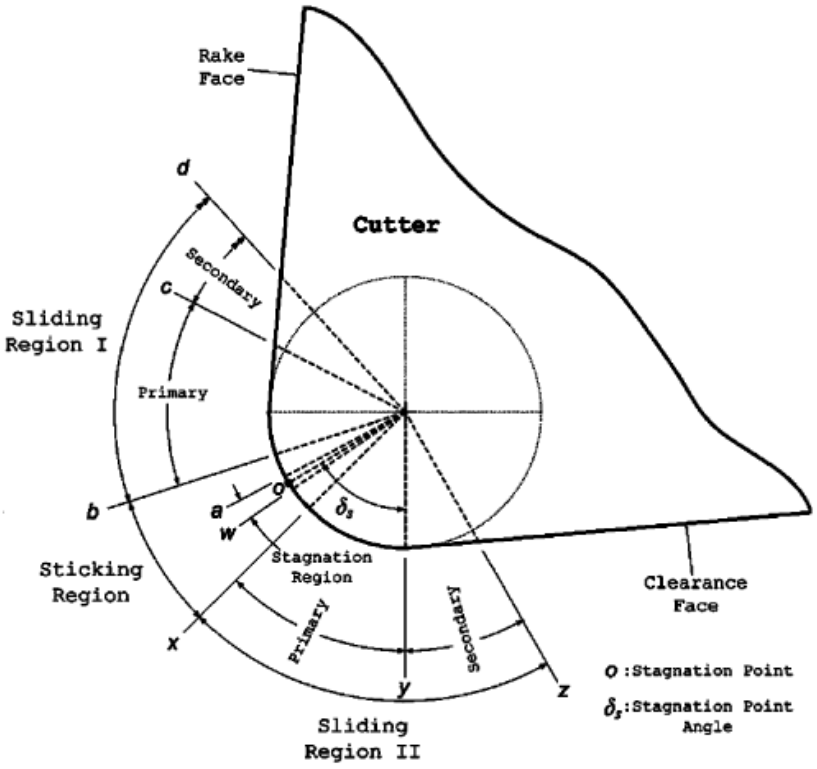

Figure 3.7: Sliding and sticking friction regions on the tool for micromachining (Woon et al. 2008)

Fang & Xiong (2008) worked on the determination of friction on round tools. They generated a new method using slip-lines to predict cutting forces and chip thickness and optimize these values to solve for friction coefficients and stagnation point. They used Al 2024-T351 and Copper 330 as their workpiece materials and a 5° rake angle carbide tool with a TiC/TiN/TiCN coating. They showed the effects of changing the ratio of uncut chip thickness (t_u or t_1) to cutting edge radius (r_n or r_β), and found that with increasing ratio, rake face friction coefficient does not change significantly (stays around 0.4), but stagnation angle increases for both materials (Figures 3.8-3.9). For Al 2024-T351, stagnation angle increased from ~20° to ~35° when the ratio increased from 0.8 to 2.1 (Figure 3.8). For 330 Copper, stagnation angle increased from ~10° to ~30-35° when the ratio increased from 0.9 to around 1.8 (Figure 3.9).

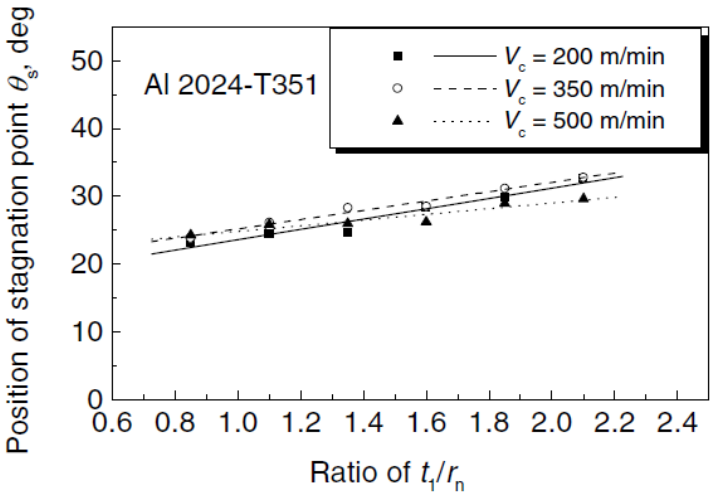

Figure 3.8: Stagnation angle vs. Ratio of t_u/r_β for Al 2024-T351 (Fang & Xiong 2008)

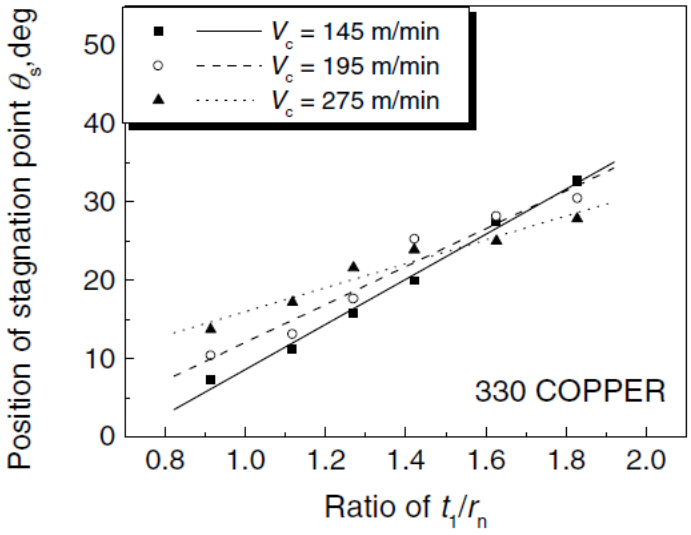

Figure 3.9: Stagnation angle vs. Ratio of t_u/r_β for 330 Copper (Fang & Xiong 2008)

4. Determination of Friction Coefficients for Round Edge Cutting Tool

The cutting tool, even when it is considered to be sharp, always has a rounded edge due to impossibility of infinite accuracy of the tool manufacturing technology. For sharp tools, this rounded edge can be assumed to have a very small radius (such as < 1 μm), or a relatively small radius (such as 2-3 μm) depending on the accuracy of the tool manufacturer. With this in mind, one can assume safely that the cutting tool is always rounded at the edge, and then start the following analysis. In this analysis, tool-

workpiece/chip interface was divided into three regions (Figure 3.10), and tool is assumed to be at or close to its fresh state of geometry.

In the first region (Region 1), the tool and the workpiece were considered to have full contact on the edge face, where the workpiece faces shearing. In this region, stick and slide conditions of friction are assumed. From the rake end of the circular region (x_1=0) to the end of the tool/chip contact (x_1=l_c), tool and workpiece were considered to have stick and slide friction conditions. In the second region (Region 2), from the flank end of the circular region (x_2=0) to the end of the wear length (x_2=l_2), the tool is assumed to have only sliding friction conditions. The sliding friction coefficients at the rake and flank faces are calculated using the procedure described below, and inserted into the FEM model created.

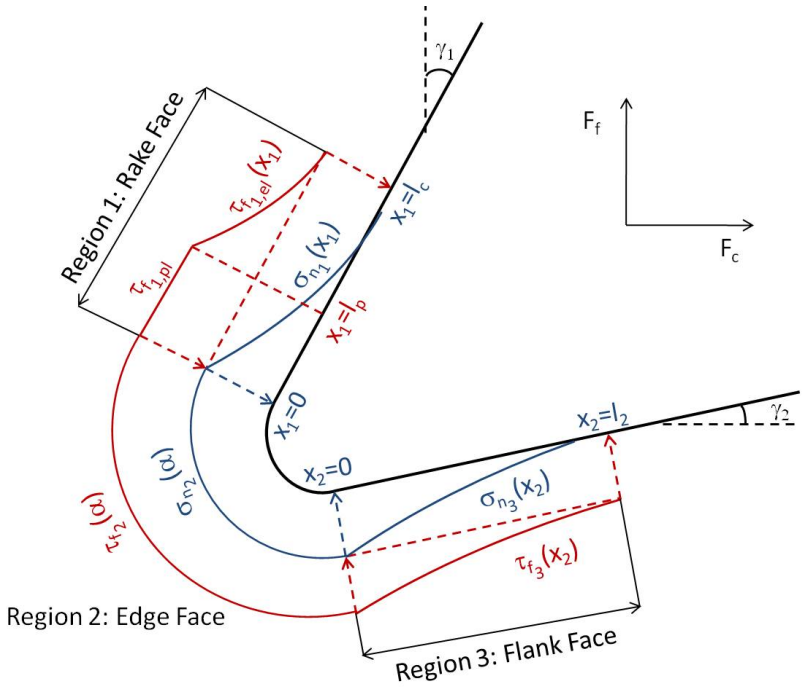

Figure 3.10: Illustration of stresses on the three regions of tool

To start the procedure, five unknown variables are searched within acceptable intervals: rake and flank face friction (μ_1 & μ_2, respectively), tool-chip contact length on

the rake region (l_c), maximum normal stress on the rake region ($\sigma_{1_{max}}$), and the maximum normal stress on the flank region ($\sigma_{3_{max}}$). The normal and tangential components of forces in all three regions are calculated and converted to cutting and feed force components (F_c & F_f, respectively), which are then summed up to result in the total cutting and feed forces:

$$F_c = F_{n_{1_c}} + F_{t_{1_c}} + F_{n_{2_c}} + F_{t_{2_c}} + F_{n_{3_c}} + F_{t_{3_c}} \quad \text{Eq. (3.6)}$$

$$F_f = F_{n_{1_f}} + F_{t_{1_f}} + F_{n_{2_f}} + F_{t_{2_f}} + F_{n_{3_f}} + F_{t_{3_f}} \quad \text{Eq. (3.7)}$$

In the first region, normal stress is assumed to have a polynomial distribution (Figure 3.11):

$$\sigma_1(x_1) = \sigma_{1_{max}} \left(1 - \frac{x_1}{l_c}\right)^n \quad \text{Eq. (3.8)}$$

When integrated from x_1=0 to l_c, normal component of force in this region is found to be:

$$F_{n_1} = \int_0^{l_c} \sigma_{1_{max}} \left(1 - \frac{x_1}{l_c}\right)^n dx_1 = \sigma_{1_{max}} \left(\frac{l_c}{n+1}\right) \quad \text{Eq. (3.9)}$$

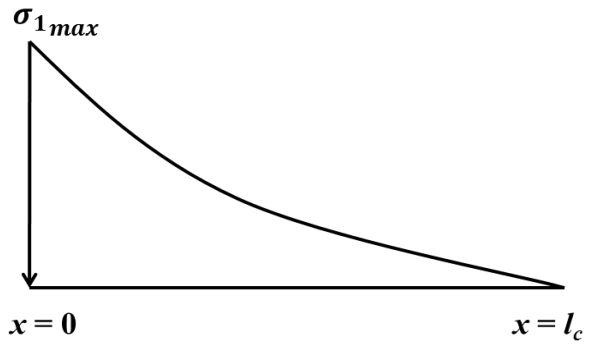

Figure 3.11: Illustration of the normal stress along the rake face region (Region 1)

There are two different types of friction in this region (Figure 3.12). Sticking friction brings plastic shear conditions, and after a certain amount of plastic contact, chip

starts to slide on the tool, which brings elastic shear conditions. Here, shear stress on the rake face can be found as:

$$\tau_1(x_1) = \begin{cases} \tau_{1_{max}}, & 0 \le x_1 \le l_p \\ \mu_1 \sigma_{1(x_1)}, & x_1 > l_p \end{cases} \qquad \text{Eq. (3.10)}$$

where $\tau_{1_{max}} = \mu_1 \sigma_{1_{max}} \left(1 - \frac{l_p}{l_c}\right)^n$. Then, after integrating shear stresses from x_1=0 to l_c, total tangential force in this region can be found as:

$$F_{t_1} = \int_0^{l_p} \tau_{1_{max}} dx_1 + \int_{l_p}^{l_c} \mu_1 \sigma_{1_{max}} \left(1 - \frac{x_1}{l_c}\right)^n dx_1$$

$$= \tau_{1_{max}} l_p + \mu_1 \sigma_{1_{max}} \frac{l_c}{n+1} \left(1 - \frac{l_p}{l_c}\right)^{n+1} \qquad \text{Eq. (3.11)}$$

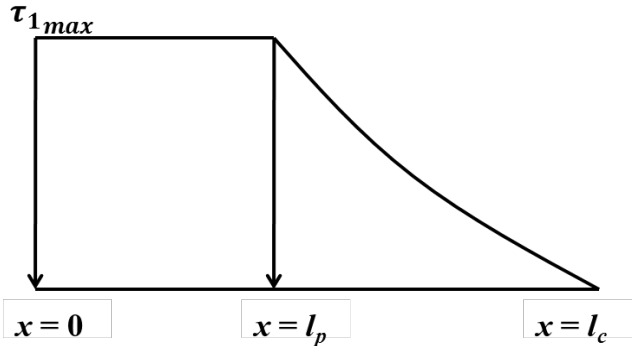

Figure 3.12: Illustration of the frictional shear stress along the rake face region (Region 1)

Using the forces in the tangential and normal directions to the rake face, feed and cutting direction components (of Eq. 3.6-3.7) can be calculated using the rake angle (γ_1):

$$F_{n_{1_c}} = F_{n_1} \cos\gamma_1 = \sigma_{1_{max}} \cos\gamma_1 \left(\frac{l_c}{n+1}\right) \qquad \text{Eq. (3.12)}$$

$$F_{n_{1_f}} = -F_{n_1} \sin\gamma_1 = -\sigma_{1_{max}} \sin\gamma_1 \left(\frac{l_c}{n+1}\right) \qquad \text{Eq. (3.13)}$$

$$F_{t_{1_c}} = F_{t_1} \sin\gamma_1 = \mu_1 \sigma_{1_{max}} \sin\gamma_1 \left(\frac{nl_p + l_c}{n+1}\right) \left(1 - \frac{l_p}{l_c}\right)^n \qquad \text{Eq. (3.14)}$$

$$F_{t_{1_f}} = F_{t_1} \cos\gamma_1 = \mu_1 \sigma_{1_{max}} \cos\gamma_1 \left(\frac{nl_p + l_c}{n+1}\right) \left(1 - \frac{l_p}{l_c}\right)^n \qquad \text{Eq. (3.15)}$$

The second contact region is edge face, which is the curvilinear section that is located between the linear rake region and the linear tool wear region (Figure 3.13). In this region, normal and shear stresses are assumed to be linearly changing throughout the angular profile. Normal stress is assumed to start from $\sigma_{1_{max}}$ at α=-γ_1, and decrease linearly to $\sigma_{3_{max}}$ at α=π/2+γ_2 (Figure 3.14). Hence, normal stress distribution in the second region can be written as Eq. (3.16). Shear stress, on the other hand, is assumed to start from $\tau_{1_{max}}$ at α=-γ_1, and decrease linearly to $\tau_{3_{max}}$ at α=π/2+γ_2 (Figure 3.15). Due to the directions of the flow of chip and machined workpiece, direction of the maximum shear stress at the flank face ($\tau_{3_{max}}$) is opposite to the direction of rake face shear stress ($\tau_{3_{max}}$), causing a stagnation point at the edge face (Kishawy et al. 2006), and stagnation angle can be found by Eq. (3.17). As a result of the assumptions, shear stress distribution in the second region can be written as Eq. (3.18). Integrating these functions through the whole region, one can find the force components in cutting and feed directions (Eq. 3.19-3.22).

$$\sigma_2(\alpha) = \frac{(\sigma_{3max}-\sigma_{1max})\alpha+\left(\gamma_1\sigma_{3max}+\left(\frac{\pi}{2}+\gamma_2\right)\sigma_{1max}\right)}{\pi/_2+\gamma_1+\gamma_2} \qquad \text{Eq. (3.16)}$$

$$\gamma_s = \frac{(\pi/_2+\gamma_2)\tau_{1max}-\gamma_1\tau_{3max}}{\tau_{1max}+\tau_{3max}} \qquad \text{Eq. (3.17)}$$

$$\tau_2(\alpha) = -\frac{(\tau_{3max}+\tau_{1max})\alpha+\left(\gamma_1\tau_{3max}-\left(\frac{\pi}{2}+\gamma_2\right)\tau_{1max}\right)}{\pi/_2+\gamma_1+\gamma_2} \qquad \text{Eq. (3.18)}$$

$$F_{n_{2_c}} = \int_{\alpha=-\gamma_1}^{\pi/_2+\gamma_2} \sigma_2(\alpha)\cos\alpha\, r_\beta d\alpha$$

$$= r_\beta\left[\begin{matrix}\sigma_{3_{max}}\sin\left(\frac{\pi}{2}+\gamma_2\right)+\sigma_{1_{max}}\sin\gamma_1+\\ \frac{\sigma_{1max}-\sigma_{3max}}{\gamma_1+\left(\frac{\pi}{2}+\gamma_2\right)}\left(\cos\gamma_1-\cos\left(\frac{\pi}{2}+\gamma_2\right)\right)\end{matrix}\right] \qquad \text{Eq. (3.19)}$$

$$F_{n_{2_f}} = \int_{\alpha=-\gamma_1}^{\pi/2+\gamma_2} \sigma_2(\alpha) \sin\alpha \, r_\beta \, d\alpha$$

$$= r_\beta \begin{bmatrix} \sigma_{1_{max}} \cos\gamma_1 - \sigma_{3_{max}} \cos\left(\frac{\pi}{2}+\gamma_2\right) - \\ \frac{\sigma_{1_{max}} - \sigma_{3_{max}}}{\gamma_1 + \left(\frac{\pi}{2}+\gamma_2\right)} \left(\sin\gamma_1 + \sin\left(\frac{\pi}{2}+\gamma_2\right)\right) \end{bmatrix} \qquad \text{Eq. (3.20)}$$

$$F_{t_{2_c}} = \int_{\alpha=-\gamma_1}^{\pi/2+\gamma_2} -\tau_2(\alpha) \sin\alpha \, r_\beta \, d\alpha$$

$$= r_\beta \begin{bmatrix} \tau_{3_{max}} \cos\left(\frac{\pi}{2}+\gamma_2\right) - \tau_{1_{max}} \cos\gamma_1 + \\ \frac{\tau_{1_{max}} - \tau_{3_{max}}}{\gamma_1 + \left(\frac{\pi}{2}+\gamma_2\right)} \left(\sin\gamma_1 + \sin\left(\frac{\pi}{2}+\gamma_2\right)\right) \end{bmatrix} \qquad \text{Eq. (3.21)}$$

$$F_{t_{2_f}} = \int_{\alpha=-\gamma_1}^{\pi/2+\gamma_2} \tau_2(\alpha) \cos\alpha \, r_\beta \, d\alpha$$

$$= r_\beta \begin{bmatrix} \tau_{3_{max}} \sin\left(\frac{\pi}{2}+\gamma_2\right) + \tau_{1_{max}} \sin\gamma_1 + \\ \frac{\tau_{1_{max}} - \tau_{3_{max}}}{\gamma_1 + \left(\frac{\pi}{2}+\gamma_2\right)} \left(\cos\gamma_1 - \cos\left(\frac{\pi}{2}+\gamma_2\right)\right) \end{bmatrix} \qquad \text{Eq. (3.22)}$$

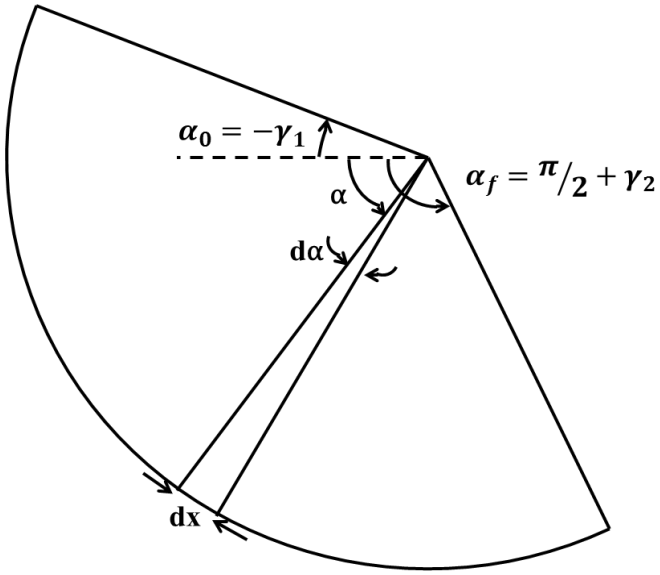

Figure 3.13: Edge face illustration (Region 2)

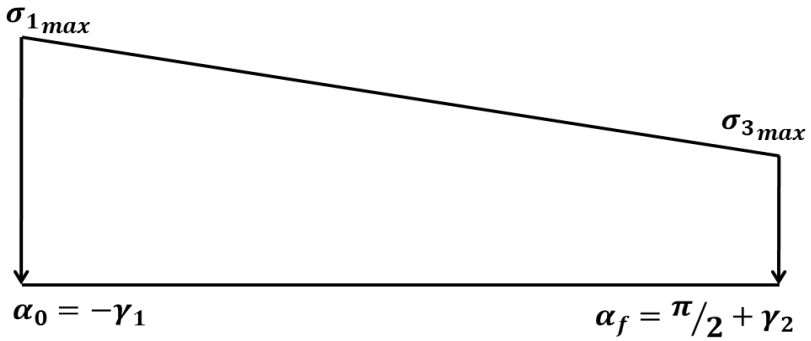

Figure 3.14: Normal stresses on the edge face (Region 2)

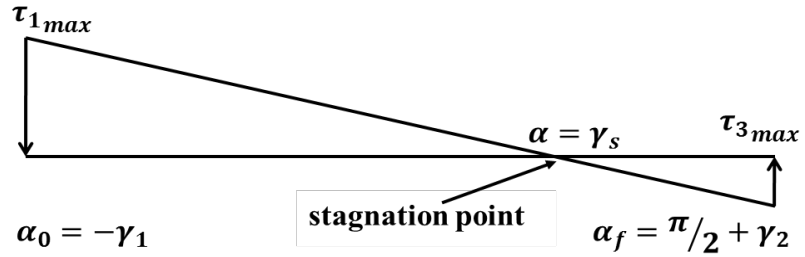

Figure 3.15: Shear stresses on the edge face (Region 2)

Forces in the third region can be found similarly to the first region, except here, there is no sticking condition is assumed. So, normal and shear stresses, and forces in those directions can be found as:

$$\sigma_3(x_2) = \sigma_{3_{max}} \left(1 - \frac{x_2}{VB}\right)^m \quad \text{Eq. (3.23)}$$

$$F_{n_3} = \int_0^{VB} \sigma_{3_{max}} \left(1 - \frac{x_2}{VB}\right)^m dx_2 = \sigma_{3_{max}} \left(\frac{VB}{m+1}\right) \quad \text{Eq. (3.24)}$$

$$\tau_3(x_2) = \mu_2 \sigma_3(x_2) \quad \text{Eq. (3.25)}$$

$$F_{t_3} = \int_0^{VB} \mu_2 \sigma_{3_{max}} \left(1 - \frac{x_2}{VB}\right)^m dx_2 = \mu_2 \sigma_{3_{max}} \frac{VB}{m+1} \quad \text{Eq. (3.26)}$$

Using these forces, and the clearance angle at the flank face (γ_1), the forces in the cutting and feed force directions can also be found as:

$$F_{n_{3_c}} = F_{n_3} \cos\gamma_2 = \sigma_{3_{max}} \cos\gamma_2 \left(\frac{VB}{m+1}\right) \quad \text{Eq. (3.27)}$$

$$F_{n_{3_f}} = -F_{n_3} \sin\gamma_2 = -\sigma_{3_{max}} \sin\gamma_2 \left(\frac{VB}{m+1}\right) \quad \text{Eq. (3.28)}$$

$$F_{t_{3_c}} = F_{t_3} \sin\gamma_2 = \mu_2 \sigma_{3_{max}} \sin\gamma_2 \left(\frac{VB}{m+1}\right) \quad \text{Eq. (3.29)}$$

$$F_{t_{3_f}} = F_{t_3} \cos\gamma_2 = \mu_2 \sigma_{3_{max}} \cos\gamma_2 \left(\frac{VB}{m+1}\right) \quad \text{Eq. (3.30)}$$

5. Determination of Friction Coefficients for Round Edge Cutting Tool in Presence of Tool Flank Wear

In machining operations such as milling and turning, the tool contacts the workpiece at the cutting edge, where chip forms, and it contacts chip at the rake face until chip separates from the tool. Considering the previous argument about even sharp tools being rounded with small edge radius, initially the tool contact at the flank face will not be a major contributor to the process. However, when the tool begins to wear, it is rapidly worn parallel to cutting speed direction, and orthogonal to feed direction. Hence, when tool becomes even slightly worn, there will be another contact region at the flank face due to tool wear. This is a common case for machining difficult-to-cut materials such as hardened steel, titanium and nickel-based alloys. As a result, contact between workpiece/chip and tool can be divided into three basic regions in presence of flank wear (Figure 3.16) (Ulutan & Özel 2012). First and third regions of this tool geometry will have similar stress and force considerations with the previous model. For the first region, there is no change at all. For the third region, stress distributions will not change, but the conversion angle is now zero, because wear is along the cutting direction, so the force components will be as Eq. (3.31-3.33).

$$F_{n_{3_c}} = F_{t_{3_f}} = 0 \quad \text{Eq. (3.31)}$$

$$F_{n_{3_f}} = F_{n_3} = \sigma_{3_{\max}} \left(\frac{VB}{m+1}\right) \quad \text{Eq. (3.32)}$$

$$F_{t_{3_c}} = F_{t_3} = \mu_2 \sigma_{3_{max}} \left(\frac{VB}{m+1}\right) \quad \text{Eq. (3.33)}$$

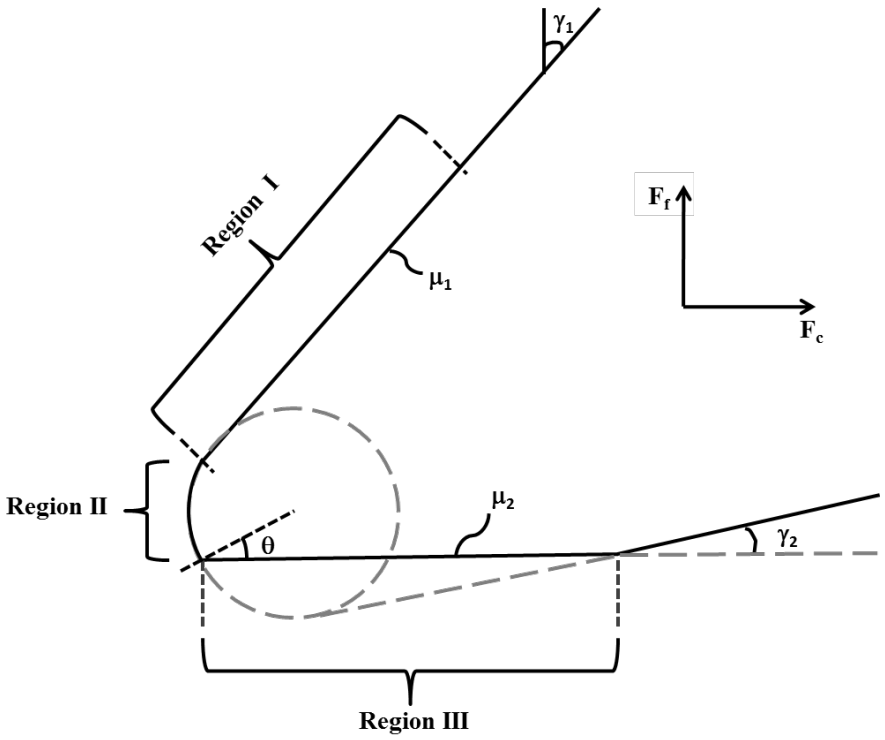

Figure 3.16: Illustration of the three regions of cutting edge of a tool in the presence of flank wear

The second contact region will change slightly from the previous (no flank geometry change) model. As shown in Figure 3.17, the angle α will still be equal to the rake angle of the tool at the rake face end, but at the flank face end, the cut-off angle (θ) will not be equal to $\pi/2+\gamma_2$ anymore. Instead, it will be calculated using the clearance angle (γ_2), cutting edge radius (r_β), and the tool wear amount (VB) via Eq. (3.34). As with the previous model, changing from Cartesian to polar coordinates helps in analyzing this region, so the stresses can be shown as a function of α. The linear changing assumption of normal and shear stresses is still used, and it will be as shown in Figures 3.18-3.19. Note that the angle at the flank face is shown as θ rather than the angle used in the previous model ($\pi/2+\gamma_2$), and the normal and shear stresses at this point are shown

differently ($\tilde{\sigma}_2$ and $\tilde{\tau}_2$ rather than $\sigma_{3_{max}}$ and $\tau_{3_{max}}$). The stagnation angle can be calculated similarly to the previous model; only the values will be different (Eq. 3.35).

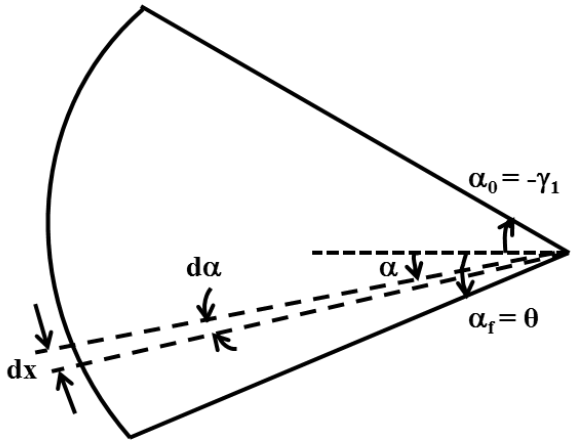

Figure 3.17: Illustration of the tool edge face and angles (Region I)

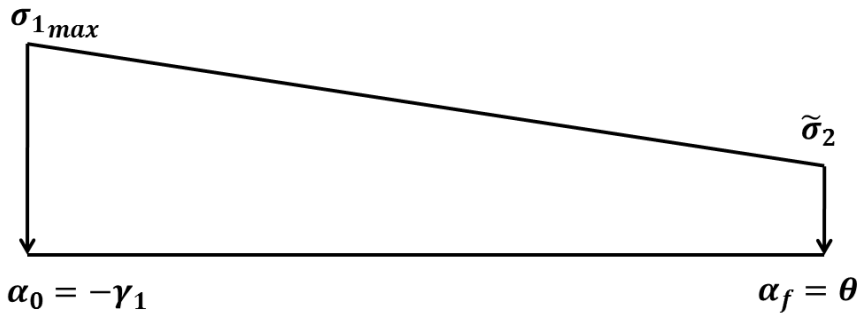

Figure 3.18: Illustration of the normal stress along the edge face region (Region II)

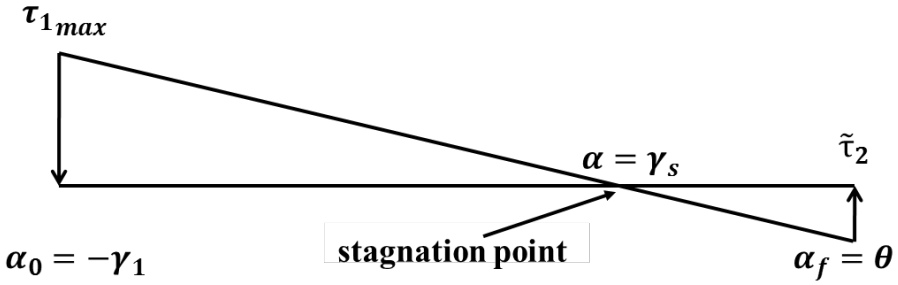

Figure 3.19: Illustration of the frictional shear stress along the edge face region (Region II)

Analyzing the tool geometry (Figure 3.16), one would realize that there is continuity in geometry from the rake face (Region I) to the edge face (Region II), so the

stresses should be continuous as well, similar to the previous model. However, the geometry is not continuous at the beginning of the flank face, due to tool wear, which is the reason for the different values of normal and shear stress shown in Figures 3.18-3.19. Here, the vector sum of the shear and normal stresses at the flank face end should be equal to the vector sum of the shear and normal stresses at the beginning of the flank face (Eq. 3.36). Using this equation, the unknown normal and shear stresses at the flank face end of Region II can be found as shown in Eq. (3.37-3.38). Then, the functions of normal and shear stress with changing angle (α) in this region will become as Eq. (3.39-3.40). Taking the integral through the whole region, the tangential and normal components of force acting on the cutting and feed directions can be found (Eq. 3.41-3.44).

$$\theta = \gamma_2 + \sin^{-1}\left(1 - \frac{VB\sin\gamma_2}{r_\beta}\right) \quad \text{Eq. (3.34)}$$

$$\gamma_s = \frac{\theta\tau_{f1_{max}} - \gamma_1\tilde{\tau}_2}{\tau_{f1_{max}} + \tilde{\tau}_2} \quad \text{Eq. (3.35)}$$

$$\overrightarrow{\tilde{\sigma}_2} + \overrightarrow{\tilde{\tau}_2} = \overrightarrow{\sigma_{3_{max}}} + \overrightarrow{\tau_{3_{max}}} \quad \text{Eq. (3.36)}$$

$$\tilde{\sigma}_2 = \sigma_{3_{max}}(\mu_2 \sin\theta - \cos\theta) \quad \text{Eq. (3.37)}$$

$$\tilde{\tau}_2 = \sigma_{3_{max}}(\mu_2 \cos\theta + \sin\theta) \quad \text{Eq. (3.38)}$$

$$\sigma_2(\alpha) = \left(\frac{\tilde{\sigma}_2 - \sigma_{1max}}{\gamma_1 + \theta}\right)(\alpha + \gamma_1) + \sigma_{1_{max}} \quad \text{Eq. (3.39)}$$

$$\tau_2(\alpha) = \left(\frac{\tilde{\tau}_2 - \tau_{1max}}{\gamma_1 + \theta}\right)(\alpha + \gamma_1) + \tau_{1_{max}} \quad \text{Eq. (3.40)}$$

$$F_{n_{2_c}} = \int_{\alpha=-\gamma_1}^{\theta} \sigma_2(\alpha)\cos\alpha\, r_\beta d\alpha$$

$$= r_\beta\left[\begin{matrix}\tilde{\sigma}_2\sin\theta + \sigma_{1_{max}}\sin\gamma_1 + \\ \frac{\sigma_{1max} - \tilde{\sigma}_2}{\gamma_1 + \theta}(\cos\gamma_1 - \cos\theta)\end{matrix}\right] \quad \text{Eq. (3.41)}$$

$$F_{n_{2_f}} = \int_{\alpha=-\gamma_1}^{\theta} \sigma_2(\alpha) \sin\alpha \, r_\beta \, d\alpha$$

$$= r_\beta \begin{bmatrix} \sigma_{1_{max}} \cos\gamma_1 - \tilde{\sigma}_2 \cos\theta - \\ \frac{\sigma_{1_{max}} - \tilde{\sigma}_2}{\gamma_1 + \theta} (\sin\gamma_1 + \sin\theta) \end{bmatrix} \quad \text{Eq. (3.42)}$$

$$F_{t_{2_c}} = \int_{\alpha=-\gamma_1}^{\theta} -\tau_2(\alpha) \sin\alpha \, r_\beta \, d\alpha$$

$$= r_\beta \begin{bmatrix} \tilde{\tau}_2 \cos\theta - \tau_{1_{max}} \cos\gamma_1 + \\ \frac{\tau_{1_{max}} - \tilde{\tau}_2}{\gamma_1 + \theta} (\sin\gamma_1 + \sin\theta) \end{bmatrix} \quad \text{Eq. (3.43)}$$

$$F_{t_{2_f}} = \int_{\alpha=-\gamma_1}^{\theta} \tau_2(\alpha) \cos\alpha \, r_\beta \, d\alpha$$

$$= r_\beta \begin{bmatrix} \tilde{\tau}_2 \sin\theta + \tau_{1_{max}} \sin\gamma_1 + \\ \frac{\tau_{1_{max}} - \tilde{\tau}_2}{\gamma_1 + \theta} (\cos\gamma_1 - \cos\theta) \end{bmatrix} \quad \text{Eq. (3.44)}$$

There is a limitation to the set of assumptions in this study, that is, selection of tool flank wear should be done according to the constraints given in Eq. (3.45) (in order to be able to calculate θ). These are basically what the geometry allows, and with less or more of a tool flank wear length (VB) than permitted; only the calculations will change slightly, and the theory behind this study will still be applicable. However, with a typical selection of clearance angle (γ_2) and cutting edge radius (r_β), the tool flank wear length limits are virtually between the minimum possible tool flank wear length after a very short machining operation to a maximum possible tool flank wear length after a very long machining operation (without tool chipping). Also, the friction coefficient at the flank face (μ_2) should be selected according to the constraint given in Eq. (3.46). This is only so that the frictional shear stress at the flank face end of the edge face region ($\tilde{\tau}_2$) is calculated negative, and the stagnation point falls at the edge face. If this constraint is not satisfied, the stagnation point cannot be calculated. Hence, the formulation given here is capable of covering almost all the geometrical selections.

$$2\sin\gamma_2 < \frac{VB}{r_\beta} < 1 + \frac{1}{\sin\gamma_2} \quad \text{Eq. (3.45)}$$

$$\mu_2 < \frac{1}{\tan\theta} \quad \text{Eq. (3.46)}$$

6. Search and Optimization Algorithm

Once all of the force components are calculated, the next step is to add them up to find the resultant forces in the cutting and feed force directions (Eq. 3.6-3.7). These predicted force components should be compared with orthogonal cutting test measurements to find the right set of variables in the search algorithm. The geometrical variables are the cutting edge radius (r_β), the rake angle (γ_1), the clearance angle (γ_2), and the tool flank wear angle (θ). The first three are geometrical constraints from the tool, and the last one will be calculated. The contact variables are the total tool-chip contact length (l_c), the plastic tool-chip contact length (l_p), and the tool flank wear length (VB). These are not known prior to the simulations, and should be searched at the initial iteration. The polynomial variables (m, n) are also not known and should be searched at the initial iteration (or they could be assumed a value for the first iteration). The stress variables ($\sigma_{1_{max}}$, $\tilde{\sigma}_2$, $\sigma_{3_{max}}$, $\tau_{1_{max}}$, $\tilde{\tau}_2$, $\tau_{3_{max}}$) are also not known prior to the first iteration, and they should be searched at the first iteration. However, the shear and normal stresses at the rake face and flank face regions are related to each other with the coefficients of friction, and the shear and normal stresses in the edge face region at the flank face end are calculated (Eq. 3.37-3.38). Hence, there are essentially only two stress variables ($\sigma_{1_{max}}$, $\sigma_{3_{max}}$) to search. Friction variables are also not known and should be searched at every iteration (see Figure 3.20 for illustration of the algorithm).

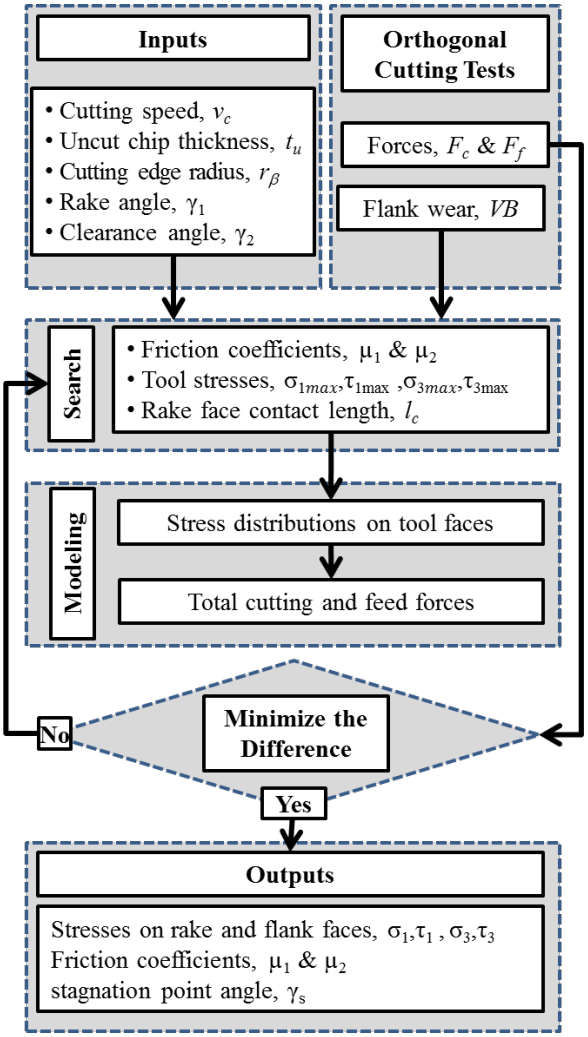

Figure 3.20: The search algorithm for the determination of friction coefficients

At the initial iteration, all the unknown variables are searched within meaningful limits. They are selected at random, and for each set of selection, forces in cutting and feed directions are found. These forces are compared to the measured forces from orthogonal cutting tests, and the error between the measured and calculated forces are used in the algorithm so that a total error is assigned to each set of variables (Figure 3.20). The selection of variables is done a satisfactory amount of times (until the minimum force error does not change), and each random set of variables has an error assigned to it. After enough number of sets are collected, the resultant variable set is

found using Eq. (3.47), where x_R is the resultant variable, x_i is the i^{th} unknown (searched) variable, e_i is the error assigned to that variable, and N is the total number of variables.

$$x_R = \frac{\sum_{i=1}^{N} x_i/e_i}{\sum_{i=1}^{N} 1/e_i} \quad \text{Eq. (3.47)}$$

After the initial calculation of unknown variables, the resultant variable set is passed to the FE-based simulations. When the simulation reaches steady-state of chip formation at forces comparable to measured forces, stress fields at the rake and flank faces are extracted. When stresses vs. distances are fit to a power curve, maximum normal ($\sigma_{1_{max}}$, $\sigma_{3_{max}}$) and frictional shear stresses ($\tau_{1_{max}}$, $\tau_{3_{max}}$) at the rake and flank face regions as well as polynomial coefficients (*m, n*) can be found. Also using rake face stresses, one can find total and plastic tool-chip contact lengths (l_c and l_p), and stagnation point can be confirmed using shear stress vector representation. At the next iteration of the friction determination method, these values are used instead of searching for all of them. As a result, at each iteration, friction coefficients are the only variables being searched (and then passed on to the FE-based simulation model), and remaining unknown parameters are retrieved from FE-based simulations. When friction coefficients are very close to each other within tolerable limits at two consecutive iterations, the algorithm is stopped and friction coefficients are determined (Figure 3.20).

7. Conclusions

Titanium and nickel-based alloys possess significant difficulty for high speed machining. Since friction plays an important role in these machining processes and is an important input to the FE-based simulation models, this work aims at introducing a new iterative technique to determine the friction coefficients and related parameters during machining titanium and nickel-based alloys. Experimental results from various sources

were used as guidance, since the experimental machining forces are needed to initiate the iterative algorithm. Tool material was uncoated tungsten carbide. Two different techniques were introduced, one with constant (unworn) tool geometry, and the other one with worn tool geometry, and the results were reflected to show the friction coefficients and related parameters under different cutting parameters. Results of these methods will be presented in Chapter 4, since FE-based simulations are also utilized for the iterative method described.

CHAPTER 4

FINITE ELEMENT-BASED SIMULATIONS: 2-D SIMULATIONS

1. Introduction

In understanding the mechanics of the machining processes, experimental analysis is very important, as there is no other physics-based method that can truly describe the process. However, conducting experiments takes excessive amount of time and resources, and is very costly. Even industrial practitioners cannot afford to do experiments for each and every set of input parameters that can be utilized in the industry. These parameters include but are not limited to tool parameters (tool material, several rake, inclination, and other tool angles, coating material, thickness, and method, nose radius, cutting edge radius, etc.), machining parameters (cutting speed, feedrate, depth of cut, width of cut, application of coolant/lubricant, type of machining, availability and utilization of post-processing, etc.), and workpiece parameters (material, chemical composition, hardness, physical properties, thermal properties, defects, pre-processing, etc.). These parameters cannot always be studied independently of each other as they have combined effects as well, which are not easy to understand through case by case trial and error. Hence, there is a substantial need for methods that can simulate the experimental analysis. These simulation methods may or may not be physics-based, but they must be validated by experimental results. Although physics-based analytical methods may seem like the best approach, it is known that they cannot cover the complete physics of the process or provide detailed analysis (such as strain, stress and temperature fields etc.) and the number of assumptions make the accuracy and reliability of the estimations and predictions made with these methods deteriorate.

In this scenario, Finite Element-based methods offer relatively fast and accurate results to simulate the physics of the process with a rich set of output variables (e.g. strain, stress, and temperature fields). Once the FE-based methods are validated, outputs of these physics-based simulations can be utilized in predicting further sets of parameters (such as tool wear and surface integrity) and may lead to elimination of the need for excessive experimentation. This way, it will be possible to conduct experiments only for selected conditions that define the range of parameters, and utilizing the physics-based simulations, any other process parameter set can be simulated. Once the simulation model is validated with physical machining experiments through measurements of forces, temperatures and stress fields on the machined surface, these simulation models can be utilized in simulation experiments in order to optimize machining parameters (tool material, tool edge geometry and cutting conditions), eliminating or minimizing costly experimentation.

In order to achieve these goals, it is important to develop expertise on the simulation software, and to discover the critical points within the software that lead to more accurate and faster working nature of the simulations, such as tolerances, time steps, flow stress and other models, contact definitions, etc. For this purpose, 2D simulation system utilizing the updated Lagrangian software DEFORM-2D is explained in detail in this chapter. Because of the more complex nature of the 3D simulations, there are differences in designing, running, controlling, and taking data from them. In this chapter, 2D simulations are explained, whereas in the next chapter, the differences of 3D simulations compared to 2D simulations are explained. The results for 2D simulations, in addition to the results of the Friction Determination Methodology described in Chapter 3

are given in this chapter. Conclusions regarding these 2D simulations are given in the last section of this chapter. 2D simulations are utilized in order to determine the friction coefficients and understand the mechanics of the process; however, 3D simulations are later utilized to achieve the final results that are compared to experimental findings.

2. Physics-Based Simulations in 2D

When two-dimensional simulations are conducted, orthogonal machining experiments are simulated. The third dimension is not considered, as if the process is viewed from a front view (Figure 4.1). The deformations resulting from 2D simulation conditions are plane strain deformations i.e. the deformations are not allowed in the third geometrical dimension. In the simulations conducted for this study, the workpiece is defined as a rectangular shape, where the cutting length (and speed) is symbolized as an accelerated thermo-mechanical process in the horizontal direction, and the feed is symbolized as the cutting thickness in the vertical direction (uncut chip thickness). The elements that are defined closer to the tool tip are smaller, allowing them to exhibit finer calculations, since the thermal and mechanical process is mostly observed in that region. The elements that are defined far from the tool tip are larger, allowing a smaller number of total elements both in the tool and the workpiece, leading to a significantly decreased simulation time. Usually, minimum element size is in the order of few micrometers and the maximum elements size is approximately 100 micrometers with a size ratio up to 30 can be utilized in the fine mesh density within the same workpiece. In order to accelerate the simulations, heat transfer coefficient of the workpiece is defined as much higher than its actual value. This assumption not only allows the simulation to illustrate mechanics of the machining process within fragments of actual machining time (0.1-0.2 seconds

compared to 10-20 seconds), but it also does not cause any calculation inaccuracies. Therefore, without sacrificing from simulation accuracy, simulation time is decreased to less than a percent. This compromise is studied in the sensitivity analysis part of this work and results are presented in Chapter 6.

(a)

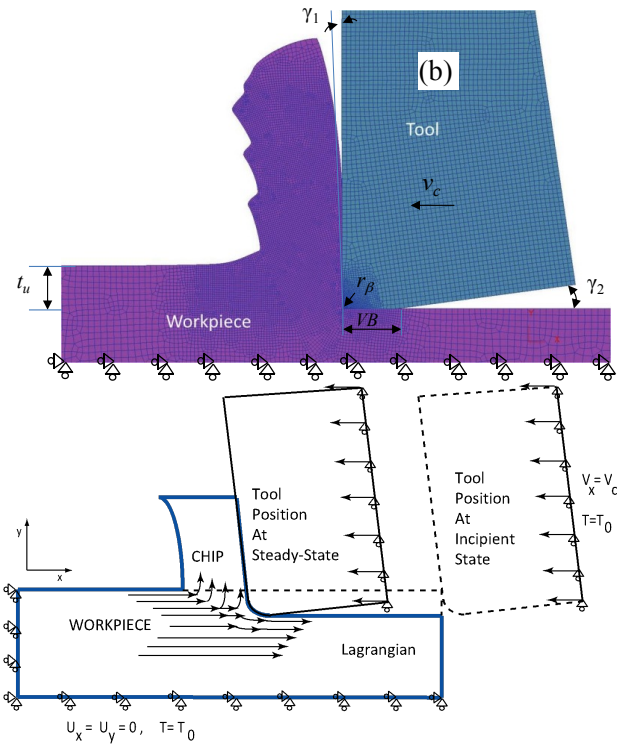

Figure 4.1: Mesh for (a) the workpiece and the tool and (b) boundary conditions (Özel & Zeren, 2007)

For any object defined within the software, there are four possible deformation mode assumptions that can be made: Rigid, elastic, plastic, or elastic-viscoplastic. When an object is selected as rigid, that object does not experience any deformation or physical change. The tool can be selected rigid (usually for simplicity) or elastic. Since elastic deformations of the tool cannot be easily simulated together with elastic-plastic workpiece assumption in 2-D analyses, and often stresses propagating into the tool are

usually less valued compared to chip formation, strains and stresses on the workpiece for conducting surface integrity studies (Özel et al. 2011).

For the purposes of this study, initial setting was to select the tool as rigid, as stresses on the tool were secondary. The second option of selecting an elastic object defines only elastic deformations on the object selected, which means that Hooke's law of stress and strain will be in effect for the object, regardless of how big these values are. Although this method might give some guidance, it is not useful for the workpiece either, because mechanics of the process are not represented, and plastic stresses and strains are not considered. The third option of selecting a plastic object defines only plastic deformations on the object selected, which means that even for a small amount of strain, there will be a stress higher than the yield strength of the material, avoiding the elastic portion of the stress-strain curves of the material. This is the closest case to physical nature of the process when there is no chance of defining the object as elastic-viscoplastic, which means that both the initial elastic portion and the following plastic portion are defined for the object.

This fourth option, when the material properties are well-defined for an object, is the imitation of the mechanics of the process, and should be used whenever possible. However, in some cases where some simulation parameters are not well-defined, or simulation controls do not allow (due to software-related numerical convergence concerns) elastic-viscoplastic model to be used for the workpiece, plastic model should be utilized to simulate as accurately as possible. In both 2D and 3D simulations, it is also sometimes possible to start with a plastic model, and switch to the elastic-viscoplastic model after few initial steps of simulation to achieve more accurately simulated results.

Table 4.1: Mechanical and thermo-physical properties of work and tool materials used in FE simulations

Property	Unit	WC/Co	Ti-6Al-4V	IN-100
E(T)	[MPa]	$5.6*10^{5}$	$0.7412*T+113375$	$-72*T+217000$
α(T)	[mm/mm°C]	$4.7*10^{-6}$	$3*10^{-9}*T+7*10^{-6}$	$1.1*10^{-5}$
λ(T)	[W/m°C]	55	$7.039*e^{0.0011*T}$	$10.3*e^{0.008*T}$
c_p(T)	[N/mm^2 °C]	$0.0005*T+2.07$	$2.24*e^{0.0007*T}$	$3.62*e^{0.0004*T}$

For the 2D simulations presented in this study, elastic-viscoplastic model (sometimes also called as elastic-viscoplastic) worked for all of the simulations, so no other deformation mode was considered for the workpiece. In the beginning of the simulations, the tool was defined as rigid so that the forces of the process could be matched first within a reasonable timeframe of simulation. When the forces were matched and a steady-state machining condition was achieved (about 1-2 millisecond), the deformation definition of the tool was changed to elastic model. Since during the machining, the tool deformation is insignificant compared to workpiece deformation, this assumption is valid. Also, stresses on the tool could be easily obtained with the elastic model, so there was no need for the plastic or elastic-viscoplastic models to be utilized for the tool. Once this change was implemented, the simulation was run for a further short while, allowing the stresses and temperatures on the tool to reach a steady-state. These stresses are assumed to be the steady-state stresses on the tool, and are used as an input to the friction determination method described in Chapter 3.

Before starting any simulation, it is important to pay attention to the simulation controls. After geometrically defining the objects and setting their object types, the material properties of the objects should be entered, or selected from the pre-defined libraries. Temperature-dependent thermal, physical and mechanical properties for the

materials used in this study can be found in Table 4.1. Temperature dependency of these properties allows higher accuracy in predicting output fields and provides more realistic physics-based simulation of the process. In addition to the elastic modulus (E), thermal expansion (α), thermal conductivity (λ), and specific heat capacity (c_p), these material properties also include the flow stress model that is defined as a function of strain, strain rate and temperature. There are several models that can be used as the flow stress model of a material, but the most common model that can be utilized is the Johnson-Cook material model (Model 1) (Eq. 4.1), where σ is the flow stress at corresponding strain (ε), strain rate ($\dot{\varepsilon}$), and temperature (T), A, B, C, n, m are the model parameters, T_0 is the room temperature, and T_m is the melting temperature of the material.

This initial model has been modified several times since it was first coined, with additions of strain hardening, strain rate hardening, and flow softening, and the flow stress model used in this study includes these additions (Model 2) (Eq. 4.2), where D, p, r, and s are modifying parameters of the constitutive equation. Determining flow stress is an important issue, as this model affects the machining forces predicted by the simulations. However, actual flow stress behaviors of the materials are not very well known at the deformation regimes seen in machining, so it is possible to change some of the parameters that are in the equation to modify the model. The set of parameters that gives the best force predictions should be selected, assuming that this set of parameters makes physical sense (Table 4.2). A more complex model of flow stress is later utilized in the 3D simulations, but the change in flow stress does not make a significant difference in 2D simulations as the main reason to conduct them was to determine the friction coefficients.

$$\sigma = [A + B\varepsilon^n]\left[1 + Cln\frac{\dot{\varepsilon}}{\dot{\varepsilon}_0}\right]\left[1 - \left(\frac{T-T_0}{T_m-T_0}\right)^m\right] \quad \text{(Eq. 4.1)}$$

$$\sigma = [A + B\varepsilon^n]\left[1 + Cln\frac{\dot{\varepsilon}}{\dot{\varepsilon}_0}\right]\left[1 - \left(\frac{T-T_0}{T_m-T_0}\right)^m\right]$$

$$\left[\mathrm{D} + (1 - \mathrm{D})\left[\tanh\left(\frac{1}{(\varepsilon+\mathrm{p})^{\mathrm{r}}}\right)\right]^{\mathrm{s}}\right] \quad \text{(Eq. 4.2)}$$

Table 4.2: Material model parameters used in FE simulations (Model 2)

Alloy	***A*[MPa]**	***B*[MPa]**	***n***	***C***	***m***	***D***	***p***	***r***	***s***
Ti-6Al-4V	1000	625	0.55	0.029	0.995	0.48	0	1.2	2.7
IN-100	1350	1750	0.65	0.017	1.3	0.6	0	1.0	5.0

Once the material models are selected, tool and workpiece mesh structures are created. It is possible to create uniform meshes for either (or both) of these objects. However, away from the location of actual machining, stresses and temperatures do not change much. Hence, it is better to concentrate dense mesh structures on the locations that machining and deformation occurs. For the tool, this is the tool tip. In order to do this, the software allows the user to create "mesh windows" that can concentrate the mesh density more to the selected windows on the object. This way, while having the same number of elements, the elements that are away from machining process become larger than average element size and the elements within the window become smaller. This allows better accuracy of the mesh to represent the geometry and mechanics of the process.

An additional possible definition is to command the program to create more elements where the strain and strain rate are increased, or near the edges of the objects to maintain the geometry. After the mesh windows are selected and these types of other concentrations are arranged by mostly trial and error, number of elements for each object should be selected. This selection should be strategic, because if high element numbers

and a large simulation file size than the computer can handle is created, the simulation will either not run, or run at a very slow rate that the speed advantage of the simulations is not observed.

On the other hand, if too few elements are selected, the mechanics of the chip formation process may not be well represented. Hence, the researcher first needs to evaluate several options to find an optimal number of elements. For the 2D simulations, this number was mostly approximately 100,000 for the workpiece, and 200,000 for the tool since tool has an edge radius to be well represented with high number of elements around the edge. Since the tool was selected rigid and no mesh distortion takes place, no remeshing is required during the simulations. Therefore, if the initialization of the tool mesh is successfully handled by the computer, the number of elements does not matter throughout the rest of the simulation. However, due to the remeshing nature of the simulation program, the initial mesh for the workpiece will be refreshed every few steps or once it is excessively distorted to ensure that geometrical changes in the workpiece/chip are represented in the simulation. Hence, the number of elements in the workpiece cannot be selected as high as the tool due to aforementioned temporal concerns and frequent remeshing.

After the mesh structures for both the tool and workpiece are defined, boundary conditions for both must be implemented. The far edges of the workpiece (left and bottom sides of the rectangle in Figure 4.1) are assumed to be far enough from machining to be at the constant ambient temperature, which is assumed to be 20°C. Likewise, the far edges of the tool (right and top edges of the tool in Figure 4.1) are too far away from machining that they are also assumed to be at ambient temperature boundary conditions.

The remaining edges of the tool and the workpiece might have a contact during machining and their temperature might change, so no constant temperature can be defined at those boundaries. Instead, heat transfer is enabled at those edges, so that with contact, heat can build up and increase the temperature to illustrate the mechanics of machining. Cutting speed is also defined using the boundary conditions. Zero speed at the bottom edge of the workpiece in vertical direction is defined so that the workpiece is prevented from irregular vertical movement, and a speed equivalent to the cutting speed is defined at the bottom edge of the workpiece in horizontal direction to illustrate the relative motion between the tool and the workpiece. As mentioned before, feedrate is the cutting depth in vertical direction in 2D simulations, so an extra definition is not required.

Following the definition of boundary conditions, an initial contact between the tool and the workpiece can be defined. Although this is not mandatory, an initially defined contact, even at a single node, helps initialization of the problem and consequently the initial speed of the simulations. It must be taken under consideration that, however, while defining contact between the objects, the geometries of the objects should not be extremely modified. In addition to contact definition, friction between (and within) each object must also be defined with a similar approach described in Chapter 3. For the friction definition in 2D, it is possible to select friction windows similar to mesh windows. Using these friction windows, friction between the tool and workpiece at different locations of contact must be defined depending on the friction calculations made according to the method described in Chapter 3. In addition, other possible contact conditions should be defined, such as the workpiece-workpiece contact. When the machining progresses for a while, the chip will form, curl, and move away from the tool

back towards to the workpiece and it might touch the workpiece during machining. This is a normal (and usually observed) condition, but unless excess amounts of chip curling happens during machining, it is considered insignificant. If the curling and workpiece-chip contact get excessive during machining, substantial temperature increase will be observed. As a result, this possible condition must also be considered by defining contact friction between workpiece and itself as well.

After all the physical conditions are defined, numerical controls of the simulation should also be defined. These include, but are not limited to, the duration of the simulation, number of steps, calculation error tolerances, remeshing tolerance, calculation and remeshing types, and numerical limits. If these are not well defined, the simulation may not work the correct way, or may stop unexpectedly. Under this guidance, 2D simulations were prepared for the titanium alloy Ti-64, and the nickel-based alloy IN-100 with machining parameters as given in Tables 4.3-4.4, and the results from these simulations were utilized within the friction determination method to achieve matching results between the two separate but connected types of computational analyses. When the iterations were finalized, these simulations were used to extract residual stress data, and compared to the experimental data. These results are presented in the "Results and Discussions" section of this chapter.

Table 4.3: Machining parameters for 2D Orthogonal Cutting Experiments of Ti-64

	r_β [μm]	V_c [m/min]	t_u [mm]	b [mm]
γ_1=0°	10	120	0.05	5
	10	120	0.1	5
γ_1=5°	10	120	0.05	5
	10	120	0.1	5
γ_1=10°	20	70	0.06	2
	20	70	0.1	2
	30	70	0.06	2
	30	70	0.1	2

Table 4.4: Machining parameters for 2D Orthogonal Cutting Experiments of IN-100

	r_β [μm]	V_c [m/min]	t_u [mm]	b [mm]
γ_1=0°	10	12	0.05	3.52
	10	12	0.1	3.52
	10	24	0.05	2.99
	10	24	0.1	2.99
	25	12	0.05	3.09
	25	12	0.1	3.09
	25	24	0.05	2.45
	25	24	0.1	2.45
γ_1=3°	10	12	0.05	2.45
	10	12	0.1	2.45
	10	24	0.05	2.45
	10	24	0.1	2.45
	25	12	0.05	3.02
	25	12	0.1	3.02
	25	24	0.05	2.96
	25	24	0.1	2.96

3. Results and Discussions

Results of the 2D physics-based simulations, together with the friction determination study are presented here with force and machining-induced stress predictions. The friction determination method explained in detail in Chapter 3, and the

FE-based simulations explained in detail in this chapter comprise the main work together. As a result of the combined nature of the method and the simulations, their results are also combined. Figure 4.2 shows this combined nature of the process, where the inputs are cutting speed, feed rate, cutting edge radius, rake angle, clearance angle, as well as material properties. In addition, forces and tool wear amounts are received from orthogonal cutting tests for comparison. With friction coefficients, maximum stress components and rake face contact lengths are searched, and when the friction coefficients do not change (more than 0.01) between two consequent iterations, they are utilized in the next (and last) iteration of simulations in order to get machining-induced stress predictions.

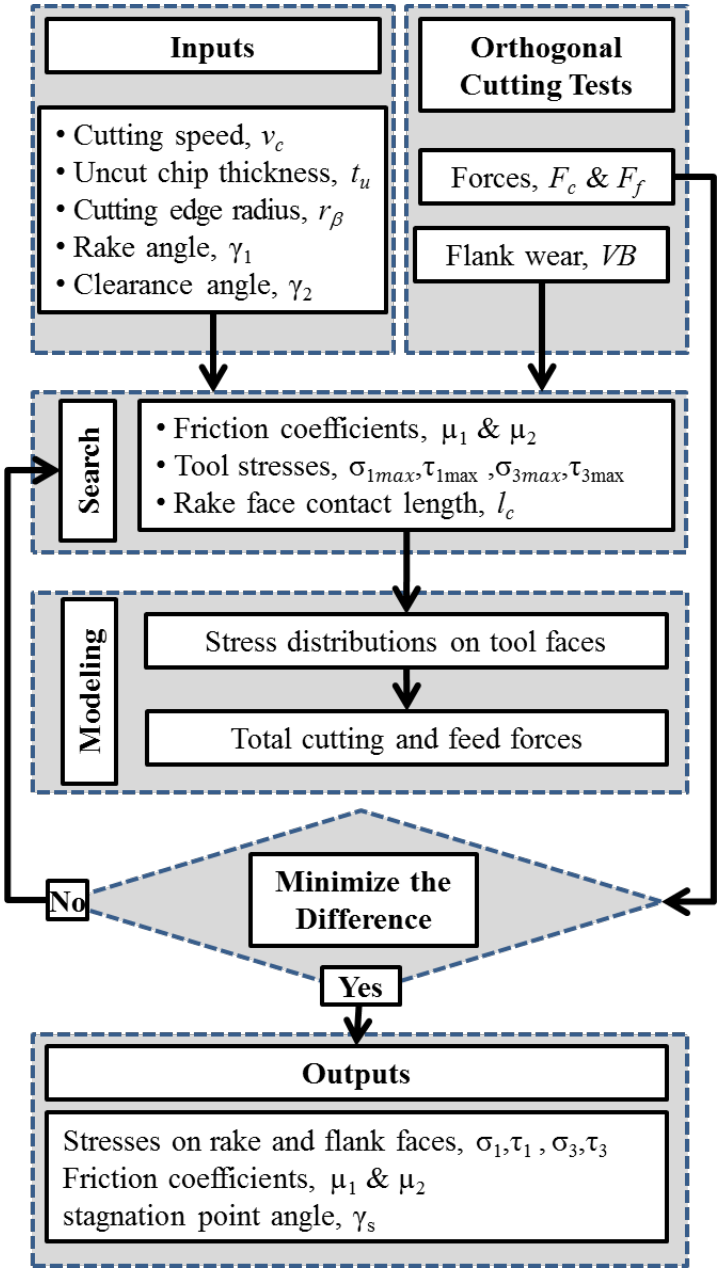

Figure 4.2: The search algorithm for the determination of friction coefficients

In 2D simulations, friction between tool and chip on the rake face was defined as hybrid, composed of both shear friction and Coulomb friction, since this was the assumption in the friction determination method explained in Chapter 3. For the same reasoning (explained in Chapter 3), the flank face friction model was defined only as Coulomb friction. All the simulations were run until chip formation was clearly

observed, and temperatures and forces acting on the tool reach steady state with the rigid tool assumption (1-2 milliseconds). After steady-state was achieved, simulations were run for a further short while under the elastic tool assumption where the stresses on the tool can also reach steady-state. This extra time corresponded to approximately 0.1 milliseconds for all of the simulations. The findings of the friction determination method on friction coefficients on the rake and flank faces for unworn tool are given in Tables 4.5-4.6 for Ti-64 and IN-100, respectively. These are the coefficients for the non-linear equations shown in Eq. 4.3-4.4, and it is important to keep in mind that these are normalized coefficients. This means that the actual coefficients for any of the parameters were divided by a mean value of the parameters so that these coefficients could be compared to each other. For Ti-64, these mean values were V_c=60 m/min, t_u=0.13 mm, and r_β=30 μm. For IN-100, these mean values were V_c=18 m/min, t_u=0.075 mm, and r_β=17.5 μm.

$$\mu_1 = a_1 V_c + b_1 t_u + c_1 r_\beta + d_1 V_c t_u + e_1 V_c r_\beta + f_1 t_u r_\beta + g_1 V_c t_u r_\beta + h_1 \quad \text{Eq. (4.3)}$$

$$\mu_2 = a_2 V_c + b_2 t_u + c_2 r_\beta + d_2 V_c t_u + e_2 V_c r_\beta + f_2 t_u r_\beta + g_2 V_c t_u r_\beta + h_2 \quad \text{Eq. (4.4)}$$

As also depicted by the coefficients of the equations in Table 4.5 for Ti-64 and Table 4.6 for IN-100, it was found that rake face friction coefficient (μ_1) decreases when the feed rate is increased, increases significantly when the cutting edge radius is increased, and decreases slightly when the cutting speed is increased, with the non-linear terms being insignificant compared to the linear terms. On the other hand, the flank face friction coefficient (μ_2) increases slightly with increasing feed rate, does not change significantly with the cutting speed, and decreases significantly with increasing edge radius at lower feed rates (0.05-0.06 mm) but decreases only slightly with increasing

edge radius at higher feed rates (0.1-0.2 mm). This is reflected on the non-linear term that includes feed rate and edge radius (f_2) being considerably higher than other coefficients when normalized. These values can be assumed to represent the interval where V_c=10-110 m/min, t_u=0.06-0.2 mm, r_β=10-50 μm for Ti-6Al-4V, and V_c=12-24 m/min, t_u=0.05-0.1 mm, r_β=10-25 μm for IN-100, since measured data used covers this interval. Although this study was designed with unworn tool, its conclusions about effects of parameters on friction coefficients were valuable, and knowledge was carried to the study with worn tool.

Table 4.5: Coefficients of nonlinear relationships for rake and flank face friction coefficients for Ti-6Al-4V with unworn tool (R^2 values for μ_1 and μ_2 are 0.972 and 0.928 respectively) (Ulutan et al. 2011)

	a	***b***	***c***	***d***	***e***	***f***	***g***	***h***
μ_1	-0.08	-0.12	0.5	0.01	0.02	-0.03	0.01	0.66
μ_2	0.04	0.12	-0.17	-0.03	-0.03	0.08	-0.02	1

Table 4.6: Coefficients of nonlinear relationships for rake and flank face friction coefficients for IN-100 with unworn tool (R^2 values for μ_1 and μ_2 are 0.959 and 0.943 respectively) (Ulutan et al. 2011)

	a	***b***	***c***	***d***	***e***	***f***	***g***	***h***
μ_1	-0.06	-0.13	0.58	-0.04	-0.01	-0.06	0.01	0.72
μ_2	0.05	0.15	-0.24	-0.13	0.05	0.06	0.04	0.98

With the worn tool calculations, the same data was used to conduct FE-based simulations, and the results for the nickel-based alloy IN-100 can be found in Table 4.7. The results presented in this table represent the last iteration, and the reason to stop the iterations was that in the previous iteration, the friction coefficients on the rake and flank faces (μ_1 and μ_2) were less than 0.01 different than the friction coefficients on the last

iteration (shown in Table 4.7). As a result, it is safe to say that in all the cutting conditions, the friction coefficient on the rake face between the tool and the chip was μ_1=0.7, while the friction coefficient on the flank face between the tool and the worn workpiece was found to be around μ_2=0.62, and these friction coefficients are not dependent on the four machining parameters at hand.

Simulations for the same 16 conditions were run with DEFORM-2D at each iteration, and stress fields for these simulations are given in Figures 4.3-4.14. Figures 4.3-4.5 are stress distributions in cutting speed, feed, and depth of cut directions, respectively for the nickel-based alloy IN-100 with 10 μm edge radius and 0° rake angle. Figures 4.6-4.8 are the stress distributions in the same directions for IN-100 with 10 μm cutting edge radius and 3° rake angle. Figures 4.9-4.11 are the stress distributions in the same directions for IN-100 with 25 μm cutting edge radius and 0° rake angle. Figures 4.12-4.14 are the stress distributions in the same directions for IN-100 with 25 μm cutting edge radius and 3° rake angle. As shown in the figures, in the cutting speed direction (hoop or tangential stress in orthogonal cutting), tensile machining-induced stresses were more apparent for lower cutting speed values (V_c=12 m/min). In this direction, stresses acting on the tool are compressive with decreasing values from the tool tip. Increasing the feed does not seem to change machining-induced stresses on the workpiece, but tool stresses become more compressive as feed increases, which can change tool wear rate and consequently surface integrity of machined product. As it can be seen from the results, rake angle does not seem to have a significant effect on stresses in this direction, while with increasing edge radius, machining-induced stresses tend to become less tensile. In feed direction (longitudinal in orthogonal cutting), tensile machining-induced

stresses are apparent in all conditions, increasing with cutting speed. Stresses on the tool become more compressive with increasing feed. Rake angle and cutting edge radius do not have a significant effect on stress distributions in this direction. In depth of cut direction (radial direction in orthogonal cutting), tensile machining-induced stresses become compressive with increasing cutting speed, while effects of feed, rake angle, and cutting edge radius seem to be insignificant.

For all the simulations, maximum shear stress on the rake face was around $\tau_{1,max}$=2000-2500 MPa for all conditions, while maximum normal and shear stresses on edge face vary substantially. It was observed that with increasing edge radius, cutting speed, feed, and rake angle, both maximum normal and shear stresses increased. Stagnation angle was mostly dependent on edge radius: with increasing edge radius from r_β=10 to 25 μm, stagnation angle was found to increase from γ_s=10-15° to γ_s=40-45°. However, tool wear was considered to be constant (VB=60 μm) in all conditions, which means that these simulations represent values after a certain tool wear amount, regardless of cutting time or distance. Other process parameters did not affect stagnation angle significantly. Figure 4.15 shows a comparison between such an extracted stress field with the findings of the friction determination method. These are the results of the last iteration, so stress field has not changed much between two consecutive iterations.

Figures 4.16-29 show effects of all input parameters on rake and flank face stress distributions, and Figure 4.30 shows a summary of all effects for IN-100. This figure shows for the nickel-based alloy IN-100 that change of rake angle from γ_1=0 to 3° mostly increases cutting forces while decreasing thrust forces, where its effect on maximum stress components on the tool rake and flank faces is negligible. Cutting edge radius and

cutting speed do not seem to affect force components significantly, whereas with increasing cutting edge radius from r_β=10 to 25 µm, flank face stresses increase significantly, as more load is applied on the flank face. This results in a decrease in rake face stresses as expected. With increasing cutting speed, flank and rake face stresses increase slightly. The effect of feed on stresses is small, whereas increasing uncut chip thickness from t_u=0.05 to 0.1 mm immensely affects force components as load on the tool is doubled.

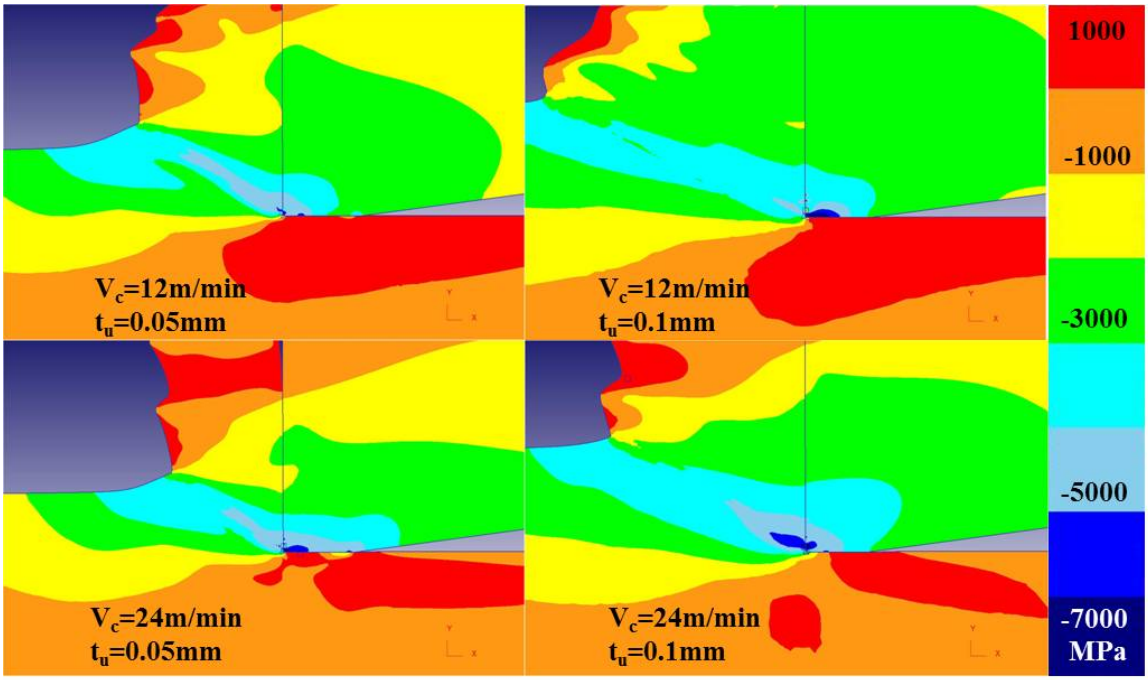

Figure 4.3: Stress distributions in cutting speed direction (IN-100, r_β=10µm, γ_1=0°)

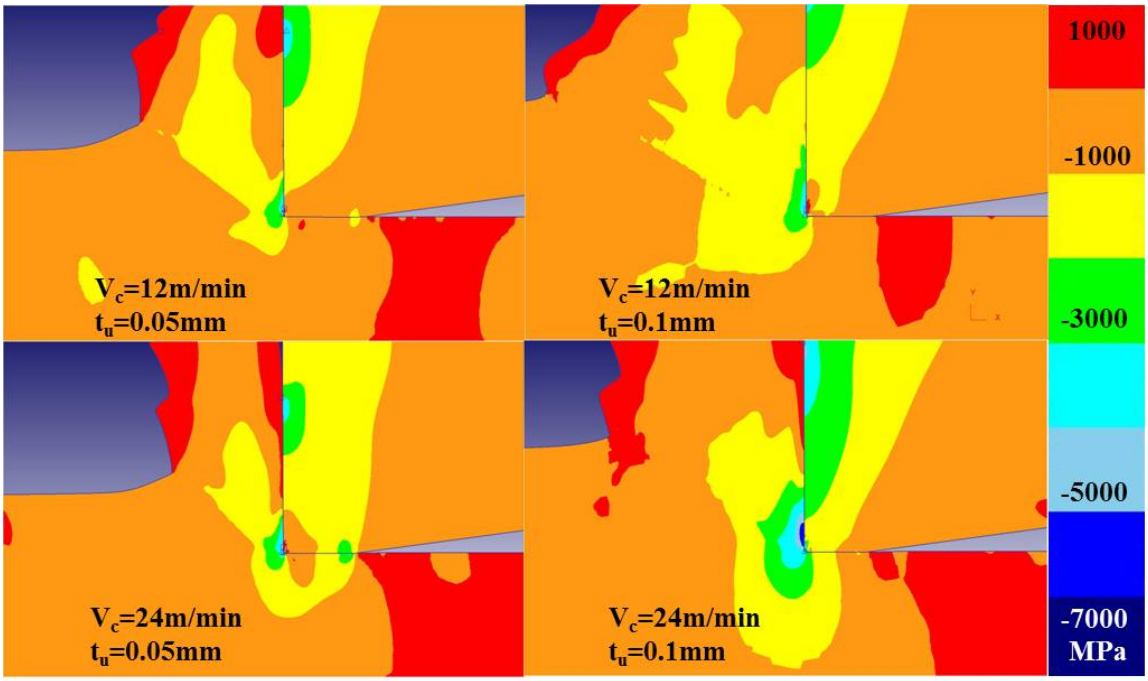

Figure 4.4: Stress distributions in feed direction (IN-100, r_β=10µm, γ_1=0°)

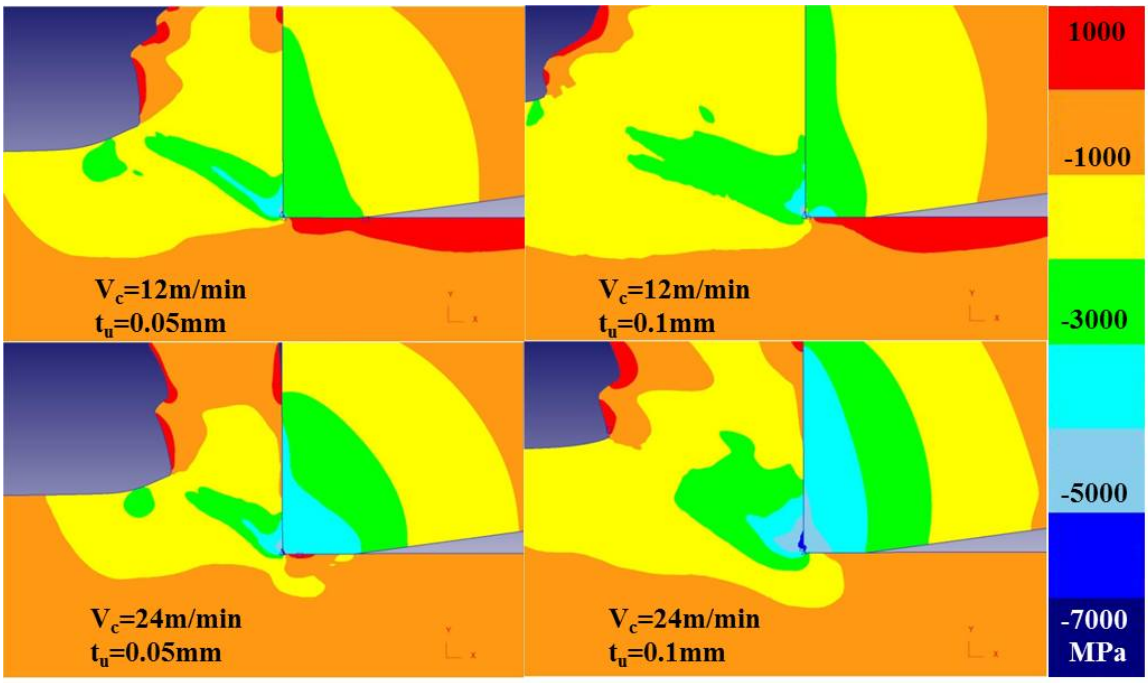

Figure 4.5: Stress distributions in depth of cut direction (IN-100, r_β=10µm, γ_1=0°)

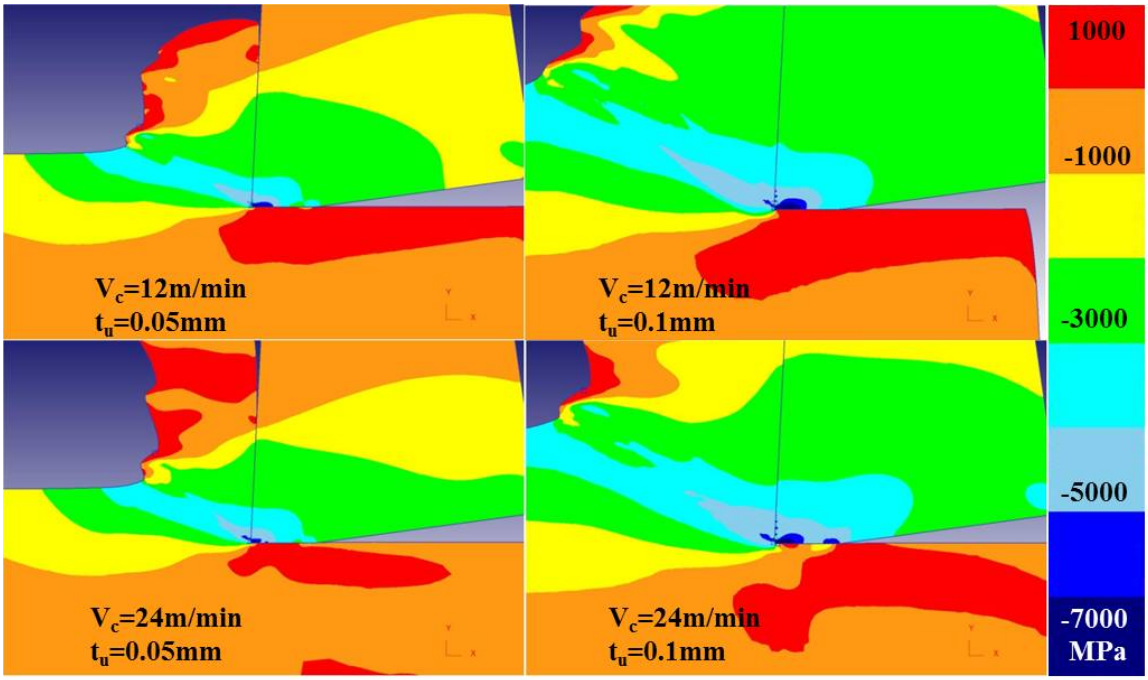

Figure 4.6: Stress distributions in cutting speed direction (IN-100, r_β=10µm, γ_1=3°)

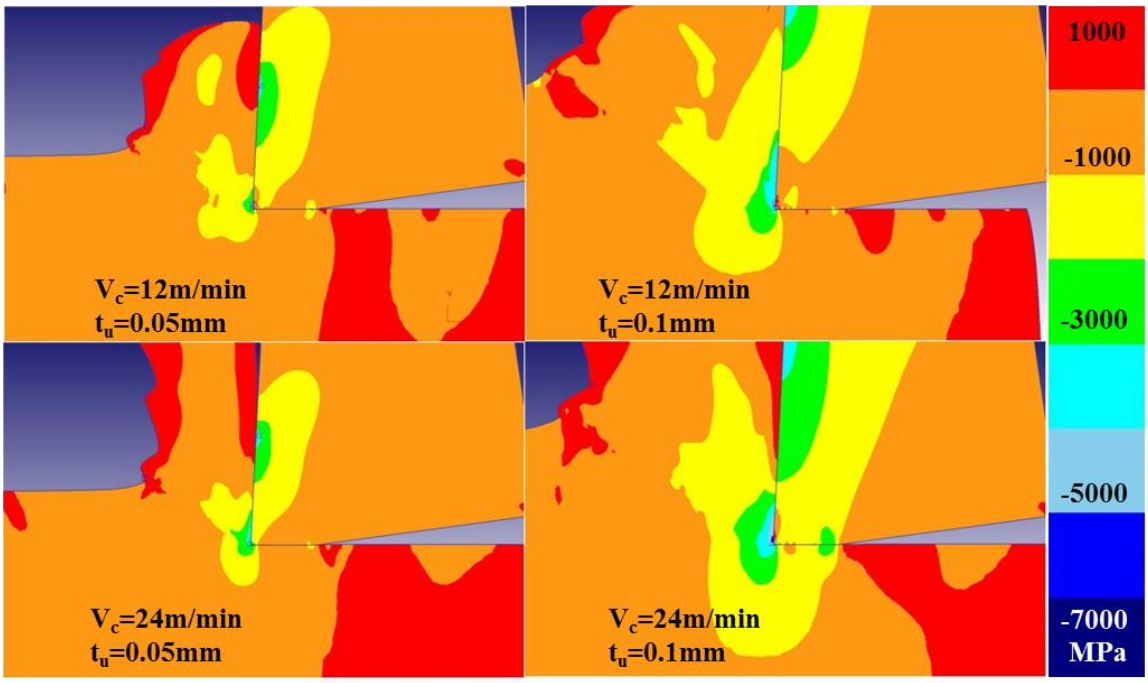

Figure 4.7: Stress distributions in feed direction (IN-100, r_β=10µm, γ_1=3°)

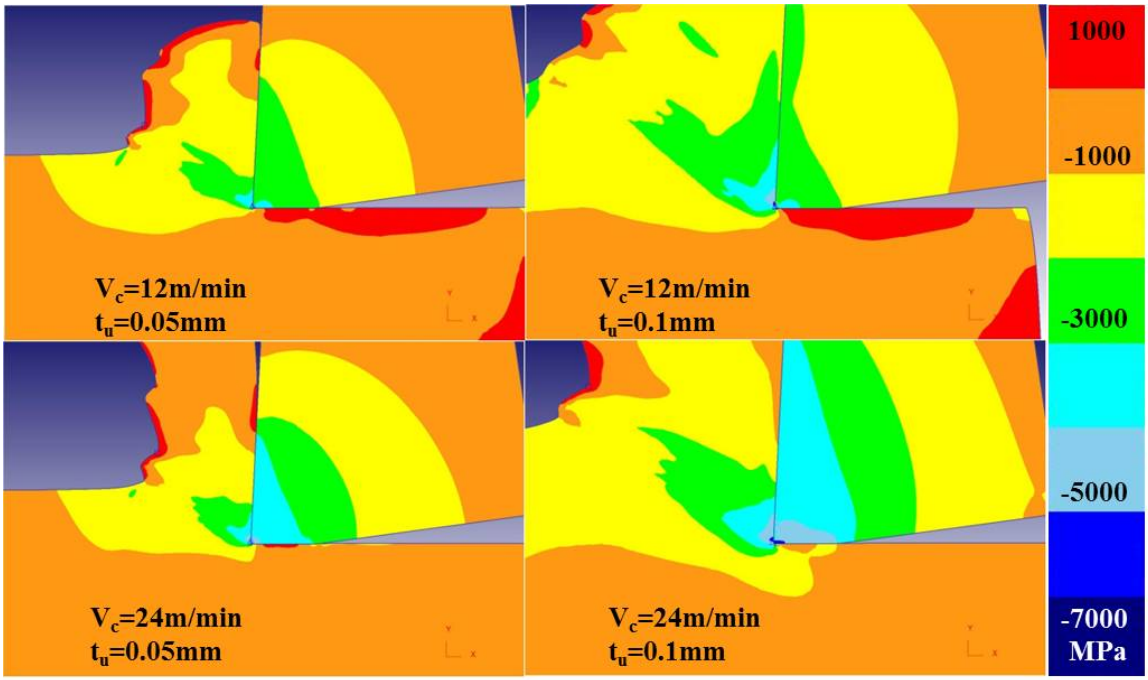

Figure 4.8: Stress distributions in depth of cut direction (IN-100, r_β=10µm, γ_1=3°)

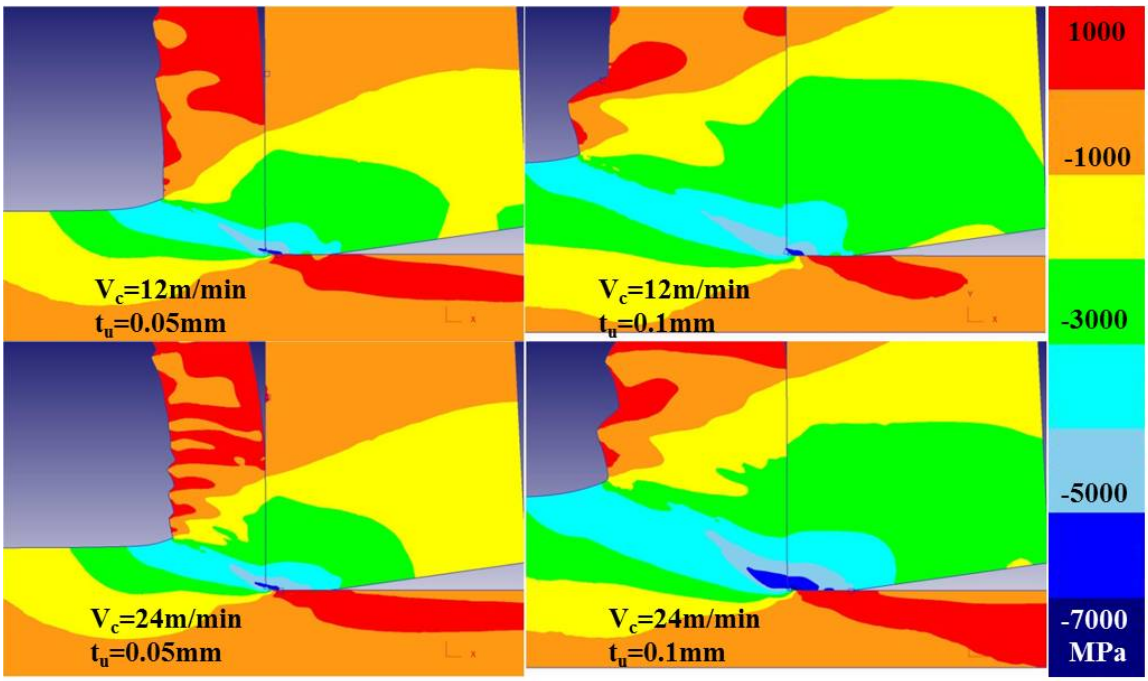

Figure 4.9: Stress distributions in cutting speed direction (IN-100, r_β=25µm, γ_1=0°)

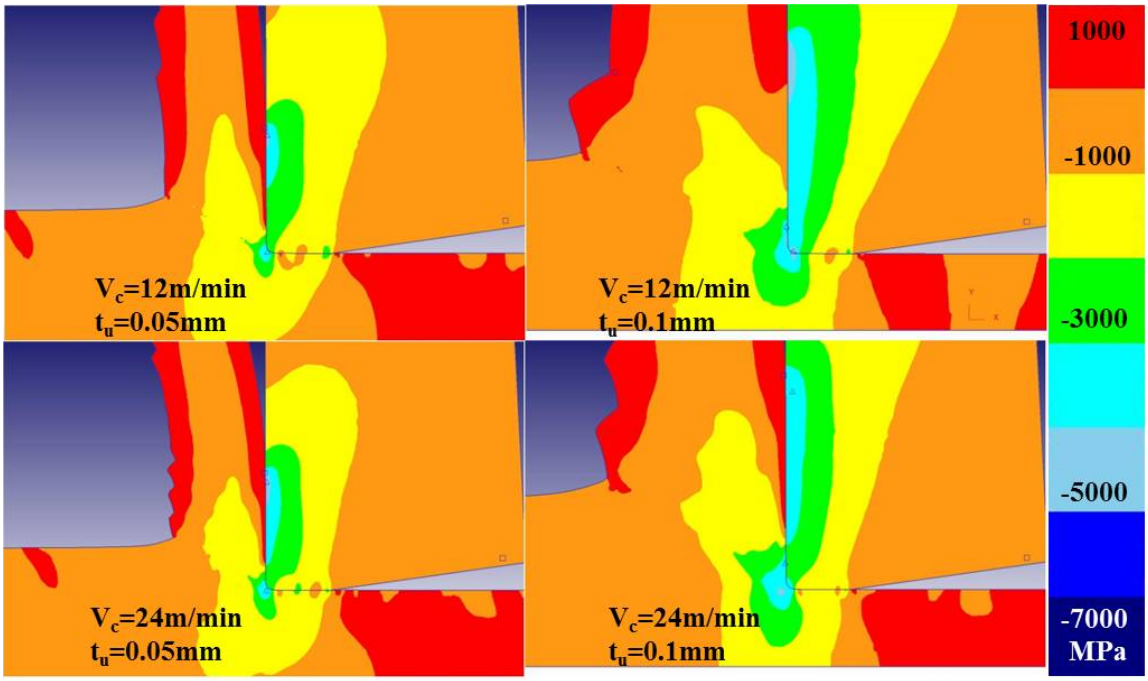

Figure 4.10: Stress distributions in feed direction (IN-100, r_β=25µm, γ_1=0°)

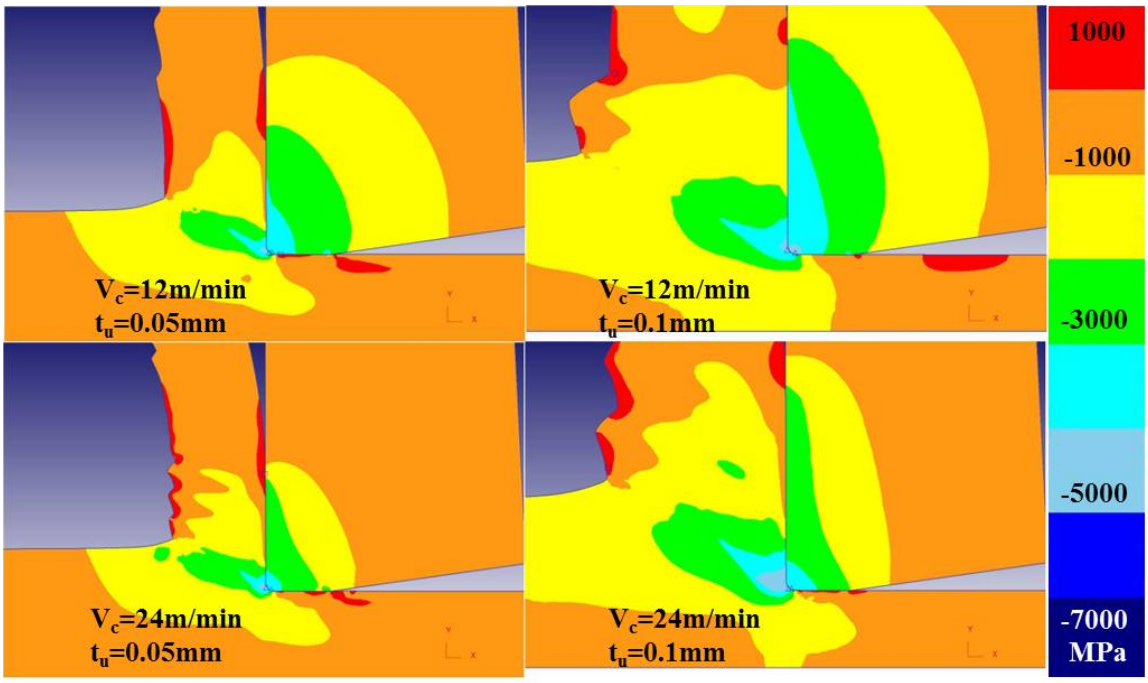

Figure 4.11: Stress distributions in depth of cut direction (IN-100, r_β=25µm, γ_1=0°)

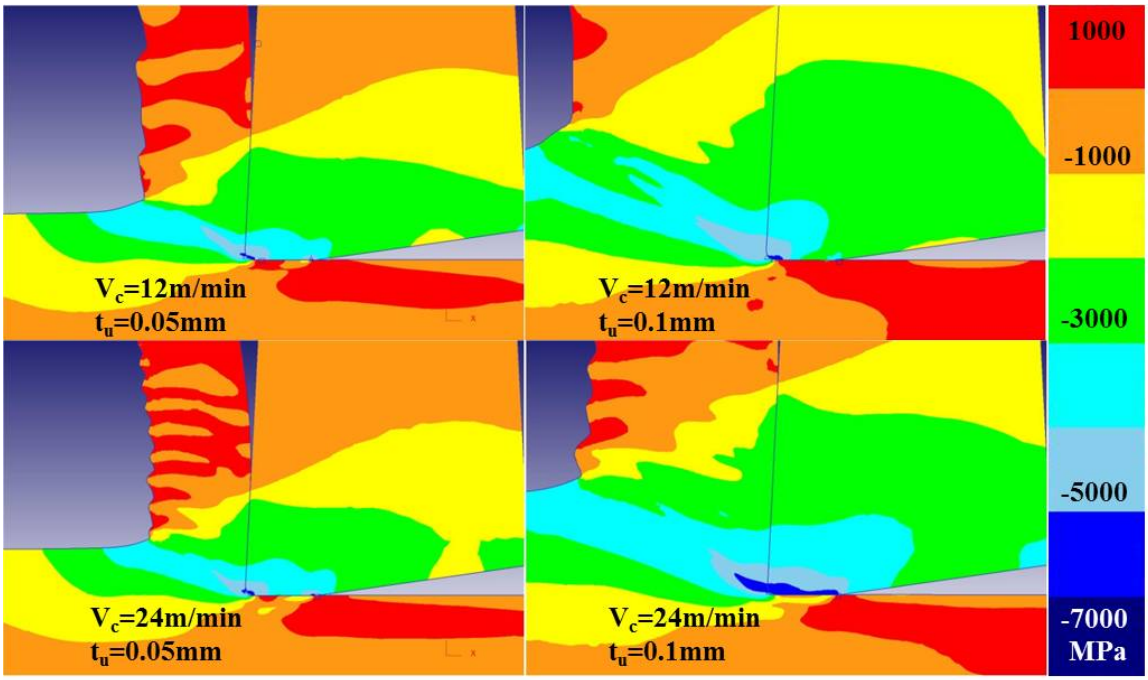

Figure 4.12: Stress distributions in cutting speed direction (IN-100, r_β=25µm, γ_1=3°)

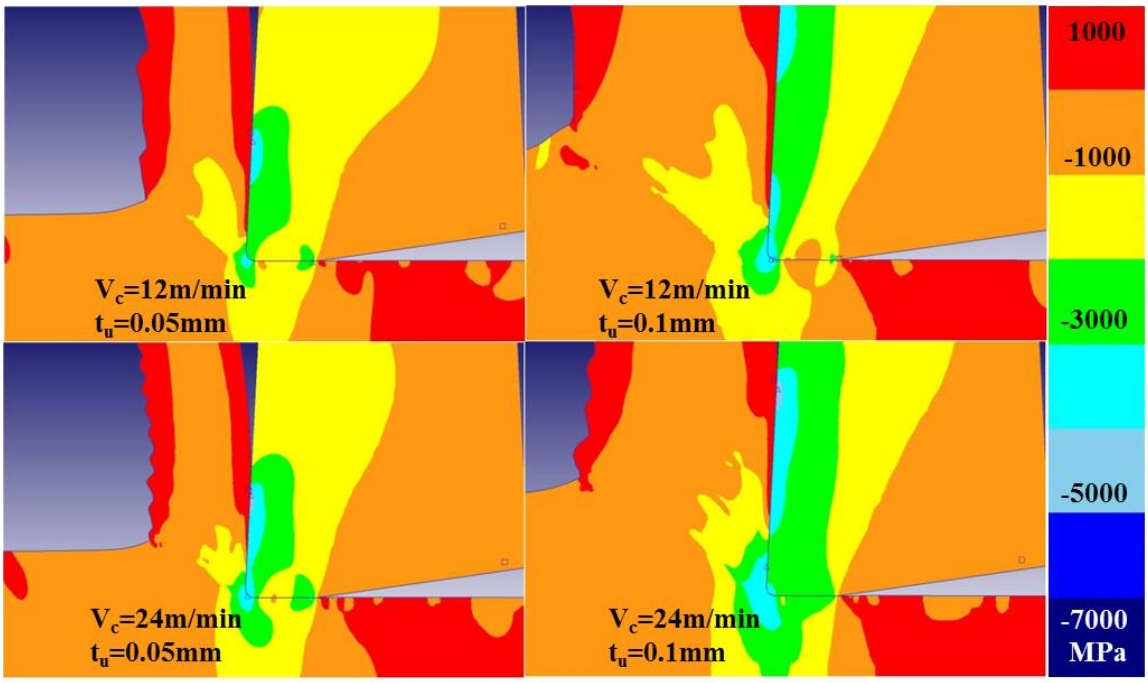

Figure 4.13: Stress distributions in feed direction (IN-100, r_β=25µm, γ_1=3°)

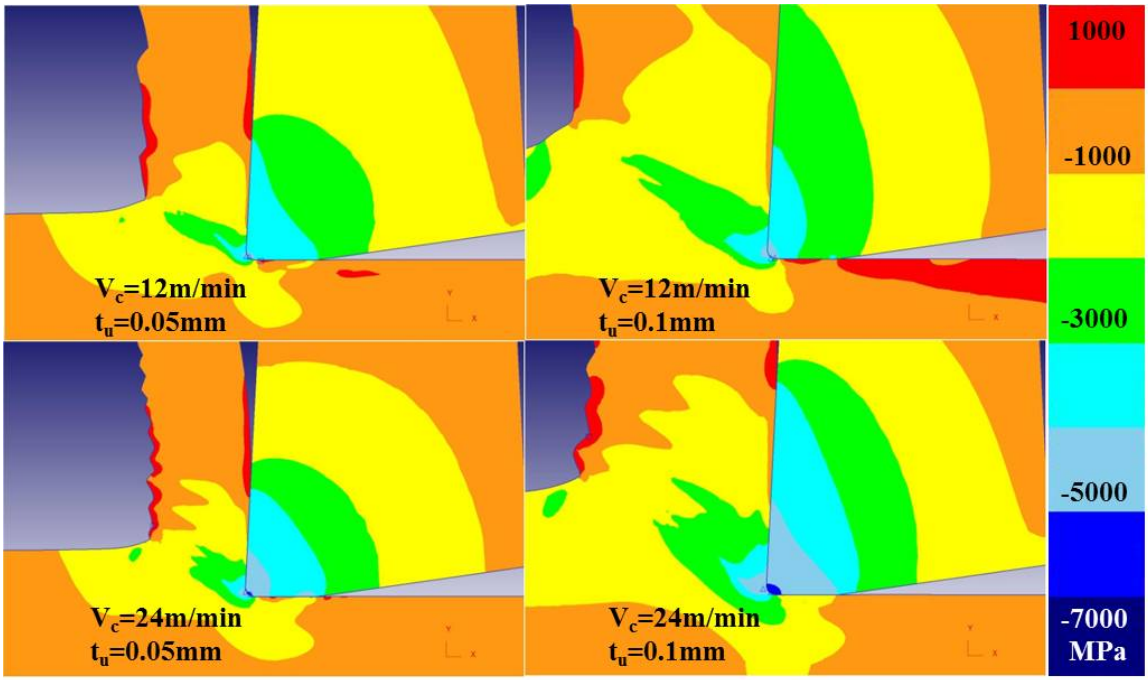

Figure 4.14: Stress distributions in depth of cut direction (IN-100, r_β=25µm, γ_1=3°)

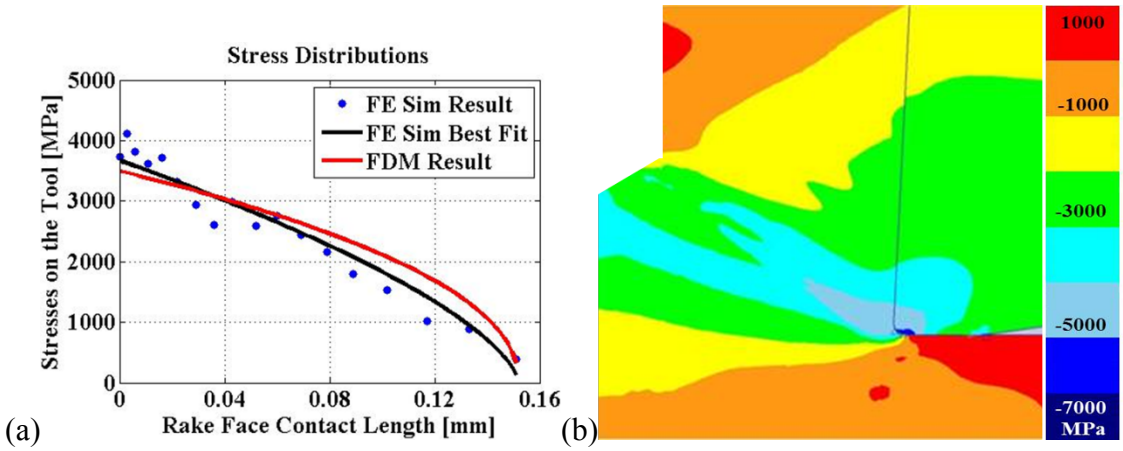

Figure 4.15: Comparison of IN-100 (a) predicted stresses and (b) FE-based simulation stress distribution

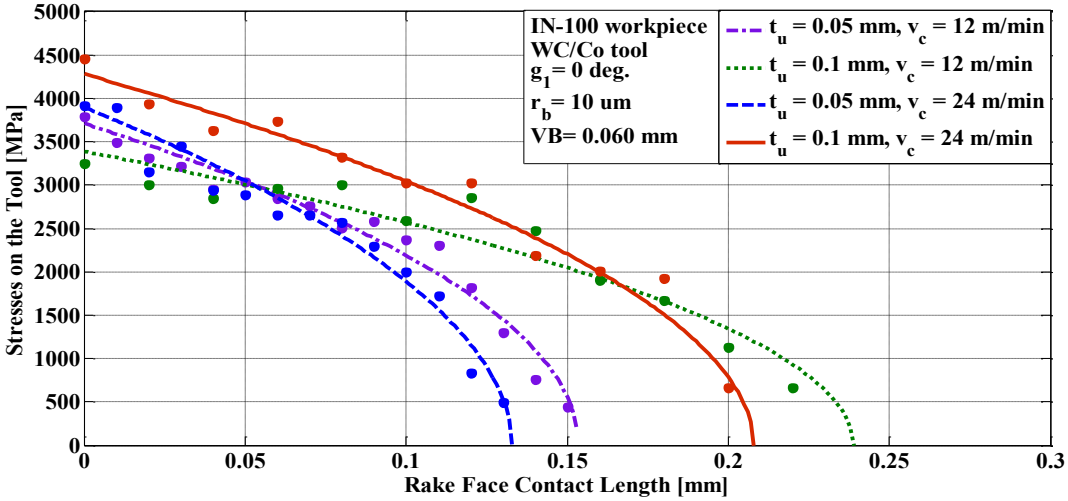

Figure 4.16: Effect of t_u and V_c on tool rake face stress distributions for machining IN-100

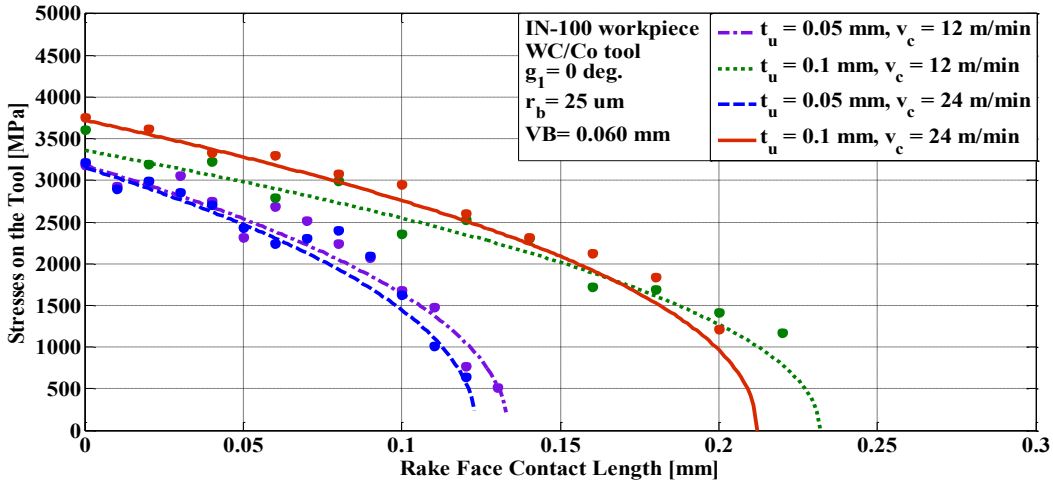

Figure 4.17: Effect of t_u and V_c on tool rake face stress distributions for machining IN-100

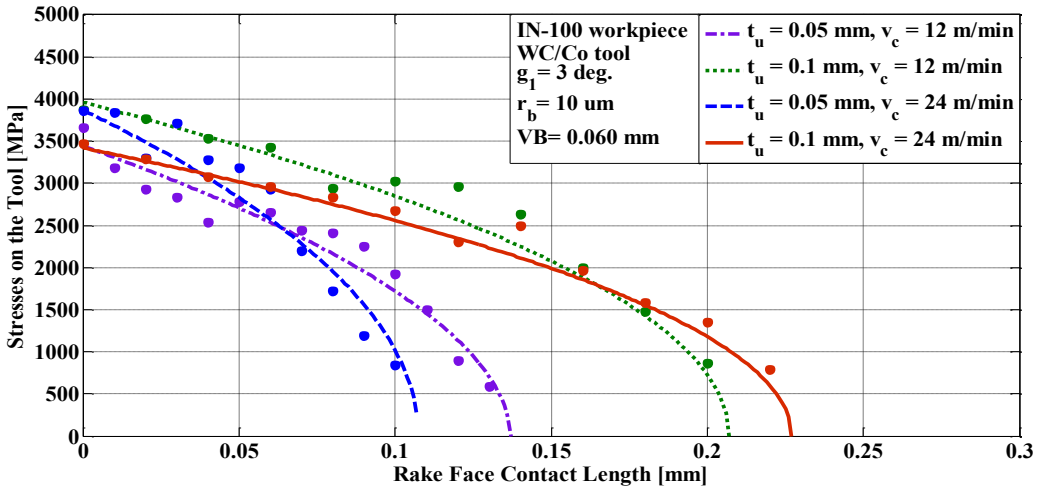

Figure 4.18: Effect of t_u and V_c on tool rake face stress distributions for machining IN-100

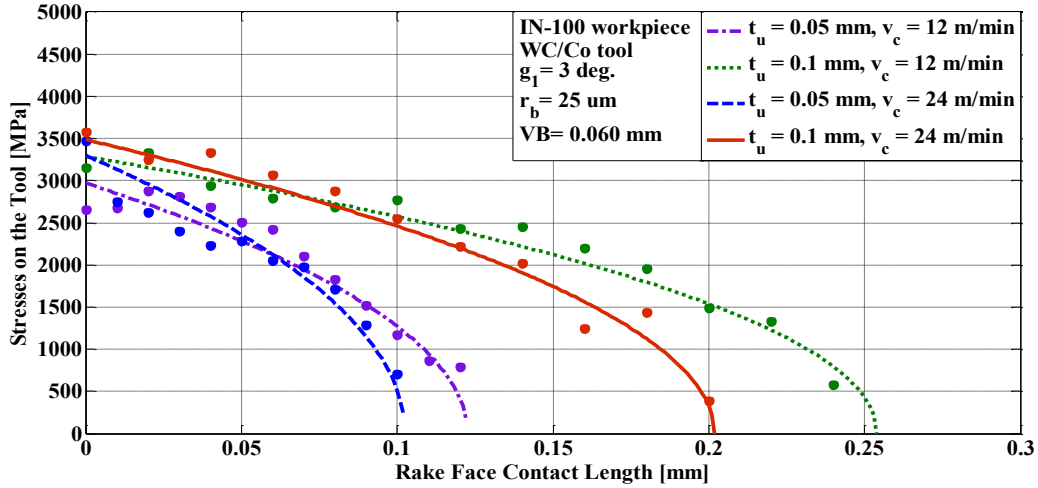

Figure 4.19: Effect of t_u and V_c on tool rake face stress distributions for machining IN-100

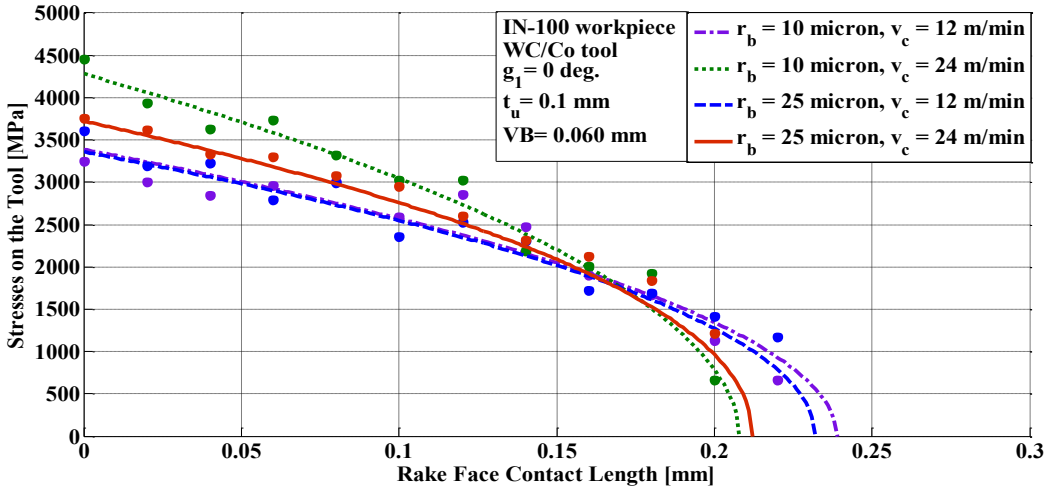

Figure 4.20: Effect of r_β and V_c on tool rake face stress distributions for machining IN-100

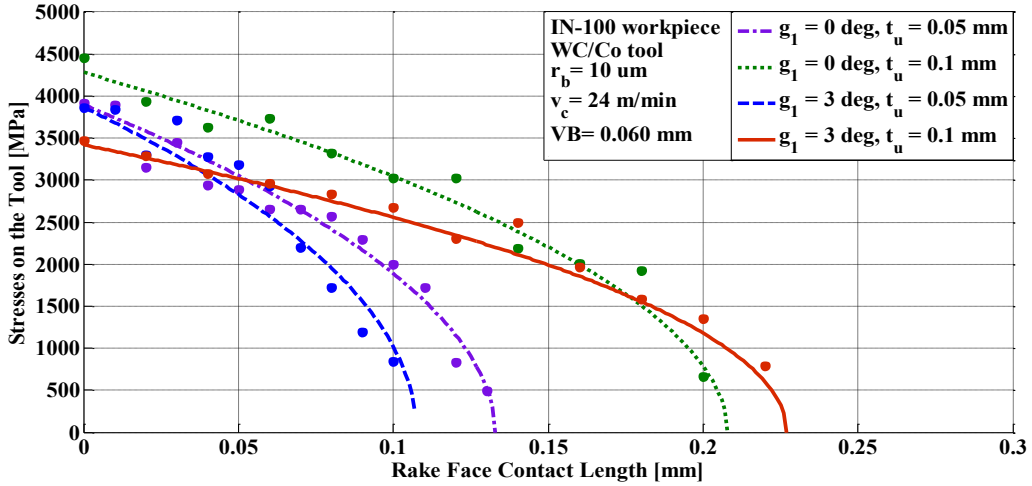

Figure 4.21: Effect of γ_1 and t_u on tool rake face stress distributions for machining IN-100

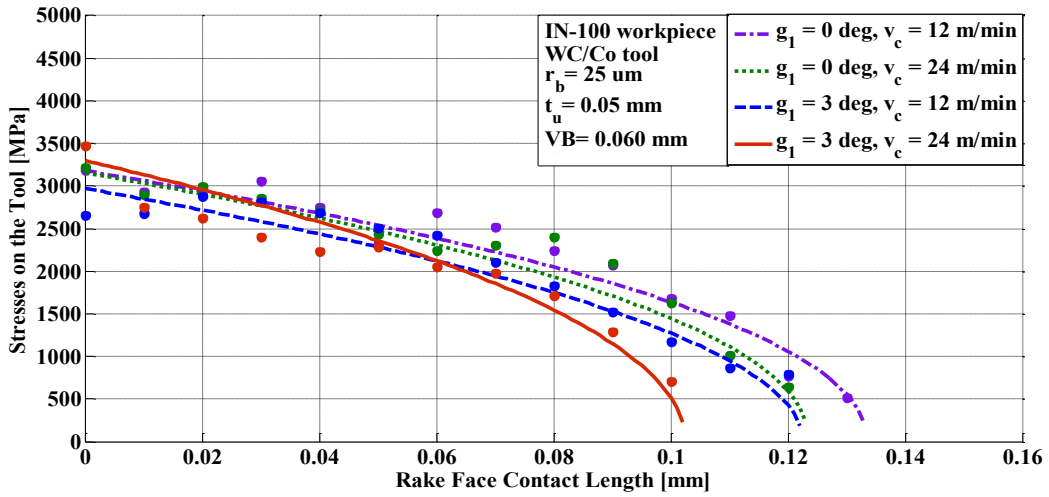

Figure 4.22: Effect of γ_1 and V_c on tool rake face stress distributions for machining IN-100

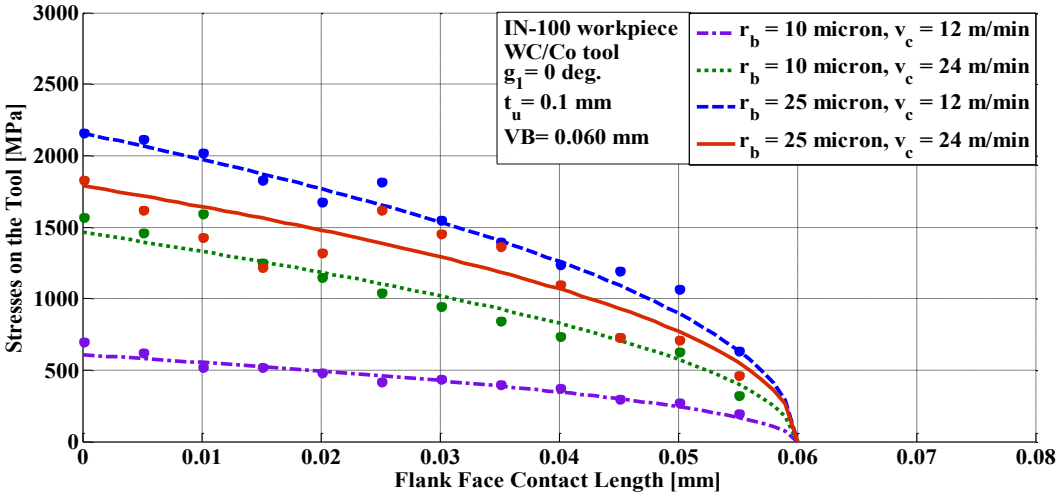

Figure 4.23: Effect of r_β and V_c on tool flank face stress distributions for machining IN-100

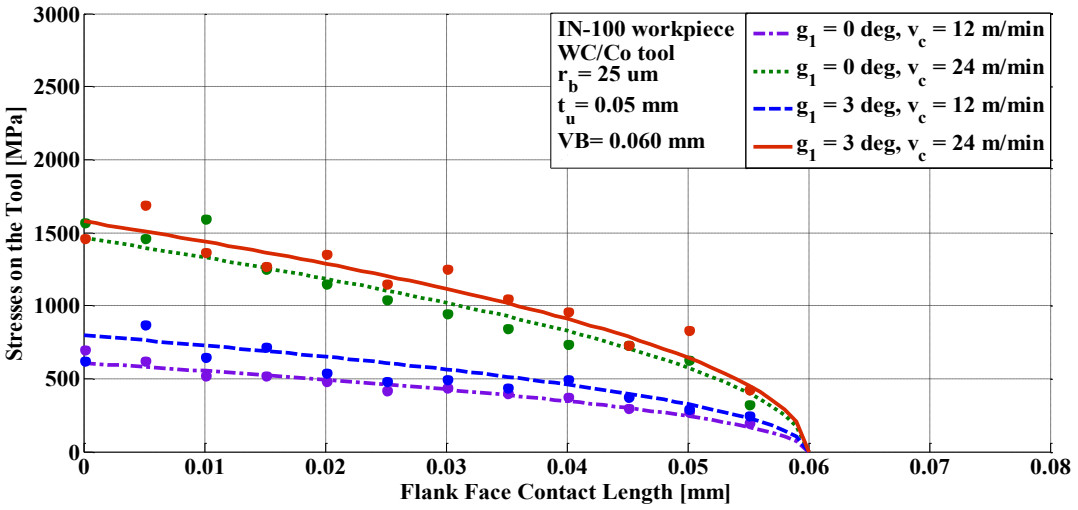

Figure 4.24: Effect of γ_1 and V_c on tool flank face stress distributions for machining IN-100

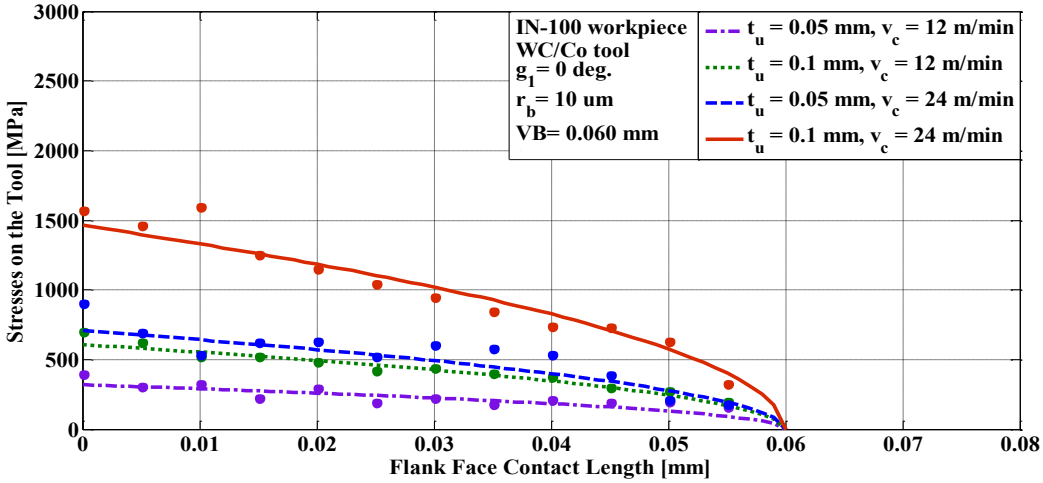

Figure 4.25: Effect of t_u and V_c on tool flank face stress distributions for machining IN-100

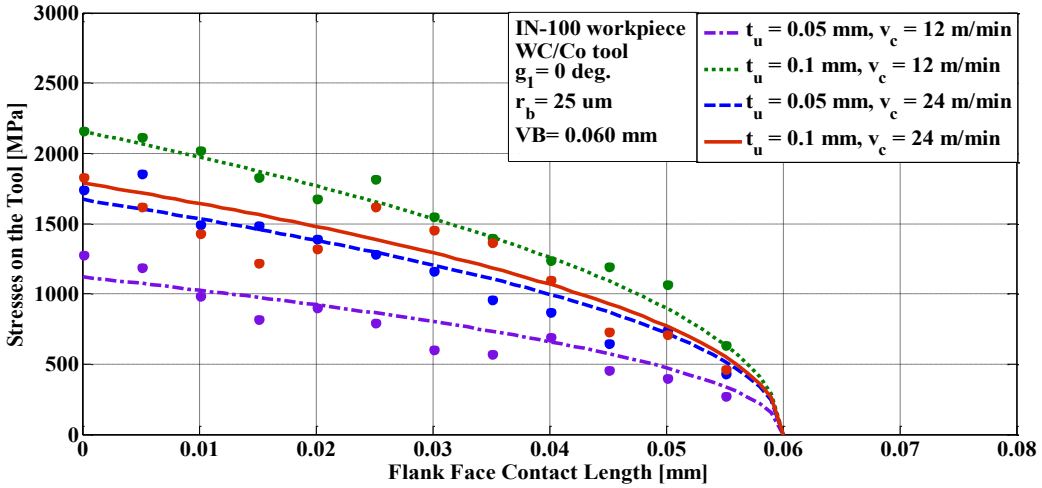

Figure 4.26: Effect of t_u and V_c on tool flank face stress distributions for machining IN-100

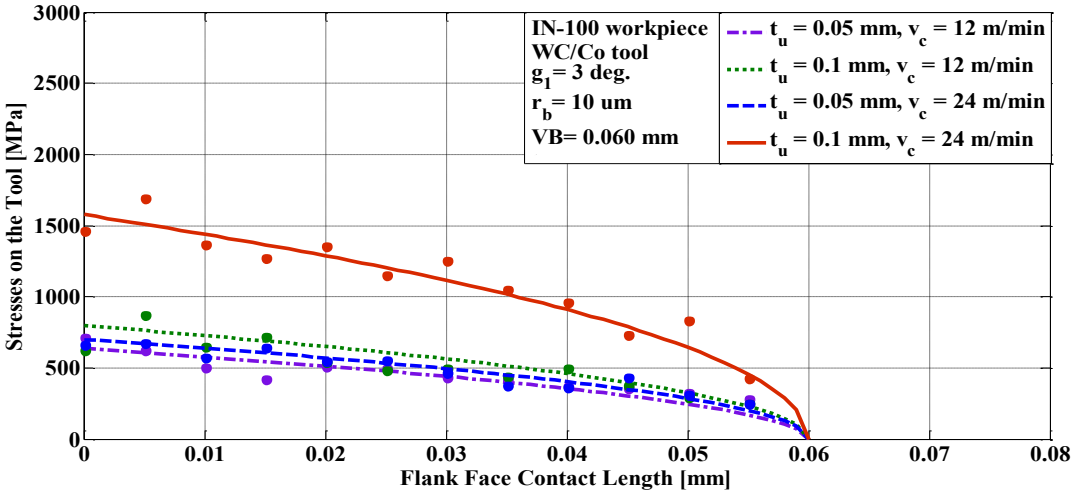

Figure 4.27: Effect of t_u and V_c on tool flank face stress distributions for machining IN-100

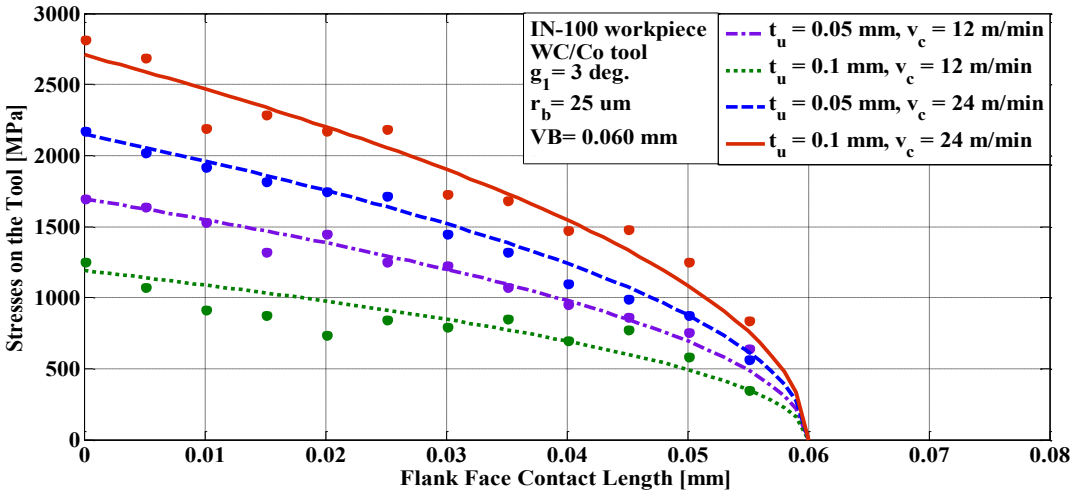

Figure 4.28: Effect of t_u and V_c on tool flank face stress distributions for machining IN-100

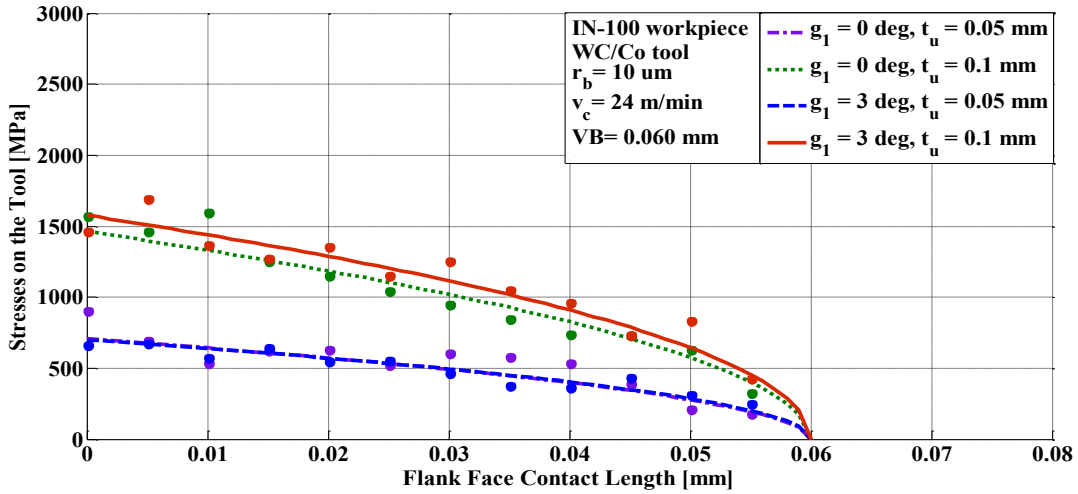

Figure 4.29: Effect of γ_1 and t_u on tool flank face stress distributions for machining IN-100

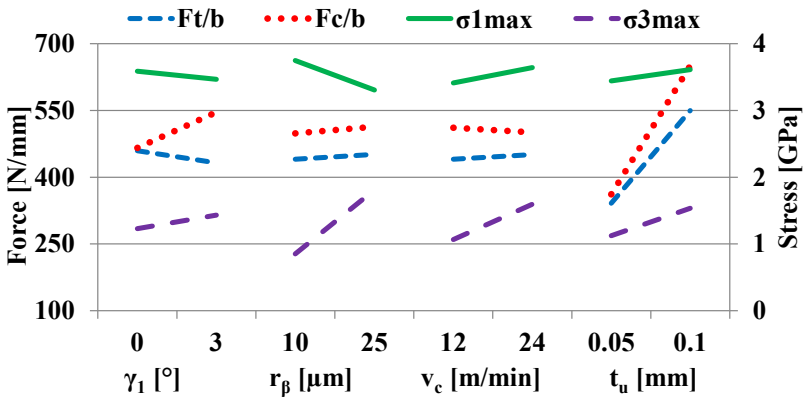

Figure 4.30: Effects of tool geometry and cutting conditions on tool forces and stresses (IN-100)

FE-based simulation results for the titanium alloy Ti-6Al-4V can be found in Table 4.8. Simulations were run for two different sets of experimentation. For higher cutting speed (V_c=120 m/min), experimental results were received from orthogonal cutting tests conducted at TechSolve Inc and reported in Özel et al. (2011). Experimental results for lower cutting speed (V_c=70 m/min) were extracted from orthogonal cutting test results of Wyen & Wegener (2010). In both experiment sets, uncoated tungsten carbide (WC) tools were used. FE-based simulations for the same 8 conditions were run with DEFORM-2D. Stress fields for these simulations can be found in Figures 4.31-4.36. Figures 4.31-4.33 are the stress distributions in cutting speed, feed, and depth of cut directions, respectively for the titanium alloy Ti-6Al-4V with 10 µm edge radius, 5 mm depth of cut and 120 m/min cutting speed. Figures 4.34-4.36 are the stress distributions in the same directions for Ti-64 with 10° rake angle, 2 mm depth of cut and 70 m/min cutting speed. As it can be observed in the figures, in the cutting speed direction (hoop or tangential stress in orthogonal cutting), tensile machining-induced stress values became less apparent with increasing feed and rake angle, but more apparent with increasing edge

radius. Tool stresses became more compressive with increasing feed, while other parameters did not have significant effects. In the feed direction (longitudinal in orthogonal cutting), machining-induced stresses on the workpiece did not seem to change much with any of the parameters, but tool stresses were observed to become more compressive with increasing feed and decreasing edge radius. In the depth of cut direction (radial direction in orthogonal cutting), increasing feed was found to increase the compressive stresses on the tool, but no other significant effects were observed.

It can be also observed from Table 4.8 that none of the parameters had any significant effect on the friction coefficients obtained from friction determination method, and the rake face friction coefficients were found to be around μ_1=0.6 for all the parameters used. It should be noted that the friction determination method uses measured force data in a range of cutting speed and feedrate for dry machining and the calculated friction coefficient represents the sliding portion of the tool-chip contact. In machining conditions, where sticking or plastic contact extended the friction coefficient becomes less sensitive to overall machining parameters. Furthermore, the flank face friction coefficient was also constant around μ_2=0.51, except for the highest cutting edge radius (r_β=30μm), where it dropped slightly to μ_2=0.45-0.49. It should also be noted that a flank wear land of 0.06 mm was assumed and this friction coefficient may change for other flank wear land situations.

Maximum shear stress on the rake face was found to increase with feed, edge radius, and rake angle, and also significantly with cutting speed. The magnitude of maximum normal and shear stresses on the edge face both increased with increasing feed, decreased with edge radius, and stayed similar with changing rake angle. Increasing

cutting speed decreased the maximum normal stress on the edge face, while not affecting significantly the maximum shear stress on the edge face. The stagnation angle was found to decrease slightly with increasing feed, and not change significantly with cutting speed or the rake angle. As with the nickel-based alloy IN-100, the stagnation angle during machining the titanium alloy Ti-64 also depended heavily on the edge radius, and with edge radius increasing from r_β=10 to 20 and 30μm, the stagnation angle increased from around γ_s=10° to γ_s=27° and γ_s=45° respectively. Figure 4.38 shows a comparison between such an extracted stress field with the findings of the friction determination method. These results, as in IN-100, belong to the last iteration. Figure 4.38-41 show the effects of the input parameters on rake and flank face stress distributions, and Figure 4.42 shows a summary of all effects for Ti-64. This figure shows that the increase of uncut chip thickness from a low amount (t_u=0.05-0.06 mm) to a higher amount (t_u=0.1 mm) increases the force components similarly, particularly the cutting force. The effect of cutting edge radius is reversed on this material, mostly due to the high rake angle in these conditions (γ_1=10°), as well as the low width of cut, which decreases the total load significantly. It can also be observed that with increasing cutting speed from v_c=70 to 120 m/min, both force components decrease. Finally, it is also seen that with increasing rake angle from γ_1=0 to 5°, as well as with increasing cutting speed from v_c=70 to 120 m/min, rake face stresses increase a noteworthy amount.

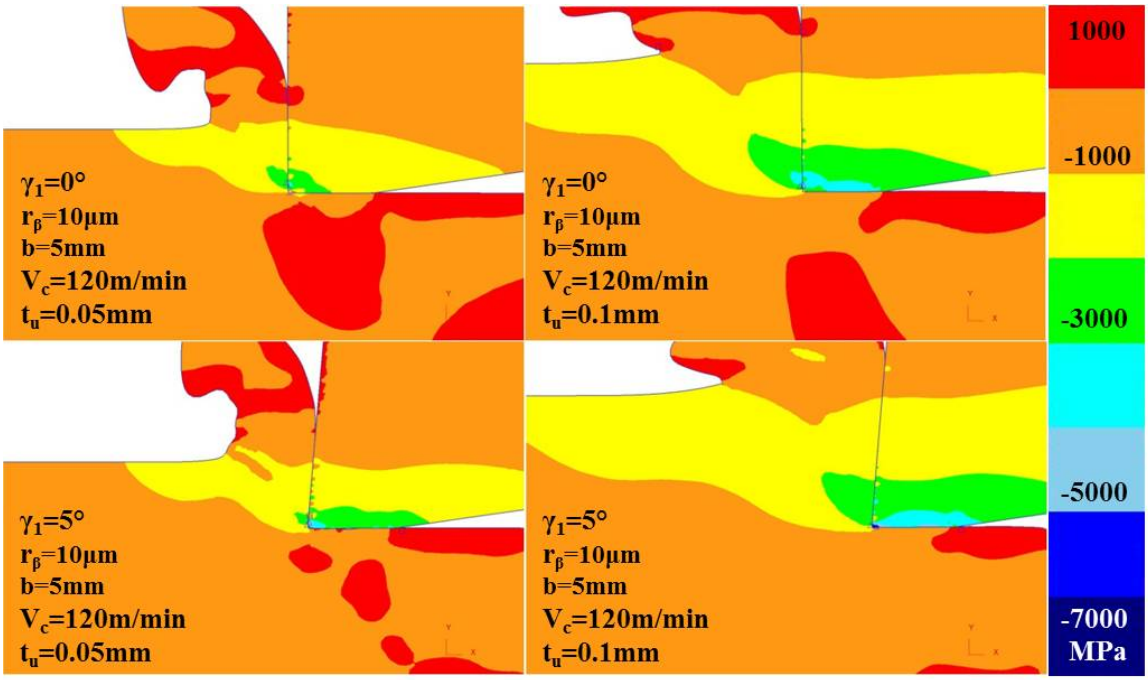

Figure 4.31: Stress distributions in cutting speed direction (Ti-64, r_β=10μm)

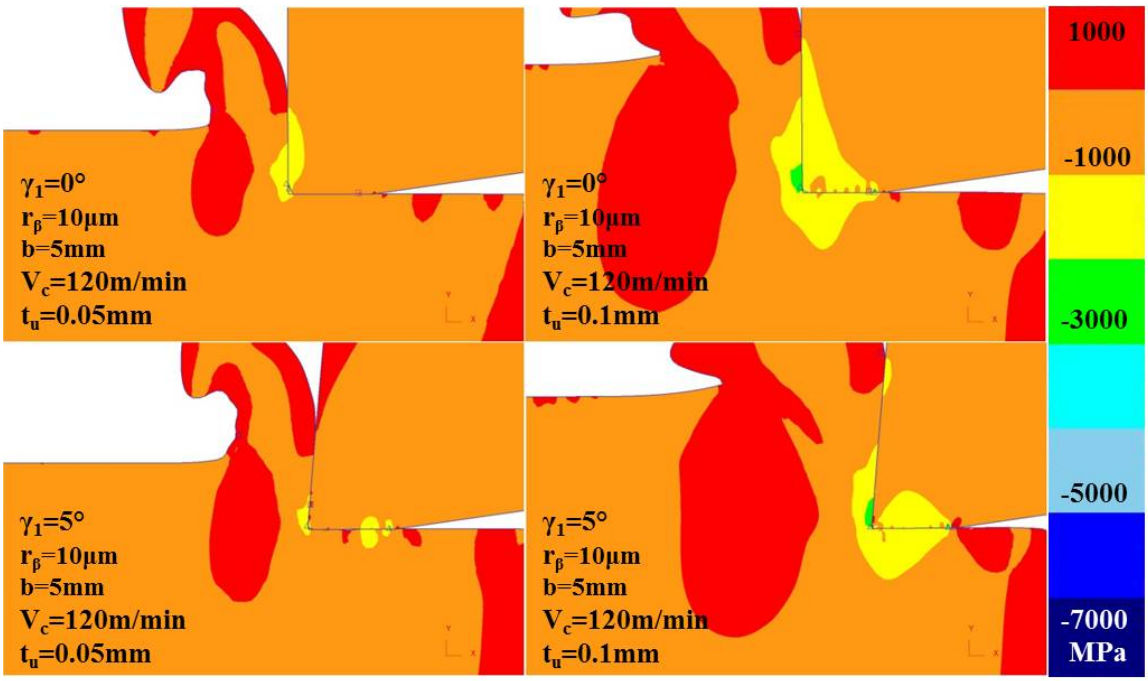

Figure 4.32: Stress distributions in feed direction (Ti-64, r_β=10 μm)

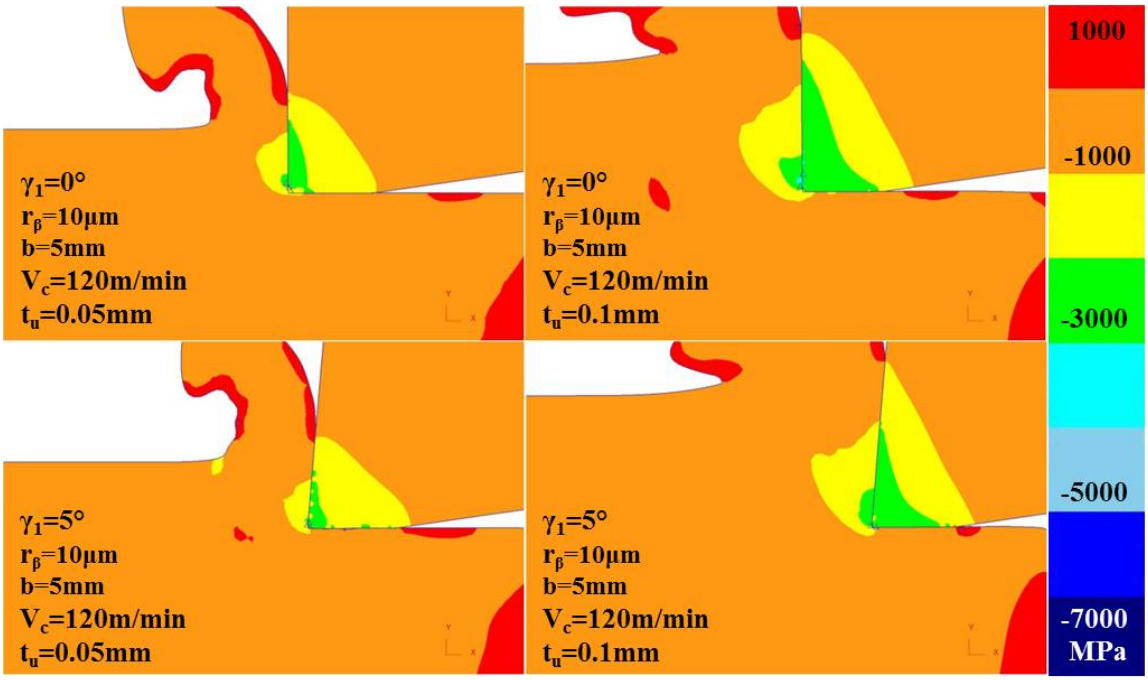

Figure 4.33: Stress distributions in depth of cut direction (Ti-64, r_β=10µm)

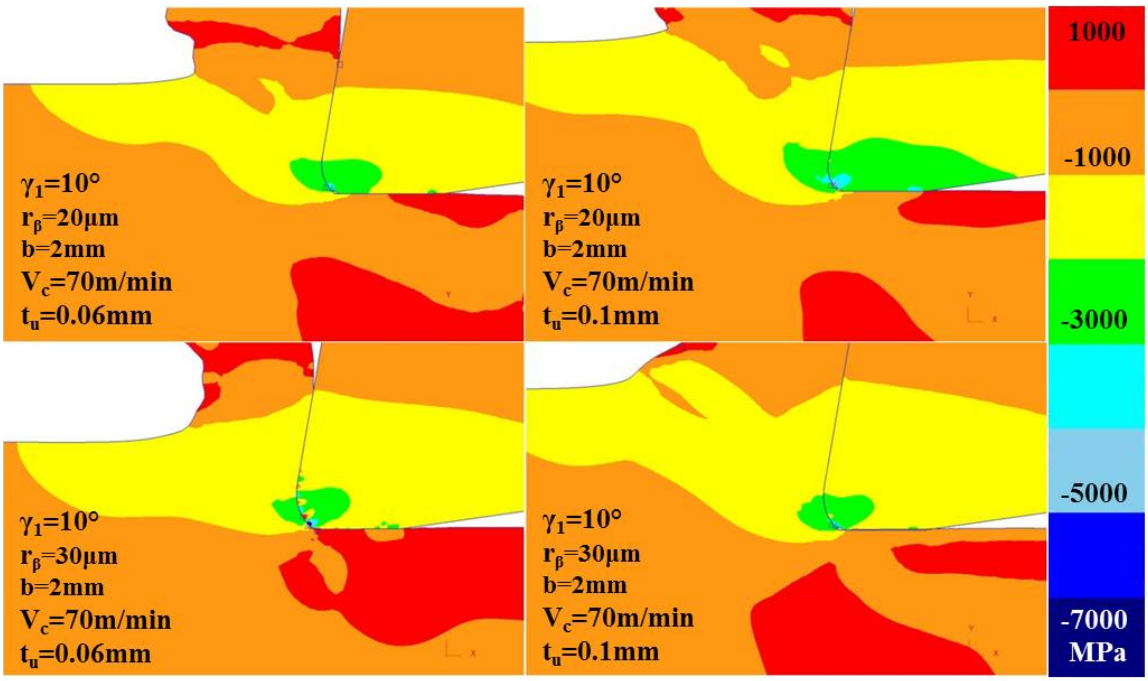

Figure 4.34: Stress distributions in cutting speed direction (Ti-64, γ_1=10°)

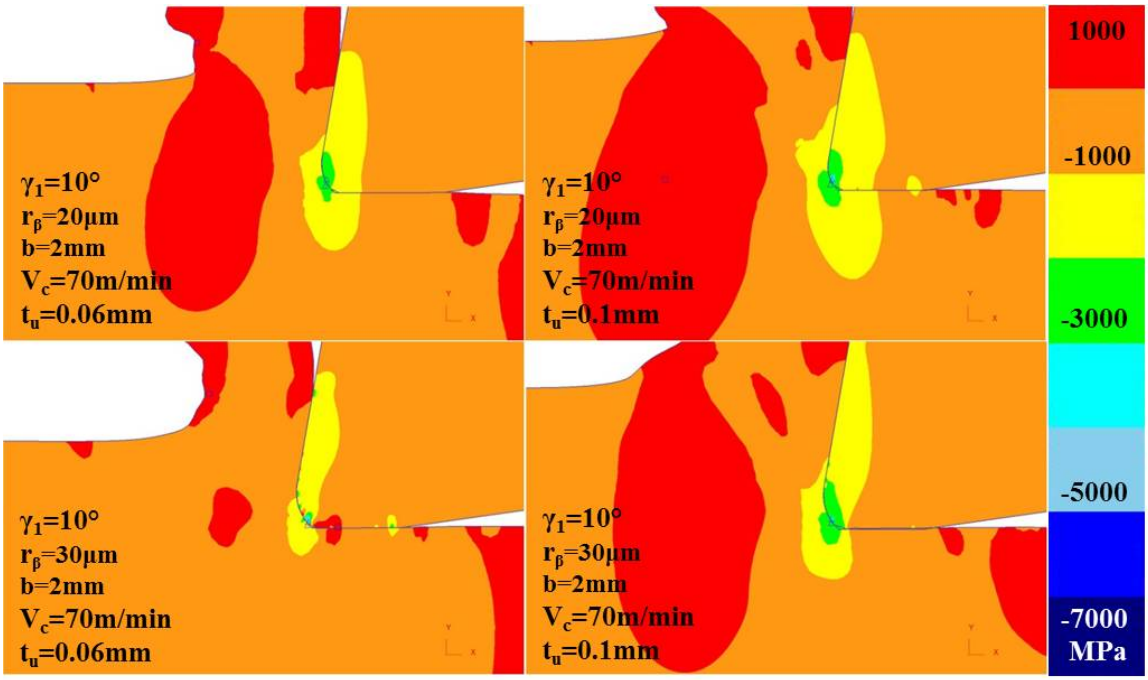

Figure 4.35: Stress distributions in feed direction (Ti-64, γ_1=10°)

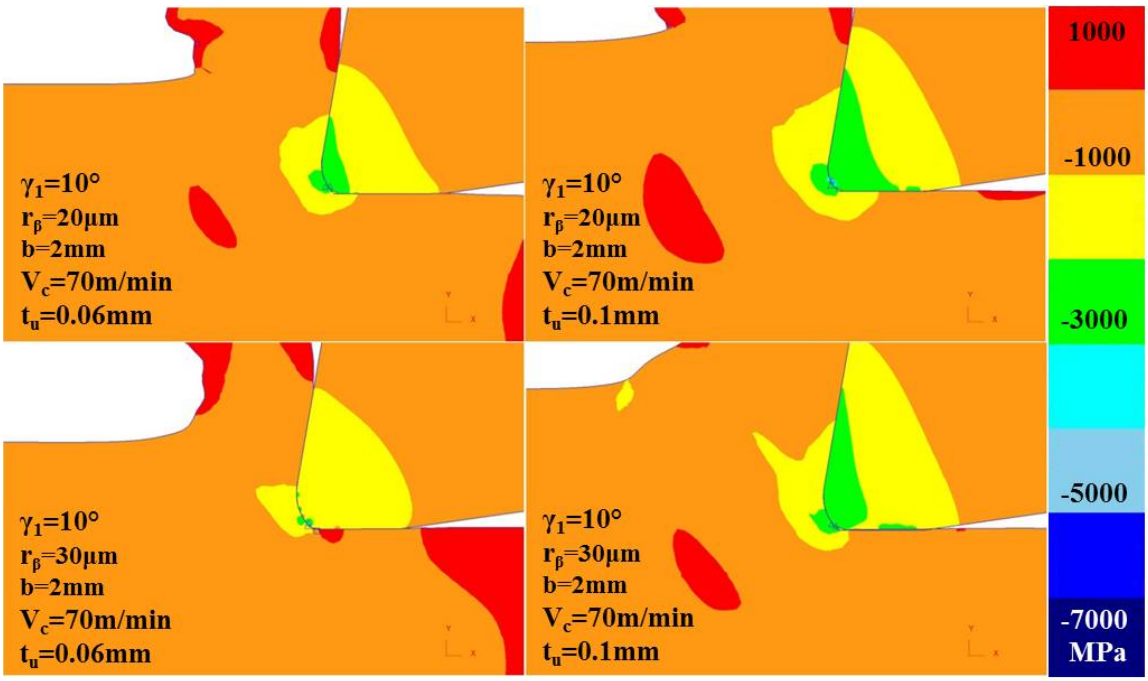

Figure 4.36: Stress distributions in depth of cut direction (Ti-64, γ_1=10°)

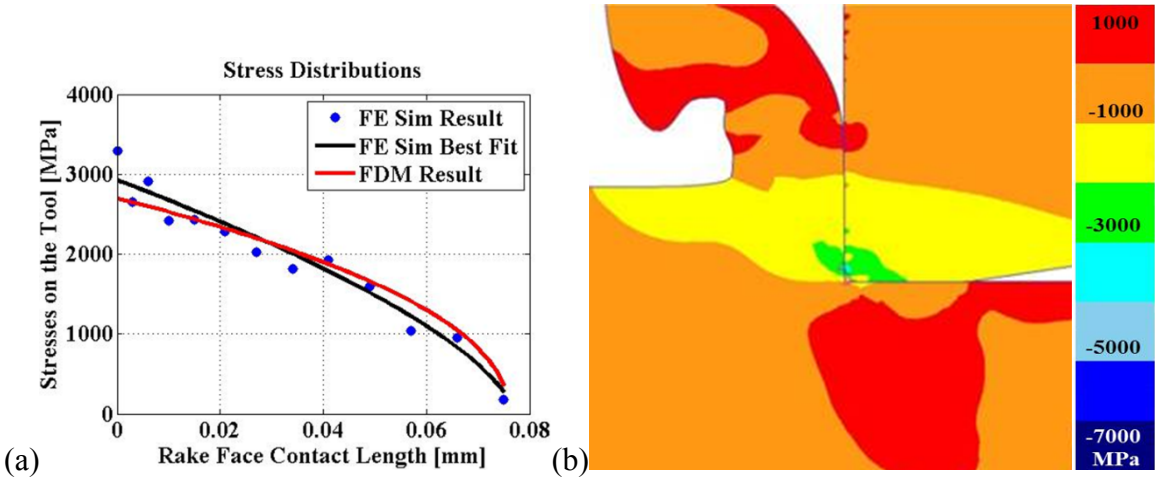

Figure 4.37: Comparison of Ti-64 (a) predicted stresses and (b) FE-based simulation stress distribution

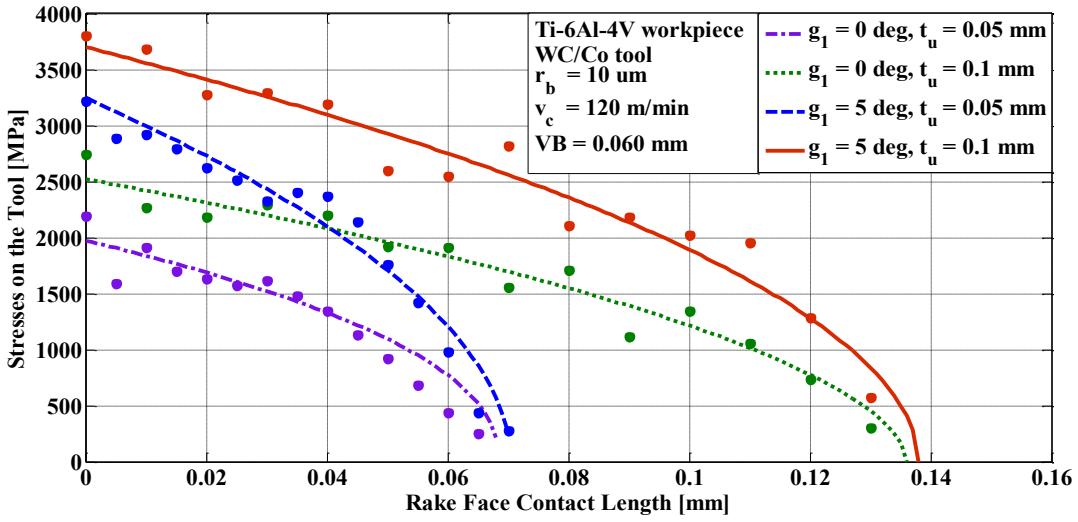

Figure 4.38: Effect of γ_1 and t_u on tool rake face stress distributions for machining Ti-6Al-4V.

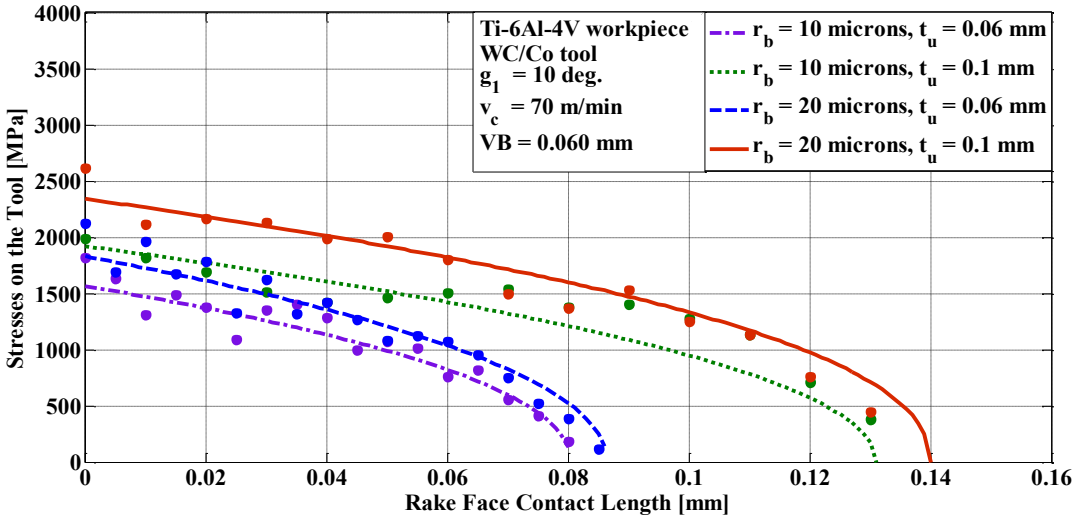

Figure 4.39: Effect of r_β and t_u on tool rake face stress distributions for machining Ti-6Al-4V.

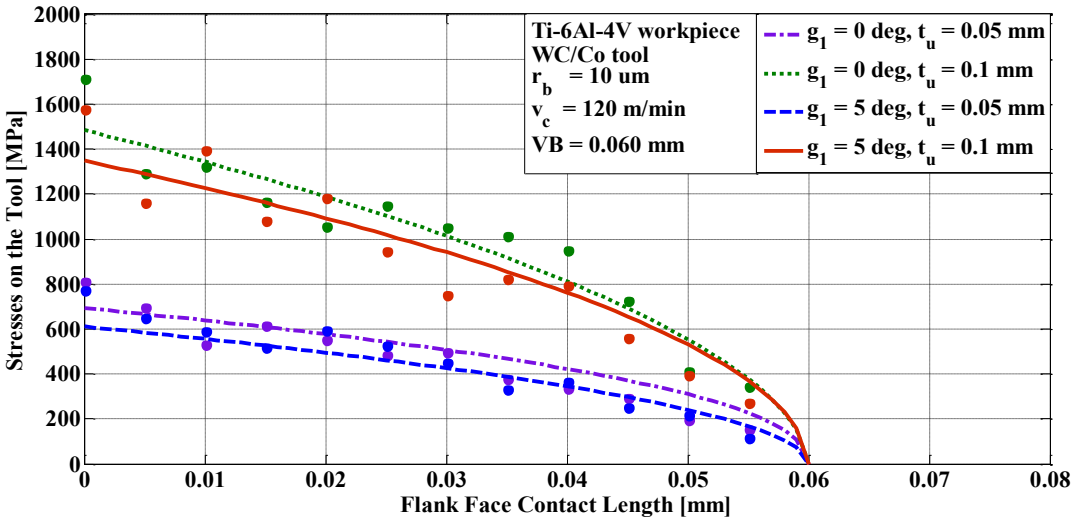

Figure 4.40: Effect of γ_1 and t_u on tool flank face stress distributions for machining Ti-6Al-4V.

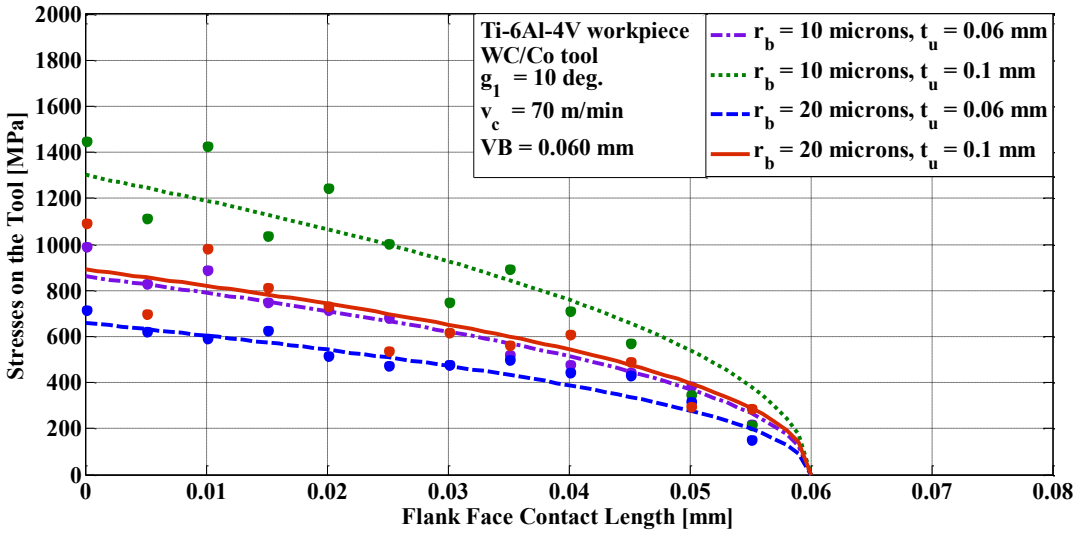

Figure 4.41: Effect of r_β and t_u on tool flank face stress distributions for machining Ti-6Al-4V.

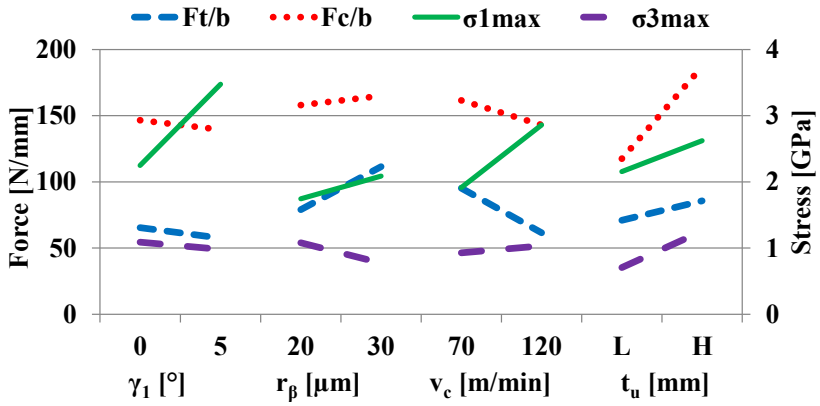

Figure 4.42: Effects of tool geometry and cutting conditions on tool forces and stresses (Ti-6Al-4V)

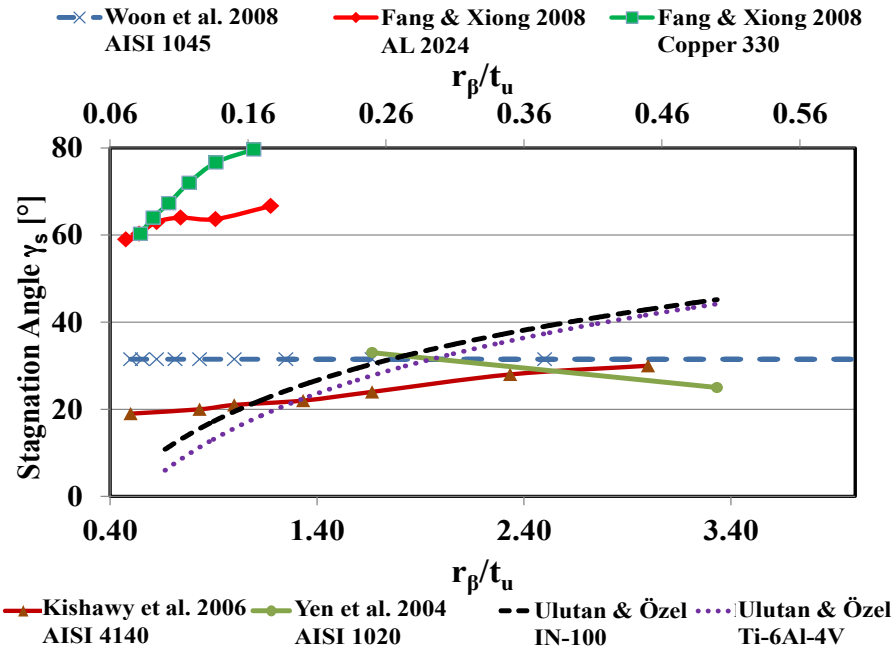

Figure 4.43: Effects of tool geometry and cutting conditions on stagnation point angle

From Figures 4.30 and 4.42, it is observed that the main effect on machining forces is the uncut chip thickness, whereas both cutting speed and feed increase the maximum stress components on the rake and flank face of the cutting tool. Rake angle and edge radius have different effects on different materials, while the increase in rake angle increased maximum stress component on the rake face of the tool during machining Ti-64, and the increase in edge radius increased the maximum stress component on the flank face of the tool during machining IN-100.

Moreover, the stagnation point angles summarized in Tables 4.7 and 4.8 have been utilized and the effects of the ratio of cutting edge radius between uncut chip thickness (r_β/t_u) on the location of stagnation point in machining Ti-6Al-4V and IN-100 have been compared with the findings summarized from literature as shown in Figure 4.43. It was observed that similar to the literature, the stagnation point angle increases with the increasing cutting edge radius to uncut chip thickness ratio. The trend lines

obtained for this increase are more aligned with the work presented by Kishawy et al. (2006) for cutting AISI 4140 steel. The study by Woon et al. (2008) shows a stagnation angle mostly not affected from the uncut chip thickness in micro-cutting of AISI 1045 steel while Fang & Xiong (2008) reports higher stagnation angles and an increase for increasing edge radius to uncut chip thickness ratio in cutting AL 2024 and Copper 330. These observations confirm that as the edge radius becomes larger or uncut chip thickness gets smaller, there will be a longer contact region around the round edge from the stagnation point into the flank face increasing the tool wear rate in machining of Ti-6Al-4V titanium and IN-100 nickel-based alloys.

4. Conclusions

In conclusion, FE-based simulations in 2D have been designed and conducted using the software DEFORM to illustrate the experimental conditions of orthogonal cutting tests presented in Chapter 2. For these simulations, comparisons with experimental results show that forces and stresses can be predicted easily with the friction coefficients calculated through the friction determination method of Chapter 3. These friction coefficients were mostly similar for different cutting conditions, which is probably because the cutting conditions selected were not too different from each other and not excessive. The effects of machining parameters on the stress fields, as well as force predictions were found, and the change in the location of stagnation point was also presented with changing cutting edge radius to uncut chip thickness ratio. Since there is not enough prior study related to the location of the stagnation point in these materials, a direct comparison could not be achieved; however, when compared to steel workpiece materials such as AISI 4140, the trends were found to be similar. Since the purpose of

the 2D simulations was to develop and validate the friction determination methodology, and ultimately, determine the friction coefficients on the rake and flank faces of the tool, further results were not pursued. Instead, utilizing these determined friction coefficients, 3D simulations were designed and conducted to better reflect the nature of the machining process, and results were extracted from those simulations.

Table 4.7: Search algorithm results compared to orthogonal cutting results for IN-100 with worn tool (*VB*=60 µm)

	Experimental						**FEM Results**								**FDM Results**					
	r_β [µm]	v_c [m/min]	t_u [mm]	b [mm]	F_t [N]	F_c [N]	$\sigma_{1_{max}}$ [MPa]	n	$\sigma_{3_{max}}$ [MPa]	m	l_c/t_u	l_p/t_u	F_t [N]	F_c [N]	μ_1	μ_2	$\tau_{1_{max}}$ [MPa]	$\tilde{\sigma}_2$ [MPa]	$\tilde{\tau}_2$ [MPa]	γ_s [°]
γ_I=0°	10	12	0.05	3.52	1185	1470	3712	0.50	318	0.51	3.07	0.55	887	1447	0.70	0.62	2346	285	-244	16
	10	12	0.1	3.52	1949	2166	3389	0.51	607	0.50	2.39	0.64	1419	2591	0.70	0.62	1987	543	-465	14
	10	24	0.05	2.99	1090	1013	3900	0.52	706	0.52	2.66	0.58	801	1214	0.70	0.62	2396	631	-541	14
	10	24	0.1	2.99	1692	1602	4281	0.52	1463	0.47	2.08	0.54	1307	2117	0.70	0.62	2558	1306	-1122	12
	25	12	0.05	3.09	1074	967	3180	0.48	1120	0.51	2.67	0.31	939	1221	0.70	0.62	2092	1304	-193	46
	25	12	0.1	3.09	1756	1854	3359	0.49	2158	0.50	2.32	0.28	1505	2024	0.70	0.62	2207	2508	-377	43
	25	24	0.05	2.45	882	707	3155	0.47	1672	0.50	2.47	0.30	720	904	0.70	0.62	2080	1941	-295	44
	25	24	0.1	2.45	1415	1513	3723	0.47	1790	0.54	2.12	0.40	1105	1615	0.70	0.62	2359	2081	-311	44
γ_I=3°	10	12	0.05	2.45	768	885	3443	0.53	636	0.50	2.74	0.49	561	980	0.70	0.62	2165	569	-488	14
	10	12	0.1	2.45	1292	1645	3961	0.50	797	0.49	2.07	0.57	848	1693	0.70	0.62	2355	713	-611	13
	10	24	0.05	2.45	810	932	3869	0.50	699	0.51	2.15	0.59	617	941	0.70	0.62	2302	624	-536	14
	10	24	0.1	2.45	1298	1631	3419	0.50	1577	0.52	2.27	0.45	1024	1708	0.70	0.62	2139	1408	-1210	10
	25	12	0.05	3.02	941	1138	2971	0.50	1697	0.49	2.45	0.30	891	1163	0.70	0.61	1950	1969	-300	43
	25	12	0.1	3.02	1710	2217	3286	0.49	1190	0.52	2.54	0.27	1302	2078	0.70	0.62	2170	1385	-206	45
	25	24	0.05	2.96	1094	1233	3298	0.50	2149	0.53	2.05	0.35	858	1113	0.70	0.61	2109	2491	-383	42
	25	24	0.1	2.96	1506	2255	3487	0.51	2709	0.50	2.02	0.48	1302	1894	0.70	0.62	2127	3145	-478	40

Table 4.8: Search algorithm results compared to orthogonal cutting results for Ti-64 with worn tool (*VB*=60 µm)

	Experimental						**FEM Results**								**FDM Results**					
	r_β [µm]	v_c [m/min]	t_u [mm]	b [mm]	F_t/b [N/mm]	F_c/b [N/mm]	$\sigma_{1_{max}}$ [MPa]	n	$\sigma_{3_{max}}$ [MPa]	m	l_c/t_u	l_p/t_u	F_t/b [N/mm]	F_c/b [N/mm]	μ_1	μ_2	$\tau_{1_{max}}$ [MPa]	$\tilde{\sigma}_2$ [MPa]	$\tilde{\tau}_2$ [MPa]	γ_s [°]
γ_1=0°	10	120	0.05	5	51	104	1974	0.45	693	0.35	1.37	0.35	59	99	0.60	0.51	1013	544	-555	11
	10	120	0.1	5	80	189	2524	0.55	1485	0.34	1.36	0.41	93	195	0.59	0.51	1215	1167	-1189	9
γ_1=5°	10	120	0.05	5	48	99	3247	0.52	611	0.32	1.41	0.52	49	104	0.60	0.52	1498	483	-489	12
	10	120	0.1	5	67	180	3701	0.52	1349	0.32	1.38	0.57	65	189	0.60	0.52	1645	1066	-1078	9
γ_1=10°	20	70	0.06	2	75	128	1566	0.47	861	0.39	1.34	0.36	75	124	0.59	0.51	793	908	-324	28
	20	70	0.1	2	83	188	1921	0.49	1301	0.40	1.31	0.33	94	189	0.58	0.51	974	1378	-487	26
	30	70	0.06	2	110	139	1831	0.48	659	0.32	1.44	0.45	88	150	0.59	0.45	897	708	-145	45
	30	70	0.1	2	113	191	2342	0.45	891	0.31	1.40	0.43	123	207	0.59	0.49	1162	958	-195	45

CHAPTER 5

FINITE ELEMENT-BASED SIMULATIONS: 3-D SIMULATIONS

1. Introduction

In simulating the orthogonal machining processes, 2D simulations are very useful. However, orthogonal machining has limited use in the industry. Therefore, it is essential to understand and analyze the 3D machining processes, where 3D simulations can be helpful. 2D simulations are still utilized to understand the basics of 3D processes by approximating the third dimension to the required symmetry, however, 3D simulations, where appropriately designed and conducted, illustrate the process better. To this end, the results of the 2D simulations were utilized as a guidance for 3D simulations, as well as an input in terms of the friction coefficients. With this guidance, 3D simulations utilizing the updated Lagrangian software DEFORM-3D are designed and conducted matching the machining conditions of the face turning experiments. In this chapter, the difference of 3D simulations from 2D simulations are explained, and the results of these simulations are presented in comparison with experimental findings.

2. Physics-Based Simulations in 3D

For 3D machining, where there is significant workpiece deformation in all directions, using 2D simulations is not sufficient, since there is no symmetry in the third dimension. Hence, there is a need for 3D simulations that can represent the physics of 3D machining and chip formation. For this reason, 3D simulations illustrating the face turning experiments were conducted for all experimental conditions, using the friction coefficients calculated from 2D simulations (see Figure 5.1). In 3D simulations, different than 2D simulations, definition of cutting speed is not through the boundary conditions,

but at the initial definition of the problem together with feedrate and depth of cut. Since 3D machining is a more complex form of metal cutting compared to orthogonal machining, these parameters have a combined effect on the mechanics of the process, and defining them as primitively as in 2D would be oversimplifying the problem at hand. Consequently, relevant velocity boundary conditions at each node of the tool have been created by the software once cutting speed, feedrate, and depth of cut are selected.

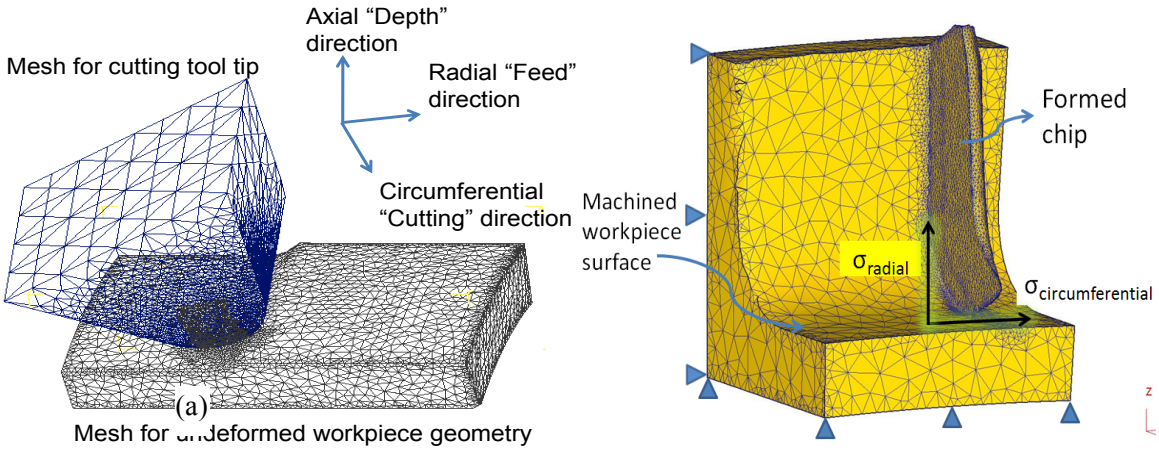

Figure 5.1: Mesh for the workpiece and the tool in 3D simulations

After this initialization of machining parameters, tool and workpiece are defined with their material properties and geometries, as well as mesh windows very similar to 2D machining. Definition of friction windows is more complex in 3D machining, and it can make the simulations unstable with slightest changes, which is why a general friction was also defined, and a special friction condition on the rake face was added to specify the different behavior of friction at that surface. The most important difference between 2D and 3D simulations is the added complexity of elastic-viscoplastic workpiece material assumption, which causes severe software-related convergence problems that prevents simulations to run.

3D simulations were conducted under the assumption of plastic workpiece material and later elastic-viscoplastic simulations are conducted at a few conditions for comparison of predicted results, to be discussed in Chapter 6. This plastic workpiece material assumption, although the closest to the actual machining conditions after the elastic-viscoplastic material assumption, ignores the elastic portion of machining deformations and treats them as fully plastic. Hence, force predictions (and consequently temperature and stress predictions) can be higher (or lower) than the 2D simulations. As a result of this, it is important to adjust friction coefficients and the flow stress model accordingly.

Friction coefficients are directly used from 2D simulation results, but friction windows were adjusted to reflect friction on the whole contact face rather than just a line (in 2D). The original Johnson-Cook (JC) flow stress model (Model 1-Eq. 5.1) was improved to the modified model, first without (Model 2-Eq. 5.2), then with (Model 3-Eq. 5.3) temperature-dependent flow softening, and the parameters used for Model 3 are given in Table 5.1. These parameters were found after a thorough sensitivity analysis described in the next section. Furthermore, machining conditions for 3D simulations were not same as 2D simulations since (1) it is not easy to find the same tools, (2) face turning tests aimed further results (e.g. effect of tool coating), and (3) the excessive machining conditions in face turning (high V_c for Ti-64) were considered to be potentially hazardous and unnecessary. It can be observed from Tables 5.2-5.3 for IN-100 and Ti-64 that not all experimental conditions have been simulated and their results gathered. The main reason for this was that the residual stress measurements were taken for these experiments, since measuring residual stress is costly and further measurements could not be achieved.

$$\sigma = [A + B\varepsilon^n]\left[1 + Cln\frac{\dot{\varepsilon}}{\dot{\varepsilon}_0}\right]\left[1 - \left(\frac{T-T_0}{T_m-T_0}\right)^m\right] \qquad \text{(Eq. 5.1)}$$

$$\sigma = [A + B\varepsilon^n]\left[1 + Cln\frac{\dot{\varepsilon}}{\dot{\varepsilon}_0}\right]\left[1 - \left(\frac{T-T_0}{T_m-T_0}\right)^m\right]$$

$$\left[D_1 + (1 - D_1)\left[\tanh\left(\frac{1}{(\varepsilon+p_1)^r}\right)\right]^s\right] \quad \text{(Eq. 5.2)}$$

$$\sigma = \left[A + B\varepsilon^n\left(\frac{1}{exp(\varepsilon^a)}\right)\right]\left[1 + Cln\frac{\dot{\varepsilon}}{\dot{\varepsilon}_0}\right]\left[1 - \left(\frac{T-T_r}{T_m-T_r}\right)^m\right]$$

$$\left[D_2 + (1 - D_2)\left[\tanh\left(\frac{1}{(\varepsilon+p_2)^r}\right)\right]^s\right] \quad \text{(Eq. 5.3)}$$

where $D_2 = 1 - \left(\frac{T}{T_m}\right)^d$, and $p_2 = \left(\frac{T}{T_m}\right)^b$.

Table 5.1: Best set of modified material flow stress model parameters for both materials (Model 3)

Alloy	***A***	***B***	***n***	***C***	***m***	***a***	***b***	***d***	***r***	***s***
Ti-64	725	300	0.65	0.035	1	0.5	2	0.5	12	-0.05
IN-100	1350	1750	0.65	0.017	1.3	1.5	10	0.01	1.5	-0.4

Table 5.2: Face turning simulation conditions for IN-100

V_c [m/min]	t_u [mm]	b [mm]	Tool	r_β [µm]
24	0.05	1	Sharp	5
			Variable Edge	10
			Variable Edge	25
			TiAlN Coated	10

Table 5.3: Face turning simulation conditions for Ti-64

t_u [mm]	Tool	r_β [µm]	b [mm]	V_c [m/min]
0.05	TiAlN Coated	10	2	90
				55
	Variable edge	25		90
				55
0.1	TiAlN Coated	10		90
				55
	Variable edge	25		90
				55

3. Flow Stress Parameter Determination

Original Johnson-Cook (JC) material model represents the flow stress (σ) of the material in terms of strain (ε), strain rate ($\dot{\varepsilon}$), and temperature (T). Using SHPB tests, the original JC material model (Model 1) parameters (A, B, C, n, m) can be determined (Eq. 5.1), where $\dot{\varepsilon}_0$ is the reference strain rate, T_0 is the ambient temperature, and T_m is the melting temperature of the material. These original JC model parameters have been determined by many researchers for different materials and many are published for Ti-64, and the ranges of the published values show that the exact parameters cannot be found (Lee & Lin 1998a, Lee & Lin 1998b, Meyer & Kleponis 2001, Chen et al. 2004, Seo et al. 2005, Li & He 2006). However, the approximate range of these parameters can be observed from these findings, and investigation of parameters can be initiated from these values. From the original parameter sets, the values given in Table 5.4 were used for Ti-64 and IN-100. Then, starting from these values, the parameters that emerge in the modified JC constitutive material model (a, b, d, r, s) are added to represent temperature-dependent flow softening based adiabatic shearing (Eq. 5.3).

Table 5.4: Original Johnson-Cook material flow stress model parameters (Model 1)

Alloy	*A*	*B*	*n*	*C*	*m*
Ti-64	725	683	0.65	0.035	1
IN-100	1350	1750	0.65	0.017	1.3

Before starting the procedure to determine the modified Johnson-Cook flow stress model parameters (a, b, d, r, s), the original model parameters (A, B, C, m, n) should be determined via SHPB tests. For this reason, the values in Table 5.4 were utilized to initiate the algorithm (Lee & Lin 1998b). 3D machining simulations were employed to represent face turning processes, and chip formation that represents steady-state results

was achieved in every simulation. These simulations were designed and conducted using DEFORM software. The first step to the algorithm (Figure 5.2) was to select meaningful values by experience for the modified JC material flow stress model parameters (a, b, d, r, s) and run initial simulations for all the machining conditions designed. Then, forces were extracted from finalized simulations, and it was verified that steady-state conditions were reached at the end of the simulations. The errors between the predicted and experimental forces were calculated and recorded for each simulation for later comparison. Different combinations of these modified model parameters were utilized to find solutions that resulted in comparable predicted steady-state forces. While selecting the different combinations of these parameters, the flow stress curve was paid attention to, because the model requires that the flow stress curve represents flow softening behavior that is dependent on temperature, while ensuring similarity with SHPB test results at low strain values.

When acceptable results were found for these parameters, it was observed that the errors could be decreased even further, so the original model parameters were considered for change. It is noteworthy to realize that C, and m represent the changes in strain rate and temperature in the original JC model, while A represents the flow stress at zero strain, reference strain rate, and ambient temperature conditions. Hence, these parameters should be kept unchanged to stay on the same curves of the original JC model. However, changing the other two original JC parameters (B and n) would only represent changes in the effect of strain on flow stress, which is already altered by the modified model through flow softening. Therefore, in order to improve the results even further, these values were

updated within the ranges reported by different references. When minimum force error is achieved, flow stress solution is said to be found for the material.

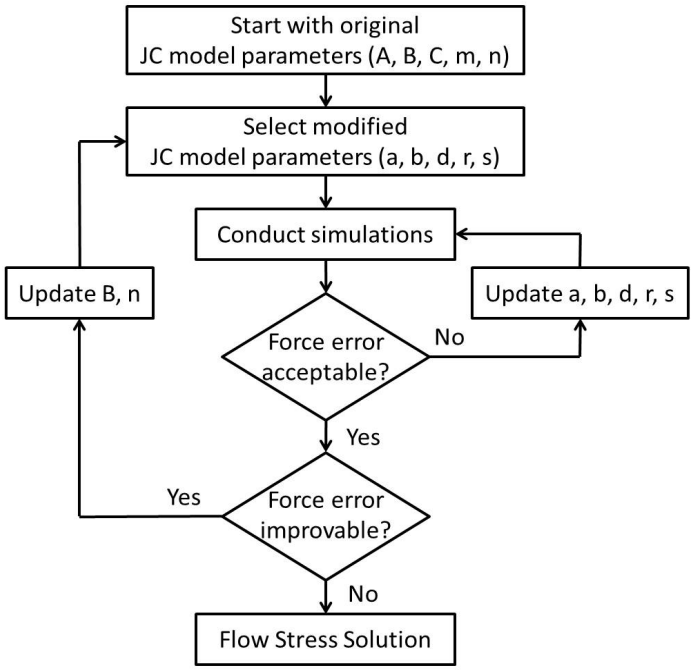

Figure 5.2: Flow diagram to achieve modified JC model parameters and the flow stress solution

Calculation of resultant error is straightforward: For the set of simulations, difference in each force component (F_c, F_p & F_t) is calculated. Then, total error is calculated using Eq. (5.4) where $F_{i,exp}$ represents the experimental value of any of the force components (cutting, thrust, or feed) and $F_{i,sim}$ represents its simulated value: Each error is squared, and sum of these squares is found for each simulation and each force component. Then, this sum of squares is divided by number of machining conditions (*M:* number of simulations in a set) and number of force components (*N*: 2 for orthogonal machining, 3 for 3D machining simulations). Square root of this value gives the resultant force error ε_{tot}, which is utilized in comparing the quality of each flow stress model representation. If resultant error for a new set improves (decreases) the resultant force error, the new set of parameters is set as the base for

next parameter iteration. If not, results from previous sets are compared with results from the new set, and next parameter set is decided based on this comparison.

Simulations with different sets of modified material flow stress model parameters were conducted for both materials and resultant errors for all sets were determined. According to these resultant errors, best sets of parameters that represent the flow stress of materials are shown in Table 5.1. For both materials, given sets of parameters led to 23% resultant error in prediction. These temperature-dependent flow softening based material model parameters can be used for further simulations in similar machining conditions, but for significantly different machining conditions, parameters should be determined again with new experiments. For these sets of parameters, force comparisons for all sets of simulations are presented in Tables 5.5-5.6 for IN-100 and Ti-64, which show results of 3D experiments and simulations, and errors associated with all machining conditions.

$$\varepsilon_{tot} = \sqrt{\frac{\sum_{j=1}^{M}\sum_{i=1}^{N}\left[\left(\frac{F_{i,exp}-F_{i,sim}}{F_{i,exp}}\right)^2\right]_j}{N \cdot M}} \qquad \text{(Eq. 5.4)}$$

4. Results and Discussions

Using the inverse methodology through experimental force measurements, modified material model parameters were determined and simulations were conducted using these parameters. Figure 5.3 shows a comparison between force measurements and simulation results for IN-100, whereas Figure 5.4 shows the same for Ti-64. As it can be observed from these results as well as Tables 5.5-5.6 that simulation findings in terms of forces are in good agreement with experimental results (mostly within 20% error), which

validates the simulations for further result extraction. For comparison, same results for simulations with Model 2 are also presented in Figures 5.5-5.6 for Ti-64 and IN-100. These figures show that despite being close, simulations with Model 2 predict forces with more error. In the predictions with Model 3, it was observed that due to the physical constraints of measurements as well as numerical constraints of simulations, some thrust force components had significantly more error than other components and machining conditions. For IN-100, cutting forces and thrust forces were slightly overpredicted while feed forces were predicted slightly lower than measurements.

For Ti-64, it was observed that cutting forces were overpredicted, while thrust forces were underpredicted. This is due to the total error minimizing nature of the iterative algorithm and the high thrust force measurements compared to the values found in the literature. Furthermore, rather than predicting a single value, simulations are utilized to gather a mean value (shown in bold) with the amount of uncertainty involved within the simulations (shown below mean). Since these simulations are based on numerical methods, at every time step, a slightly different force prediction is observed, and although a steady-state is achieved, the force predictions still vary in small amounts at every step. Therefore, a mean value is obtained, and the variances can be interpreted as uncertainties of the simulations. Sensitivity of these results to changes in physical and numerical parameters is investigated in the next chapter.

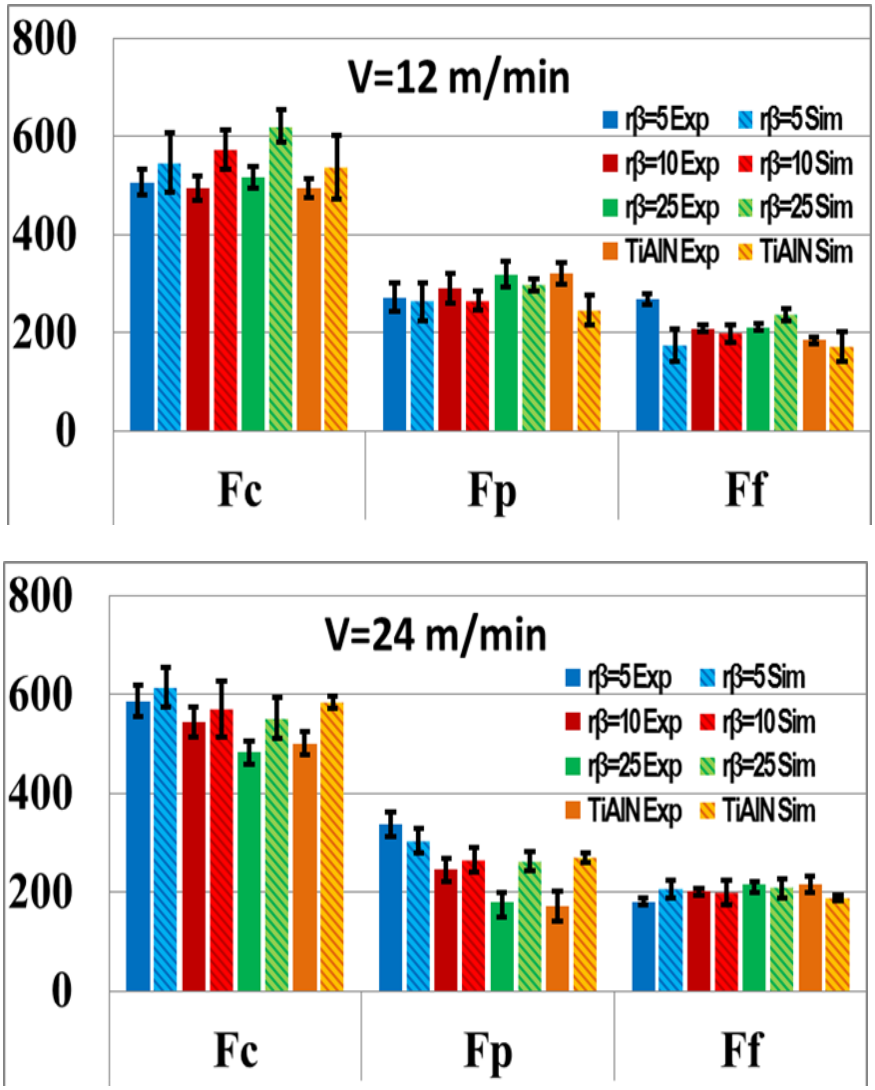

Figure 5.3: Comparison of experimental and simulated results for force components (IN-100) at (a) V_c=12 m/min and (b) V_c=24 m/min (Model 3)

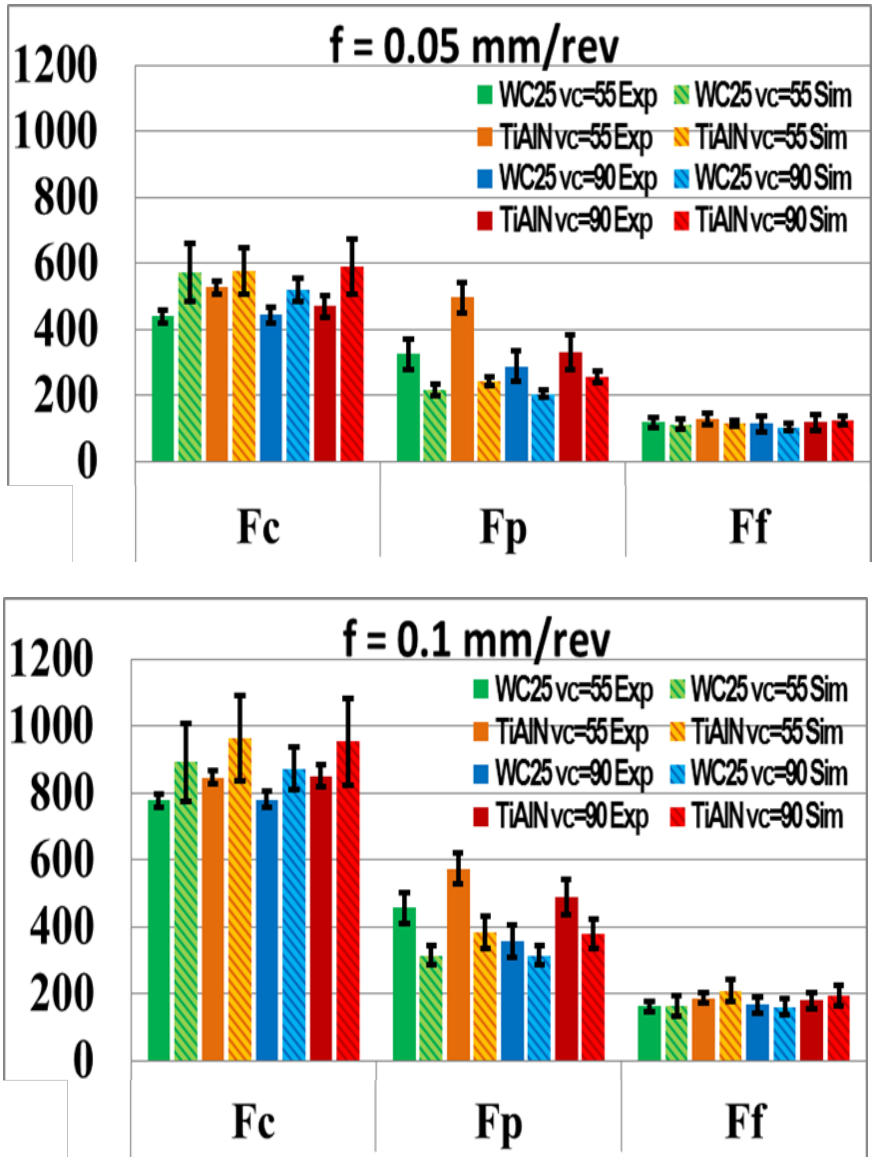

Figure 5.4: Comparison of experimental and simulated results for force components (Ti-64) at (a) t_u=0.05 mm and (b) t_u=0.1 mm (Model 3)

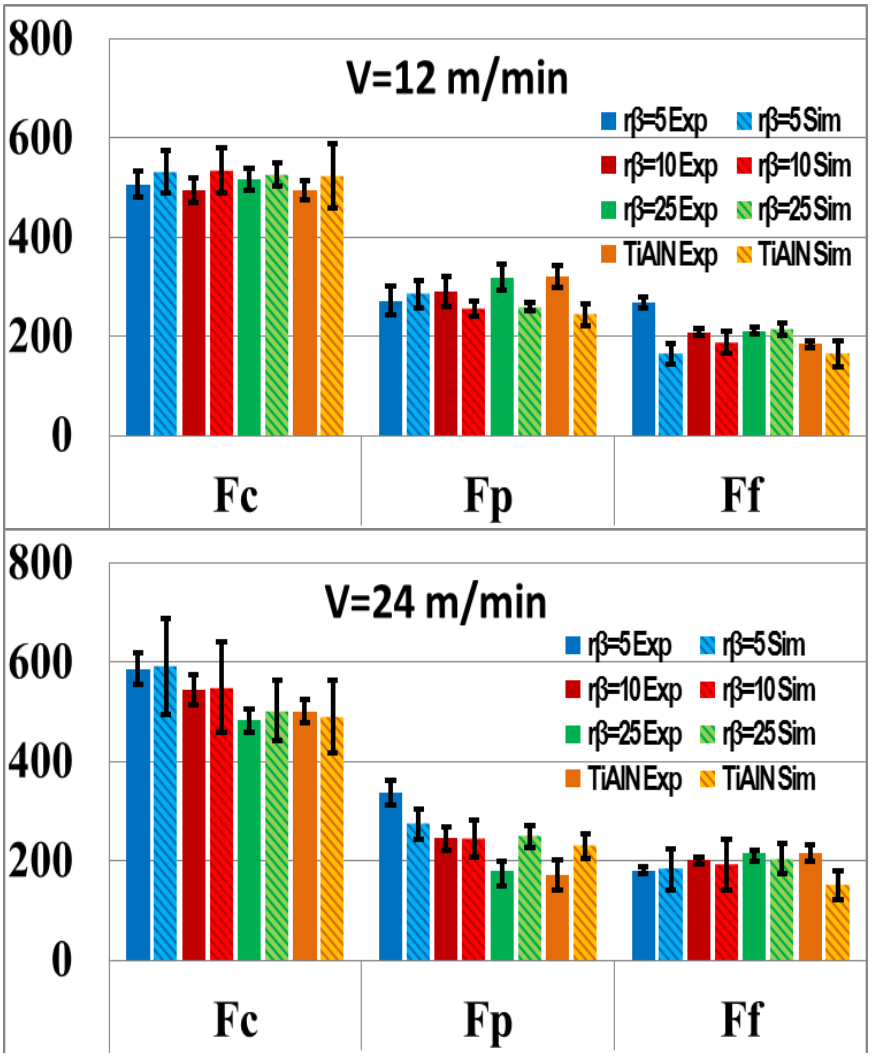

Figure 5.5: Comparison of experimental and simulated results for force components (IN-100) at (a) V_c=12 m/min and (b) V_c=24 m/min (Model 2)

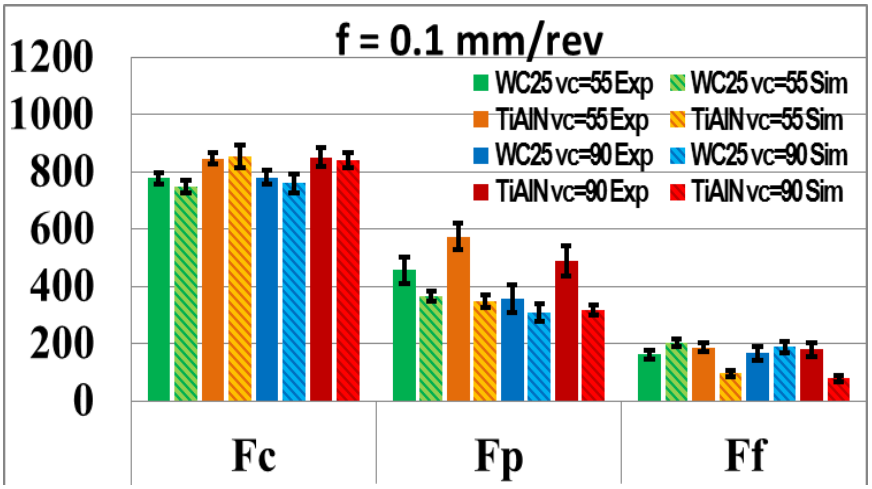

Figure 5.6: Comparison of experimental and simulated results for force components (Ti-64) at t_u=0.1 mm (Model 2)

Based on these simulation results, residual stresses were extracted from the simulations (at the last iteration of the friction determination methodology) and compared with the experimental findings. Figure 5.7 shows a sample stress field obtained from 3D face turning simulations. Figures 5.8-5.9 show the comparison of residual stresses in both radial (feed) and circumferential (cutting speed) directions for IN-100 found with flow stress models 3 and 2, respectively. Figures 5.10-5.11 illustrate the same comparison for Ti-64. From these figures, it was found that simulations with Model 3 predict the circumferential residual stresses with negligible errors, while the radial direction residual stresses had considerably more errors in Ti-64. Model 2 results were also not bad, but the error involved was more with these simulations.

Tables 5.7-5.8 show results of these predictions in tabular form, representing the measurements and simulations in terms of peak tensile and compressive values. Errors between measured and simulated results show that residual stresses extracted from

simulations also match the experimental values, and the validated simulations can be utilized to predict residual stresses.

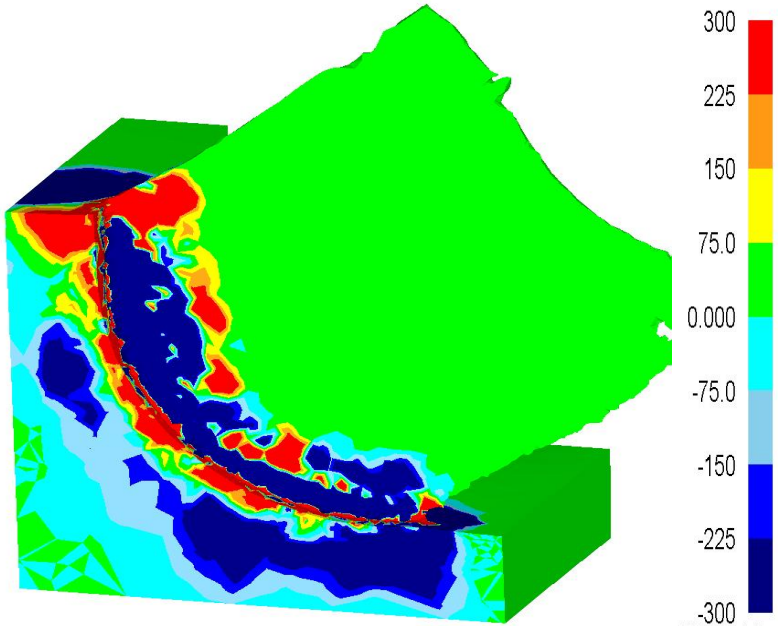

Figure 5.7: Sample 3D stress field [MPa] from FE-based face turning simulations

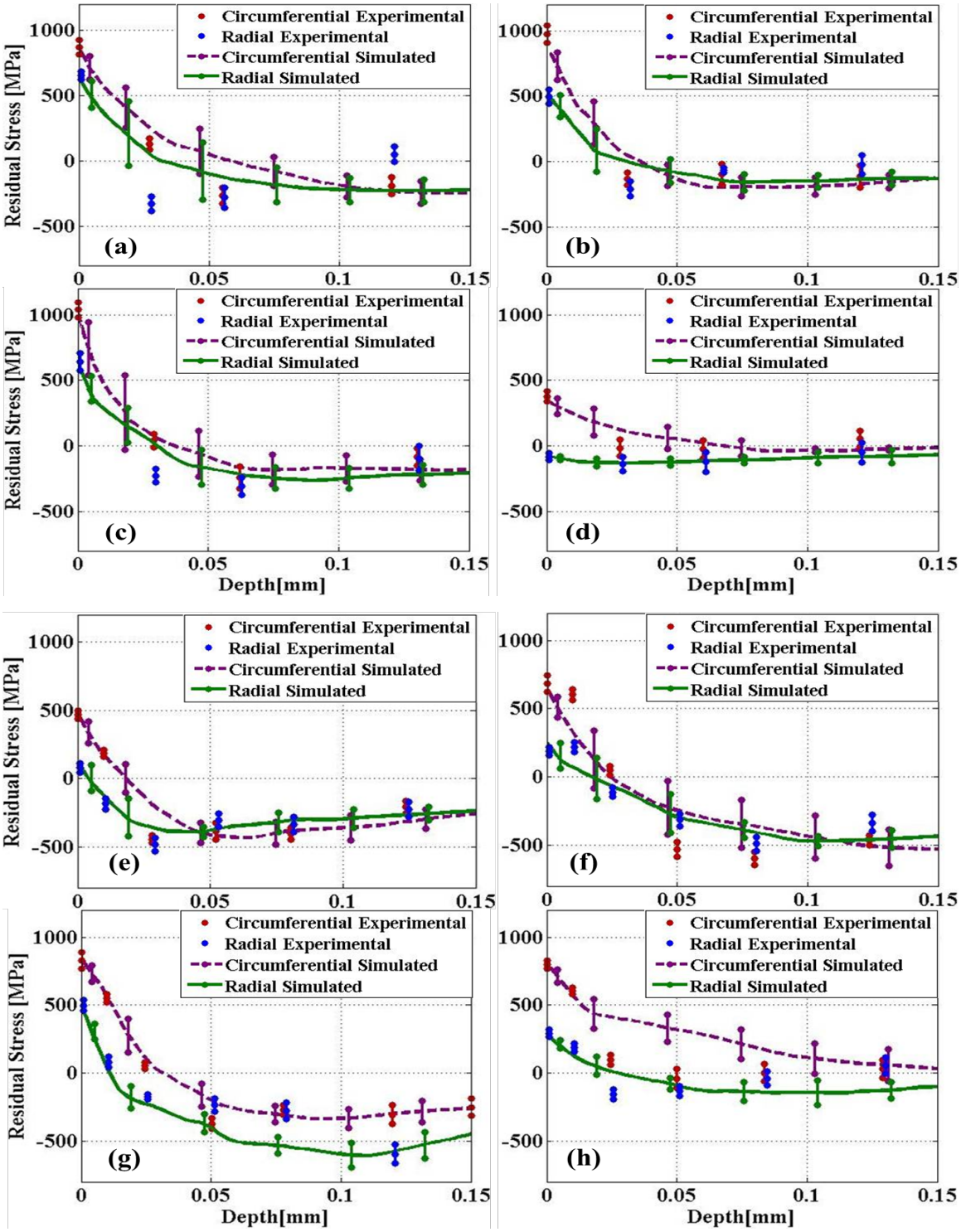

Figure 5.8: Comparison of residual stresses in face turning of IN-100 at (a-d) V_c=12 m/min and (e-h) V_c=24 m/min, with (a&e) uncoated sharp tool (r_β≈5µm), (b&f) uncoated tool (r_β≈10µm), (c&g) uncoated tool (r_β≈25µm), (d&h) TiAlN coated tool (r_β≈10µm) (Model 3)

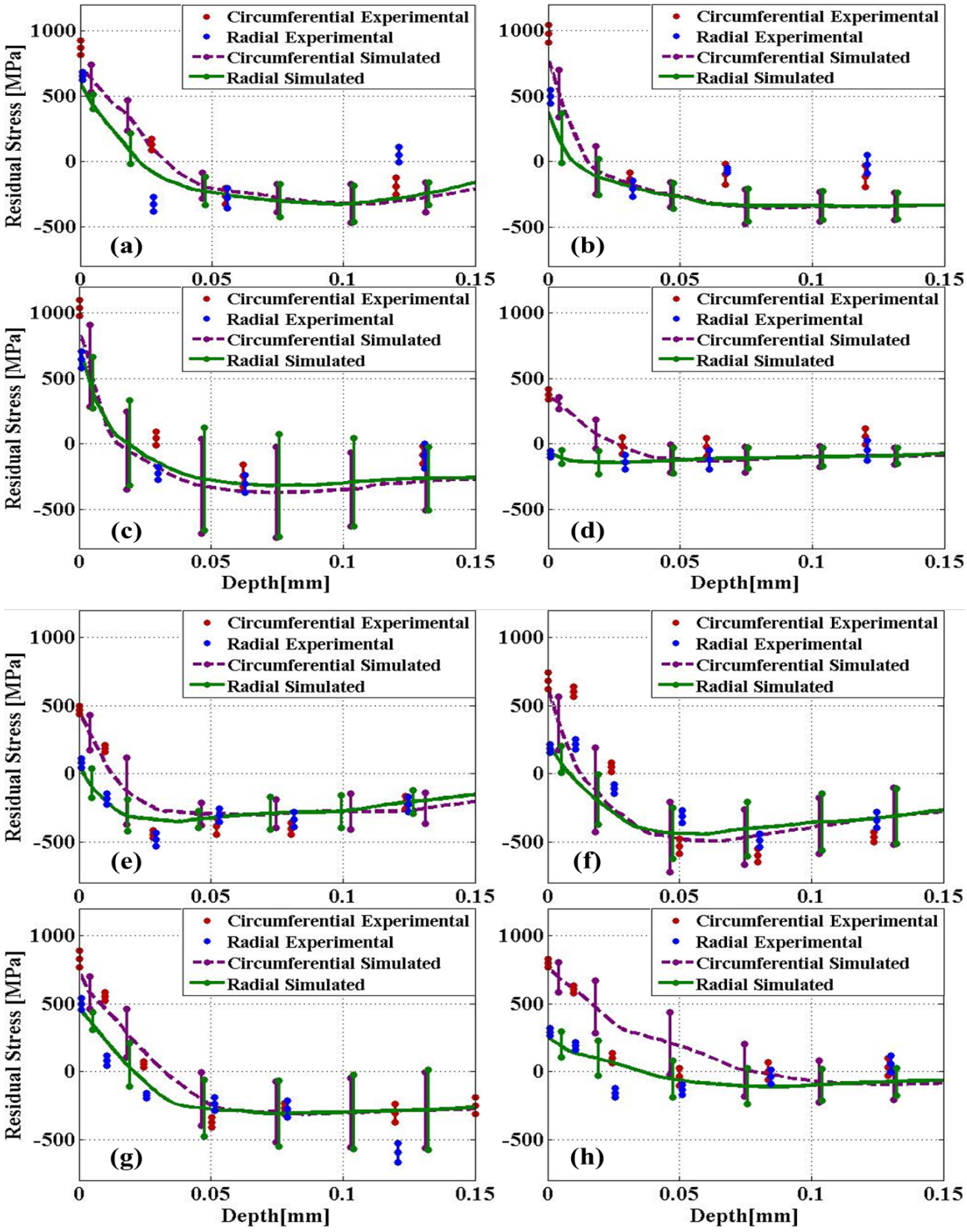

Figure 5.9: Comparison of residual stresses in face turning of IN-100 at (a-d) V_c=12 m/min and (e-h) V_c=24 m/min, with (a&e) uncoated sharp tool (r_β≈5µm), (b&f) uncoated tool (r_β≈10µm), (c&g) uncoated tool (r_β≈25µm), (d&h) TiAlN coated tool (r_β≈10µm) (Model 2)

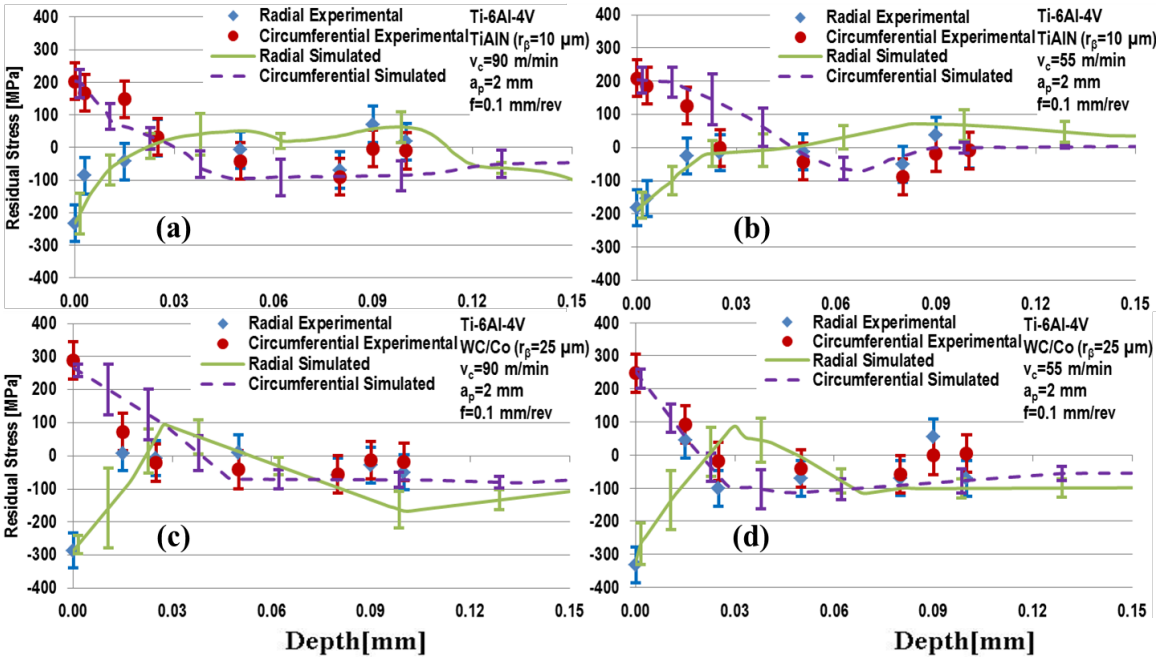

Figure 5.10: Comparison of residual stresses in face turning of Ti-64 with (a-b) TiAlN coated tool (r_β≈10µm) and (c-d) uncoated tool (r_β≈25µm) at (a&c) V_c=90m/min and (b&d) V_c=55m/min (Model 3)

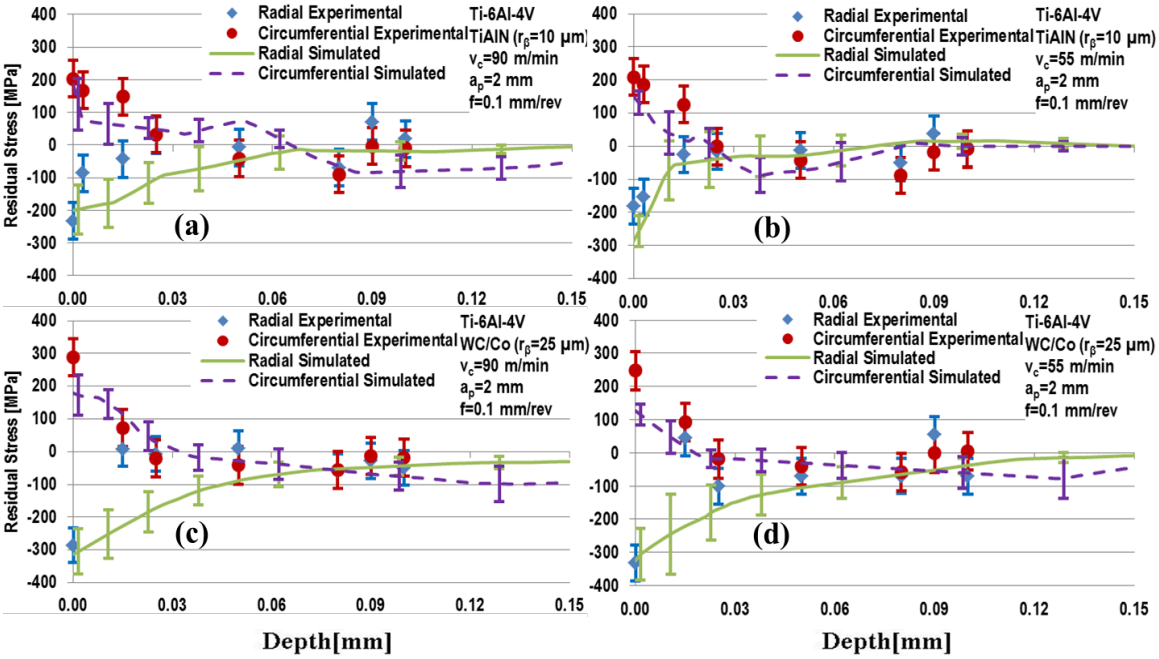

Figure 5.11: Comparison of residual stresses in face turning of Ti-64 with (a-b) TiAlN coated tool (r_β≈10µm) and (c-d) uncoated tool (r_β≈25µm) at (a&c) V_c=90m/min and (b&d) V_c=55m/min (Model 2)

5. Conclusions

In conclusion, FE-based simulations in 3D have been designed and conducted using the software DEFORM to illustrate the experimental conditions of face turning experiments presented in Chapter 2. Using the friction coefficients obtained in 2D simulations, these designed simulations were first utilized to determine flow stress parameters, and then to achieve force and residual stress results. After validating the methodology through force comparison with experimental findings in 3D, machining-induced residual stresses were extracted for the simulations and compared to experimental results, and the findings show that there is good accuracy between experimental and predicted values. Although it is not numerically possible to compare the entire residual stress graph with experimental findings, tensile and compressive peak values were compared. After a sensitivity analysis described in Chapter 6, these findings were optimized using a Particle Swarm Optimization algorithm described in Chapter 7.

Table 5.5: Face turning simulation force comparison (simulated vs. experimental) and simulated temperature results for IN-100 (ε_{tot} = 23%)

b [mm]	t_u [mm]	Tool	r_β [µm]	V_c [m/min]	$F_{c,exp}$ [N]	$F_{c,sim}$ [N]	Error %	$F_{p,exp}$ [N]	$F_{p,sim}$ [N]	Error %	$F_{f,exp}$ [N]	$F_{f,sim}$ [N]	Error %	T_{tool} [°C]	T_{chip} [°C]
1	0.05	Sharp	5	12	**507** ±25	**541** ±84	**7**	**272** ±30	**276** ±69	**1**	**268** ±10	**172** ±43	**36**	**582** ±54	**611** ±58
		Variable Edge	10		**494** ±25	**583** ±39	**18**	**290** ±30	**302** ±22	**4**	**208** ±7	**204** ±15	**2**	**539** ±49	**580** ±56
		Variable Edge	25		**517** ±23	**630** ±42	**22**	**319** ±26	**323** ±18	**1**	**211** ±6	**229** ±13	**9**	**582** ±46	**616** ±54
		TiAlN Coated	10		**494** ±19	**600** ±52	**21**	**320** ±22	**305** ±24	**5**	**185** ±7	**197** ±22	**6**	**557** ±61	**586** ±59
		Sharp	5	24	**587** ±32	**629** ±50	**7**	**337** ±25	**354** ±33	**5**	**180** ±7	**222** ±26	**23**	**607** ±51	**645** ±44
		Variable Edge	10		**545** ±30	**566** ±16	**4**	**245** ±23	**300** ±9	**22**	**201** ±7	**204** ±7	**1**	**556** ±63	**602** ±62
		Variable Edge	25		**484** ±22	**543** ±22	**12**	**179** ±20	**290** ±15	**62**	**215** ±6	**209** ±10	**3**	**590** ±64	**637** ±57
		TiAlN Coated	10		**501** ±24	**564** ±59	**13**	**172** ±30	**289** ±25	**68**	**215** ±16	**191** ±28	**11**	**580** ±57	**623** ±52

Table 5.6: Face turning simulation force comparison (simulated vs. experimental) and simulated temperature results for Ti-64 (ε_{tot} = 23%)

b [mm]	t_u [mm]	Tool	r_β [µm]	V_c [m/min]	$F_{c,exp}$ [N]	$F_{c,sim}$ [N]	Error %	$F_{p,exp}$ [N]	$F_{p,sim}$ [N]	Error %	$F_{f,exp}$ [N]	$F_{f,sim}$ [N]	Error %	T_{tool} [°C]	T_{chip} [°C]
2	0.05	TiAlN Coated	10	90	**470** ±42	**563** ±47	**20**	**330** ±53	**239** ±20	**28**	**117** ±9	**126** ±14	**8**	**518** ±38	**555** ±44
				55	**526** ±31	**568** ±56	**8**	**495** ±49	**241** ±13	**51**	**128** ±16	**120** ±11	**6**	**459** ±51	**501** ±48
		Variable edge	25	90	**443** ±24	**468** ±8	**6**	**288** ±42	**187** ±6	**35**	**114** ±13	**98** ±5	**14**	**522** ±49	**553** ±46
				55	**439** ±39	**519** ±53	**18**	**324** ±36	**205** ±10	**37**	**117** ±15	**105** ±8	**10**	**442** ±44	**514** ±61
	0.1	TiAlN Coated	10	90	**850** ±33	**939** ±92	**10**	**488** ±51	**355** ±27	**27**	**179** ±24	**172** ±22	**4**	**614** ±47	**667** ±58
				55	**845** ±20	**1041** ±152	**23**	**573** ±47	**387** ±32	**32**	**187** ±16	**191** ±17	**2**	**503** ±66	**587** ±53
		Variable edge	25	90	**780** ±24	**951** ±102	**22**	**356** ±48	**344** ±19	**3**	**167** ±24	**174** ±17	**4**	**596** ±56	**643** ±75
				55	**777** ±20	**953** ±141	**23**	**456** ±47	**340** ±26	**25**	**161** ±16	**166** ±23	**3**	**485** ±52	**564** ±46

Table 5.7: Face turning simulation residual stress comparison (simulated vs. experimental) results for IN-100 (Total RS Error: 11%)

t_u [mm]	Tool	r_β [μm]	V_c [m/min]	Circumferential Residual Stress						Radial Residual Stress					
				PTS_{exp} [MPa]	PTS_{sim} [MPa]	Error %	PCS_{exp} [MPa]	PCS_{sim} [MPa]	Error %	PTS_{exp} [MPa]	PTS_{sim} [MPa]	Error %	PCS_{exp} [MPa]	PCS_{sim} [MPa]	Error %
0.05	Sharp	5	12	868	865	1	264	249	4	654	635	4	327	229	23
	Variable Edge	10		975	852	29	296	198	23	495	525	7	208	158	12
	Variable Edge	25		1038	1025	3	242	185	13	643	624	4	307	264	10
	TiAlN Coated	10		377	341	8	26	39	3	-81	-54	6	138	131	2
	Sharp	5	24	467	483	4	445	434	2	78	116	9	485	393	21
	Variable Edge	10		682	648	8	598	537	14	217	245	6	490	421	16
	Variable Edge	25		830	839	2	372	336	8	499	484	3	597	609	3
	TiAlN Coated	10		800	796	1	39	3	8	292	286	1	157	147	2

Table 5.8: Face turning simulation residual stress comparison (simulated vs. experimental) results for Ti-64 (Total RS Error: 20%)

t_u [mm]	Tool	r_β [μm]	V_c [m/min]	Circumferential Residual Stress						Radial Residual Stress					
				PTS_{exp} [MPa]	PTS_{sim} [MPa]	Error %	PCS_{exp} [MPa]	PCS_{sim} [MPa]	Error %	PTS_{exp} [MPa]	PTS_{sim} [MPa]	Error %	PCS_{exp} [MPa]	PCS_{sim} [MPa]	Error %
0.1	TiAlN Coated	10	90	203	204	1	90	97	5	70	64	4	233	231	1
			55	208	204	3	89	70	12	37	72	23	181	187	4
	Variable edge	25	90	288	267	14	56	82	17	10	94	55	286	287	1
			55	247	252	3	58	114	37	54	86	21	333	323	7

CHAPTER 6

SENSITIVITY ANALYSIS

1. Introduction

2D and 3D FE-based simulations of machining processes include many parameters that are not exactly known via experimentation or analytical findings. These include physical parameters such as friction coefficients and material flow stress as well as numerical parameters such as mesh size and time step. This chapter presents a thorough sensitivity analysis of input parameters, one that shows the effect of changing these parameters on outputs of interest such as forces as well as machining-induced residual stresses. It is important to understand the effect of these inputs on results to be confident about the models selected and used for final results that were presented in Chapters 4 & 5. Although these models were initially selected based on findings in the literature as an educated guess, it is still essential to be confident about the assumptions that apply to the particular problem at hand.

Using models that are verified through such a sensitivity analysis, residual stresses can be predicted as given in the previous chapters. However, due to substantial amount of uncertainties within the machining process, experimental values are always accompanied with some errors. Main reasons for these uncertainties are misalignments, machine backlashes, rigidity problems, rounding of parameters, and many other significant sources of variation. Therefore, it would not be scientific to assume that simulations do not carry such errors. In order to identify such errors, a substantial number of data points were extracted from simulations and expected values and variances of

predictions were also obtained. Hence, with each changing parameter, change of error between measured and simulated values (forces and residual stresses) is calculated. The squares of these errors are summed and the square root of the final sum is taken to achieve a final number for the total resultant error of any given set of parameters for comparison with other sets.

2. Sensitivity on Physical Parameters

While conducting simulations, many different models are tried and the best model that represents the physics of the process while resulting in the most accurate predictions is selected. However, it is important to know the sensitivity of results towards these changes in models, and verify that the model being selected is the optimal choice. Hence, a sensitivity analysis for physical parameters was conducted to see the effects of changes in these parameters on force and stress results. If results change greatly with slight changes in parameters, then the researcher needs to be careful about the uncertainty involved with that parameter before making a decision.

2.1 Material Flow Stress Models

Flow stress model is one of the most important parameters in FE-based simulations. This model determines the amount of stress on any element depending on the strain and strain rate at the current temperature. Initial flow stress model used was the original Johnson-Cook model (Model 1 - Eq. 6.1), which took into account changes in all three parameters (strain, strain rate, temperature) and resulted in such stresses. However, this primitive flow stress model, despite covering basics of the process (particularly at low strain amounts – $\varepsilon<0.3$) such as strain rate hardening, cannot handle some of the physical behavior of materials. These include strain (or flow) softening (that happens at higher

strains – ε>>0.3), and strain rate hardening at higher strains. In addition, while machining, high straining causes machining temperature to rise, and at higher temperatures, material softens because of a different phenomenon called "flow softening". As its nature requires, at higher temperatures, flow softening is more effective compared to lower temperatures.

In order to handle these phenomena, modifications (such as Eq. 6.2 and Eq. 6.3) to the original Johnson-Cook flow stress model have been developed. With the second model (Model 2 - Eq. 6.2), flow softening is included in the material flow stress model through a tangent hyperbolic function, and amount of flow softening can be adjusted by the factor *D*. However, despite the fact that the material flow stress model is temperature-dependent, the flow-softening model involved within it is independent of temperature changes. Therefore, although giving an edge to the original model with the flow softening model, its effects on different temperatures cannot be adjusted properly as required by the process. In the third model (Model 3 - Eq. 6.3), same flow softening model is kept, but its flow softening is now dependent on material's temperature. An additional term was also introduced in order to increase the effect of flow softening. Comparison of these flow stresses in graphical form can be found in Figure 6.1 where the effect of each change can be observed.

$$\sigma = [A + B\varepsilon^n]\left[1 + Cln\frac{\dot{\varepsilon}}{\dot{\varepsilon}_0}\right]\left[1 - \left(\frac{T-T_0}{T_m-T_0}\right)^m\right] \quad \text{(Eq. 6.1)}$$

$$\sigma = [A + B\varepsilon^n]\left[1 + Cln\frac{\dot{\varepsilon}}{\dot{\varepsilon}_0}\right]\left[1 - \left(\frac{T-T_0}{T_m-T_0}\right)^m\right]\left[D + (1-D)\left[\tanh\left(\frac{1}{(\varepsilon+p)^r}\right)\right]^S\right] \quad \text{(Eq. 6.2)}$$

$$\sigma = \left[A + B\varepsilon^n\left(\frac{1}{exp(\varepsilon^a)}\right)\right]\left[1 + Cln\frac{\dot{\varepsilon}}{\dot{\varepsilon}_0}\right]\left[1 - \left(\frac{T-T_r}{T_m-T_r}\right)^m\right]\left[D_2 + (1-D_2)\left[\tanh\left(\frac{1}{(\varepsilon+p_2)^r}\right)\right]^S\right] \quad \text{(Eq. 6.3)}$$

where $D_2 = 1 - \left(\frac{T}{T_m}\right)^d$, and $p_2 = \left(\frac{T}{T_m}\right)^b$.

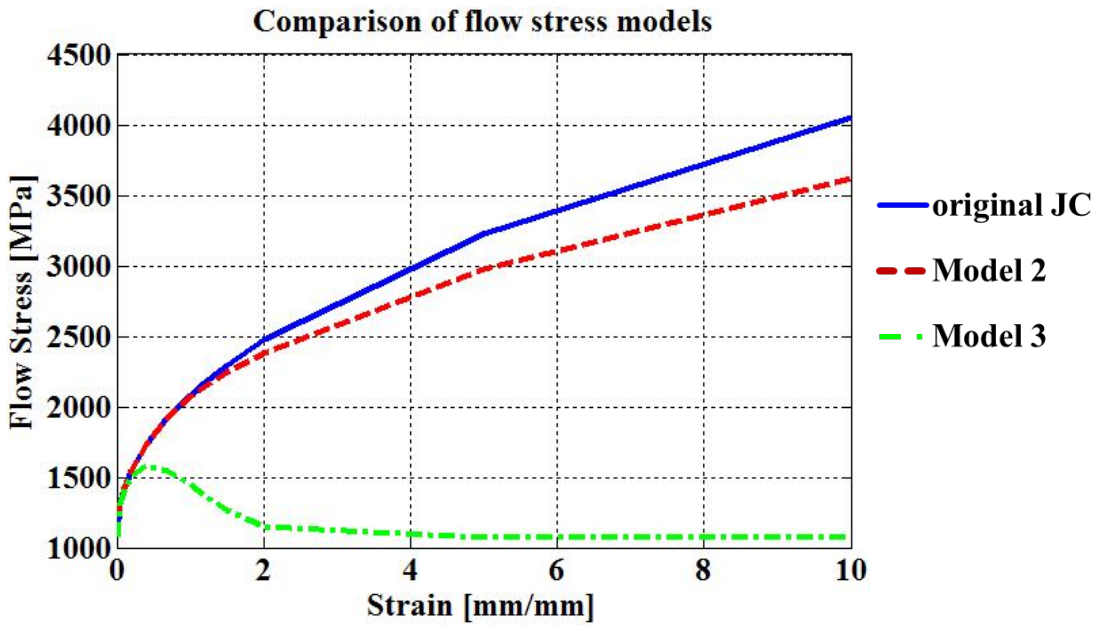

Figure 6.1: Comparison of flow stress models (sample graph for IN-100)

Although it was anticipated that the third model (which handles the process in the most complex way) would give the best results and thus was utilized in the process, the other two models were also tested in order to understand the effect of material flow stress models on the force and residual stress predictions. Original Johnson-Cook (JC) material model parameters are gathered using Split-Hopkinson Pressure Bar (SHPB) tests, so these experimental results were not altered in either that model or the other models. Different parameter sets for the second and third models were utilized to find the sets that give the best results compared to the experimental results. However, since the flow stress parameter determination methodology described in Chapter 5 was only utilized for the third model, the comparison reflects the optimized third model with non-optimized second model. A better comparison between the second and third models is presented in the Material Deformation Assumption section. The method that was described in Chapter 5 to find errors between experimental and predicted forces and residual stresses was utilized in order to get representative numbers for all models, and these results are

presented in Table 6.1. Figure 6.2 also shows the effect of the model change on different output parameters, where it can also be observed that the third model results in the least amount of error between experimental and simulated findings. Furthermore, since it takes a considerable amount of time to simulate all conditions, only one set of parameters was simulated for all models as a representative condition. This condition was selected from the Ti-64 simulations, but in order to be able to compare the residual stresses, simulations with higher feed (t_u=0.1 mm) were considered.

From the four possible machining conditions for Ti-64, the set of parameters that gave a median amount of error was selected in order to minimize the bias toward any of the models, which was the uncoated carbide tool with 25 µm cutting edge radius, machined at 55 m/min cutting speed. From these results, one can conclude that using the third model was the best choice of the three, and using the other two (less complex) models would have given results that are not as compliant as the third model with the experimental results.

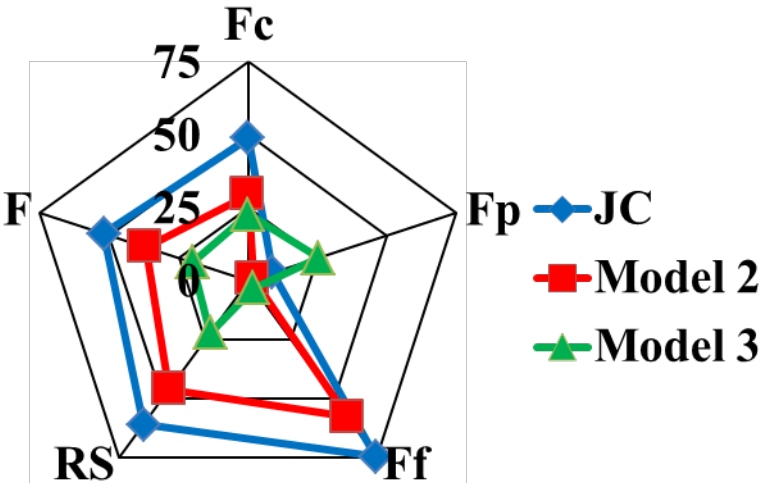

Figure 6.2: Effect of flow stress models on force and residual stress results in Ti-64 (Plastic)

2.2 Material Flow Stress Model Parameters

Once decided on the flow stress model, it is possible, and also essential, to fine tune the model parameters to achieve the best possible results. Methodology to determine flow stress model parameters is discussed in detail in Chapter 5. Original JC model parameters are gathered from SHPB tests and they are retrieved from literature for different materials. Therefore, parameters *A*, *B*, *C*, *m*, and *n* are initially not changed during this study. However, modified model parameters *a, b, d, r*, and *s* are modified several times in order to get the best results, and parameters *B* and *n* were also changed slightly. Despite they were changed many times, only results of a selection of best sets are presented in terms of residual stress and force findings. Four best sets of parameters are given in Table 6.2, and their effects on forces and residual stresses can be found in Table 6.3, as well as in Figure 6.3. According to these results, it was finalized that Set 4 is the best set to use for Ti-64 in terms of force and residual stress match. Although Set 1 also gave a similar amount of error, Set 4 was selected because its *A* parameter was unchanged. A similar study was also conducted for IN-100, and parameters presented in Chapter 5 were obtained accordingly. Obtained sets of parameters from these studies were utilized in final FE-based simulations to achieve residual stress predictions to be optimized.

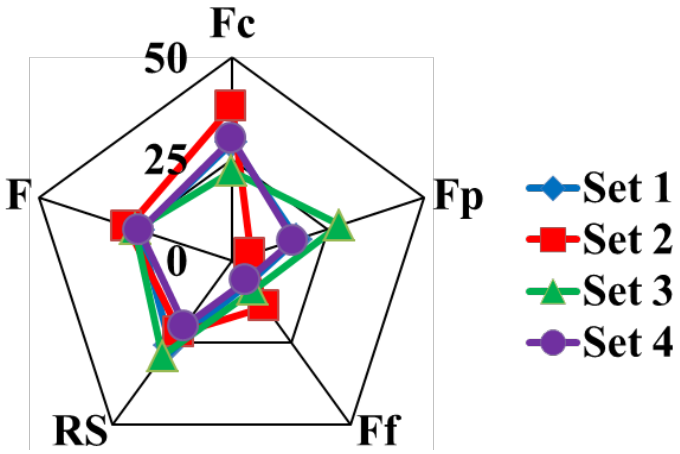

Figure 6.3: Effect of flow stress model parameter sets on force and residual stress results in Ti-64 (Model 3 - Plastic)

2.3 Friction Models

The friction model described in Chapter 3 corresponds to the hybrid friction model in DEFORM. This hybrid model combines effects of Coulomb and shear friction models to create a stick and slide friction condition. The software automatically determines the translation between two models, making the hybrid model work. However, it is also possible to utilize these two models separately, as Coulomb friction, or shear friction model only. Using Coulomb friction, shear friction, or a hybrid model utilizing both of these friction models changes the results. In reality, these friction models act together, so using a hybrid friction model makes more sense in terms of illustrating the process correctly. Also, since using hybrid friction does not increase run time of simulations, there is no burden of taking advantage of this opportunity. As it can be observed from Table 6.4 as well as Figure 6.4, hybrid friction model results in less error in predictions, while simulations are found sensitive to the used friction model. Hence, employing hybrid friction model is strongly suggested, and this approach is used in the simulations.

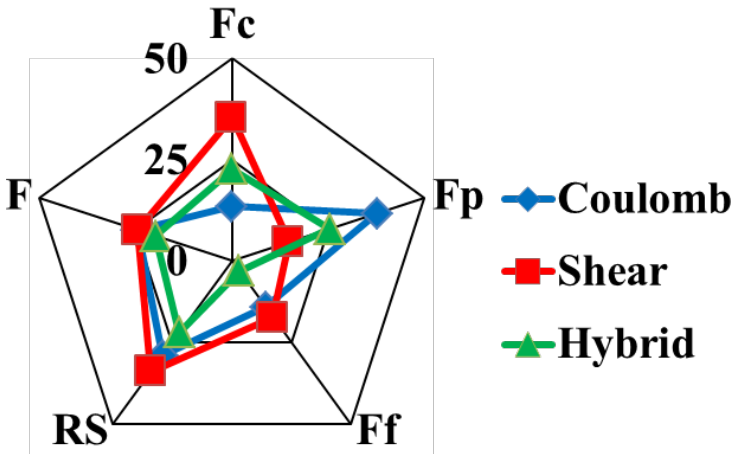

Figure 6.4: Effect of friction model on force and residual stress results in Ti-64 (Model 3 - Plastic)

2.4 Friction Coefficients

Although friction coefficients are determined using the friction determination method proposed in Chapter 3, effects of small changes in friction coefficients should also be investigated to understand the importance of these coefficients, as well as making sure the methodology works in the best interest of the study. For most simulations, very small changes in friction coefficients (less than 10%) do not affect results significantly. However, if the friction coefficients are changed significantly, results also change accordingly.

For this purpose, friction coefficients presented in Chapter 4 were changed in both positive and negative directions in incremental amounts to understand their effects on output parameters. Effect of friction factor, which was not calculated but rather assumed, can be found in Table 6.5 and Figure 6.5, whereas effect of rake (μ_1) and flank (μ_2) face friction coefficient can be found in Tables 6.6-6.7 and Figures 6.6-6.7, respectively. According to these results, it can be deduced that, changing m from 0.9 to 0.8 does not affect results significantly. While changing rake face friction coefficient (μ_1) in 0.1

increments did not make a significant impact either, changing it more increased errors significantly, confirming the findings of the friction determination methodology (Figure 6.6). In the case of flank face friction coefficient, while increasing it affected results negligibly, decreasing it made results significantly worse (Figure 6.7). In conclusion, friction factor and coefficients utilized in the simulations were results of good educated guesses and accurate model of friction coefficient determination.

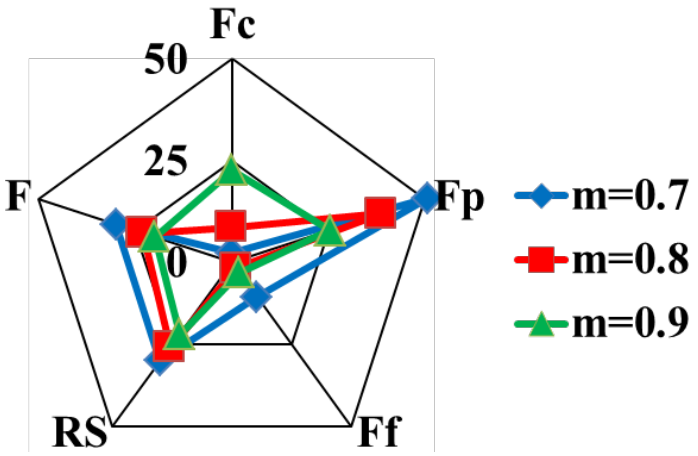

Figure 6.5: Effect of shear friction factor on force and residual stress results in Ti-64 (Model 3 - Plastic) (μ_1=0.6, μ_2=0.5)

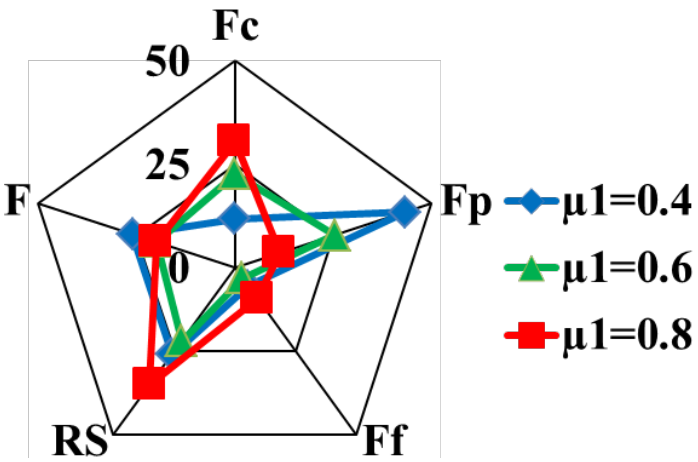

Figure 6.6: Effect of rake face friction coefficient on force and residual stress results in Ti-64 (Model 3 - Plastic) (m=0.9, μ_2=0.5)

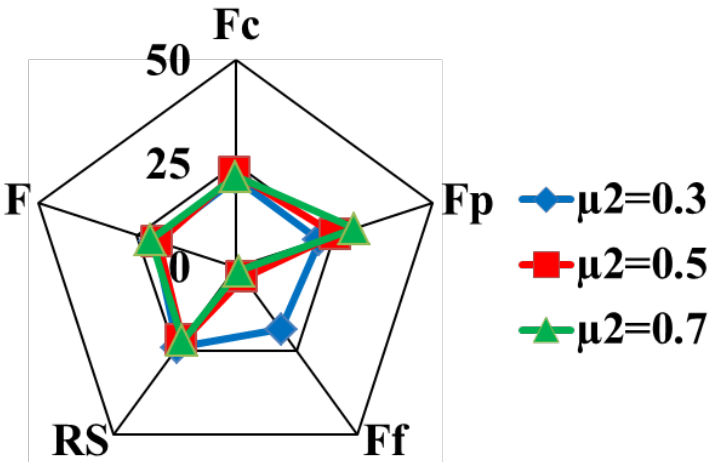

Figure 6.7: Effect of flank face friction coefficient on force and residual stress results in Ti-64 (Model 3 - Plastic) (m=0.9, μ_1=0.6)

2.5 Material Deformation Assumption (plastic vs. elastic-viscoplastic)

Assumptions of material deformation models represent how well the physical process in machining operations is illustrated within the simulations. As mentioned before in Chapter 4, elastic-viscoplastic model is the closest assumption to the physical phenomenon of machining. Hence, whenever possible, this model is selected for use. However, due to software limitations, this model cannot be used for every simulation, and it is also observed that for the simulations within this study, 3D elastic-viscoplastic simulations do not succeed regularly. Therefore, plastic material deformation model is assumed for regular 3D simulations. On the other hand, in order to observe how much this assumption affects force and residual stress results and be confident in the simulations with plastic assumption, effect of material deformation model assumption on the results are studied. Table 6.8 and Figure 6.8 show the effect of changing from viscoplastic to elastic-viscoplastic material deformation assumption with two different models (Model 2 and Model 3) of flow stress.

According to these results, the difference between plastic and elastic-viscoplastic assumptions was not significant for Model 3; in fact the plastic model assumption had less error in residual stresses. For Model 2 (see parameters used at Table 6.9), the difference was more apparent, and the benefit of using the elastic-viscoplastic model can be seen clearly. Although the improved accuracy with plastic assumption was probably only a coincidence due to the amount of uncertainty involved within predictions, it is safe to conclude from these results that elastic-viscoplastic material deformation assumption was not required during these simulations for Model 3, which is the model used for all simulations. This is a very important finding, as the elastic-viscoplastic simulations take considerably (~3-4 times) more time and disk space than plastic simulations. Since there is not a significant benefit of using the elastic-viscoplastic assumption, the significantly extra time requirement to run simulations is not worth exploring.

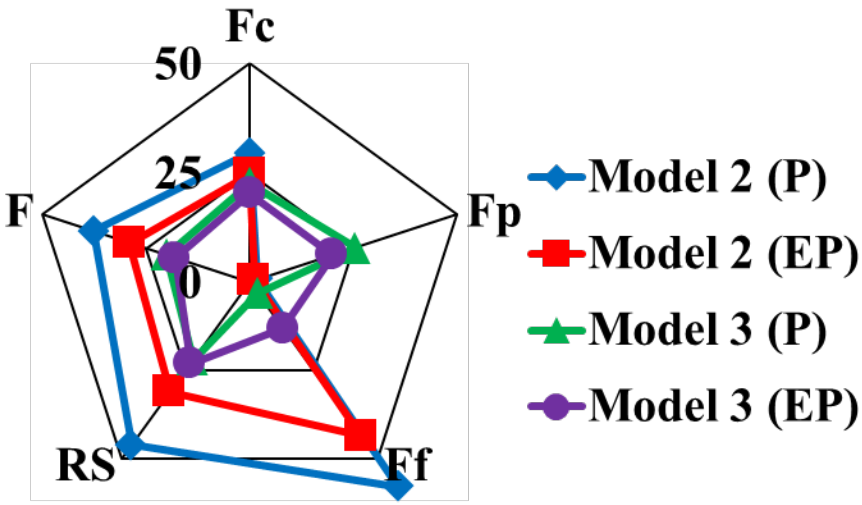

Figure 6.8: Effect of material deformation assumption on force and residual stress results in Ti-64

2.6 Heat Transfer Coefficient

Heat transfer coefficient is the constant that effects how fast heat is permeated through any material. This rate of heat transfer should not affect the results, but only should affect how fast the results are achieved. Hence, a very high heat transfer coefficient (in the order of 10^5 compared to the actual value in the order of 10^2) is assumed in order to accelerate the simulations. However, the assumption that heat transfer coefficient does not affect results should be verified. Therefore, simulations were repeated with different heat transfer coefficients (h=10^2-10^3-10^4) than the value used in the regular simulations (10^5) to understand this effect. With h=10^4, it took a considerably longer time (2 milliseconds compared to 0.8 milliseconds) to reach steady-state forces, which caused the simulations to take longer. With heat transfer coefficient decreasing even further to h=10^3 and 10^2, steady-state forces were not achieved by the end of simulations. If the simulations are designed and conducted with much bigger workpiece geometries, these simulations probably would reach steady-state forces, despite being in a considerably longer time. However, this is not feasible with the current technology.

Comparison of results can be found in Table 6.10 and Figure 6.9, which show an insignificant change between h=10^4 and 10^5, whereas the other two sets give much less forces. This is merely due to force components not reaching steady-state, and these results do not reflect a direct comparison. The lack of difference between h=10^4 and 10^5 shows that heat transfer coefficient does not have a significant effect on the simulation results, but it speeds up the thermal loading. It does not affect chip formation, so any value greater than 100,000 is not needed. With a higher value, chip would still be formed around 1 millisecond, although temperature would achieve a steady-state somewhat

earlier, which would not be beneficial without proper chip formation. Therefore, larger values of heat transfer coefficient are unnecessary, and the benefits of smaller values of heat transfer coefficient are deemed insignificant, considering the time and computational power requirements that nullify the worth.

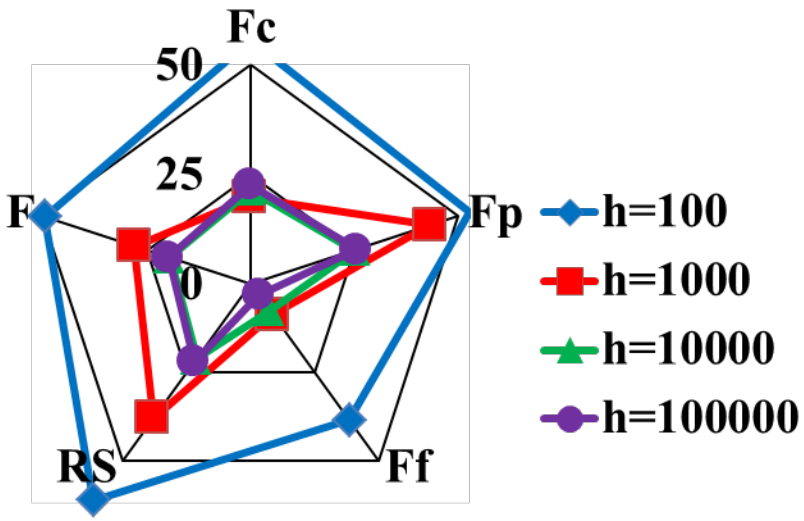

Figure 6.9: Effect of heat transfer coefficient on force and residual stress results in Ti-64 (Model 3 - Plastic)

3. Sensitivity on Numerical Parameters

In every numerical analysis, numerical parameters have some effects on results of the simulations. It is important to find an optimal set of parameters where simulation time is small enough to be worth the simulations, but numerical parameters have minimal amount of effect on simulation results as well. As in most numerical analyses, temporal and spatial increment amounts as well as error tolerances are the most important numerical parameters that affect the results of simulations. Therefore, in this section, effects of changing mesh size (size of elements), as well as force error tolerances on results are investigated. Effect of time step increment parameter was not studied, since the software automatically sets this parameter depending on convergence.

3.1 Mesh Size

The mesh is the most important numerical parameter in machining simulations. It has to be of enough quality to allow correct calculation of outputs and also chip formation. In order to increase quality, size of the mesh can be increased (number of elements being used) so that for the same volume, more elements can represent the physics of the process. However, this creates computer capacity problems after a certain value, so different methods are utilized in order to optimize the mesh size. For example, the mesh is usually more concentrated on the region where process parameters have more important changes (such as where tool and workpiece contact). Thus, these regions are defined as having more elements (denser mesh) and the other regions are defined as having fewer elements (coarser mesh).

Despite these efforts, higher number of elements could be required in order to achieve better convergence and/or better results. After analyzing the requirements of the process as well as simulations, N=50,000 was decided to be the optimal number of elements. This assumption required validation through a sensitivity analysis, so doubling and halving the number of elements was tried. Results of this analysis can be found in Table 6.11 and in Figure 6.10, and it can easily be observed that with lower number of elements (N=25,000), there is a slight but noticeable spike in errors of both force and residual stress outputs. Moreover, simulation time is about 80-85% of the original simulations with N=50,000 elements. Thus, it can be concluded that decreasing number of elements is not optimal. Meanwhile, increasing number of elements to N=100,000 did not increase the accuracy of results significantly, where force and residual stress errors were very similar. However, simulation time increased to approximately 250% of the

original simulations, which suggests that this increase is not required in these simulations. Therefore, original simulations with *N*=50,000 elements are at (or very close to) the optimal point in terms of number of elements being used.

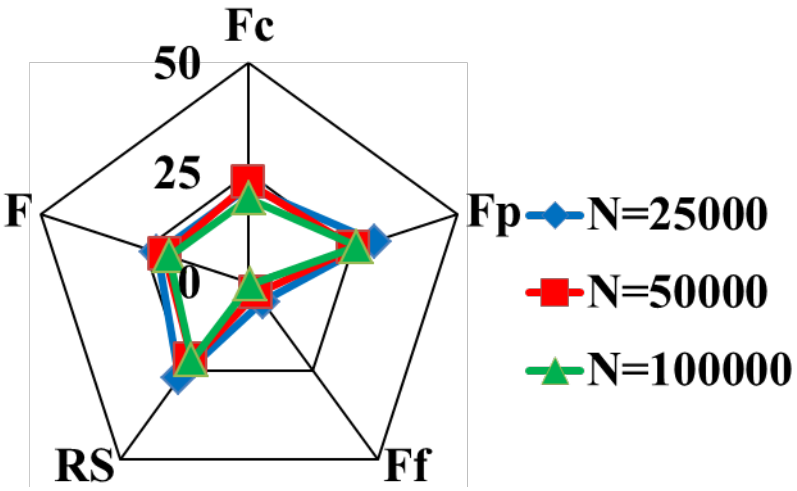

Figure 6.10: Effect of mesh size on force and residual stress results in Ti-64 (Model 3 - Plastic)

3.2 Force Error Tolerances

During simulations, at each step, forces at every element are calculated. Then, forces at neighboring elements are compared. Since they represent the same physical location, the forces should be the same. However, due to computational variances, these forces cannot be exactly the same. The difference between these elements can cause error build up, so the software includes a force error tolerance parameter that prevents force error between two neighboring elements to be bigger than a certain value. When this tolerance is exceeded, the software recalculates forces at those elements until forces that result in error lower than force error tolerance are achieved. This parameter should not be set too high so that accuracy of simulation results is not sacrificed, but it should not be set too low to avoid convergence problems.

In the original simulations, this tolerance was set to 0.01, meaning that until forces are within 0.01 N of each other at neighboring elements, calculations would go on for each step. In order to understand the sensitivity of results and computing time to this parameter, this tolerance was doubled and halved, and results can be seen in Table 6.12 and Figure 6.11. These results show that outputs were not affected greatly by force error tolerance. However, computing time increased approximately 50% with decreasing error tolerance, while decreasing about 20% with increasing error tolerance. Since there is not too much difference between outputs, the prudent choice is to select the highest tolerance that solves the simulations the fastest. However, it should be noted that these are results for plastic simulations. With elastic-viscoplastic material deformation assumption, high force error tolerances lead to significantly more amount of issues, whereas with lower tolerances, with increased accuracy, simulations tend to run more smoothly.

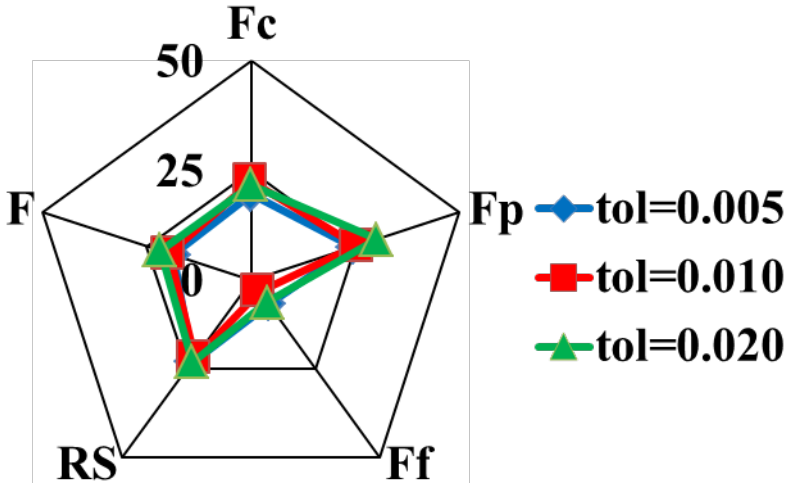

Figure 6.11: Effect of force error tolerance on force and residual stress results in Ti-64 (Model 3 - Plastic)

4. Conclusions

Finite Element-based simulations provide many advantages over excessive experimentation, but physical parameters inputted to these simulations as well as the numerical parameters should be selected carefully. As in most numerical methods, convergence and computation time are the two major concerns against accuracy. Parameters that can be altered to improve the accuracy of predictions usually cause convergence issues or require too much computational power that cannot be satisfied easily. Hence, compromising values of parameters are used so that the process is best illustrated but it is still convergent. To this end, material flow stress models and parameters, friction models and coefficients, material deformation assumption, and heat transfer coefficient were analyzed, as well as mesh size and force error tolerances, and the best values for these parameters are determined. Simulations were then designed and conducted according to these findings, and force and residual stress results were gathered. These predicted forces and residual stresses are then compared to experimental findings, and the process is optimized according to these predictions. This optimization work is described in the next chapter, while the simulations have been explained in Chapters 4 & 5.

Table 6.1: Effect of material flow stress models on the force and residual stress results (Ti-64) (Plastic)

	Circumferential Residual Stress				Radial Residual Stress				Forces						Error	
	Peak Tensile		Peak Compressive		Peak Tensile		Peak Compressive		Experimental			Simulated			RS	Force
	Exp	Sim	Exp	Sim	Exp	Sim	Exp	Sim	F_c	F_p	F_f	F_c	F_p	F_f		
	MPa	MPa	MPa	MPa	MPa	MPa	MPa	MPa	N	N	N	N	N	N	%	%
JC	247	314	58	79	54	213	333	197	777	456	161	1157	496	281	**61**	**52**
Model 2	247	289	58	104	54	171	333	267	777	456	161	1006	447	254	**46**	**37**
Model 3	247	252	58	114	54	86	333	323	777	456	161	953	340	166	**22**	**20**

Table 6.2: Best sets of modified Johnson-Cook material flow stress model parameters (Ti-64)

Set	A	B	n	C	m	a	b	d	r	s
Set 1	500	300	0.65	0.035	1	0.5	2	0.5	15	-0.05
Set 2	600	300	0.65	0.035	1	0.5	2	0.5	12	-0.05
Set 3	600	300	0.65	0.035	1	0.5	2	0.5	15	-0.05
Set 4	725	300	0.65	0.035	1	0.5	2	0.5	12	-0.05

Table 6.3: Effect of material flow stress model parameters on the force and residual stress results (Ti-64) (Model 3 - Plastic)

	Peak Tensile	Peak Compressive	F_c	F_p	F_f	Total RS Error	Total Force Error
	%	%	%	%	%	%	%
Set 1	21	30	29	17	7	**26**	**24**
Set 2	20	24	38	5	14	**22**	**27**
Set 3	24	33	22	28	9	**29**	**25**
Set 4	23	15	30	16	6	**20**	**24**

Table 6.4: Effect of friction models on the force and residual stress results (Ti-64) (Model 3 - Plastic)

	Circumferential Residual Stress				**Radial Residual Stress**				**Forces**						**Error**	
	Peak Tensile		**Peak Compressive**		**Peak Tensile**		**Peak Compressive**		**Experimental**			**Simulated**			**RS**	**Force**
	Exp	**Sim**	**Exp**	**Sim**	**Exp**	**Sim**	**Exp**	**Sim**	F_c	F_p	F_f	F_c	F_p	F_f		
	MPa	MPa	MPa	MPa	MPa	MPa	MPa	MPa	N	N	N	N	N	N	%	%
Coulomb (μ_1=0.6)	247	224	58	95	54	81	333	197	777	456	161	881	284	138	**29**	**25**
Shear (m=0.9)	247	244	58	104	54	121	333	339	777	456	161	1052	388	189	**34**	**24**
Hybrid (μ_1=0.6, m=0.9)	247	252	58	114	54	86	333	323	777	456	161	953	340	166	**22**	**20**

Table 6.5: Effect of friction factor (m) on the force and residual stress results (Ti-64) (Model 3 - Plastic)

	Circumferential Residual Stress				**Radial Residual Stress**				**Forces**						**Error**	
	Peak Tensile		**Peak Compressive**		**Peak Tensile**		**Peak Compressive**		**Experimental**			**Simulated**			**RS**	**Force**
	Exp	**Sim**	**Exp**	**Sim**	**Exp**	**Sim**	**Exp**	**Sim**	F_c	F_p	F_f	F_c	F_p	F_f		
	MPa	MPa	MPa	MPa	MPa	MPa	MPa	MPa	N	N	N	N	N	N	%	%
m=0.7	247	208	58	129	54	98	333	284	777	456	161	795	224	144	**30**	**30**
m=0.8	247	221	58	117	54	96	333	296	777	456	161	844	279	158	**26**	**23**
m=0.9	247	252	58	114	54	86	333	323	777	456	161	953	340	166	**22**	**20**

Table 6.6: Effect of rake face friction coefficient (μ_1) on the force and residual stress results (Ti-64) (Model 3 - Plastic)

	Circumferential Residual Stress				**Radial Residual Stress**				**Forces**						**Error**	
	Peak Tensile		**Peak Compressive**		**Peak Tensile**		**Peak Compressive**		**Experimental**			**Simulated**			**RS**	**Force**
	Exp	**Sim**	**Exp**	**Sim**	**Exp**	**Sim**	**Exp**	**Sim**	F_c	F_p	F_f	F_c	F_p	F_f		
	MPa	MPa	MPa	MPa	MPa	MPa	MPa	MPa	N	N	N	N	N	N	%	%
μ_1=0.4	247	238	58	124	54	68	333	259	777	456	161	869	258	152	**26**	**26**
μ_1=0.5	247	221	58	108	54	88	333	295	777	456	161	908	301	154	**22**	**22**
μ_1=0.6	247	252	58	114	54	86	333	323	777	456	161	953	340	166	**22**	**20**
μ_1=0.7	247	269	58	119	54	79	333	309	777	456	161	995	376	177	**23**	**20**
μ_1=0.8	247	248	58	98	54	142	333	392	777	456	161	1014	404	176	**35**	**20**

Table 6.7: Effect of flank face friction coefficient (μ_2) on the force and residual stress results (Ti-64) (Model 3 - Plastic)

	Circumferential Residual Stress				**Radial Residual Stress**				**Forces**						**Error**	
	Peak Tensile		**Peak Compressive**		**Peak Tensile**		**Peak Compressive**		**Experimental**			**Simulated**			**RS**	**Force**
	Exp	**Sim**	**Exp**	**Sim**	**Exp**	**Sim**	**Exp**	**Sim**	F_c	F_p	F_f	F_c	F_p	F_f		
	MPa	MPa	MPa	MPa	MPa	MPa	MPa	MPa	N	N	N	N	N	N	%	%
μ_2=0.3	247	228	58	101	54	91	333	317	777	456	161	944	359	131	**24**	**21**
μ_2=0.5	247	252	58	114	54	86	333	323	777	456	161	953	340	166	**22**	**20**
μ_2=0.7	247	239	58	126	54	88	333	341	777	456	161	947	318	163	**22**	**22**

Table 6.8: Effect of material deformation assumption on the force and residual stress results (Ti-64)

	Circumferential Residual Stress				**Radial Residual Stress**				**Forces**						**Error**	
	Peak Tensile		**Peak Compressive**		**Peak Tensile**		**Peak Compressive**		**Experimental**			**Simulated**			**RS**	**Force**
	Exp	**Sim**	**Exp**	**Sim**	**Exp**	**Sim**	**Exp**	**Sim**	F_c	F_p	F_f	F_c	F_p	F_f		
	MPa	MPa	MPa	MPa	MPa	MPa	MPa	MPa	N	N	N	N	N	N	%	%
Plastic (Model 2)	247	289	58	104	54	171	333	267	777	456	161	1006	447	254	**46**	**37**
Elasto-plastic (Model 2)	247	278	58	79	54	125	333	303	777	456	161	969	467	231	**31**	**29**
Plastic (Model 3)	247	252	58	114	54	86	333	323	777	456	161	953	340	166	**22**	**20**
Elasto-plastic (Model 3)	247	259	58	88	54	110	333	312	777	456	161	934	365	182	**23**	**18**

Table 6.9: Material model parameters used in simulations (Model 2)

Alloy	***A*[MPa]**	***B*[MPa]**	***n***	***C***	***m***	***D***	***p***	***r***	***s***
Ti-6Al-4V	1000	625	0.55	0.029	0.995	0.48	0	1.2	2.7

Table 6.10: Effect of heat transfer coefficient (h) on the force and residual stress results (Ti-64) (Model 3 - Plastic)

	Circumferential Residual Stress				**Radial Residual Stress**				**Forces**						**Error**	
	Peak Tensile		**Peak Compressive**		**Peak Tensile**		**Peak Compressive**		**Experimental**			**Simulated**			**RS**	**Force**
	Exp	**Sim**	**Exp**	**Sim**	**Exp**	**Sim**	**Exp**	**Sim**	F_c	F_p	F_f	F_c	F_p	F_f		
	MPa	MPa	MPa	MPa	MPa	MPa	MPa	MPa	N	N	N	N	N	N	%	%
h=10^2	247	162	58	31	54	119	333	156	777	456	161	344	216	99	**61**	**50**
h=10^3	247	184	58	51	54	100	333	203	777	456	161	624	259	147	**38**	**28**
h=10^4	247	254	58	108	54	89	333	319	777	456	161	944	342	149	**21**	**20**
h=10^5	247	252	58	114	54	86	333	323	777	456	161	953	340	166	**22**	**20**

Table 6.11: Effect of mesh size (*N*) on the force and residual stress results (Ti-64) (Model 3 - Plastic)

	Circumferential Residual Stress				**Radial Residual Stress**				**Forces**						**Error**	
	Peak Tensile		**Peak Compressive**		**Peak Tensile**		**Peak Compressive**		**Experimental**			**Simulated**			**RS**	**Force**
	Exp	**Sim**	**Exp**	**Sim**	**Exp**	**Sim**	**Exp**	**Sim**	F_c	F_p	F_f	F_c	F_p	F_f		
	MPa	MPa	MPa	MPa	MPa	MPa	MPa	MPa	N	N	N	N	N	N	%	%
N=25000	247	218	58	106	54	112	333	315	777	456	161	946	318	152	**27**	**22**
N=50000	247	252	58	114	54	86	333	323	777	456	161	953	340	166	**22**	**20**
N=100000	247	251	58	109	54	91	333	318	777	456	161	925	337	162	**22**	**19**

Table 6.12: Effect of error tolerances on the force and residual stress results (Ti-64) (Model 3 - Plastic)

	Circumferential Residual Stress				**Radial Residual Stress**				**Forces**						**Error**	
	Peak Tensile		**Peak Compressive**		**Peak Tensile**		**Peak Compressive**		**Experimental**			**Simulated**			**RS**	**Force**
	Exp	**Sim**	**Exp**	**Sim**	**Exp**	**Sim**	**Exp**	**Sim**	F_c	F_p	F_f	F_c	F_p	F_f		
	MPa	MPa	MPa	MPa	MPa	MPa	MPa	MPa	N	N	N	N	N	N	%	%
tol=0.005	247	237	58	105	54	92	333	315	777	456	161	929	344	172	**23**	**19**
tol=0.010	247	252	58	114	54	86	333	323	777	456	161	953	340	166	**22**	**20**
tol=0.020	247	242	58	105	54	83	333	382	777	456	161	946	318	171	**23**	**22**

CHAPTER 7

MULTI-OBJECTIVE OPTIMIZATION

1. Introduction

In this chapter, work regarding multi-objective optimization of input parameters is discussed. After analyzing the sensitivity of the important numerical and physical parameters on outputs, the parameter set that gives the optimal results in optimal time is selected. Then, finite element simulations are designed and conducted for that set of parameters, and the results are gathered for every machining condition. After these simulations are finished and their results obtained, the objective of this chapter is to optimize these results in terms of multiple objective functions that are important in the industry in order to find the optimal decision variables, which are the machining parameters. The results from experimental findings are also optimized in a similar fashion to show a comparison between the two, however, since the simulations are validated (as described in the previous chapters), it is important to discuss the optimization results based on simulations.

Objective functions used in industrial applications may vary depending on requirements of each process. For most processes, the material removal rate determines the efficiency of the manufacturing process, so maximizing this rate is very important. When a tool wears rapidly, it needs frequent changing, which reduces this rate. In order to prevent rapid tool wear, machining forces should be kept low. Also, keeping machining forces low enables better surface quality due to lower surface roughness.

Because of these reasons, total force (resultant force) is an important factor in machining processes, and minimizing the total force is an essential objective.

In addition, tensile surface residual stresses cause crack formation and propagation in the end-part, which adversely affects the fatigue life of the end product. This means that with increasing tensile surface residual stresses, reliability of the product decreases. Therefore, it is important to minimize surface residual stresses. On the other hand, compressive peak residual stresses at ~30-60 μm deep into material are known to provide better dimensional accuracy to the end product. This means that with increasing compressive peak residual stresses (decreasing residual stress value since compressive means negative), better tolerances are achieved. Therefore, it is also essential to maximize compressive peak residual stresses.

Finally, experimental values of residual stresses have some uncertainty due to machine accuracy or measurement uncertainties. These uncertainties multiply when the simulation results are validated with experimental findings, as the simulations add more sources of uncertainty. However, it is essential to know the amount of residual stress (at the tensile or compressive peak value) so that it can be decreased or increased according to the requirements of the process. With high uncertainty, researchers are left with difficult choices that are more reliant on experience and educated guesses rather than scientific findings. Therefore, it is essential to minimize the uncertainties associated with these simulation findings of tensile and compressive peak residual stresses.

All of the objective functions are important in different aspects of manufacturing. To this end, this chapter proposes using a multi-objective optimization scheme rather than a single-objective function. In order to handle this multi-objective optimization, the

particle swarm optimization procedure was selected and employed in optimizing process parameters. Objectives are solved for minimizing tensile residual stresses on the surface, maximizing peak compressive residual stresses, minimizing total force component during machining, and minimizing the variance of residual stresses in order to increase certainty in the predictions. The optimum machining parameters corresponding to this multi-objective optimization are represented in both objective function and decision variable spaces.

2. Development of Predictive Models

Using Finite-Element simulations, a rich set of computational results were generated, as the software allows data collection at different steps that represent the stochastic nature of the simulation medium. Then, averages of the results were found to represent the expected values, and standard deviations of the results were calculated using a normal distribution. Using experimental results as well as the simulation results, a second order generic regression model is developed to form relationships between input and output variables, as given in Eq. (7.1). Here, β_i (i=1,2…) represent regression coefficients and ε is the residual error. This generic form is then modified to understand the effects of cutting speed (V_c) and edge radius (r_β) on the outputs such as the expected values of resultant force (F), peak tensile and circumferential residual stresses (PTS and PCS), as well as the standard deviation of the residual stress measurements and simulations. Hence, the equations become as Eq. (7.2), where the output variables are presented in Eq. 7.3, and the resultant coefficients are presented in Table 7.1. It must be noted that since there are only two levels of cutting speed (V_c), the coefficient for the square term that belongs to that input variable (β_{11}) is always zero. Table 7.1 also shows

the R^2 values for each variable that show how good the regression coefficients fit the data, and it can be observed that most of them have over 90% R^2 values. This model can be easily extended with further experimentation to include other machining parameters such as feedrate (t_u), depth of cut (a_p), rake angle (γ_1), tool wear (VB), and tool material and coating.

$$y = \beta_0 + \sum_{i=1}^{k} \beta_i x_i + \sum_{i=1}^{k} \beta_{ij} x_i x_j + \sum_{i=1}^{k} \beta_{ii} x_i^2 + \square \qquad \text{(Eq. 7.1)}$$

$$y = \beta_0 + \beta_1 V_c + \beta_2 r_\beta + \beta_{12} V_c * r_\beta + \beta_{11} V_c^2 + \beta_{22} r_\beta^2 + \varepsilon \qquad \text{(Eq. 7.2)}$$

$$y = E[F],\ E[PTS],\ E[PCS],\ \text{or}\ \sigma[PTS\&PCS] \qquad \text{(Eq. 7.3)}$$

Table 7.1: Model parameters for the response

Variable Factors	**Experimental Results**							
		Circumferential		**Radial**		**Combination**		
	F	PTS_{cm}	PCS_{cm}	PTS_{rm}	PCS_{rm}	PTS_m	PCS_m	σ_{std}
β_0	585	1069	206	1289	248	1105	-28	48.9
β_1	8.24	-34.8	-22.2	-48.5	-145	-36.8	-17.8	-1.34
β_2	-4.42	38	-46.3	-42.3	32.9	7.31	-6.27	4.48
β_{12}	0.40	-1.26	1.39	0.82	0.91	-0.43	0.25	-0.12
β_{22}	-0.61	0.73	0.38	1.56	-0.43	0.93	-0.08	0.003
R^2	99.8	99.5	93.9	95.9	97.6	98.3	95.5	100.0
	Simulation Results							
β_0	595	792	-17.6	1087	-132	873	-72.9	-74.7
β_1	5.02	-21.7	-6.58	-35.4	-6.49	-24.4	-6.67	6.53
β_2	-2.23	32	-49.5	-42	-26.8	3.16	-38.3	26.9
β_{12}	0.19	-1.03	1.38	1.39	0.79	0.05	1.08	-0.28
β_{22}	-0.30	0.53	0.38	0.72	0.24	0.48	0.32	-0.64
R^2	95.8	98.7	63.5	90.9	81.0	95.0	69.3	97.6

3. Multi-Objective Optimization

3.1 Objective Functions

In machining processes, many objective functions can be defined, since there are many industrial constraints and requirements. In the first years of industrial manufacturing, the main concern was the material removal rate, which represents the machining time and production speed. In order to increase the production speed, and hence increase the industrial profits, increasing the cutting speed, feedrate, and depth of cut were the initial priorities. When any (or all) of these parameters were increased, the production will speed up in a directly proportional manner, and higher number of products could be manufactured in unit time.

However, increasing cutting speed, feedrate, and depth of cut brought other problems, which created constraints for this initial objective. When these three parameters were increased, the tool started to wear more rapidly, which meant that the tool tip required a change more frequently. Hence, the manufacturing time was decreased, but set-up time was increased. Hence, it was necessary to decrease these values so that tool wear could be decreased, and an optimal point for all four parameters could be achieved. Another idea was coined that changing the tool geometry (rake angle and cutting edge radius) also minimized tool wear for most materials, and that needed investigation as well.

It was also found out by researchers that tool wear, as well as increased machining parameters caused excessive heat building up during the machining process, which also negatively affected the tool wear results. In addition, all of these parameters also influenced the machining forces, which created difficulties in machining and needed

to be handled. Therefore, in addition to changes in tool geometry, researchers also considered to add a coating to the tool to decrease the heat build-up, which became advantageous for select conditions.

After years of manufacturing, the primitive problems regarding machining processes have been determined and solved, and researchers look into methods to increase end product quality. Two major interpretations of product quality are dimensional accuracy and product reliability. In order to achieve both goals, surface integrity of the end product needs to be studied, and the major contributors of surface integrity are the residual stresses, microhardness, and surface roughness. Within these measures, surface roughness is focused more on the surface quality, which affects dimensional accuracy, and has been studied excessively by researchers. Microhardness affects more on the sub-surface quality, which affects product reliability. Residual stresses, on the other hand, affect both surface and sub-surface quality, and the work on the effects of machining parameters on residual stresses has not been conclusive so far. Therefore, this study targets to fulfill this need by developing a multi-objective optimization that is concerned with adjusting residual stresses occurring during machining processes.

Residual stresses during machining usually occur in a hook-shaped manner. At the surface, residual stresses are observed to be tensile (positive), and the amount of positivity affects the surface quality. After a certain depth into the material, these stresses are found to be negative, and this depth is called the machining-affected zone thickness. After this depth, the residual stresses make a compressive (negative) peak. Finally, ~100 μm deep into the end product, the residual stresses level at a near-zero value. The

positive peak at the surface is directly related by researchers to the possibility of crack initiation during product usage and therefore reliability of the product under loading conditions. Therefore, it is important to decrease this value to a minimum. Also, the residual stresses at the compressive peak are considered to be beneficial against fatigue failure of the product, so maximizing the negativity of this peak is yet another objective.

Furthermore, measurements and predictions of residual stress (and also forces) carry high amounts of uncertainty due to machining conditions. Due to these uncertainties, reliability prediction of the end products is adversely affected. Therefore, other than optimizing the mean value of the two parameters, the uncertainty of the predictions should also be minimized. The variance of predictions can be calculated and the minimizing input parameters can be selected in order to reduce these uncertainties in the output parameters.

3.2 Multi-Objective Particle Swarm Optimization

Although it is significantly easier to consider any one of the objective functions listed in the previous section, industrial applications usually require handling of more than one objective function at a time. In order to conduct optimization of multiple objective functions, Particle Swarm Optimization (PSO) method, an evolutionary computation method similar to genetic algorithms, is utilized. This technique has been applied to many complex systems in order to find quick solutions for decision making process, including machining systems (Karpat & Özel 2007, Ciurana et al. 2009, Özel et al. 2011).

In a similar study (Özel et al. 2011), multi-objective optimization of objective functions of minimizing surface roughness and burr width in micro-milling process was

investigated using regression models and particle swarm optimization. In this technique, a population of random solutions to the system is first initiated, and then the evolution of these solutions toward the optimal input set is observed over generations. Different than genetic algorithms (GA), PSO particles do not die or mutate, but instead move in the decision variable space freely with velocities that change over generations. In multi-objective PSO (MOPSO), there is more than one objective, so it is possible to lead to more complex Pareto fronts. However, the results have to be non-dominated, which means no optimal solution can have higher values in all dimensions than any other optimal solution.

When the initial population is generated, each particle is assigned a position and a velocity in the decision variable space. By considering previous position and current velocity of particles, a new particle position is found at every generation (Eq. 7.4). Accordingly, particle velocity is updated by considering previous velocity and acceleration terms (Eq. 7.5), where x_i^k is the position and ,v_i^k is the velocity for particle *i* at generation *k*, $pbest_i$ is the best personal solution of particle *i*, *gbest* is the best global solution ever encountered throughout population, c_i are the fixed acceleration terms for the personal and global bests, $rand_i$ are the random numbers in [0,1] to introduce stochastic effects of acceleration terms, *w* is the weighting function for the previous velocity term, and δ is a random number in [-1,1] used in avoiding local minima. The random values were determined separately for each coordinate, as these coordinates are independent from each other.

At the initial steps, *w* is set at a relatively higher value to make sure initial accelerations do not spread all particles in the decision variable space. At the later

generations, this value is decreased so that particles can have more freedom in searching for possible better solutions, while the global best is stored. At each generation, objective functions are computed for current positions, and if personal or global best values change, they are updated. These generations are stopped when the algorithm reaches a predetermined iteration number, or there is no further movement of *pbest* values of particles. At each generation, when the velocities are updated, velocities are bounded in predetermined maximum and minimum values in order to prevent uncontrolled increase in velocities that causes instabilities in the search algorithm. Likewise, particle positions can never leave the decision variable space boundaries.

$$x_i^{k+1} = x_i^k + v_i^{k+1} \quad \text{(Eq. 7.4)}$$

$$v_i^{k+1} = \omega v_i^k + c_1 rand_1\left(pbest_i - x_i^k\right) + c_2 rand_2\left(gbest - x_i^k\right) + \delta \quad \text{(Eq. 7.5)}$$

When the optimal Pareto front is found, the optimum machining parameters corresponding to this multi-objective optimization are represented in both objective function and decision variable spaces. A brief formulation of optimization work proposed can be given as Eq. 7.6, where $f_1(\mathbf{x}), f_2(\mathbf{x}), \dots, f_k(\mathbf{x})$ represent the aforementioned objective functions and $g_j(\mathbf{x}), h_j(\mathbf{x})$ are the constraints and process limitations with a set of decision variables ($\mathbf{x} = x_1, \dots, x_n$) (i.e. *n* number of process parameters). **X** is the solution space with all feasible values for the process parameters.

$$\begin{aligned} &\text{min. (or max.)} && \{f_1(\mathbf{x}), f_2(\mathbf{x}), \dots, f_k(\mathbf{x})\} \\ &\text{subject to} && g_j(\mathbf{x}) \le b_j \text{ for j} = 1,2, \dots, \text{m}, \\ &\text{and} && h_j(\mathbf{x}) = b_j \text{ for j} = \text{m}+1, .., \text{m}+\text{p}, \ \mathbf{x} \in \mathbf{X} \end{aligned} \quad \text{(Eq. 7.6)}$$

4. Results and Discussions

In order to apply the multi-objective optimization algorithm, results for the nickel-based alloy IN-100 were selected. This is because experimental values for this material in both force and residual stress measurements are considered to be more reliable, and it is possible to use two cutting speeds (V_c=12 & 24 m/min) and three different cutting edge radii (r_β=5, 10 & 25 μm). While utilizing the Particle Swarm Optimization algorithm, each simulation was run with a population size of 1000 for 100 generations. The algorithm was also set to stop if three consecutive generations resulted in the same location of the whole population, which was activated after securing the first 20 generations. This made sure that the particle motion converged before stopping, but also allowed to halt a simulation if the optimal Pareto front is obtained before 100 generations. The full simulation of 100 generations took approximately 20 minutes on a PC with Pentium Dual Core processor until reaching to an acceptable solution.

Furthermore, although it is possible to use all four objective functions (expected values of resultant force, peak tensile surface residual stress and peak compressive residual stress, and standard deviation of residual stresses), it is possible to visualize three objective functions in 3-dimensional space. Therefore, the results are presented in two different scenarios. In both of them, two dimensions are peak tensile and peak compressive residual stresses in MPa. In the first scenario (Figure 7.1), the third dimension is the resultant force in N. Figure 7.1 shows the Pareto front belonging to these three objective functions in objective function space as well as the decision variable space. Figure 7.2, on the other hand, shows the second scenario, where the third dimension is the standard deviation of residual stresses rather than the resultant force,

similarly showing the Pareto front in both objective function space as well as the decision variable space. Both of the figures compare measured and simulated forces and residual stresses in order to validate the results of simulations. In order to compare residual stresses, resultant residual stress values were utilized by vector summing the circumferential and radial residual stresses which are orthogonal to each other. Once the simulations are validated, Figure 7.3 shows the Pareto fronts of simulated circumferential and radial residual stresses according to the second scenario, where the third axis is the collective standard deviation of residual stresses.

Figure 7.1 shows that in the objective function space, with resultant force on the third axis, simulations and experiments are aligned with each other. Decision variable space not only supports but strengthens this suggestion, as the Pareto fronts lie on the same line. It can be observed that when resultant force is lower (blue for measurements and black for simulations), peak compressive residual stress decreases (becomes less negative) and peak tensile residual stress increases, which are both not favorable. With resultant force getting slightly higher, peak compressive residual stress increases (becomes more negative) and peak tensile residual stress decreases, so that location might be the best solution for the decision maker. In any case, a higher cutting speed (at V_c=24 m/min) was favored by both measurements and simulations, and in order to get lower resultant force, higher cutting edge radius was favored. With lower cutting edge radius, it was observed that although higher resultant force was faced, peak tensile residual stresses were obtained, which might be of interest for a specific application where tool wear, material removal rate, and surface roughness are not as important as product reliability.

Figure 7.2 shows, both in objective function space and the decision variable space, more difference between the measurements and simulations. However, since the errors associated with the measurements were significantly less than the errors associated with the simulations, the standard deviation of results made an important difference in the behavior of the Pareto fronts. The measurements, with the standard deviation being considerably lower and more or less the same value throughout the findings, favored less uncertainty and smaller peak tensile residual stress at higher cutting speed (blue circles), but with slightly increasing values in these two, the peak compressive residual stress became much lower (more negative), favoring lower cutting speeds (red circles). The optimal cutting edge radius in terms of these three objective functions for measurement results was found to be approximately r_β=18 μm. However, for the simulations, standard deviation values were much higher and changing throughout the Pareto front. For these results, lower cutting speeds favored lower uncertainty, while with increasing cutting speed, peak compressive residual stress increased (became more negative), and peak tensile residual stresses decreased, although the standard deviation of the findings increased. These two figures show that the four objective functions utilized are conflicting with each other, which makes it not possible to come up with a single solution, but rather a set of solutions that all are optimal for some objectives. It is then up to the decision maker to determine which point on this set of solutions, or the Pareto front, is going to be the solution for the specific application.

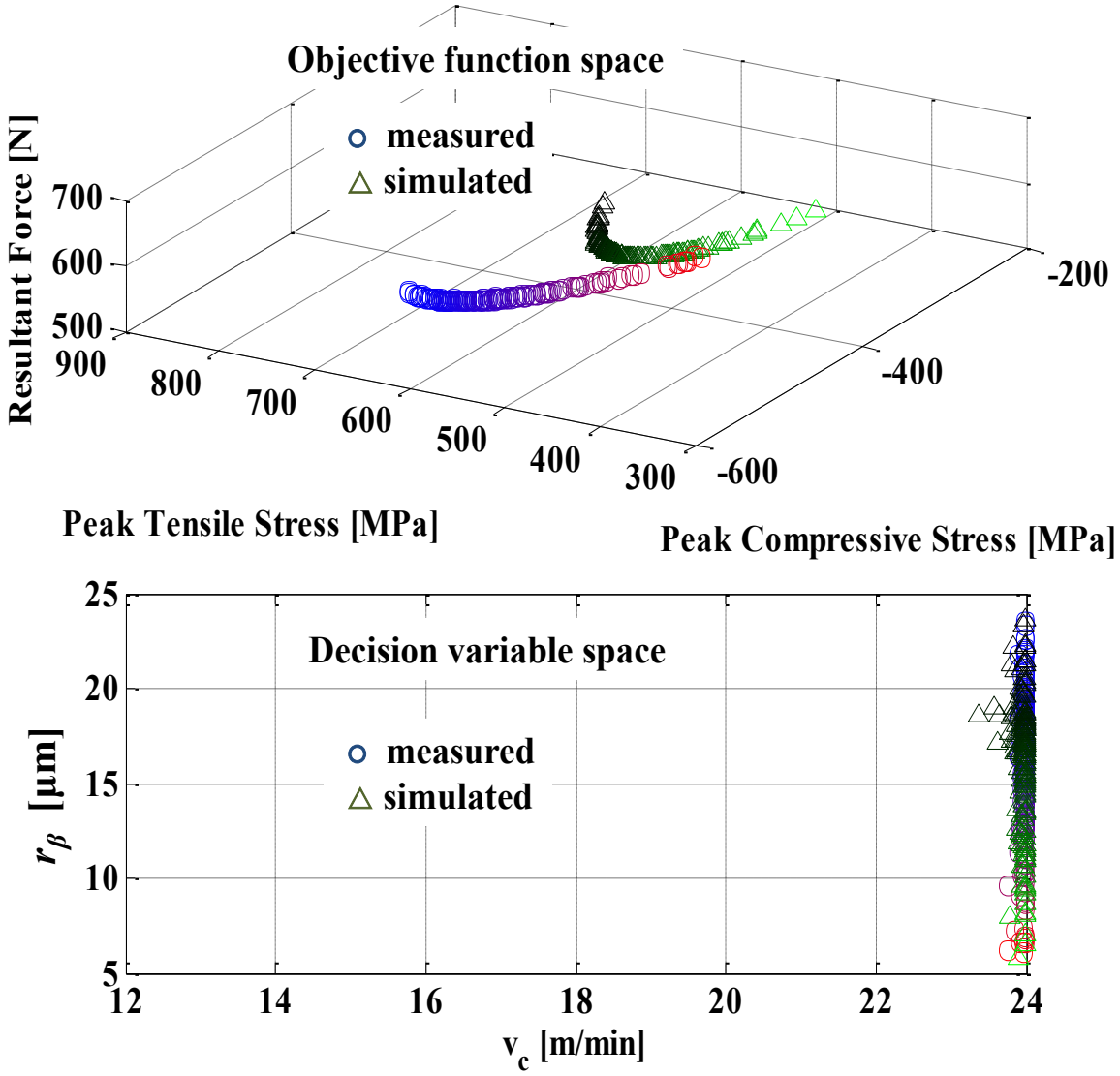

Figure 7.1: Comparison of optimum solutions for minimizing measured and simulated stresses with minimizing resultant force

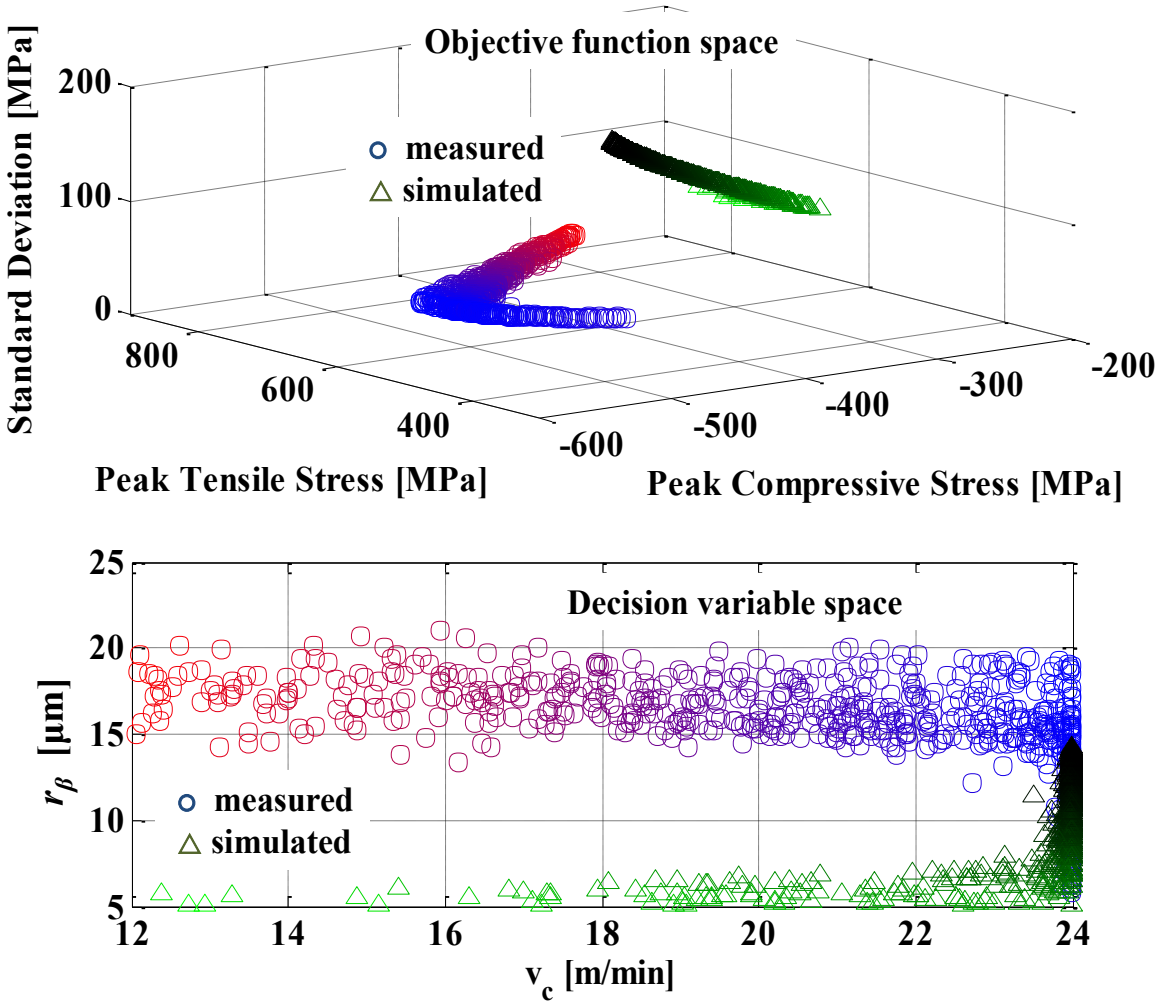

Figure 7.2: Comparison of optimum solutions for measured and simulated stresses with minimizing standard deviation

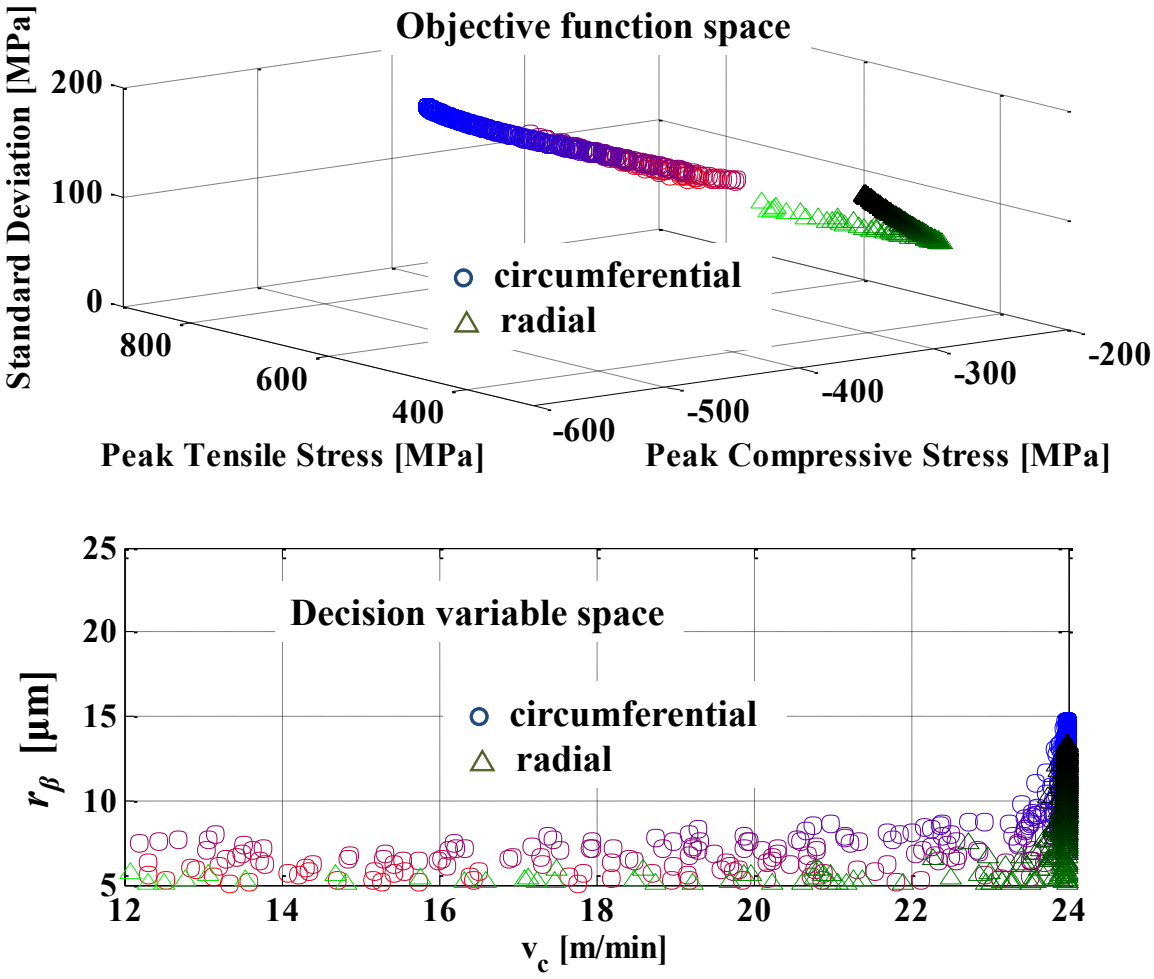

Figure 7.3: Comparison of optimum solutions for simulated circumferential and radial stresses with minimizing standard deviation

Once the simulations were validated with the experiments, circumferential and radial components of peak tensile and peak compressive residual stresses were also investigated. Figure 7.3 shows the comparison for these two in terms of simulated results. It can be observed that the high amount of standard deviation in the results in mainly due to the circumferential component of the residual stresses, and this separates the two Pareto fronts. Since the circumferential and radial components of residual stresses are not supposed to be the same, the two graphs are not directly comparable. However, both components of residual stress were observed to favor lower cutting speeds

for lower uncertainty (green triangles and red circles), but with increasing cutting speed (black triangles and blue circles), peak tensile residual stress decreased and peak compressive residual stress increased (became more negative). Both components of residual stress preferred comparably lower cutting edge radii for the whole Pareto front, staying lower than 15 μm at all times. Hence, the two components acted in the same manner toward changes in the two input parameters, although their values are different from each other.

5. Conclusions

In this chapter, the multi-objective particle swarm optimization algorithm and its results were presented. The results of experiments and simulations for machining IN-100 alloy were utilized in order to find the Pareto fronts of optimal solutions in terms of expected values of resultant force, peak tensile residual stress, and peak compressive residual stress, as well as the collective standard deviation of residual stresses. Results show that the simulations and measurements suggest the same Pareto fronts when the uncertainty of findings is not considered. However, with the inclusion of the standard deviations, since simulations have considerably more uncertainty compared to the experiments, the results vary slightly. However, the general trends are observed to be similar. It was decided that while for lower resultant forces, cutting edge radius was favored; for the sake of the other three objective functions, lower cutting edge radii were favored. Furthermore, lower cutting speeds were favored only for smaller uncertainty in the results, but for the other three objective functions, highest possible cutting speeds were favored.

CHAPTER 8

CONTRIBUTIONS AND FUTURE WORK

Motivation of this dissertation is in understanding the effects of friction, flow stress, tool material, coating and geometry and machining parameters on the mechanics of metal cutting especially prediction of machining induced stresses on the workpiece surface. Titanium alloy Ti-6Al-4V (Ti-64) and nickel-based alloy IN-100 were the main focus of this study, although the findings can be expanded to other materials as well. The main objectives of this study were to establish a methodology to determine the friction coefficients on the rake and flank faces of the tool with a round edge during machining, and utilizing these coefficients, design Finite Element (FE)-based simulations that have the capability of illustrating machining processes, decreasing the dependence on experimentation, and optimize the machining parameters using the results of these predictions. In terms of machining parameters, different cutting speeds, feedrates, rake angles and tool edge preparations were utilized. For the tool edge, sharp tools were used, as well as tools with variable round edge preparation. For the sharp tools, coated and uncoated options were investigated to understand the effect of tool coating. Main contributions of this study towards these objectives can be listed as follows.

1. Experimental Analysis of Orthogonal Machining and Face Turning (Chapter 2)
    - Orthogonal machining experiments of Ti-64 and IN-100 were conducted, and the results were analyzed. Although not fully applicable to industrial applications, these experiments provide an understanding of the machining

process and guidance towards machining parameters. The results of these experiments are later utilized in the development and implementation of the friction determination methodology.

- Face turning experiments on Ti-64 and IN-100 were conducted. These experiments are applicable to the industry, therefore they provide useful experimental data as the effect of machining parameters. Measured force results of these experiments are later utilized in flow stress parameter determination methodology, as well as for validation purposes of FE-based simulations (Özel & Ulutan 2012, Sima et al. 2011).

2. Residual Stress Measurement (Chapter 2)
    - Residual stresses were measured on machined Ti-64 disks in radial and circumferential directions using the X-ray diffraction method. Residual stresses on machined IN-100 disks were outsourced for measurement and later analysis. These measurements are utilized in the comparison of residual stress findings from FE-based simulations (Özel & Ulutan (2012).
3. Development of Friction Determination Methodology (Chapter 3)
    - A methodology to determine the friction coefficients on the tool rake and flank faces was introduced. The friction coefficients during machining of Ti-64 and IN-100 workpiece materials were utilized for further use. Different machining parameters were investigated in terms of cutting speed, feed, cutting edge radius, and tool rake angle, and friction coefficients were found to be mostly constant for different combinations of

parameters (Ulutan & Özel 2012a, Ulutan et al. 2011, Ulutan & Özel 2013a).

- Change in the location of stagnation point during machining was studied. During machining processes, chip and machined workpiece flow in different directions. While the chip is flowing on the tool rake face, machined workpiece flows on the tool flank face, creating a point of stagnation on the edge face of the tool. The location of this point is significant, as it may lead to the location of tool wear (Ulutan & Özel 2013a).

4. Stress-Based Modeling and Analysis of Orthogonal Machining (Chapter 4)
    a. Orthogonal machining experiments were illustrated utilizing 2D updated Lagrangian software DEFORM-2D. These simulations represent the experimental conditions, and aid to determine the friction coefficients via the friction determination methodology. They provide a validation of stress distributions on the tool rake and flank faces, as well as an understanding of change of residual stresses with changing machining forces (Ulutan et al. 2011).
5. Determination of Flow Stress Model Parameters for Temperature-Dependent Flow Softening-Based Modified Constitutive Material Model (Chapter 5)
    - Flow stress is one of the most important inputs to the FE-based simulations. Different types of flow stress models were studied, including the original Johnson-Cook material model, modified Johnson-Cook material model with flow softening, and temperature-dependent flow

softening-based constitutive material model. Among these models, the third one represents the dynamic material behavior best, so this model was utilized in the final simulations. The parameters of this model were determined by utilizing the force results of FE-based simulations that are compared to the experimental values (Ulutan & Özel 2013b).

6. Modeling and Analysis of Face Turning (Chapter 5)
    - Face turning experiments were illustrated utilizing 3D updated Lagrangian software DEFORM-3D. These simulations provide an understanding of the change of parameters in the industrial applications. They are validated via experimental force results and then their findings in terms of residual stresses are compared against residual stress measurements (Özel & Ulutan 2012, Sima et al. 2011).
7. Sensitivity Analysis of Physical and Numerical Parameters Related to FE-Based Simulations (Chapter 6)
    - FE-based simulations have multiple parameters that affect the results of the simulation predictions. These parameters can be physical parameters as well as numerical, and the sensitivity of the simulations on the change of these parameters was investigated. Time and computational power requirements of the parameters are also studied for a thorough understanding of their effects, and the optimal values of parameters are obtained (Ulutan & Özel 2013b).

8. Multi-Objective Particle Swarm Optimization of Machining Processes (Chapter 7)

    - For machining processes, there are many objectives. These can be the machining forces, amount of tool wear, machining temperatures, or surface integrity-related objectives after the machining is finished. These surface integrity-related objectives can be related to residual stresses, microhardness change, machining-affected zone thickness, surface roughness, and other aspects of surface quality. In this study, objectives of minimizing total machining force and minimizing the tensile peak residual stresses were determined as the first priority, as they are related to tool wear (and hence material removal rate – efficiency), and end product reliability. In addition, maximizing the compressive peak residual stresses was added as an additional objective, as it is related to dimensional accuracy of the end product. Furthermore, residual stress errors (measurement or prediction) related to experimental results as well as FE-based simulations were considered to be another important objective, as they show the uncertainty related to the machining process, either experimental or simulation related. These multiple objectives were optimized by utilizing a Particle Swarm Optimization algorithm and were realized in objective and decision variable spaces (Ulutan & Özel 2012b).

Based on aforementioned contributions of this dissertation, some possible future directions can be listed as follows.

1. Experimental analysis given in Chapter 2 can be expanded for different machining parameter sets. In particular, higher cutting speeds and feeds can be investigated, as these would increase the material removal rate, hence the efficiency of machining. This aspect has an important part in the industrial applications. For the same reasons, different depth/width of cut values can also be studied. Also, different tool geometries (rake angle and cutting edge radius) can be studied for further understanding of their effects on machining outputs. Different workpiece materials such as the nickel-based alloy IN-718, as well as different tool materials and coating materials and application types can be studied to expand the material database the study covers. Residual stress measurements can be expanded for better understanding on the stress outputs.
2. Friction Determination Methodology given in Chapter 3 can be expanded with more experimental analysis for various different sets of machining parameters. Also, tool wear amount (VB) can be added as a searched parameter rather than a constant value. Alternatively, different (progressive) values of VB can be used to conduct the same analysis multiple times to understand the effect of tool wear evolution on friction coefficients. Furthermore, the friction factor (m) can be added to the hybrid friction study as another parameter to be searched.
3. With expanding machining conditions, FE-based simulations given in Chapters 4 & 5 can be also expanded to cover more different sets of parameter ranges. 2D simulations presented in Chapter 4 can be conducted with the modified flow stress

parameters that belong to temperature-dependent flow softening-based constitutive material model (Model 3) to increase the accuracy of the Friction Determination Methodology. 3D simulations presented in Chapter 5 can be conducted with elastic-viscoplastic material deformation assumption, especially with developing software and computational power capabilities for better representation of the machining processes.

4. Sensitivity analysis given in Chapter 6 can be expanded to different values of the parameters for a better understanding of the effects of these parameters. This way, it could be possible to locate local minima or maxima that might be missed during this study, although this requires a very thorough analysis that would take long time which may not be worth the incremental gains. The analysis can also be expanded to include combinations of parameters such as the effect of change in both friction coefficients on the rake and flank faces, rather than investigating them separately.
5. Multi-objective particle swarm optimization algorithm given in Chapter 7 can be expanded to include all results rather than just cutting speed and cutting edge radius, with more experimentation on residual stresses. In addition, tool coating or workpiece material can be added as integer (or Boolean) parameters to the algorithm for a more thorough investigation. Moreover, different types of multi-objective optimization algorithms can be utilized to analyze the result accuracy as well as time requirements of different algorithms.
6. In addition to residual stresses, many different surface integrity aspects can be integrated into the study. Microhardness change, microstructural alterations, white

layer formation, surface roughness, and burr formation are some surface integrity problems that can be studied. Also in addition to turning, milling and drilling processes can be studied for a more thorough understanding of the mechanics of other machining processes.

BIBLIOGRAPHY

Albrecht P. "New Developments in the Theory of the Metal-Cutting Process." *Transactions of the ASME – Journal of Engineering for Industry* (1960): 348-358.

Arrazola P. & Meslin F. "A Technique for the Identification of Friction at Tool/Chip Interface during Machining." *Proceedings of the Second Asia International Conference on Tribology* (2002).

Arrazola P. & Özel T. "Investigations on the Effects of Friction Modeling in Finite Element Simulation of Machining." *International Journal of Mechanical Sciences* 52 (2010): 31-42.

Arrazola P., Ugarte D. & Domínguez X. "A New Approach for the Friction Identification during Machining Through the Use of Finite Element Modeling." *International Journal of Machine Tools & Manufacture* 48 (2008): 173-183.

Arunachalam R.M., Mannan M.A. & Spowage A.C. "Surface Integrity When Machining Age Hardened Inconel 718 with Coated Carbide Cutting Tools." *International Journal of Machine Tools and Manufacture* 44 (2004): 1481-1491.

Arunachalam R.M, Mannan M.A. & Spowage A.C. "Residual Stress and Surface Roughness When Facing Age Hardened Inconel 718 with CBN and Ceramic Cutting Tools." *International Journal of Machine Tools & Manufacture* 44 (2004): 879-887.

Aspinwall D.K., Dewes R.C., Ng E.-G., Sage C. & Soo S.L. "The Influence of Cutter Orientation and Workpiece Angle on Machinability When High-Speed Milling Inconel 718 Under Finishing Conditions." *International Journal of Machine Tools & Manufacture* 47 (2007): 1839-1846.

Axinte D.A., Andrews P., Li W., Gindy N. & Withers P.J. "Turning of Advanced Ni Based Alloys Obtained via Powder Metallurgy Route." *Annals of the CIRP* 55 (2006).

Belassel M., Pineault J. & Brauss M.E. "Comparison and Evaluation of Residual Stress Measurement Techniques, A Technical and Economical Study." *Proceedings of the SEM Annual Conference & Exposition on Experimental & Applied Mechanics* 2 (2011): 756-762.

Bonnet C., Valiorgue F., Rech J., Claudin C., Hamdi H., Bergheau J.M. & Gilles P. "Identification of a Friction Model – Application to the Context of Dry Cutting of an AISI 316L Austenitic Stainless Steel with a TiN Coated Carbide Tool." *International Journal of Machine Tools & Manufacture* 48 (2008): 1211-1223.

Che-Haron C.H. & Jawaid A. "The Effect of Machining on Surface Integrity of Titanium." *Journal of Materials Processing Technology* 166 (2005): 188-192.

Che-Haron C.H. "Tool Life and Surface Integrity in Turning Titanium Alloy." *Journal of Materials Processing Technology* 118 (2001): 231-237.

Chen L., El-Wardany T.I. & Harris W.C. "Modeling the Effects of Flank Wear Land and Chip Formation on Residual Stresses." *CIRP Annals – Manufacturing Technology* 53.1 (2004): 95-98.

Childs T.H.C. "Friction Modeling in Metal Cutting." *Wear* 260 (2006): 310-318.

Childs T.H.C. "Numerical Experiments on the Influence of Material and Other Variables on Plane Strain Continuous Chip Formation in Metal Machining." *International Journal of Mechanical Sciences* 48 (2006): 307-322.

Chrzanowski W., Ali Abou Neel E., Armitage D.A. & Knowles J.C. "Effect of Surface Treatment on the Bioactivity of Nickel-Titanium." *Acta Biomaterialia* 4 (2008): 1969-1984.

Ciurana, J., Arias, G. & Özel, T. "Neural Network Modeling and Particle Swarm Optimization (PSO) of Process Parameters in Pulsed Laser Micromachining of Hardened AISI H13 Steel." *Materials and Manufacturing Processes* 24.3 (2009): 358-368.

Coelho R.T., Silva L.R., Braghini Jr. A. & Bezerra A.A. "Some Effects of Cutting Edge Preparation and Geometric Modifications When Turning Inconel 718 at High Cutting Speeds." *Journal of Materials Processing Technology* 148.1 (2004) 147–153.

Courbon C., Kramar D., Krajnik P., Pusavec F., Rech J. & Kopac J. "Investigation of Machining Performance in High-Pressure Jet Assisted Turning of Inconel 718: An Experimental Study." *International Journal of Machine Tools and Manufacture* 49 (2009): 1114-1125.

Darwish S.M. "The Impact of Tool Material and the Cutting Parameters on Surface Roughness of Supermet 718 Nickel Superalloy." *Journal of Materials Processing Technology* 97 (2000): 10–18.

Derrien S. & Vigneau J. "High Speed Milling of Difficult to Machine Alloys." in: D. Dudzinski, A. Devillez, A. Moufki, D. Larrouquerre, V. Zerrouki, J. Vigneau. A review of developments towards dry and high speed machining of Inconel 718 alloy, International Journal of Machine Tools and Manufacture 44 (2004) 439-456.

Dudzinski D., Devillez A., Moufki A., Larrouquerre D., Zerrouki V. & Vigneau J. "A Review of Developments Towards Dry and High Speed Machining of Inconel 718 Alloy." *International Journal of Machine Tools and Manufacture* 44 (2004) 439-456.

Ezugwu E.O. & Tang S.H. "Surface Abuse When Machining Cast Iron (G-17) and Nickel-Base Superalloy (Inconel 718) with Ceramic Tools." *Journal of Materials Processing Technology* 55 (1995): 63–69.

Ezugwu E.O., Wang Z.M. & Okeke C.I. "Tool Life and Surface Integrity When Machining Inconel 718 with PVD and CVD Coated Tools." *Tribology Transactions* 42.2 (1999): 353–360.

Fang N. "Slip-Line Modeling of Machining with a Rounded-Edge Tool – Part II: Analysis of the Size Effect and the Shear Strain-Rate." *Journal of the Mechanics and Physics of Solids* 51 (2003): 743-762.

Fang N. & Xiong L.S. "Determination of Friction and Material-Flow Boundary Conditions on the Tool Round Cutting Edge." *Transactions of NAMRI/SME* 36 (2008): 413-420.

Field M., Kahles J.F. & Koster W.P. "Surface Finish and Surface Integrity." USAF Technical Report AFML-TR-74-60 Metcut Research. Associates Inc., Cincinatti, Ohio, 1974.

GADDS User Manual (1999). Bruker Advanced X-Ray Solutions.

Ghanem F., Braham C., Fitzpatrick M.E. & Sidhom H. "Effect of Near-Surface Residual Stress and Microstructure Modification from Machining on the Fatigue Endurance of a Tool Steel." *Journal of Materials Engineering and Performance* 11.6 (2002): 631-639.

Ginting A. & Nouari M. "Surface Integrity of Dry Machined Titanium Alloys." *International Journal of Machine Tools & Manufacture* 49 (2009): 325-32.

Guerville L. & Vigneau J. "Influence of Machining Conditions on Residual Stresses." in: D. Dudzinski, A. Devillez, A. Moufki, D. Larrouquerre, V. Zerrouki, J. Vigneau. A review of developments towards dry and high speed machining of Inconel 718 alloy, International Journal of Machine Tools and Manufacture 44 (2004) 439-456.

Guo Y.B., Anurag S. & Jawahir I.S. "A Novel Hybrid Predictive Model and Validation of Unique Hook-Shaped Residual Stress Profiles in Hard Turning." *CIRP Annals - Manufacturing Technology* 58.1, (2009): 81-84.

Guo Y.B., Li W. & Jawahir I.S. "Surface Integrity Characterization and Prediction in Machining of Hardened and Difficult-to-Machine Alloys; A State-of-the-Art Research Review and Analysis." *Machining Science and Technology* 13 (2009): 437-470.

Hedenqvist P. & Olsson M. "Sliding Wear Testing of Coated Cutting Tool Materials." *Tribology International* 23.3 (1991): 143-150.

Jacobus K., DeVor R.E. & Kapoor S.G. "Machining-Induced Residual Stress: Experimentation and Modeling." *Journal of Manufacturing Science and Engineering* 122 (2000): 20-31.

Jemielniak K. "Finish Turning of Inconel 718." *Advances in Manufacturing Science and Technology* 33.1 (2009): 59-69.

Kalpakjian S. & Schmid S.R. "Manufacturing Processes for Engineering Materials." Prentice-Hall, 5th Edition (2007).

Karpat Y. & Özel T. "Multi-Objective Optimization for Turning Processes Using Neural Network Modeling and Dynamic-Neighborhood Particle Swarm Optimization."

International Journal of Advanced Manufacturing Technology 35.3-4 (2007): 234-247.

Kishawy H.A., Haglund A.J. & Deiab I.M. "An Analysis of Machining with Honed Tools Using ALE Finite Element Model: Ploughing Force and Minimum Chip Thickness." *Transactions of NAMRI/SME* 34 (2006): 277-284.

Kitagawa T., Kubo A., Maekawa K. "Temperature and Wear of Cutting Tools in High-Speed Machining of Inconel 718 and Ti-6Al-6V-2Sn." *Wear* 202 (1997): 142-148.

Kortabarria A., Madariaga A., Fernandez E., Esnaola J.A. & Arrazola P.J. "A Comparative Study of Residual Stress Profiles on Inconel 718 Induced by Dry Face Turning." *Procedia Engineering* 19 (2011): 228-234.

Li L., He N., Wang M. & Wang Z.G. "High Speed Cutting of Inconel 718 with Coated Carbide and Ceramic Inserts." *Journal of Materials Processing Technology* 129.1-3 (2002): 127–130.

Liao Y.S. & Shiue R.H. "Carbide Tool Wear Mechanism in Turning of Inconel 718 Superalloy." *Wear* 193 (1996): 16–24.

Lord J.D., Grant P.V., Fry A.T. & Kandil F.A. "A UK Residual Stress Intercomparison Exercise – Development of Measurement Good Practice for the XRD and Hole Drilling Techniques. *Materials Science Forum* 404-407 (2002): 567-572.

Lorentzon J., Järvstråt N. & Josefson B.L. "Modelling of Chip Formation of Alloy 718." *Journal of Materials Processing Technology* 209 (2009): 4645-4653.

Lu Y. & Guo C. "Finite Element Modeling of Multi-Pass Machining of Inconel 718." *CD Proceedings of 2009 ASME International Conference on Manufacturing Science and Engineering.* Paper No. 84086, October 5-7 (2009), Lafayette, Indiana, USA.

Mantle A.L. & Aspinwall D.K. "Surface Integrity and Fatigue Life of Turned Gamma Titanium Aluminide." *Journal of Materials Processing Technology* 72 (1997): 413-420.

Mantle A.L. & Aspinwall D.K. "Surface Integrity of a High Speed Milled Gamma Titanium Aluminide." *Journal of Materials Processing Technology* 118 (2001): 143-150.

Mitrofanov A.V., Babitsky V.I. & Silberschmidt V.V. "Finite Element Analysis of Ultrasonically Assisted Turning of Inconel 718." *Journal of Materials Processing Technology* 153-154 (2004): 233-239.

Molinari A., Cheriguene R. & Miguelez H. "Numerical and Analytical Modeling of Orthogonal Cutting: The Link between Local Variables and Global Contact Characteristics." *International Journal of Mechanical Sciences* 53 (2011): 183-206.

Moufki A., Molinari A. & Dudzinski D. “Modelling of Orthogonal Cutting with a Temperature Dependent Friction Law.” *Journal of the Mechanics and Physics of Solids* 46.10 (1998): 2103-2138.

M’Saoubi R., Outeiro J.C., Chandrasekaran H., Dillon Jr. O.W. & Jawahir I.S. “A Review of Surface Integrity in Machining and Its Impact on Functional Performance and Life of Machined Products.” *International Journal of Sustainable Manufacturing* 1.1-2 (2008): 203-236.

Nurul-Amin A.K.M., Ismail A.F. & Nor Khairusshima M.K. “Effectiveness of Uncoated WC-Co and PCD Inserts in End Milling of Titanium Alloy – Ti-6Al-4V.” *Journal of Materials Processing Technology* 192-193 (2007): 147-58.

Olsson M, Soderberg S., Jacobson S. & Hogmark S. “Simulation of Cutting Tool Wear by a Modified Pin-on-Disc Test.” *International Journal of Machine Tools & Manufacture* 29.3 (1989): 377-390.

Outeiro J.C., Pina J.C., M'Saoubi R., Pusavec F. & Jawahir I.S. “Analysis of Residual Stresses Induced by Dry Turning of Difficult-To-Machine Materials.” *CIRP Annals - Manufacturing Technology* 57.1 (2008): 77-80.

Österle W. & Li P.X. “Mechanical and Thermal Response of a Nickel-Base Superalloy upon Grinding with High Removal Rates.” *Materials Science and Engineering A* 238 (1997): 357-366.

Özel T. “The Influence of Friction Models on Finite Element Simulations of Machining.” *International Journal of Machine Tools & Manufacture* 46 (2006): 518-530.

Özel T. “Experimental and Finite Element Investigations on The Influence of Tool Edge Radius in Machining Nickel-Based Alloy,” *CD Proceedings of 2009 ASME International Conference on Manufacturing Science and Engineering*, Paper No. 84362, October 5-7, 2009, Lafayette, Indiana, USA.

Özel T., Llanos I., Soriano J. & Arrazola P.J. “3D Finite Element Modelling of Chip Formation Process for Machining Inconel 718: Comparison of FE Software Predictions.” *Machining Science and Technology* 15.1 (2011): 21-46.

Özel T., Sima M., Srivastava A.K. & Kaftanoglu K. “Investigations on the Effects of Multi-Layered Coated Inserts in Machining Ti-6Al-4V Alloy with Experiments and Finite Element Simulations.” *CIRP Annals – Manufacturing Technology* 59.2 (2010): 77–82.

Özel, T., Sima, M., Ulutan, D. & Srivastava, A.K. “Collaborative Research: Improving Machinability of Titanium Alloys Using Physics-Based Simulation Modeling.” *2011 NSF Engineering Research and Innovation Conference* (2011), Atlanta, Georgia.

Özel, T. & Ulutan, D. “Prediction of Machining Induced Residual Stresses in Turning of Titanium and Nickel Based Alloys with Experiments and Finite Element Simulations,” *CIRP Annals - Manufacturing Technology* 61.2 (2012): 547-550.

Özel, T., Yıldız, S., Sima, M.D. & Srivastava, A. "Collaborative Research: Improving Machinability of Titanium Alloys using Physics-Based Simulation Modeling," *CD Proceedings of 2009 NSF Engineering Research and Innovation Conference*, Honolulu, Hawaii, Grant #0758220.

Özel T. & Zeren E. "Finite Element Modeling the Influence of Edge Roundness on the Stress and Temperature Fields Induced by High-Speed Machining." *International Journal of Advanced Manufacturing Technology* 35 (2007): 255-267.

Özlü E., Budak E. & Molinari A. "Analytical and Experimental Investigation of Rake Contact and Friction Behavior in Metal Cutting." *International Journal of Machine Tools & Manufacture* 49.11 (2009): 865-875.

Pawade R.S., Joshi S.S., Brahmankar P.K. & Rahman M. "An Investigation of Cutting Forces and Surface Damage in High-Speed Turning of Inconel 718." *Journal of Materials Processing Technology* 192-193 (2007): 159-146.

Pawade R.S., Sonawane H.A. & Joshi S.S. "An Analytical Model to Predict Specific Shear Energy in High-Speed Turning of Inconel 718." *International Journal of Machine Tools and Manufacture* 49 (2009): 979-990.

Pawade R.S. Joshi S.S. & Brahmankar P.K. "Effect of Machining Parameters and Cutting Edge Geometry on Surface Integrity of High-Speed Turned Inconel 718." *International Journal of Machine Tools and Manufacture* 48 (2008): 15-28.

Rahman M., Seah W.K.H. & Teo T.T. "The Machinability of Inconel 718." *Journal of Materials Processing Technology* 63 (1997): 199–204.

Rahman M., Wong Y.S. & Zareena A.R. "Machinability of Titanium Alloys." *JSME Series C* 46.1 (2003): 107-115.

Ranganath S., Guo C. & Hegde P. "A Finite Element Modeling Approach to Predicting White Layer Formation in Nickel Superalloys." *CIRP Annals – Manufacturing Technology* 58 (2009): 77-80.

Ranganath S., Guo C. & Holt S. "Experimental Investigations into the Carbide Cracking Phenomenon on Inconel 718 Superalloy Material." *ASME 2009 International Manufacturing Science and Engineering Conference* (2009).

Ratchev S.M., Afazov S.M., Becker A.A. & Liu S. "Mathematical Modelling and Integration of Micro-Scale Residual Stresses into Axisymmetric FE Models of Ti6Al4V Alloy in Turning." *Manufacturing Science and Technology* 4 (2011): 80-89.

Ruud C.O., DiMascio P.S. & Yavelak J.J. "Comparison of Three Residual Stress Measurement Methods on a Mild Steel Bar." *Experimental Mechanics* 25.4 S(1985): 338-343.

Sadat A.B. "Surface Region Damage of Machined Inconel 718 Nickel-Base Superalloy Using Natural and Controlled Contact Length Tools." *Wear* 119 (1987): 225–235.

Sadat A.B., Reddy M.Y. & Wang B.P. "Plastic Deformation Analysis in Machining of Inconel 718 Nickel-Base Superalloy Using Both Experimental and Numerical Methods." *International Journal of Mechanical Sciences* 33.10 (1991): 829–842.

Schlauer C., Peng R.L. & Oden M. "Residual Stresses in a Nickel-Based Superalloy Introduced by Turning." *Material Science Forum* 404-407 (2002): 173-178.

Sharman A.R.C, Hughes J.I. & Ridgway K. "Workpiece Surface Integrity and Tool Life Issues When Turning Inconel 718 Nickel Based Superalloy." *Machining Science and Technology* 8.3 (2004): 399–414.

Sharman A.R.C., Hughes J.I. & Ridgway K. "An Analysis of the Residual Stresses Generated in Inconel 718 When Turning." *Journal of Materials Processing Technology* 173 (2006): 359-367.

Sharman A.R.C., Hughes J.I. & Ridgway K. "Surface Integrity and Tool Life When Turning Inconel 718 Using Ultra-High Pressure and Flood Coolant Systems." *Proc. Inst. Mech. Engrs. Part B: Journal of Engineering Manufacture* 222 (2008): 653-664.

Sima M. & Özel T. "Modified Material Constitutive Models for Serrated Chip Formation Simulations and Experimental Validation in Machining of Titanium Alloy Ti-6Al-4V." *International Journal of Machine Tools and Manufacture* 50 (2010): 943–960.

Sima M., Ulutan D. & Özel, T. "Effects of Tool Micro-Geometry and Coatings in Turning of Ti-6Al-4V Titanium Alloy." *Proceedings of the 39th North American Manufacturing Research Conference*, June 13-17 (2011), Oregon State University, Corvallis, Oregon.

Sun J. & Guo Y.B. "A Comprehensive Experimental Study on Surface Integrity by End Milling Ti-6Al-4V." *Journal of Materials Processing Technology* 209 (2009): 4036-4042.

Sun S., Brandt M. & Dargusch M.S. "Characteristics of Cutting Forces and Chip Formation in Machining of Titanium Alloys." *International Journal of Machine Tools and Manufacture* 49 (2009): 561-68.

Sutter G. & Molinari A. "Analysis of the Cutting Force Components and Friction in High Speed Machining." *Journal of Manufacturing Science and Engineering* 127 (2005): 245-250.

Thomas M., Turner S. & Jackson M. "Microstructural Damage during High-Speed Milling of Titanium Alloys." *Scripta Materialia* 62 (2010): 250-253.

Uhlmann E., Graf von der Schulenburg M. & Zettier R. "Finite Element Modeling and Cutting Simulation of Inconel 718." *Annals of the CIRP* 56.1 (2007): 61-64.

Ulutan D. & Özel T. "Machining Induced Surface Integrity in Titanium and Nickel Alloys: A Review." *Int J Mach Tool Manu* 51 (2011): 250-280.

Ulutan, D. & Özel, T. "A Methodology to Determine Friction in Orthogonal Cutting with Application to Machining Titanium and Nickel Based Alloys." *Proceedings of ASME Manufacturing Science and Engineering Conference (MSEC)*, paper no: MSEC2012-7275, June 3-7 (2012), University of Notre Dame, Indiana.

Ulutan, D. & Özel, T. "Determination of Constitutive Material Model Parameters in FE-Based Machining Simulations of Ti-6Al-4V and IN-100 Alloys: An Inverse Methodology" (under review).

Ulutan, D. & Özel, T. "Determination of Tool Friction in Presence of Flank Wear and Stress Distribution Based Validation using Finite Element Simulations in Machining of Titanium and Nickel Based Alloys" (under review).

Ulutan, D., Sima, M. & Özel, T. "Prediction of Machining Induced Surface Integrity using Elastic-Viscoplastic Simulations and Temperature-Dependent Flow Softening Material Models in Titanium and Nickel-based alloys." *Advanced Materials Research* 223 (2011): 401-410.

Walker D. "Residual Stress Measurement Techniques." *Advanced Materials & Processes* 159.8 (2001): 30-33.

Wang Z.G., Rahman M. & Wong Y.S. "Tool Wear Characteristics of Binderless CBN Tools Used in High-Speed Milling of Titanium Alloys." *Wear* 258 (2005): 752-758.

Woon K.S., Rahman M., Neo K.S. & Liu K. "The Effect of Tool Edge Radius on the Contact Phenomenon of Tool-Based Micromachining." *International Journal of Machine Tools & Manufacture* 48 (2008): 1395-1407.

Wu Q. "Serrated Chip Formation and Tool-Edge Wear in High-Speed Machining of Advanced Aerospace Materials." Utah State University, Logan, Utah, 2007.

Wyen C.-F., Wegener K. "Influence of Cutting Edge Radius on Cutting Forces in Machining Titanium." *CIRP Annals – Manufacturing Technology* 59.1 (2010): 93-96.

Yen Y.C., Jain A. & Altan T. "A Finite Element Analysis of Orthogonal Machining Using Different Tool Edge Geometries." *Journal of Materials Processing Technology* 146 (2004): 72-81.

Zhang B., Mynors D.J., Mugarra A. & Ostolaza K. "Representing the Superplasticity of Inconel 718." *Journal of Materials Processing Technology* 153-154 (2004): 694-698.

Zhang B., Shen W., Liu Y., Tang X. & Wang Y. "Microstructures of Surface White Layer and Internal White Adiabatic Shear Band." *Wear* 211 (1997): 164-168.

Zorev N.N. "Interrelationship between Shear Processes Occurring Along Tool Faces and on Shear Plane in Metal Cutting." *International Research in Production Engineering, Proceedings of the International Production Engineering Research Conference* (1963): 42-49.

Zou B., Chen M., Huang C. & An Q. "Study on Surface Damages Caused by Turning NiCr20TiAl Nickel-Based Alloy." *Journal of Materials Processing Technology* 209 (2009): 5802-5809.

Zoya Z.A. & Krishnamurty R. "The Performance of CBN Tools in the Machining of Titanium Alloys." *Journal of Materials Processing Technology* 100 (2000): 80-86.

CURRICULUM VITA

DURUL ULUTAN

EDUCATION

2009 – 2013	**Ph.D.**, Industrial and Systems Engineering **Rutgers University**, New Brunswick, NJ
2008 – 2009	Mechanical Engineering and Applied Mechanics **University of Rhode Island,** Kingston, RI
2005 – 2007	**M.S.**, Mechanical Engineering **Koç University**, Istanbul, TURKEY
2006	Mechanical Engineering **University of British Columbia**, Vancouver, BC
2001 – 2005	**B.Sc.**, Mechanical Engineering **Koç University**, Istanbul, TURKEY

PUBLICATIONS

D. Ulutan, T. Özel. "Determination of Constitutive Material Model Parameters in FE-Based Machining Simulations of Ti-6Al-4V and IN-100 Alloys: An Inverse Methodology" (under review).

D. Ulutan, T. Özel. "Determination of Tool Friction in Presence of Flank Wear and Stress Distribution Based Validation using Finite Element Simulations in Machining of Titanium and Nickel Based Alloys" (under review).

T. Özel, **D. Ulutan**. "Investigations on Mechanics of Machining Nickel-Based Super Alloy IN-100" (under review).

A. Kortabarria, A. Madariaga, E. Fernandez, J.A. Esnaola, P.J. Arrazola, C. Cappellini, **D. Ulutan**, T. Özel. "On the Machining Induced Residual Stresses in IN718 Nickel-Based Alloy: Experiments and Predictions with Finite Element Simulation" (under review).

D. Ulutan, T. Özel. "Multi-objective Optimization of Experimental and Simulated Residual Stresses in Turning of Nickel-alloy IN100." *Materials and Manufacturing Processes* (2012).

D. Ulutan, T. Özel. "A Methodology to Determine Friction in Orthogonal Cutting with Application to Machining Titanium and Nickel Based Alloys." *Proceedings of ASME Manufacturing Science and Engineering Conference (MSEC)*, paper no: MSEC2012-7275, June 3-7 (2012), University of Notre Dame, Indiana.

T. Özel, **D. Ulutan.** "Prediction of Machining Induced Residual Stresses in Turning of Titanium and Nickel Based Alloys with Experiments and Finite Element Simulations," *CIRP Annals - Manufacturing Technology* 61.2 (2012), Accepted.

D. Ulutan, T. Özel. "Machining Induced Surface Integrity in Titanium and Nickel Alloys: A Review." *International Journal of Machine Tools and Manufacture 51.3* (2011): 250-280.

D. Ulutan, M. Sima, T. Özel. **"**Prediction of Machining Induced Surface Integrity using Elastic-Viscoplastic Simulations and Temperature-Dependent Flow Softening Material Models in Titanium and Nickel-Based Alloys." *Advanced Materials Research 223* (2011): 401-410.

T. Özel, M. Sima, **D. Ulutan**, A.K. Srivastava. "Collaborative Research: Improving Machinability of Titanium Alloys Using Physics-Based Simulation Modeling." *2011 NSF Engineering Research and Innovation Conference* (2011)*,* Atlanta, Georgia.

T. Özel, T. Thepsonthi, **D. Ulutan**, B. Kaftanoğlu. "Experiments and Finite Element Simulations on Micro-Milling of Ti-6Al-4V Alloy with Uncoated and cBN Coated Micro-Tools." *CIRP Annals – Manufacturing Technology 60* (2011): 85-88.

M. Sima, **D. Ulutan**, T. Özel. "Effects of Tool Micro-Geometry and Coatings in Turning of Ti-6Al-4V Titanium Alloy." *Proceedings of NAMRI/SME 39* (2011): 395-402.

D. Ulutan, I. Lazoglu, C. Dinc. "Three-Dimensional Temperature Prediction in Machining Processes Using Finite Difference Method." *Journal of Materials Processing Technology 209* (2009): 1111-1121.

I. Lazoglu, **D. Ulutan**, B. E. Alaca, S. Engin. "An Enhanced Analytical Model for Residual Stress Prediction in Machining." *CIRP Annals 57.1* (2008): 81-84.

D. Ulutan, B. Erdem Alaca, I. Lazoglu. "Analytical Modeling of Residual Stresses in Machining." *Journal of Materials Processing Technology 183* (2007): 77-87.